Preparation of advanced porous structures by stereolithography for application in tissue engineering

Ferry Melchels

PhD thesis with references and summaries in English and Dutch
University of Twente, Enschede, The Netherlands
February 2010

The research in this thesis was carried out from 2005 until 2009 in the research group Polymer Chemistry and Biomaterials of the MIRA Institute for Biomedical Technology and Technical Medicine, University of Twente, Enschede, The Netherlands. The research was financially supported by the European Union in the 6th framework program 'A Systems Approach to Tissue Engineering Processes and Products', www.stepsproject.com.

Cover art by Annie Keijsers-Duijf

This publication is supported by:
Nederlandse vereniging voor Biomaterialen en Tissue Engineering
Netherlands society for Biomaterials and Tissue Engineering

Printed by Wöhrmann Print Service, Zutphen, The Netherlands

Samenstelling van de commisie:

Voorzitter	prof. dr. G. van der Steenhoven
Promotor	prof. dr. J. Feijen
Promotor	prof. dr. D.W. Grijpma
Leden	prof. dr. G.J. Vancso Universiteit Twente, Nederland
	prof. dr. V. Subramaniam Universiteit Twente, Nederland
	prof. dr. L. Ambrosio Università di Napoli Federico II, Italia
	prof. dr. W.E. Hennink Universiteit Utrecht, Nederland
	prof. dr. P. Buma Radboud Universiteit Nijmegen, Nederland

PREPARATION OF ADVANCED POROUS STRUCTURES BY STEREOLITHOGRAPHY FOR APPLICATION IN TISSUE ENGINEERING

PROEFSCHRIFT

ter verkrijging van
de graad van doctor aan de Universiteit Twente,
op gezag van de rector magnificus,
prof. dr. H. Brinksma,
volgens besluit van het College voor Promoties
in het openbaar te verdedigen
op vrijdag 21 mei 2010 om 16:45 uur

door

FERRY PETRUS WILHELMUS MELCHELS

geboren op 2 december 1979
te Gendt

Dit proefschrift is goedgekeurd door de promotoren:
prof. dr. Jan Feijen
prof. dr. Dirk W. Grijpma

ISBN: 978-90-365-3019-4

This publication is sponsored by

GE Healthcare

Publications

Published or accepted

Chapter 2: F. P. W. Melchels, J. Feijen, D. W. Grijpma, A review on stereolithography and its applications in biomedical engineering. *Biomaterials,* accepted

Chapter 3: J. Jansen, F. P. W. Melchels, D. W. Grijpma, J. Feijen, Fumaric acid monoethyl ester-functionalised poly(D,L-lactide)/N-vinyl-2-pyrrolidone resins for the preparation of tissue engineering scaffolds by stereolithography. *Biomacromolecules* **2009**, *10*, 214

Chapter 4: F. P. W. Melchels, J. Feijen, D. W. Grijpma, A poly(D,L-lactide) resin for the preparation of tissue engineering scaffolds by stereolithography. *Biomaterials* **2009**, *30*, 3801

Appendix A: F. P. W. Melchels, J. Feijen, D. W. Grijpma, Poly(D,L-lactide)/hydroxyapatite composite tissue engineering scaffolds prepared by stereolithography. in *2nd Chinese-European Symposium on Biomaterials in Regenerative Medicine*, Barcelona **2009**

Submitted for publication

Chapter 5: F. P. W. Melchels, A. H. Velders, J. Feijen, D. W. Grijpma, Hydrolytically degradable poly(D,L-lactide) networks characterised by NMR

Chapter 6: F. P. W. Melchels, K. Bertoldi, R. Gabbrielli, A. H. Velders, J. Feijen, D. W. Grijpma, Advanced tissue engineering scaffolds with designed pore network architectures prepared by stereolithography

Chapter 7: F. P. W. Melchels, A. M. C. Barradas, C. A. van Blitterswijk, J. de Boer, J. Feijen, D. W. Grijpma, Effects of the architecture of tissue engineering scaffolds on cell seeding and culturing

Chapter 9: T. M. Seck, F. P. W. Melchels, J. Feijen, D. W. Grijpma, Designed biodegradable hydrogel structures prepared by stereolithography using poly(ethylene glycol)/poly(D,L-lactide)-based resins

Table of Contents

Chapter 1 - General introduction

Biomaterials and tissue engineering

One of the most distinctive features that distinguish man from other species is that man adapts his environment to his own benefit. For thousands of years, man has built houses for shelter, domesticated animals for food and labour, and cultivated crops to improve the quality and the length of his life. With the development of medicine, man started to interfere with the processes that occur within the human body as well. The first surgeries took place in ancient Egypt over 4000 years ago, and involved the use of non-viable or 'dead' materials. For example, amputated toes were replaced with wooden toes and linen was used for suturing.[1] Two thousand years later, dental implants made of gold or wrought iron were used by the Romans, Chinese and Aztecs.[2] Other materials that were applied in these times were ivory and bamboo, for example for bone replacement. Now -another two thousand years later- we live in a world where a substantial part of the population carries plastic, metal, ceramic or silicone rubber parts in their body. Such materials, which are "*intended to interface with biological systems to evaluate, treat, augment or replace any tissue, organ or function in the body"* are termed biomaterials.[3]

Biomaterials as implants or in medical devices in contact with the body, have improved the quality of life of many people that have lost a body part or its function. However, no medical solution is as good as the original: undamaged tissues and organs. The human body has a tremendous capacity of recovering after trauma or disease. Particularly stem cells can induce the regeneration of tissues. A relatively new area of medicine that aims to aid the body in the regeneration of defected tissues and organs is tissue engineering. This term was introduced in a groundbreaking *Science*-paper by Langer and Vacanti in 1993, as "*an interdisciplinary field, that applies the principles of engineering and the life sciences toward the development of biological substitutes that restore, maintain or improve the tissue function*".[4]

However, as is often the case in young areas of science, the definition of tissue engineering has been discussed and redefined many times. A recent definition by Williams that covers the current consensus very well, is stated as follows:[5] "*Tissue engineering is the creation (or formation) of new tissue for the therapeutic reconstruction of the human body, by the deliberate and controlled stimulation of selected target cells through a systematic combination of molecular and mechanical signals.*"

Tissue engineering involves the use of cells, scaffolds, and often also bioactive molecules such as growth factors or cell-adhesive peptides. A scaffold is a porous material that acts as a mechanical support or artificial extracellular matrix for the cells that are to generate new tissue. The growth factors or peptides provide molecular signals that direct cells to proliferate or to differentiate into a specific lineage. In practice, cells are isolated from a patient or donor, cultured to become a large population, and then seeded into a porous scaffold. The cell-seeded scaffold can either be implanted directly to regenerate the defected tissue, or the construct is matured *in vitro* prior to implantation (Figure 1.1). Tissue maturation refers to the proliferation and differentiation of cells, secretion of extracellular matrix proteins, and possibly formation of a vascular network.

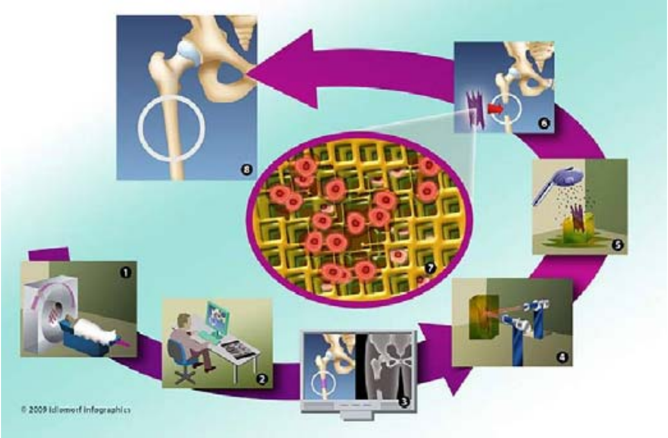

Figure 1.1: Principle of scaffold-based tissue engineering. A tailored scaffold is prepared based on medical imaging data (1-5) and implanted into the patient (6), after seeding with cells (7), In time, the scaffold is resorbed and the implanted construct is remodelled, to finally form functional tissue (8).

Most often a biodegradable material is chosen to prepare the scaffold, as in time the newly formed extracellular matrix will take over its supporting function. The material can be polymeric, ceramic, natural or composite in nature. The choice of material determines mechanical properties, degradation behaviour and biological functionality of the scaffold. Besides the material, the shape and internal pore network architecture of the scaffold also influence these characteristics.

An important part of this thesis focuses on **the architecture of the pore network of tissue engineering scaffolds**; on the preparation of scaffolds with different architectures and their functionality in tissue engineering.

The preparation of scaffolds using solid freeform fabrication methods

Conventional techniques for preparing porous structures to use as tissue engineering scaffolds comprise porogen leaching, phase-separation/freeze-drying and gas foaming processes. However, in the last decade, solid freeform fabrication (SFF) methods have increasingly been applied for this purpose.

SFF refers to the computer-controlled fabrication of parts in an additive process, from a computer-aided design. Using these techniques, it is possible to generate individual products or small series of products with complex structures in a fast way.[6] The first intended and most common use is rapid prototyping (RP), in which SFF techniques speed up and improve the design process by enabling the making of physical models of designed products in a matter of hours. For high-end applications such as tissue engineering, the relatively high cost per produced part can be acceptable to employ SFF techniques for manufacturing purposes. As a result of the development of these technologies, tissue-engineered constructs can be prepared that contain a controlled spatial distribution of cells and growth factors, as well as engineered gradients of scaffold materials with a designed microstructure.[7]

For the fabrication of tissue engineering scaffolds, SFF techniques have several advantages over conventional techniques:

- Excellent control over (pore network) design and properties; optimisation is possible
- Excellent reproducibility; small sample-to-sample variations
- Improved mechanical properties of the scaffolds
- Higher pore interconnectivities, enhanced permeability of the scaffolds
- Better suited for modelling (computational flow dynamics, cell proliferation and differentiation behaviour)

Stereolithography and photo-polymerisation

Common and well-established SFF technologies are stereolithography, selective laser sintering, 3D printing and fused deposition modelling. Of these techniques, stereolithography is the most versatile method with the highest accuracy and precision.[8] Its working principle is based on spatially controlled solidification of a liquid photo-polymerisable resin. Using a computer-controlled laser beam or a digital light projector with a computer-driven building stage, a solid, 3-dimensional object can be constructed in a layer-by-layer fashion.

Spatial control is one of the advantages of photo-initiated polymerisation, next to short polymerisation times, temporal control and the ability to carry out the polymerisation under mild conditions. This has led to the application of photo-initiated biodegradable networks as surgical implants,[9] glues[10] and drug delivery devices.[11] By altering the chemistry, the material properties of such networks (mechanical properties, hydrophilicity, cell-material interactions and degradation kinetics) can be tailored.[12] Photo-initiated networks can be prepared in any shape using stereolithography, if one can make a liquid photo-curable resin that forms a mechanically stable, solid material upon photo-polymerisation. So far, the number of stereolithography resins available for use in biomedical applications is limited. The development of new biodegradable resins would allow the preparation of well-defined tissue engineering scaffolds for a wide range of tissues, as well as other biomedical devices.

Aims and outline of the thesis

The aims of this thesis are:

- to develop new photo-crosslinkable resins (particularly ones based on poly(lactide)) that result in biocompatible, biodegradable materials, and can be processed by stereolithography
- to characterise these photo-crosslinked materials with respect to properties relevant for biomedical applications
- to design, prepare and characterise porous tissue engineering scaffolds, prepared by stereolithography using the developed resins
- to investigate the implications and opportunities of a well-defined scaffold pore architecture in tissue engineering

In **Chapter 2**, the stereolithography technique is described. Its principles of operation are explained, as well as the possibilities and limitations regarding choice of materials and accuracy of the fabrication process. Particularly, the biomedical applications of stereolithography are reviewed.

In **Chapter 3**, we describe the preparation of polymer networks with tailored hydrophilicity, by photo-crosslinking fumarate-functionalised PDLLA oligomers using N-vinyl-2-pyrrolidone as a hydrophilic reactive diluent. The networks are characterised with respect to their thermal and mechanical properties, and designed network structures are prepared by stereolithography.

Chapter 4 reports on the use of methacrylate-functionalised PDLLA oligomers and a *non-reactive* diluent as a new stereolithography resin. Macromers of different molecular architectures are prepared, and their corresponding resins and photo-crosslinked networks are characterised with respect to their mechanical-, thermal- and network properties. Stereolithographic scaffold fabrication and cell proliferation on these networks are also assessed.

Chapter 5 describes the molecular characterisation of photo-crosslinked PDLLA networks by nuclear magnetic resonance spectroscopy in the solid solvent-swollen state, enabling the determination of the average chain length of the poly(methacrylate) crosslink chains. The *in vitro* degradation behaviour of the networks is investigated and reported here as well.

Chapter 6 describes the design and fabrication of different porous architectures by stereolithography. Rigid PDLLA structures are prepared, as well as highly flexible poly(D,L-lactide-*co*-ε-caprolactone) structures. The mechanical properties of precisely fabricated structures are determined and compared to the outcomes of predictive numerical analyses.

Chapter 7 reports on the results of a comparative study on cell seeding and cell culturing using porous PDLLA scaffolds with either a well-defined, open gyroid pore network architecture prepared by stereolithography, or a random-pore network architecture obtained by salt-leaching.

Chapter 8 presents a model system for the perfusion seeding of porous scaffolds with different pore network designs. The distributions of cells seeded in scaffolds with an isotropic gyroid pore network are compared with scaffolds that have a gradient in porosity and pore size. The outcomes are related to flow profiles throughout the perfused scaffolds. These profiles are obtained by computational fluid dynamics modelling.

In **Chapter 9** we describe the preparation of designed biodegradable hydrogel structures using stereolithography. Poly(ethylene glycol) oligomers are extended with hydrolytically degradable D,L-lactide blocks and then functionalised with methacrylate end groups. Porous hydrogel structures are fabricated using these macromers, and subsequently characterised.

References

[1] B. D. Ratner, in *Advances in Biomaterials 2008*, Washington **2008**.

[2] E. Crubezy, P. Murail, L. Girard, J. P. Bernadou, *Nature* **1998**, *391*, 29.

[3] D. F. Williams, *The Williams Dictionary of Biomaterials*, Liverpool University Press, Liverpool **1999**.

[4] R. Langer, J. P. Vacanti, *Science* **1993**, *260*, 920.

[5] D. F. Williams, *Biomaterials* **2009**, *30*, 5897.

[6] B. Wendel, D. Rietzel, F. Kuhnlein, R. Feulner, G. Hulder, E. Schmachtenberg, *Macromolecular Materials and Engineering* **2008**, *293*, 799.

[7] D. W. Hutmacher, *Trends in Biotechnology* **2004**, *22*, 354.

[8] M. M. Savalani, R. A. Harris, *Proceedings of the Institution of Mechanical Engineers Part H-Journal of Engineering in Medicine* **2006**, *220*, 505.

[9] M. D. Timmer, C. G. Ambrose, A. G. Mikos, *Journal of Biomedical Materials Research Part A* **2003**, *66A*, 811.

[10] D. Miki, K. Dastgheib, T. Kim, A. Pfister-Serres, K. A. Smeds, M. Inoue, D. L. Hatchell, M. W. Grinstaff, *Cornea* **2002**, *21*, 393.

[11] B. Amsden, *Soft Matter* **2007**, *3*, 1335.

[12] J. L. Ifkovits, J. A. Burdick, *Tissue Engineering* **2007**, *13*, 2369.

Chapter 2 - A review on stereolithography and its applications in biomedical engineering

Ferry Melchels[1], Jan Feijen[1] and Dirk Grijpma[1, 2]

Stereolithography is a solid freeform technique (SFF) that was introduced nearly 25 years ago. Although many other techniques have been developed since then, stereolithography remains one of the most powerful and versatile of all SFF techniques. It has the highest fabrication accuracy and an increasing number of materials that can be processed is becoming available. In this chapter we discuss the characteristic features of the stereolithography technique and compare it to other SFF techniques. The biomedical applications of stereolithography are reviewed, as well as the biodegradable resin materials that have been developed for use with stereolithography. Finally, an overview of the application of stereolithography in preparing porous structures for tissue engineering is given.

---

[1] MIRA Institute for Biomedical Technology and Technical Medicine, and Department of Polymer Chemistry and Biomaterials, University of Twente, P.O. Box 217, 7500 AE, Enschede, The Netherlands

[2] Department of Biomedical Engineering, University Medical Centre Groningen and University of Groningen, P.O. Box 196, 9700 AD Groningen, The Netherlands

Introduction

The advance of solid freeform fabrication techniques has significantly improved the ability to prepare structures with precise geometries, using computer aided designs and data from (medical) imaging.[1] These techniques include selective laser sintering, fused deposition modelling, 3D printing and stereolithography. Stereolithography is particularly versatile with respect to the freedom of designing structures and the scales at which these can be built: sub-micron sized structures as well as decimetre-sized objects have been fabricated. In the biomedical field, these developments have led to the fabrication of patient-specific models for mould-assisted implant fabrication,[2] aids for complex surgery[3] and tailor-made parts such as hearing aids. More recently, biocompatible and biodegradable materials have been developed for the preparation of medical implants, such as tissue engineering scaffolds, by stereolithography.[4-12]

In this chapter we review the materials that have been developed for stereolithography, and their use in the biomedical field. The principles of operation of the technique are discussed. The chemistry, mechanical properties and degradation behaviour of structures built by stereolithography are considered, especially with regard to their application as an implantable device.

Rapid prototyping and manufacturing

Originally, solid freeform fabrication techniques were developed to create prototypes for purposes of designing new products. Traditional prototyping methods involve laborious mould making and casting steps,[13] whereas the ability to create an object within hours from a computer design by rapid prototyping (RP) significantly speeds up the development of products. Currently, rapid prototyping using SFF techniques is common practice in the automotive industry, for jewellery making and for designing end-user devices and appliances.[14] Also in designing surgical tools, implants and other biomedical devices, these additive fabrication methods have been used.

As solid freeform fabrication technologies are continuously evolving, fabrication costs are decreasing and the properties of the manufactured parts are becoming better. Therefore, these techniques are more and more being used for the rapid manufacturing of products in small series. The time gain in product development, freedom of design and tool-free fabrication can outweigh the increased fabrication costs per item.[14]

Stereolithography was developed by 3D Systems in 1986, being the first commercially available SFF technique. Several other techniques have been developed over the past 20 years, of which Figure 2.1 gives an overview. Different setups are required to build objects of different sizes, but each technique has a lower limit in size of the smallest details that can be produced. In general, there is a clear relationship between the scale at which an object can be built by an SFF technique and the resolution with which it is built: the higher the resolution with which a part can be built, the smaller will be its maximum size.

Regarding accuracy and resolution, stereolithography is superior to all other SFF techniques. While in most fabrication techniques the smallest details are 50-200 μm in size, many commercially available stereolithography setups can build objects that measure several cubic centimetres at an accuracy of 20 μm. Stereolithography setups have been developed that make use of two-photon initiation of the polymerisation reaction, and in the laboratory micron-sized structures with sub-micron resolution have been fabricated using these setups.[15] This accuracy has not been achieved with other RP techniques.

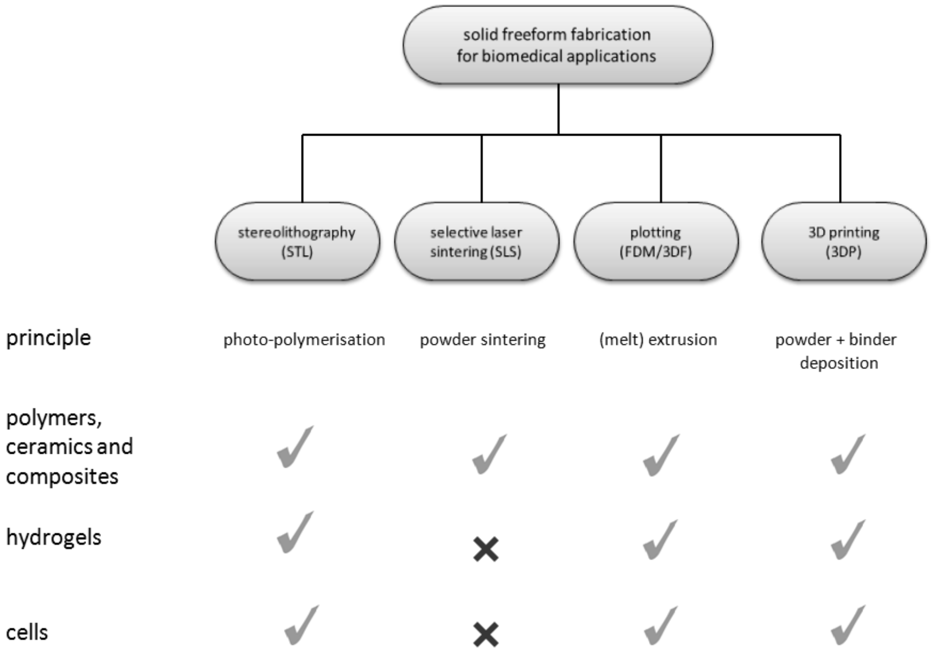

	stereolithography (STL)	selective laser sintering (SLS)	plotting (FDM/3DF)	3D printing (3DP)
principle	photo-polymerisation	powder sintering	(melt) extrusion	powder + binder deposition
polymers, ceramics and composites	✓	✓	✓	✓
hydrogels	✓	✗	✓	✓
cells	✓	✗	✓	✓

Figure 2.1: Overview of additive processing/solid freeform fabrication technologies applied for biomedical applications. For each technique, the symbols indicate whether polymers and/or ceramics, hydrogels, and living cells have been employed.

Stereolithography

Like most solid freeform fabrication techniques, stereolithography is an additive fabrication process that allows the fabrication of parts from a computer-aided design (CAD) file. The designed external and internal (pore) geometry of the structure that is to be built can either be devised using 3D drawing computer software, be described using mathematical equations,[16] or be derived from scanning data of (clinical) imaging technologies such as magnetic resonance imaging (MRI), or tomography techniques.[17] The possibility to use data from scans make these manufacturing technologies particularly useful for many applications in biomedical engineering, as it enables to fabricate patient-specific models or implants. The CAD-file describes the geometry and size of the parts to be built. For this, the STL file format was developed; an STL file lists the coordinates of triangles that together make up the surface of the designed 3D structure. This designed structure is (virtually) sliced into layers of the thickness that is used in the layer-by-layer fabrication process (usually in the range of 25-100 μm). These data are then uploaded to the stereolithography apparatus (SLA) and the structure is fabricated (Figure 2.2). Computed tomography (CT)-scanning of the built structures allows assessing the accuracy of the process, by comparing the scan data to the design.

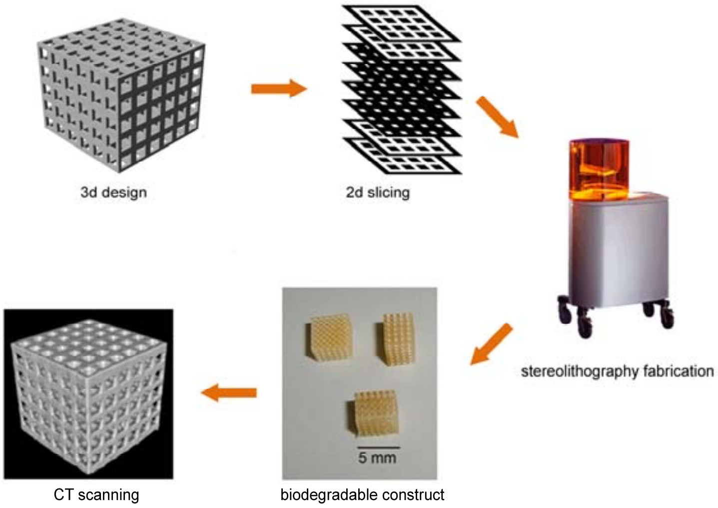

Figure 2.2: Overview of the processes involved in the design and fabrication of structures by stereolithography.

The manufacturing of 3D objects by stereolithography is based on the spatially controlled solidification of a liquid resin by photo-polymerisation. Using a computer-controlled laser beam or a digital light projector with a computer-driven building stage, a pattern is illuminated on the surface of a resin. As a result of this, the resin in the pattern is solidified to a defined depth, causing it to adhere to a support platform. After photo-polymerisation of the first layer, the platform is moved away from the surface and the built layer is recoated with liquid resin. A pattern is then cured in this second layer. As the depth of curing is slightly larger than the platform step height, good adherence to the first layer is ensured (unreacted functional groups on the solidified structure in the first layer polymerise with the illuminated resin in the second layer).

These steps (the movement of the platform and the curing of an individual pattern in a layer of resin) are repeated to construct a solid, three-dimensional object. After draining and washing-off excess resin, an as-fabricated (or green) structure is obtained. In this structure, the conversion of reactive groups is usually incomplete, and post-curing with (stroboscopic) ultraviolet light is often done to improve mechanical properties of the structures.

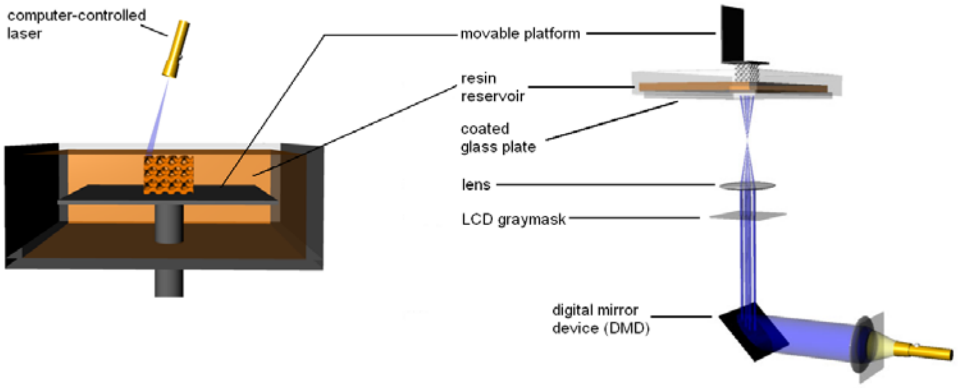

Figure 2.3: Schematic of two types of stereolithography setups. Left: a bottom-up system with scanning laser. Right: a top-down setup with digital light projection.

Figure 2.3 shows schematic diagrams of two types of stereolithography setups. In both systems objects are built in a layer-by-layer manner by spatially-controlled photo-polymerisation of a liquid resin; differences are in the build orientation and in the method of illumination.

To date, most SLA setups in use resemble the ones first developed.[4, 8, 12, 18] Using a computer-controlled laser beam to draw a pattern, structures are built bottom-up from a support platform that rests just below the resin surface (Figure 2.3, left). Only a thin layer of resin is illuminated from above, and cured on top of the structure as it is built in a layer-by-layer manner. A top-down approach is increasingly being applied in stereolithography. In such setups, light is projected on a transparent, non-adhering plate from underneath (the transparent plate forms the bottom of the vessel that contains the resin), and the support or build platform is dipped into the resin from above (Figure 2.3, right). Although the structures are subjected to larger mechanical forces, as they have to be separated from the bottom plate after illumination of each layer, this approach has several advantages over the bottom-up systems: recoating of the structure is not required, the surface being illuminated is always smooth, only small amounts of resin are required, and the illuminated layer is not exposed to the atmosphere, so oxygen inhibition is limited.

Digital light projection (DLP) is emerging as a method of illuminating the resin. [10, 11, 19-21] In this technology a digital mirror device (DMD), an array of up to several millions of mirrors that can be rotated independently to an on- and off state, is used. By projecting a two-dimensional pixel-pattern onto the transparent plate, a complete layer of resin can be cured at once (Figure 2.3 right). Build times are much reduced, as they only depend on the layer thickness and on the required exposure time, and not on their size in the x,y-plane or on the number of structures being built simultaneously.

In stereolithography, control of the thickness of the layer that is cured is essential. For a given resin, the cure depth is determined by the energy of the light to which the resin is exposed. This energy can be controlled by adjusting the power of the light source, and the scanning speed (for laser systems) or the exposure time (for projection systems). The kinetics of the curing reactions taking place are quite complex. Although the different stages of the addition-type polymerisation (initiation-propagation-termination) can be expressed mathematically, the presence of multifunctional monomers and the transition of the polymerising liquid to a solid make its description more complicated. The kinetics of photo-initiated multi-vinyl polymerisations have been discussed in an extensive review by Andrzejewska.[22]

In practice, much simpler equations are used to describe the polymerisation kinetics in the fabrication of structures by stereolithography. A semi-empirical equation that relates the thickness of a solidified layer (the cure depth, C_d in μm) to the light irradiation dose E (mJ/cm^2) is used:

$$C_d = D_p \ln \frac{E}{E_c}$$

A plot of the determined cure depth (or cured layer thickness) versus the applied irradiation dose is termed a working curve,[23] and is constructed to determine the correct settings for stereolithography fabrication. This equation is an adapted form of the Beer-Lambert equation, which describes the exponential decay of the intensity of light as it passes through a medium in which it is absorbed. In photo-polymerisations, the time required to reach the gel point depends linearly on the intensity of the light at that specific location. Therefore, the depth at which the resin is cured to the gel point (C_d) increases logarithmically with time, and thus with the applied irradiation dose (E). For a specific stereolithography setup, a resin can be characterised by a critical energy E_c (mJ/cm^2) and a penetration depth D_p (μm). As the applied irradiation dose (E) exceeds the critical energy required to reach the gel point (E_c), a solidified layer forms from the resin surface. The value of E_c depends, among others, on the concentrations of photo-initiator, and of dissolved oxygen and other inhibiting species. The penetration of light into the resin is directly related to the extinction coefficient in the Beer-Lambert equation, and is characterised by D_p.

To ensure chemical and mechanical bonding between the layers during building, the macromer conversion at the interface between layers should be slightly higher than the gel point. However, this overexposure results in (further) curing into the preceding layer, and volume elements in the preceding layer that according to the design were intended to remain uncured, will now have partially polymerised. Particularly when preparing porous structures, the effect of over-cure can be significant.[24] A high extinction coefficient of the resin corresponds to a low light penetration depth (D_p), and will allow most accurate control of the polymerisation process and minimal over-cure. The penetration depth can be decreased by increasing the photo-initiator concentration, or by including a dye in the resin. This non-reactive component competes with the photo-initiator in absorbing light. Although particularly useful when visible light sources are employed (as in general photo-initiators have low extinction coefficients in this range), the use of UV absorbers is also reported.[25] It should be realised that decreasing the light penetration depth will lead to increased building times.

Resins used in stereolithography

The limited number of resins that are commercially available for processing by stereolithography has often been considered the main limitation of the technique. The resin should be a liquid that rapidly solidifies upon illumination with light. The first resins developed for use in stereolithography were based on low-molecular weight polyacrylate or –epoxy macromers that form glassy networks upon photo-initiated polymerisation and crosslinking. Several resins have been developed over the past two decades, and the mechanical properties of the networks obtained after curing cover a wide range. The properties of parts built by stereolithography are continuously improving, making them not only useful as prototypes but also as functional parts for more demanding end-use applications.[26] Resins that can be used to create biodegradable devices for application in medicine are being developed as well, see below.

Most of the available stereolithography resins are based on low-molecular weight, multi-functional monomers, and highly crosslinked networks are formed. These materials are predominantly glassy, rigid and brittle. Only few resins have been described that allow the preparation of elastomeric objects by stereolithography. These resin formulations include macromers with low glass transition temperatures and relatively high molecular weights (1-5 kg/mol), often in combination with non-reactive diluents such as N-methylpyrrolidone (NMP) or water to reduce the viscosity of the resin.[24, 27-29]

To create polymer-ceramic composite objects,[30-33] ceramic particles (*e.g.* alumina or hydroxyapatite) are homogeneously suspended in the stereolithography resin and photo-polymerised in the SLA. Processing of the resin is more difficult, as the viscosity of the resin can significantly increase upon addition of the powder. Maximum ceramic contents of up to 53 wt% have been reported.[34] Furthermore, the ceramic particle size should be smaller than the layer thickness in the building process to prepare the objects accurately. The fabricated composite structures are in general, stiffer and stronger than the polymeric structures. Starting from these composite structures, all-ceramic objects have been made by first fabricating a composite structure by stereolithography and then burning out the polymer (pyrolysis) and sintering the ceramic particles.[34-36]

Different resins have been processed using stereolithography, leading to objects with widely differing characteristics. Although the number of resins that is available continues to increase, the technique is still limited to the use of a single resin at a time. (Note that 3D printing- and plotting techniques related to fused deposition modelling allow the use of multiple cartridges to prepare structures using different materials simultaneously.) The ability to pattern multiple resins in a construct (and even within a single layer) is possible in stereolithography too, but complex sequential polymerisation and rinsing steps are required for each layer built.[28, 37] A major technological challenge lies in developing an automated system to remove uncured resin and exchange resin reservoirs. The restriction to use one resin in stereolithography is perhaps the true major limitation of the technique.

Applications of stereolithography in biomedical engineering

The possibilities for using stereolithographic fabrication methods for biomedical applications are numerous. But, despite that the technique has been commercially available for more than 20 years; it is still not extensively used in the medical field. Below, an overview is given of (possible) biomedical applications of stereolithography.

Patient-specific models and functional parts

The ability to use data from (clinical) imaging techniques like MRI or CT makes stereolithography particularly useful for biomedical applications. Initially, these images were only used for diagnosis and pre-operative planning. With the progress in computer-aided design and manufacturing technologies, it is now possible to make use of this information in conducting the surgery itself: by making use of patient-specific models of parts of the body fabricated by stereolithography, the time in the operating theatre and the risks involved can significantly be reduced.[38, 39] In implantations using drill guides built by stereolithography, the accuracy of the implantation was much improved when compared to using conventional surgical guides, particularly in oral surgery.[3, 40] Stereolithography has been also used to fabricate moulds for the preparation of implants in cranial surgery, using data from CT scans.[2, 41]

In the abovementioned cases, the function of the structures prepared by stereolithography is in aiding the surgeon. Furthermore, the combination of medical imaging and stereolithography has been used to make models or moulds for preparing anatomically shaped implants. In this way, Sodian *et al.* prepared customised heart valves that could be placed without the need for suturing.[42] Other studies on such use of computer-aided fabrication are ear-shaped implants[43] and aortas.[44] Other tailored parts, such as hearing aids, have specific functionalities as well and are applied in contact with the body;[45] they are now routinely manufactured using stereolithography. These applications illustrate the benefits of stereolithography in the manufacturing of tailored parts for use in the clinical practice.

Implantable devices

Besides for the fabrication of surgical models, stereolithography can be used to fabricate patient-specific implantable devices. In trauma surgery, for example, a tailored implant for facial reconstruction can be obtained by imaging the undamaged side of the head and reproducing its mirror image by stereolithography. Also, a CT-image of bone with a defect due to the removal of a tumour could be used to prepare a custom-fit, biodegradable implant that supports the regeneration of bone.

For prototyping, the appearance of the built parts, its mechanical properties and biocompatibility are not very important, and most commercially available resins suffice for this purpose. However, for the direct fabrication of implantable devices, these properties are of utmost importance and special resins need to be developed and used.

The implantation of devices prepared by stereolithography has only been reported in a few cases. Matsuda *et al.* showed that degradable crosslinked structures prepared by stereolithography using poly(trimethylene carbonate-*co*-ε-caprolactone) resins caused no adverse effects after a 1 month implantation period under the dorsal skin of rats.[5] Popov *et al.* prepared non-resorbable polyacrylate and hydroxyapatite composite parts, and implanted them into the femurs of rats for time periods of up to 8 weeks. [32] Although many crosslinked polymers are not cytotoxic, the unreacted monomer and photo-initiator residues trapped in the densely crosslinked networks can be. For this reason, the built parts were extracted before the implantation using supercritical CO_2. It was shown that the extracted composite implants integrated well with surrounding bone, and that new bone had formed at the surface of the implants. This shows that anatomically shaped implants, compatible with cells and surrounding tissues can be manufactured using stereolithography.

Numerous other medical implants with tailored geometries and physical properties, such as bone fracture fixation devices, parts for artificial hips or knees, nerve guidance channels or prostheses, can be manufactured by stereolithography. Liska and co-workers characterised an extensive library of photo-curable biocompatible resin materials with a wide range of physical and chemical properties that could be used for these long-term applications (Figure 2.4).[21, 46, 47]

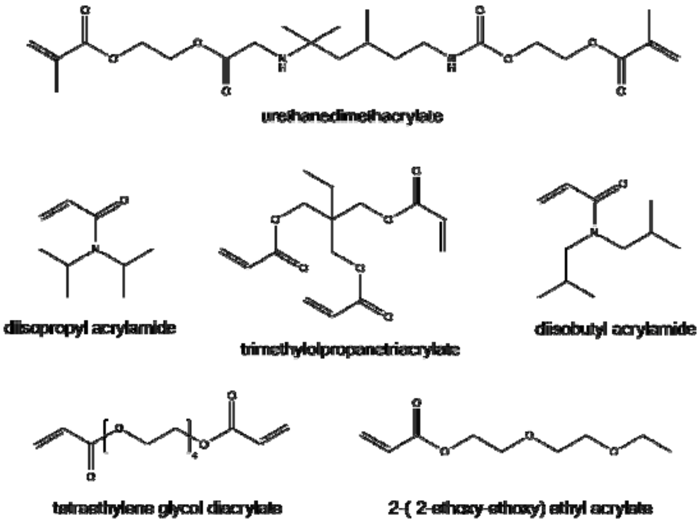

Figure 2.4: Biocompatible macromers for use in the formulation of resins for stereolithographic fabrication of durable implants.[21]

Tissue engineering

Tissue engineering is a field in biomedical engineering that is developing fast. In tissue engineering, a resorbable scaffolding structure is used in combination with cells and/or biologically active compounds to induce the (re)generation of tissues *in vitro* or *in vivo*.[48] The scaffold is a porous implant, intended as a temporary support structure for seeded cells and formed tissues. Upon implantation, it should not elicit severe inflammatory responses, and it should degrade into non-toxic compounds as newly formed tissue is formed. The scaffold is a template that allows cell adhesion and directs the formation of tissue, therefore the architecture of its inner pore network and its outer geometry need to be well-defined. For this reason, solid freeform fabrication techniques play an important role in the manufacturing of advanced tissue engineering scaffolds.

The fabrication of precisely defined tissue engineering scaffolds by stereolithography is becoming a new standard. Much work has been done in developing biocompatible and biodegradable macromers and resins. In 2000, a first report on the preparation of biodegradable structures by stereolithography appeared.[6] Liquid low molecular weight copolymers of ε-caprolactone and trimethylene carbonate were prepared by ring opening polymerisation using a polyol as initiator, and subsequently derivated at the hydroxyl termini with coumarin. Later, the same group published the use of similar oligomers, but now end-functionalised with methacrylate groups.[5] Figure 2.5 shows the structures fabricated using these macromers.

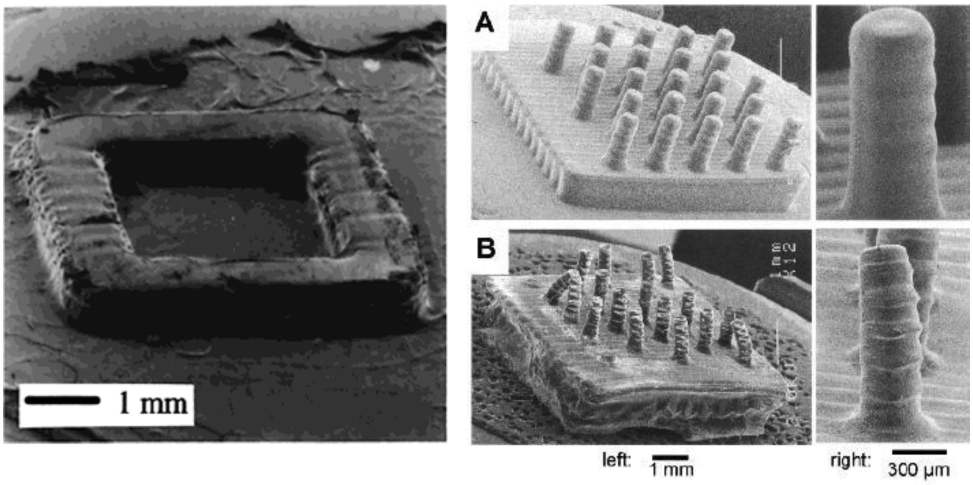

Figure 2.5: SEM images of biodegradable structures built by stereolithography intended for application in tissue engineering. Left: structures prepared from P(TMC-*co*-CL)-coumarin macromers (Matsuda *et al.*, 2000).[6] Right: structure prepared from P(TMC-*co*-CL)-acrylate (A) before and (B) after 1 month of implantation (Matsuda *et al.*, 2002).[5]

The biodegradable macromers that have been applied in stereolithography are based on functionalised oligomers with hydrolysable ester- or carbonate linkages in the main chain. Among these macromers are those based on poly(propylene fumarate)

(PPF)[12], trimethylene carbonate (TMC) and ε-caprolactone (CL)[5, 6, 9], or D,L-lactide (DLLA)[7, 11] (Figure 2.6).

The viscosity of low molecular weight macromers that have a low glass transition temperature (such as those based on TMC and CL) can be sufficiently low to allow direct processing in the stereolithography apparatus (although it should be noted that this can result in crosslinked structures with relatively poor mechanical properties). For macromers of higher molecular weights, or with relatively high glass transition temperatures (such as those based on DLLA or PPF) a diluent is required to reduce the viscosity of the resin. Typically, the highest resin viscosities that can be employed in stereolithography are approximately 5 Pa·s.[34] Macromers that contain fumarate (end)groups require a reactive diluent such as diethyl fumarate[8] or N-vinyl-2-pyrrolidone[7] to reach appropriate reaction rates. Solid or highly viscous macromers that are functionalised with more reactive groups such as (meth)acrylates, can also be diluted with non-reactive diluents. In this case, the cured material shrinks upon extraction of the diluent. As this shrinkage is isotropic, it can be taken into account when designing the scaffold structures.[11] scaffolds with well-defined architectures built by stereolithography, the size scales are relevant for tissue engineering. Scaffolds with hexagonal and cubic pores (both prepared from a PPF/DEF resin)

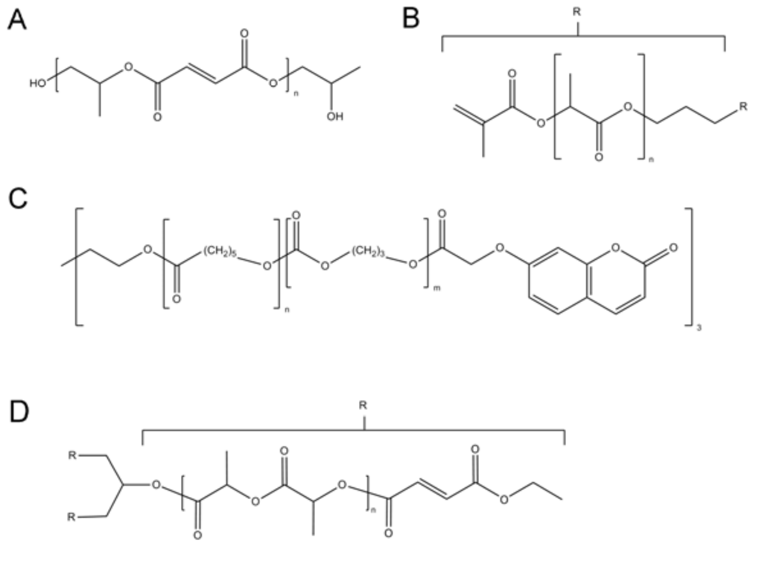

**Figure 2.6: Examples of biodegradable macromers used in stereolithography. A. Polypropylene fumarate (PPF).[8, 12, 49] B. Linear poly(D,L-lactide)-methacrylate.[11]
C. Poly(TMC-co-CL)-coumarin.[50] D. Star-shaped poly(D,L-lactide)-fumarate.[7]**

The stereolithography resins summarised above have enabled the fabrication of biodegradable tissue engineering scaffolds with a range of properties. Figure 2.7 gives two examples of tissue engineering and scaffolds with gyroid pore network architecture (PDLLA-fumarate/NVP resin) are depicted in the figure.

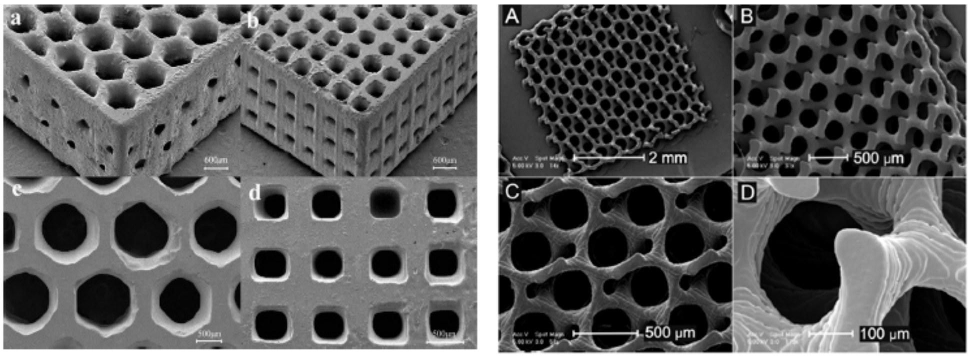

Figure 2.7: Examples of tissue engineering scaffolds built by stereolithography using PPF or PDLLA-fumarate and a reactive diluent. Left: structures prepared from PPF and DEF as a reactive diluent by Lee *et al.* (2007).[8] Right: structures prepared from PDLLA-fumarate and NVP as a reactive diluent by Jansen *et al.* (2009).[7]

The scaffold materials presented above have shown to support cell adhesion and growth. In general however, the interaction between cells and synthetic polymers is not very strong, and adhesion of the cells is facilitated by the adsorption of proteins (from the culture medium) on the surface of the pores of the scaffold. Alternatively, bioactive compounds can be included in the scaffold fabrication process. To improve the bioactivity of scaffolds in bone tissue engineering, for example, composite structures containing hydroxyapatite have been fabricated using resins containing dispersed hydroxyapatite particles. By mixing PPF and hydroxyapatite particles in diethyl fumarate as reactive diluent, a photo-polymerisable composite resin was obtained.[30] Also a PDLLA resin, containing dispersed hydroxyapatite particles, was prepared using NMP as a non-reactive diluent and subsequently employed in stereolithography.[51] Furthermore, specific protein-binding molecules have been included in the resins,[52] and proteins have been grafted onto the surface of the scaffold network.[53] Most promising are recent developments in the functionalisation of natural polymers. For the first time, using methacrylate-functionalised gelatin, an object has been made by stereolithography from a natural polymer.[54] Before, porous structures prepared by photo-curing modified chitosan showed very good endochondral ossification upon implantation.[55] Other natural polymers that have been modified to enable photo-curing are (meth)acrylated oligopeptides[56] and methacrylated hyaluronic acid.[57] It is likely that these materials will be used in stereolithography in the near future.

Stereolithography requires the use of a liquid photo-sensitive formulation that solidifies upon illumination. In general, photo-initiated addition polymerisations lead to stable non-degradable polymer chains. For application in tissue engineering, it is important that degradation products of the material from which the scaffold is prepared do not accumulate in the body. This is also of importance in other areas where degradable implants are used. The molecular weight and character of the remaining addition-type polymer determines if it can be excreted by renal clearance.[58] The kinetic chain length strongly depends on the initiating conditions of the polymerisation (nature and concentration of the photo-initiator, light intensity), and has been determined after degradation of the network[59-61] or by characterisation of the network before degradation.[62] Widely ranging values, corresponding to several monomer repeat units[60, 62] or to several thousands of monomer repeat units[59] have been reported. When employing light-induced dimerisation reactions, such as has been done with the photo-polymerisation of macromers functionalised with coumarin[6] or phenyl azide[63] end groups, long kinetic chains are not formed.

Stereolithography enables the reproducible manufacturing of tissue engineering scaffolds with well-defined architectures. However, only few attempts have been made to investigate the influence of the scaffold architecture on cell culture and tissue formation. Chu *et al.* used stereolithography to prepare hydroxyapatite scaffolds with two different pore network architectures, and investigated the regeneration of bone in the mandibles of Yucatan minipigs.[36] Significant differences between the different scaffold designs were observed with regard to the amount, distribution and functionality of the generated tissue. This indicates the importance of the pore architecture of the scaffold in *in vivo* bone formation, although extensive research is needed to draw general conclusions.

Using the various resins developed for use in stereolithography, biodegradable scaffolds have been manufactured. Although these scaffolds proved to be biocompatible as shown by *in vitro* or *in vivo* tests, the major advantage of using stereolithography, being able to prepare well-defined designed architectures, has not yet been fully utilised. Scaffolds that have been designed to have optimal mechanical and cell-delivery properties for specific applications can now be fabricated, allowing to verify the numerical models.[64] The effect of scaffold (pore network) architecture on tissue (re)generation can be investigated in detail. In the regeneration of bone for example, many different values for the optimal pore size in bone regeneration have been reported. In these studies comparisons are made in which not only the average pore size of the scaffolds differs, but different materials with different pore network architectures are employed under different experimental conditions.[65-67]

Cell-containing hydrogels

By encapsulating cells in fabricated structures, higher cell densities might be achieved than by seeding into built porous scaffolds. Also, the distribution of cells might be better controlled. Various studies have reported the use of water-soluble di(meth)acrylated poly(ethylene glycol) (PEG-DMA) to create structured, cell-containing hydrogels by stereolithography. Dhariwala *et al.* were the first to successfully encapsulate (Chinese hamster ovary) cells in PEG-DMA hydrogels, using stereolithography.[27] Later, PEG-DMA constructs containing encapsulated human dermal fibroblasts (Figure 2.8),[37] and PEG-diacrylate gel structures containing marrow stromal cells[10] were reported. In these cases, large numbers of cells could be encapsulated at high densities (several millions of cells per mL). The cells showed good survival after fabrication of the construct, especially when peptides containing RGD-sequences were incorporated in the gels.[37]

In the given examples, the cell-containing structures that were prepared by stereolithography were very elementary and consisted of only a few built layers. To create more complex 3D structures, multiple layers and longer build times would have been required. The most biocompatible of known photo-initiators, Irgacure 2959 (2-hydroxy-1-[4-(2-hydroxyethoxy)phenyl]-2-methyl-1-propanone),[68] is cytotoxic at the concentrations necessary: cell survival is approximately 25 % after 24 h in an aqueous PEG-DMA resin containing 0.5 % w/v Irgacure 2959.[37] The limited availability of cells and the possibility of non-homogeneous cell distributions due to settling of the cells in time could be other reasons why more complex structures were not prepared. With elastic modulus values of approximately 1 kPa,[27] these hydrogels seem well suited for the engineering of soft tissues, although it seems clear that much more research will need to be conducted in this direction.

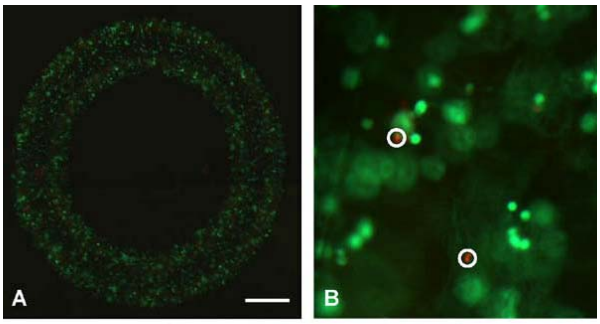

Figure 2.8: Poly(ethylene glycol)-dimethacrylate hydrogels with encapsulated cells prepared by stereolithography.[37] Live/Dead assay on human dermal fibroblasts encapsulated in the gel. Scalebar represents 1 mm.

New developments in stereolithography and related technologies

Two-photon polymerisation is increasingly used in stereolithographic fabrication. In two-photon polymerisation, the photo-initiator is excited by the (nearly) simultaneous absorption of two photons with relatively low intensity, which together introduce enough energy to break the labile bond and initiate the polymerisation reaction. As a result, two-photon polymerisation is a non-linear optical process in which the polymerisation rate is proportional to the square of the laser intensity, as opposed to a linear relationship as is the case for single-photon polymerisations. This leads to a more localised initiation of the polymerisation, and therefore to higher resolutions. Using stereolithography setups based on two-photon absorption, resolutions as high as 200 nm can be obtained. A review on two-photon polymerisation was published by Lee *et al.*,[69] and first applications in tissue engineering have also been reported.[70]

Holography or interference lithography is a technique in which two or more light sources are used to create an interference pattern. By superposition of the light waves, regular patterns with locally varying light intensities are obtained [71] It is a well-known process for the creation of micro- and nanostructures like nanopillars, nanostructured substrates, microframes, 3D photonic crystals and microsieves.[72] Interference holography provides a faster and more accurate method to solidify patterns in a photo-curable resin than can be achieved with stereolithography, and although it is restricted to a limited number of patterns it could be of interest to prepare repetitive porous structures for tissue engineering.

Conclusions

Stereolithography is a solid freeform fabrication technique that is particularly versatile with respect to the freedom of design of the structures that are to be built, and to the scales at which these can be built. It has a strong prospective for biomedical applications, especially in combination with medical imaging techniques such as MRI and CT. It has proven to facilitate, speed up, and improve the quality of surgical procedures such as implant placements and complex surgeries. Also, anatomically-shaped implants and tailor-made biomedical devices have been prepared using stereolithography. The development of new resins has enabled to directly fabricate implantable devices like biodegradable tissue engineering scaffolds. With the introduction of hydroxyapatite composites, peptide-grafted structures, cell-containing hydrogels and modified natural polymers, stereolithography has developed into a broadly applicable technique for biomedical engineering purposes.

References

[1] D. W. Hutmacher, *Trends in Biotechnology* **2004**, *22*, 354.

[2] P. S. D'Urso, W. J. Earwaker, T. M. Barker, M. J. Redmond, R. G. Thompson, D. J. Effeney, F. H. Tomlinson, *British Journal of Plastic Surgery* **2000**, *53*, 200.

[3] D. P. Sarment, P. Sukovic, N. Clinthorne, *International Journal of Oral & Maxillofacial Implants* **2003**, *18*, 571.

[4] I. K. Kwon, T. Matsuda, *Biomaterials* **2005**, *26*, 1675.

[5] T. Matsuda, M. Mizutani, *Journal of Biomedical Materials Research* **2002**, *62*, 395.

[6] T. Matsuda, M. Mizutani, S. C. Arnold, *Macromolecules* **2000**, *33*, 795.

[7] J. Jansen, F. P. W. Melchels, D. W. Grijpma, J. Feijen, *Biomacromolecules* **2009**, *10*, 214; Chapter 3 of this thesis.

[8] K. W. Lee, S. F. Wang, B. C. Fox, E. L. Ritman, M. J. Yaszemski, L. C. Lu, *Biomacromolecules* **2007**, *8*, 1077.

[9] S.-J. Lee, H.-W. Kang, J. Park, J.-W. Rhie, S. Hahn, D.-W. Cho, *Biomedical Microdevices* **2008**, *10*, 233.

[10] Y. Lu, G. Mapili, G. Suhali, S. C. Chen, K. Roy, *Journal of Biomedical Materials Research Part A* **2006**, *77A*, 396.

[11] F. P. W. Melchels, J. Feijen, D. W. Grijpma, *Biomaterials* **2009**, *30*, 3801; Chapter 4 of this thesis.

[12] M. N. Cooke, J. P. Fisher, D. Dean, C. Rimnac, A. G. Mikos, *Journal of Biomedical Materials Research Part B-Applied Biomaterials* **2003**, *64B*, 65.

[13] D. T. Pham, R. S. Gault, *International Journal of Machine Tools & Manufacture* **1998**, *38*, 1257.

[14] B. Wendel, D. Rietzel, F. Kuhnlein, R. Feulner, G. Hulder, E. Schmachtenberg, *Macromolecular Materials and Engineering* **2008**, *293*, 799.

[15] S. Maruo, K. Ikuta, H. Korogi, *Journal of Microelectromechanical Systems* **2003**, *12*, 533.

[16] R. Gabbrielli, I. G. Turner, C. R. Bowen, *Key Engineering Materials* **2008**, *361-363 II*, 901.

[17] N. J. Mankovich, D. Samson, W. Pratt, D. Lew, J. Beumer, *Otolaryngologic Clinics of North America* **1994**, *27*, 875.

[18] J. W. Lee, P. X. Lan, B. Kim, G. Lim, D.-W. Cho, *Microelectronic Engineering* **2007**, *84*, 1702.

[19] J. W. Choi, R. Wicker, S. H. Lee, K. H. Choi, C. S. Ha, I. Chung, *Journal of Materials Processing Technology* **2009**, *209*, 5494.

[20] L. H. Han, G. Mapili, S. Chen, K. Roy, *Journal of Manufacturing Science and Engineering-Transactions of the Asme* **2008**, *130*.

[21] R. Liska, M. Schuster, R. Infuhr, C. Tureeek, C. Fritscher, B. Seidl, V. Schmidt, L. Kuna, A. Haase, F. Varga, H. Lichtenegger, J. Stampfl, *Journal of Coatings Technology and Research* **2007**, *4*, 505.

[22] E. Andrzejewska, *Progress in Polymer Science* **2001**, *26*, 605.

[23] P. F. Jacobs, *Rapid Prototyping & Manufacturing: Fundamentals of Stereolithography*, Society of Manufacturing Engineers, Dearborn, MI **1992**.

[24] F. P. W. Melchels, K. Bertoldi, R. Gabbrielli, A. H. Velders, J. Feijen, D. W. Grijpma; Chapter 6 of this thesis.

[25] C. Heller, M. Schwentenwein, G. Russmueller, F. Varga, J. Stampfl, R. Liska, *Journal of Polymer Science Part a-Polymer Chemistry* **2009**, *47*, 6941.

[26] S. Mansour, A. Gilbert, R. Hague, *Materials Science and Engineering a-Structural Materials Properties Microstructure and Processing* **2007**, *447*, 277.

[27] B. Dhariwala, E. Hunt, T. Boland, *Tissue Engineering* **2004**, *10*, 1316.

[28] G. Mapili, Y. Lu, S. C. Chen, K. Roy, *Journal of Biomedical Materials Research Part B-Applied Biomaterials* **2005**, *75B*, 414.

[29] A. Bens, H. Seitz, G. Bermes, M. Emons, A. Pansky, B. Roitzheim, E. Tobiasch, C. Tille, *Rapid Prototyping Journal* **2007**, *13*, 38.

[30] J. W. Lee, G. Ahn, D. S. Kim, D. W. Cho, *Microelectronic Engineering* **2009**, *86*, 1465.

[31] C. Provin, S. Monneret, *Ieee Transactions on Electronics Packaging Manufacturing* **2002**, *25*, 59.

[32] V. K. Popov, A. V. Evseev, A. L. Ivanov, V. V. Roginski, A. I. Volozhin, S. M. Howdle, *Journal of Materials Science-Materials in Medicine* **2004**, *15*, 123.

[33] T. M. Chu, K. Szczepkowski, W. C. Wagner, J. W. Halloran, *Journal of Dental Research* **1996**, *75*, 3046.

[34] C. Hinczewski, S. Corbel, T. Chartier, *Journal of the European Ceramic Society* **1998**, *18*, 583.

[35] A. Licciulli, C. E. Corcione, A. Greco, V. Amicarelli, A. Maffezzoli, *Journal of the European Ceramic Society* **2005**, *25*, 1581.

[36] T. M. G. Chu, D. G. Orton, S. J. Hollister, S. E. Feinberg, J. W. Halloran, *Biomaterials* **2002**, *23*, 1283.

[37] K. Arcaute, B. K. Mann, R. B. Wicker, *Annals of Biomedical Engineering* **2006**, *34*, 1429.

[38] D. P. Sarment, K. Al-Shammari, C. E. Kazor, *International Journal of Periodontics & Restorative Dentistry* **2003**, *23*, 287.

[39] T. M. Binder, D. Moertl, G. Mundigler, G. Rehak, M. Franke, G. Delle-Karth, W. Mohl, H. Baumgartner, G. Maurer, *Journal of the American College of Cardiology* **2000**, *35*, 230.

[40] F. Valente, G. Schiroli, A. Sbrenna, *International Journal of Oral & Maxillofacial Implants* **2009**, *24*, 234.

[41] G. Wurm, B. Tomancok, K. Holl, J. Trenkler, *Surgical Neurology* **2004**, *62*, 510.

[42] R. Sodian, M. Loebe, A. Hein, D. P. Martin, S. P. Hoerstrup, E. V. Potapov, H. A. Hausmann, T. Lueth, R. Hetzer, *Asaio Journal* **2002**, *48*, 12.

[43] A. Naumann, J. Aigner, R. Staudenmaier, M. Seemann, R. Bruening, K. H. Englmeier, G. Kadegge, A. Pavesio, E. Kastenbauer, A. Berghaus, *European Archives of Oto-Rhino-Laryngology* **2003**, *260*, 568.

[44] R. Sodian, P. Fu, C. Lueders, D. Szymanski, C. Fritsche, M. Gutberlet, S. P. Hoerstrup, H. Hausmann, T. Lueth, R. Hetzer, *Thoracic and Cardiovascular Surgeon* **2005**, *53*, 144.

[45] M. Klare, R. Altmann, Rtejournal, *Forum für Rapid Technologie* **2005**, *2*.

[46] M. Schuster, C. Turecek, B. Kaiser, J. Stampfl, R. Liska, F. Varga, *Journal of Macromolecular Science Part a-Pure and Applied Chemistry* **2007**, *44*, 547.

[47] M. Schuster, C. Turecek, A. Mateos, J. Stampfl, R. Liska, F. Varga, *Monatshefte Fur Chemie* **2007**, *138*, 261.

[48] R. Langer, J. P. Vacanti, *Science* **1993**, *260*, 920.

[49] J. P. Fisher, T. A. Holland, D. Dean, P. S. Engel, A. G. Mikos, *Journal of Biomaterials Science, Polymer Edition* **2001**, *12*, 673.

[50] T. Matsuda, M. Mizutani, *Macromolecules* **2000**, *33*, 791.

[51] F. P. W. Melchels, J. Feijen, D. W. Grijpma, in *2nd Chinese-European Symposium on Biomaterials in Regenerative Medicine*, Barcelona **2009**; Appendix A of this thesis.

[52] M. Farsari, G. Filippidis, T. S. Drakakis, K. Sambani, S. Georgiou, G. Papadakis, E. Gizeli, C. Fotakis, *Applied Surface Science* **2007**, *253*, 8115.

[53] T. R. Northen, D. C. Brune, N. W. Woodbury, *Biomacromolecules* **2006**, *7*, 750.

[56] M. Schuster, C. Turecek, G. Weigel, R. Saf, J. Stampfl, F. Varga, R. Liska, *Journal of Polymer Science Part a-Polymer Chemistry* **2009**, *47*, 7078.

[55] Y. Z. Qiu, N. Zhang, Q. Kang, Y. H. An, X. J. Wen, *Journal of Biomedical Materials Research Part A* **2009**, *89A*, 772.

[56] J. Zimmermann, K. Bittner, B. Stark, R. Mulhaupt, *Biomaterials* **2002**, *23*, 2127.

[57] K. A. Smeds, A. Pfister-Serres, D. L. Hatchell, M. W. Grinstaff, *Journal of Macromolecular Science-Pure and Applied Chemistry* **1999**, *A36*, 981.

[58] T. Yamaoka, Y. Tabata, Y. Ikada, *Journal of Pharmaceutical Sciences* **1994**, *83*, 601.

[59] J. A. Burdick, T. M. Lovestead, K. S. Anseth, *Biomacromolecules* **2003**, *4*, 149.

[60] A. K. Burkoth, K. S. Anseth, *Macromolecules* **1999**, *32*, 1438.

[61] S. He, M. D. Timmer, M. J. Yaszemski, A. W. Yasko, P. S. Engel, A. G. Mikos, *Polymer* **2001**, *42*, 1251.

[62] F. P. W. Melchels, A. H. Velders, J. Feijen, D. W. Grijpma; Chapter 5 of this thesis.

[63] M. Mizutani, S. C. Arnold, T. Matsuda, *Biomacromolecules* **2002**, *3*, 668.

[64] S. J. Hollister, R. D. Maddox, J. M. Taboas, *Biomaterials* **2002**, *23*, 4095.

[65] V. Karageorgiou, D. Kaplan, *Biomaterials* **2005**, *26*, 5474.

[66] S. F. Yang, K. F. Leong, Z. H. Du, C. K. Chua, *Tissue Engineering* **2001**, *7*, 679.

[67] X. H. Liu, P. X. Ma, *Annals of Biomedical Engineering* **2004**, *32*, 477.

[68] S. J. Bryant, C. R. Nuttelman, K. S. Anseth, *Journal of Biomaterials Science-Polymer Edition* **2000**, *11*, 439.

[69] K. S. Lee, R. H. Kim, D. Y. Yang, S. H. Park, *Progress in Polymer Science* **2008**, *33*, 631.

[70] T. Weiss, G. Hildebrand, R. Schade, K. Liefeith, *Engineering in Life Sciences* **2009**, *9*, 384.

[71] J. H. Moon, S. Yang, *Journal of Macromolecular Science-Polymer Reviews* **2005**, *C45*, 351.

[72] A. M. Prenen, J. C. A. van der Werf, C. W. M. Bastiaansen, D. J. Broer, *Advanced Materials* **2009**, *21*, 1751.

Chapter 3 - Fumaric acid monoethyl ester-functionalised poly(D,L-lactide)/N-vinyl-2-pyrrolidone resins for the preparation of tissue engineering scaffolds by stereolithography

Janine Jansen[1], Ferry Melchels[1], Dirk Grijpma[1, 2] and Jan Feijen[1]

Polymer networks were prepared by photo-crosslinking fumaric acid monoethyl ester (FAME) functionalised, three-armed poly(D,L-lactide) oligomers using N-vinyl-2-pyrrolidone (NVP) as diluent and comonomer. The use of NVP together with FAME-functionalised oligomers resulted in copolymerisation at high rates, and networks with gel contents in excess of 90 % were obtained. The hydrophilicity of the poly(D,L-lactide) networks increases with increasing amounts of NVP, networks containing 50 wt% of NVP absorbed 40 % of water. As the amount of NVP was increased from 30 to 50 wt%, the Young's modulus after equilibration in water decreased from 0.8 to 0.2 GPa, as opposed to an increase from 1.5 to 2.1 GPa in the dry state. Mouse pre-osteoblasts readily adhered and spread onto all prepared networks. Using stereolithography, porous structures with a well-defined gyroid architecture were prepared from these novel materials. This allows the preparation of tissue engineering scaffolds with optimised pore architecture and tuneable material properties.

---

[1] MIRA Institute for Biomedical Technology and Technical Medicine, and Department of Polymer Chemistry and Biomaterials, University of Twente, P.O. Box 217, 7500 AE, Enschede, The Netherlands

[2] Department of Biomedical Engineering, University Medical Centre Groningen and University of Groningen, P.O. Box 196, 9700 AD Groningen, The Netherlands

Introduction

Stereolithography is a versatile solid free-form fabrication technique that can be applied to fabricate tissue engineering scaffolds.[1, 2] It is based on spatially controlled photo-polymerisation of a liquid resin. As the resin only solidifies where illuminated, a specific pattern can be created in one single layer. By repeating this process, three-dimensional structures can be built in a layer-by-layer manner. Unlike most other solid free-form fabrication techniques, stereolithography allows the manufacturing of nearly any designed 3D geometry. This enables the preparation of tissue engineering scaffolds with most favourable architectures for cell seeding and culturing. Besides this, stereolithography facilitates personalised tissue engineering scaffolds based on medical imaging data.

Commercially available materials for use in stereolithography are epoxy- or acrylate-based resins that give networks that often are neither biocompatible nor biodegradable. In biomedical applications, the ideal resin material should not only show fast photo-crosslinking kinetics, but should also promote cell adhesion and growth, and have suitable mechanical properties after crosslinking. Different resins that have been proposed are based on poly(propylene fumarate) (PPF)[3, 4], trimethylene carbonate (TMC) (co)polymers[5-8] and poly(ethylene glycol) (PEG).[9, 10] Lactide polymers are well-known polymers that have been applied successfully in medical applications such as resorbable bone fixation devices[11] and in the preparation of tissue engineering scaffolds.[1] To allow polylactide network formation by photo-crosslinking, double bond-containing lactide oligomers are required. Fumaric acid derivatives are attractive compounds for end-functionalisation, since fumaric acid is naturally found in the body. However, compared to the frequently used (meth)acrylate-functionalised oligomers, the reactivity of fumarate-functionalised oligomers is much lower. This can be overcome by choosing a suitable comonomer in the crosslinking reaction. N-vinyl-2-pyrrolidone (NVP) is a monomer that can copolymerise with fumaric acid derivatives at high rates,[12, 13] and poly(N-vinyl-2-pyrrolidone) (PVP) is a hydrophilic biocompatible polymer that is used as an additive in pharmaceuticals.[14] Using the Q-e scheme,[15, 16] the calculated copolymerisation constants for diethyl fumarate and NVP are, respectively, 0.0004 and 0.0007. This implies that alternating copolymers will form when fumaric acid derivatives and NVP are copolymerised. As a result of the strong polar interactions between diethyl fumarate and NVP, rapid polymerisation of diethyl fumarate derivatives is also to be expected. In stereolithography, high photo-polymerisation and crosslinking rates are required.

In this chapter we describe the preparation and characterisation of photo-crosslinked networks based on fumaric acid monoethyl ester (FAME) end-functionalised poly(D,L-lactide) (PDLLA) oligomers and N-vinyl-2-pyrrolidone. The influence of the amount of hydrophilic component on the properties of the resulting networks was studied. Liquid mixtures of three-armed (PDLLA 3-FAME) macromers and NVP as a reactive diluent were photo-polymerised.

One PDLLA 3-FAME/NVP resin was applied in stereolithography to prepare pre-designed biodegradable tissue engineering scaffolds.

Experimental

Materials

D,L-lactide was purchased from Purac Biochem (The Netherlands). Tin 2-ethylhexanoate ($Sn(Oct)_2$), glycerol, fumaric acid monoethyl ester (FAME), hematoxyline and paraformaldehyde were obtained from Sigma Aldrich (USA). 4-Dimethylaminopyridine (DMAP) was obtained from Merck (Germany). 1,3-Dicyclohexylcarbodiimide (DCC), triethyl amine (TEA) and N-vinyl-2-pyrrolidone (NVP), were purchased from Fluka (Switzerland). Irgacure 2959 (2-hydroxy-1-[4-(2-hydroxyethoxy)phenyl]-2-methyl-1-propanone) and Orasol Orange G, an orange dye soluble in organic solvents, were obtained from Ciba Specialty Chemicals (Switzerland). Lucirin TPO-L (ethyl 2,4,6-trimethylbenzoylphenyl phosphinate) was obtained from BASF (Germany). Alpha-MEM (minimum essential medium), and trypsin were purchased from Invitrogen (USA). L-glutamine, and foetal bovine serum (FBS) were purchased from Lonza (Switzerland). Phosphate-buffered saline (PBS) was obtained from B. Braun (Germany). Analytical grade dichloromethane (DCM from Biosolve, The Netherlands) was dried over CaH2 and distilled. All other solvents were of technical grade and were used as received from Biosolve (The Netherlands).

Synthesis of star-shaped FAME-functionalised PDLLA oligomers

Functionalised star-shaped oligomers (PDLLA 3-FAME macromers) were prepared by esterification of PDLLA oligomeric triols with FAME in the presence of DCC as a coupling agent and DMAP as a catalyst at room temperature (Figure 3.1).[17, 18]

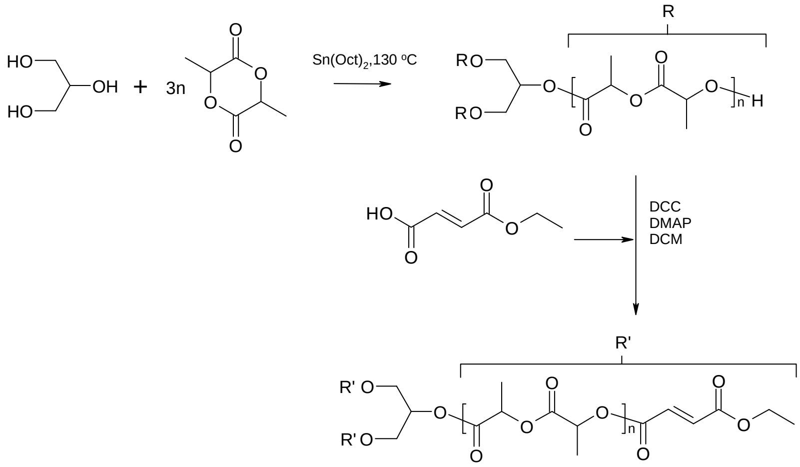

Figure 3.1: Scheme of the synthesis of FAME-functionalised PDLLA oligomers.

Batches (of 200 g and 175 g) of PDLLA oligomers were synthesised by ring opening polymerisation of D,L-lactide in the presence of glycerol, a trifunctional initiator. D,L-lactide, glycerol and Sn(Oct)2 as a catalyst were reacted in the melt at 130 °C for 24-48 h under argon. The targeted molecular weight was 3100 g/mol, which corresponds to approximately 7 lactide units per arm.

Amounts of oligomer (10-100 g) were charged into a three-necked flask, dried for 2 h at 110 °C *in vacuo*, and cooled to room temperature under argon. The oligomer was dissolved in dry DCM and, after addition and dissolution of FAME, further cooled to 0 °C. Then a dichloromethane solution of DCC and DMAP was added drop wise to the vigorously stirred oligomer solution. In the coupling reaction, 1.2 moles of FAME and DCC and 0.03 moles of DMAP per mole of hydroxyl groups were used. The reaction was continued overnight, letting the contents warm up slowly to room temperature. After completion of the reaction, the formed dicyclohexylurea was removed by filtration and the macromer was purified by precipitation in isopropanol, washing with water and freeze-drying.

High molecular weight (high MW) PDLLA (M_n = 4.7x10^5 g/mol, M_w = 6.3x10^5 g/mol, determined by gel permeation chromatography using a Viscotek GPC system equipped with a TDA 302 Triple Detector Array) was synthesised by ring opening polymerisation of D,L-lactide at 130 °C using $Sn(Oct)_2$ as a catalyst and used as a reference material.

Photo-crosslinking of PDLLA 3-FAME macromers and NVP

Solutions containing macromer (50-80 wt%), NVP (20-50 wt%) and Irgacure 2959 photo-initiator (2 mole% per mole of macromer double bonds) were prepared. Photo-crosslinking was carried out by exposing specimens cast from these solutions to long-wave UV light (Ultralum crosslinking cabinet, wavelength 365 nm) for 15 min at a distance of 15 cm in a nitrogen atmosphere. The light intensity was 3-5 mW/cm^2. Upon irradiation, the initiator molecules dissociate into radicals which initiate the addition copolymerisation of FAME-end groups and NVP diluent. A crosslinked network is thereby formed (Figure 3.2). After crosslinking, the samples were extracted with acetone in a Soxhlet apparatus for 1 d and dried under a nitrogen flow at 90 °C overnight and then at 120 °C for a few more hours.

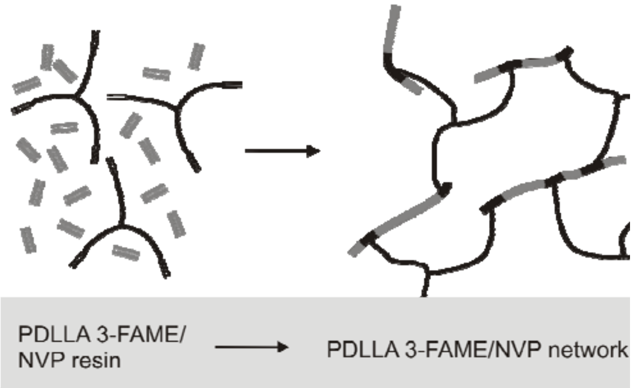

Figure 3.2: Schematic formation of PDLLA 3-FAME/NVP networks from PDLLA 3-FAME macromers (black) and NVP (grey) by photo-initiated radical polymerisation. In the network (right), the three-armed PDLLA part is depicted by thin black lines, while the linking chains formed by copolymerisation of the FAME-end groups of the macromers and NVP are depicted by thick black/grey lines.

Characterisation of oligomers, macromers and networks

Proton nuclear magnetic resonance (^{1}H-NMR) spectra were recorded on a Varian Inova 300 MHz NMR spectrometer, deuterated chloroform was used as a solvent. The oligomer molecular weights and the degrees of functionalisation of the macromers were determined from the spectra.

The thermal properties of oligomers, macromers and extracted networks were evaluated using a Perkin Elmer Pyris 1 differential scanning calorimeter (DSC). Oligomer and macromer samples (5-10 mg) were heated from -20 °C to 70 °C at a heating rate of 10 °C/min, quenched rapidly at 300 °C/min to -20 °C, then a second heating scan was recorded after 3 min. Network samples (5-10 mg) were analysed in the same manner, in the temperature range of 20 °C to 150 °C. The glass transition temperature (T_g) was taken as the midpoint of the heat capacity change in the second heating run.

To determine the gel content of the prepared networks, specimens (n = 3) were weighed (m_0), extracted and dried. The mass of the dry network (m_1) was determined. The gel content is defined as:

$$\text{gel content} = \frac{m_1}{m_0} \cdot 100\%$$

For water uptake measurements, specimens of extracted networks (n = 3) were weighed (m_d) and equilibrated in distilled water for 1 d. The samples were removed from the water, blotted dry, and weighed again (ms). The water uptake was calculated using:

$$\text{water uptake} = \frac{m_s - m_d}{m_d} \cdot 100\%$$

Contact angle measurements were carried out using an OCA 20 contact angle system from Dataphysics. Measurements were performed at room temperature on samples equilibrated in MilliQ water for 1 d using the captive air bubble method. Four measurements were performed per material. The air bubble volume was 70 µL.

For tensile testing, samples (n = 3) with dimensions of approximately 100x5x0.5 mm^3 were prepared by crosslinking macromer solutions containing 30 to 50 wt% NVP in a Teflon mold. Solutions containing 20 wt% NVP were found to be quite viscous, making it difficult to prepare specimens that were free of air bubbles. The high molecular weight PDLLA samples that were used as a reference were prepared by compression moulding at 140 °C using stainless steel moulds. The maximal tensile strength, Young's modulus and elongation at break for the polymer networks were determined at room temperature using a Zwick Z020 tensile tester operated at a cross-head speed of 50 mm/min and an initial grip-to-grip separation of 50 mm. The deformation was determined from the grip-to-grip separation and therefore the calculated Young's modulus values are only an indication of the stiffness of the networks.

Cell adhesion

Mouse pre-osteoblasts, from the MC3T3 cell line (ATCC number = CRL-2593) were cultured in T75 cell culture flasks in α-MEM medium supplemented with 2 mM L-glutamine and 10 % FBS. The cells were cultured for 2 d at 37 °C in a 5 % CO_2 atmosphere, trypsinised at 37 °C for about 5 min, and redispersed in medium. The concentration of cells was adjusted to 200,000 cells/mL.

Disk-shaped network samples (∅ = 12 mm) were prepared in a Teflon mold, while high molecular weight PDLLA samples were prepared by compression moulding (140 °C). From these compression moulded samples, 12 mm diameter disks were cut out with a hollow punch. Of all materials, 3 samples were disinfected in isopropanol (2x15 min), washed with PBS (2x15 min) and placed in ultra-low cell binding 24-well plates. An amount of 500 μl of cell suspension, containing 100,000 cells, was then pipetted onto each sample. As a control, tissue culture polystyrene (TCPS) was seeded at the same density as the PDLLA 3-FAME/NVP networks and PDLLA samples. The cell-seeded disks were kept at 37 °C under 5 % CO_2 for 6 h.

After this time period, culture medium and unattached cells were removed by rinsing the materials twice with PBS. The remaining cells were then fixed with formalin (4 % formaldehyde) for 15 min and subsequently washed with PBS. The samples were stained with hematoxylin and washed twice with distilled water. Cell adhesion to the different substrates was examined using an inverted light microscope.

Stereolithography

The viscosities of the PDLLA 3-FAME/NVP solutions were determined using a Brookfield DV-E viscometer equipped with a small sample adapter. For different macromer concentrations, the viscosity at 10 rpm (corresponding to a shear rate of 0.93 s^{-1}) was determined at 25 °C.

To a solution containing 65 wt% PDLLA 3-FAME and 35 wt% NVP, 5 wt% of Lucirin TPO-L photo-initiator and 0.5 wt% Orasol Orange G dye (both relative to the amount of macromer) were added. This resin was used to prepare porous structures by stereolithography with a commercially available set-up (Perfactory Mini Multilens, EnvisionTec). This stereolithography apparatus makes use of blue light of a wavelength of 400-550 nm, with a peak at 440 nm. In this range of wavelengths, Lucirin TPO-L is suited to photo-initiate radical polymerisation, while Orasol Orange G allows control of light penetration into the resin.

Porous gyroid structures,[19] with a porosity of 76 % were designed and built at a resolution of 16.5 μm in the x- and y-directions, the layer thickness (and the resolution in the z-direction) was 15 μm. The curing time per layer was 8 s at a light intensity of 20 mW/cm^2.

Scaffold characterisation

Scanning electron microscopy (SEM) (Philips XL30 operated at 5 kV) and micro-computed tomography (μCT) (GE eXplore Locus SP μCT scanner, the spatial resolution applied was 8 μm) were used to visualise and to characterise the built scaffolds. The greyscale image obtained from the μCT scan was thresholded to distinguish between polymer voxels and pore voxels (voxels being 8x8x8 μm^3 volume-elements).

The porosity was calculated as the fraction of pore voxels within the scaffold. To determine pore size, pores are entirely filled with as large as possible (overlapping) spheres.[20] To every pore voxel, a pore size that corresponds to the diameter of the largest sphere that contains that voxel is then assigned. From the distribution of pore sizes, a volume-averaged pore size can be calculated. The accessible pore volume is determined as the volume of the scaffold that can be reached from the exterior by simulating the percolation of a spherical particle through the interconnected pore network.[21] This was done for a range of diameters of 8 to 400 μm. The specific surface area was calculated as the sum of the areas of the boundaries between pore voxels and polymer voxels.

Results and Discussion

Synthesis of star-shaped, FAME-functionalised PDLLA oligomers

Using glycerol as a trifunctional initiator, D,L-lactide was polymerised by ring opening polymerisation to yield three-armed oligomers. The number average molecular weights of the prepared batches were 3.1×10^3 and 3.2×10^3 g/mol as determined from the glycerol to lactide ratio in NMR spectra.

The coupling of fumaric acid monoethyl ester (FAME) to PDLLA oligomers to form PDLLA 3-FAME was confirmed by appearance of a -CH=CH- (e) peak at δ 6.90, of -CH2- (f) peaks at δ 4.28 and of -CH3 (g) peaks at δ 1.32 in the NMR spectra of PDLLA 3-FAME, as shown in Figure 3.3. Based on the relative intensities of peaks (e) and (a), the calculated degrees of functionalisation varied between 86 and 97 %. When calculating the degrees of functionalisation from peaks (a) and (g), values between 99 % and 100 % were obtained.

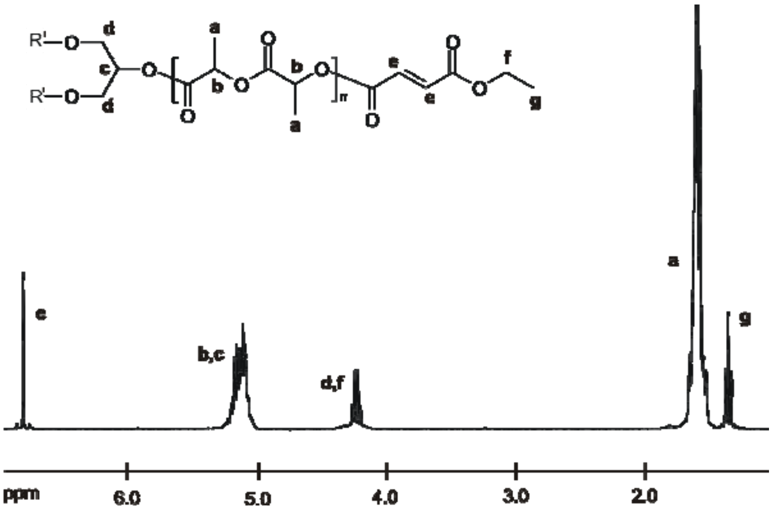

Figure 3.3: Example of a ^{1}H-NMR spectrum of PDLLA 3-FAME.

Photo-crosslinking of PDLLA 3-FAME macromers and NVP

Networks were formed from PDLLA 3-FAME macromers and NVP by UV irradiation (365 nm) using Irgacure 2959 as a biocompatible initiator.[22, 23] The NVP content was varied from 20 to 50 wt%, as only compositions containing more than 20 wt% NVP are liquid at room temperature.

The influence of NVP content on the network properties was evaluated. The gel content of the networks obtained after a polymerisation time of only 15 min was above 90 % in all cases (Table 3.1). When similar 3-FAME macromers were crosslinked under comparable conditions in the absence of NVP, a long irradiation time of 3 h was required to reach a gel content of 81 %.[17] The addition of NVP as a comonomer clearly results in a significant increase in crosslinking rates. This will enable application of PDLLA 3-FAME macromers in stereolithography.

Table 3.1: Gel contents and glass transition temperatures of networks prepared from PDLLA 3-FAME macromers and NVP. T_g values of PDLLA oligomers, high MW PDLLA and high MW PVP are given as a reference.

	NVP content (wt%)	gel content (%)	T_g (°C)
PDLLA oligomer	0	-	31.1
PDLLA 3-FAME macromer	0	-	38.1
PDLLA 3-FAME network[a]	0	81.4	38.6
PDLLA 3-FAME/NVP network	20	93.5±1.8	66.8
PDLLA 3-FAME/NVP network	30	93.3±0.3	81.4
PDLLA 3-FAME/NVP network	40	92.7±0.2	85.3
PDLLA 3-FAME/NVP network	50	90.9±0.6	95.6
HMW PDLLA	0	-	55.1
HMW PVP[b]	100	-	179

The glass transition temperatures of the oligomers, macromers and extracted networks in the dry state were determined by DSC and are presented in Table 3.1. It can be seen that upon network formation, the glass transition temperature increases. The NVP-containing networks have T_g values that are significantly higher than that of high MW PDLLA. With higher NVP contents, T_g of the networks increases as expected. All networks showed a single glass transition, which indicates that NVP was homogeneously incorporated into the network structure.

PDLLA 3-FAME networks containing NVP absorb significantly more water than high-molecular weight PDLLA (Figure 3.4). Due to the hydrophilic character of NVP, the water uptake of the networks increases with increasing NVP content. The hydrophilicity of the resulting networks can readily be adjusted and materials ranging from hydrophobic glassy polymer networks to hydrogels can be prepared.

Networks containing NVP had a lower contact angle than high MW PDLLA. The contact angle of the networks is comparable to that of tissue culture polystyrene (TCPS). As a result of poor wetting cell seeding into porous PLA scaffolds 0can be problematic.[24] It can be expected that the increased hydrophilicity of PDLLA 3-FAME/NVP will facilitate cell seeding into porous scaffolds prepared from these networks. The water uptake of the networks showed a much stronger dependence on the NVP content than the contact angle. When increasing the NVP content in

---

[a] Data from [18]. Non-extracted networks, prepared from macromers with M_n = 4750 g/mol. The macromer films were cast from chloroform and irradiated at 365 nm for 3 h.

[b] Data from reference 15. $M_w = 9x10^5$ g/mol.

the networks from 20 % to 50 %, the contact angles remain essentially constant. Apparently, the concentration of hydrophilic components at the surface of the specimens is similar. This may be caused by reorganisation of the PVP-containing copolymer chains.

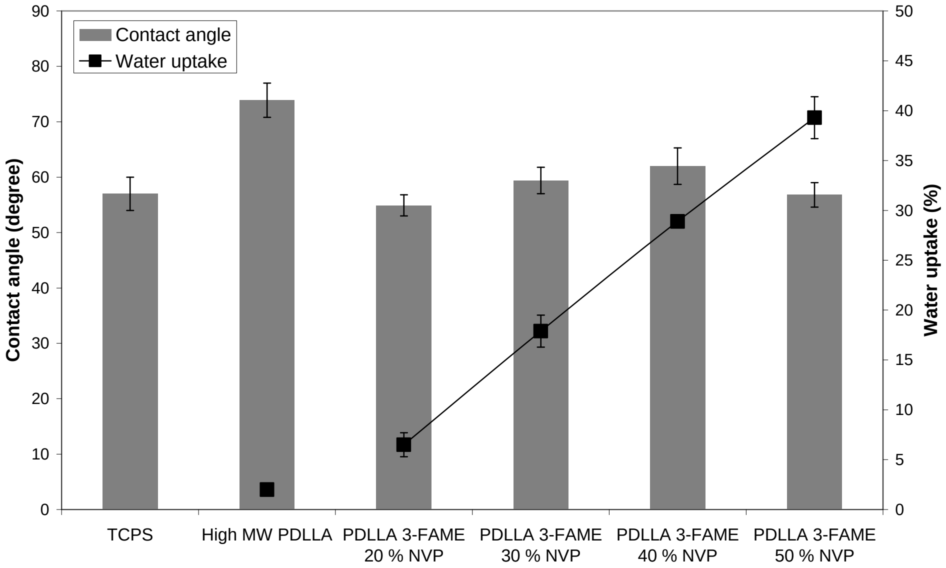

Figure 3.4: Contact angles (bars) and water uptake (■) of PDLLA 3-FAME/NVP networks conditioned in water at 37 °C for 2 days. Reference values for TCPS and high MW PDLLA are given as well.

During cell seeding and culturing, and upon implantation in the human body, tissue engineering scaffolds can take up significant amounts of water. To investigate the effect of water uptake on the mechanical properties of PDLLA 3-FAME/NVP networks, specimens were analysed in the dry state and after equilibration in water. Their tensile properties are given in Table 3.2.

Table 3.2: Tensile properties of PDLLA 3-FAME/NVP networks in the dry state and after equilibration in water.

	NVP content (wt%)	dry/ wet	Young's modulus (GPa)[d]	tensile strength (MPa)	elongation at break (%)
PDLLA 3-FAME network[e]	0	dry	0.01	1.3	106
High MW PDLLA	0	dry	1.6±0.1	48±1	4.5±0.2
PDLLA 3-FAME/NVP network	30	dry	1.5±0.1	42±4	3.1±0.3
PDLLA 3-FAME/NVP network	40	dry	1.8±0.1	34±10	2.2±0.8
PDLLA 3-FAME/NVP network	50	dry	2.1±0.1	56±10	3.4±0.9
High MW PDLLA[f]	0	wet	1.5	42	2.9
PDLLA 3-FAME/NVP network	30	wet	0.8±0.1	20±3	3.0±0.7
PDLLA 3-FAME/NVP network	40	wet	0.8±0.1	19±1	3.9±0.2
PDLLA 3-FAME/NVP network	50	wet	0.2±0.0	7±1	7.3±1.8

In the dry state, the Young's modulus of the networks increased with increasing NVP content. In the wet state this trend is reversed, as networks with higher NVP contents absorb larger amounts of water. High molecular weight PDLLA absorbed only 2 wt% of water, and showed the smallest difference in Young's modulus values between the dry and wet states. PDLLA 3-FAME networks containing 50 % NVP absorbed 40 % of water, and showed the lowest modulus upon conditioning. A scaffold material with suitable properties for a specific tissue can be synthesised by adjusting NVP content. The tensile strength of dry networks does not significantly change with NVP content. In the wet state however, tensile strengths of the networks decrease significantly with increasing NVP contents. No major differences in the elongation at break as a function of NVP content were observed.

When compared to PDLLA 3-FAME networks prepared previously in our group without a reactive diluent,[17] these NVP-containing networks show much higher Young's modulus and tensile strength values. Although, this can partly be explained by the presence of a sol fraction and chloroform remaining in the non-extracted

---

[d] The deformation was determined from the grip-to-grip separation, therefore the given Young's modulus values are only an indication of the stiffness of the networks.

[e] Data from [18]. Non-extracted networks, prepared from macromers with M_n = 4750 g/mol. The macromer films were cast from chloroform and irradiated at 365 nm for 3 h.

[f] Single measurement.

networks described in our earlier work, the number of elastically inactive chains in the network is significantly reduced upon copolymerisation of the PDLLA macromer with NVP. This results in networks with much better mechanical properties.

Cell adhesion to PDLLA 3-FAME/NVP networks

To assess the suitability of these networks for cell culturing and tissue engineering, initial cell adhesion experiments were performed. Representative micrographs of the surfaces of different PDLLA 3-FAME/NVP and reference materials six hrs after cell seeding are shown in Figure 3.5. It can be observed that the MC3T3 cells adhered well to the copolymer networks, showing a spread morphology. This is indicative of interactions of cell membrane integrins with surface-adsorbed proteins, facilitating subsequent cell spreading. The behaviour of the cells on the network films is comparable to that on the high molecular weight PDLLA and TCPS controls. Even though it seems that the cells had a slightly higher tendency to aggregate on the networks with the highest NVP contents, the results indicate good cell adhesion for the range of PDLLA 3-FAME/NVP networks investigated. Although surface hydrophilicity is only one parameter that influences cell adhesion, the observed cell adhesion is consistent with the similarity of the contact angles. For all the NVP-containing networks, the contact angles are comparable to each other and to TCPS (Figure 3.4). Thus, by adjusting the NVP content, water uptake and mechanical properties of these photo-crosslinked PDLLA 3-FAME/NVP networks can be tailored without consequences for their cell adhesion properties.

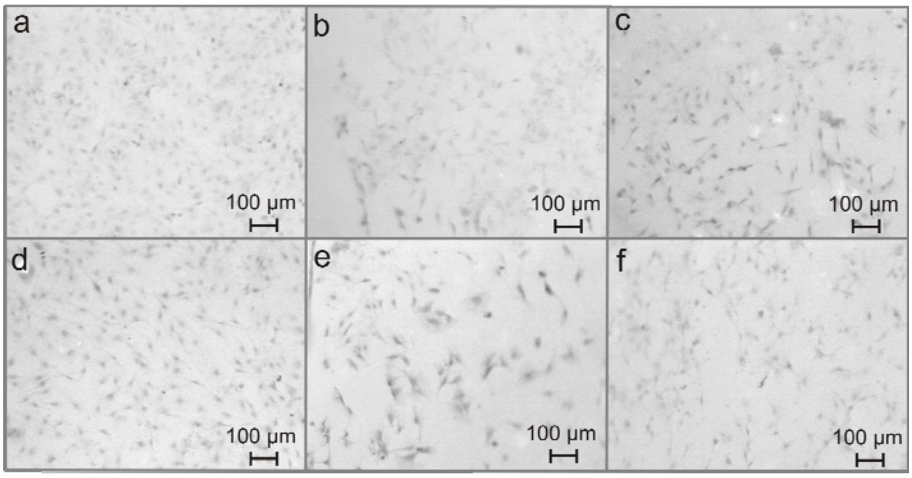

Figure 3.5: Light microscopy images of the adhesion of MC3T3 cells after 6 hrs to (a) TCPS, (b) high MW PDLLA, (c) PDLLA 3-FAME/20 % NVP network, (d) PDLLA 3-FAME/30 % NVP network, (e) PDLLA 3-FAME/40 % NVP network and (f) PDLLA 3-FAME/50 % NVP network.

Stereolithography

The favourable mechanical and biological properties of the prepared networks encourage their application in tissue engineering. Therefore, we investigated the possibility of preparing porous structures from PDLLA 3-FAME macromers and NVP formulations by stereolithography.

Besides a high curing rate upon irradiation, a suitable viscosity of the resin is important to allow processing by stereolithography. The viscosities of resins that are applied in stereolithography range from 0.25 Pa·s for a pentaerythritol tetra-acrylate resin to 5 Pa·s for ceramic suspensions.[25] The viscosity of PDLLA 3-FAME/NVP resins could easily be adjusted by variation of the amount of reactive NVP diluent. As the NVP content was increased from 35 to 45 wt %, the viscosity of the resin at 25 °C and a shear rate of 9.3 s^{-1} decreased from 4.1 to 0.7 Pa·s. These resin viscosities are suitable for application in stereolithography.

To build porous tissue engineering scaffolds in a stereolithography setup, a mixture of PDLLA 3-FAME, 35 wt% NVP, 5 wt% (relative to the amount of macromer) Lucirin photo-initiator and 0.5 wt% (relative to the amount of macromer) Orasol Orange G dye was prepared. The three dimensional design that was chosen for the scaffolds was a gyroid. Structures built according to this mathematically defined architecture, have a large specific surface area and high pore interconnectivity. These characteristics make it an excellent architecture for tissue engineering, as it enables cell-seeding at high densities, and allows homogeneous distribution of cells and flow of nutrients throughout the scaffold. In the design we used, the porosity and pore size (i.e. the diameter of the open channels running through the structure) were 76 % and 260 μm, respectively.

Figure 3.6 shows SEM images of a built porous gyroid structure. It follows that use of the PDLLA 3-FAME/NVP resin in stereolithography enables the preparation of biodegradable scaffolds with highly controlled architectures. The built scaffolds measured approximately 4.5x4.5x1.8 mm and closely resembled the design. It can be seen that the pore network is homogenous in size and fully interconnected. At higher magnifications, the layer-by-layer nature of the construct is clearly visible.

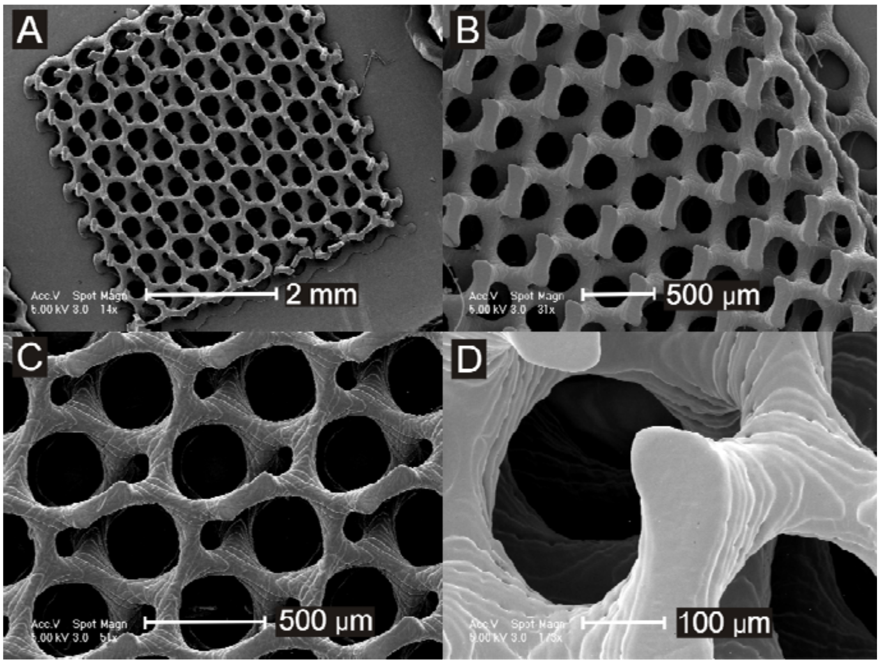

Figure 3.6: SEM images of porous PDLLA 3-FAME/NVP gyroid structures built by stereolithography.

The occurrence of polymerisation shrinkage can be seen at the edges of the construct in Figure 3.6B. This has resulted in a size reduction of 16 %; the width of the top part of the structure is 4.2 mm, while the designed structure was 5 mm wide. The top part of the scaffold has shrunk more than the lower part, and some fractures can be observed as well (Figure 3.6A). By incorporating a support structure into the design (which has not yet been done here), the effects of polymerisation shrinkage in stereolithography can be dealt with.

Figure 3.7 depicts a μCT-visualisation of part of an equivalent scaffold built using the PDLLA 3-FAME/NVP resin. It is apparent that the prepared structure is highly regular in all three dimensions. The μCT data can also be used to quantify relevant scaffold parameters.

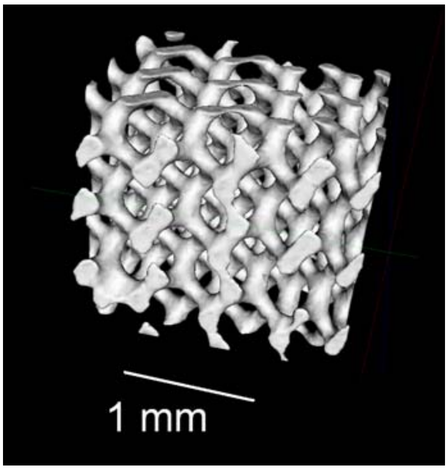

Figure 3.7: μCT-visualisation of part of a porous gyroid structure built using PDLLA 3-FAME/NVP.

A porosity of 80 % and an average pore size of 256 μm were determined. The values for porosity and pore size match those of the design closely. The deviations are less than 5 % and can be the result of inaccuracies in the digitalisation procedure during the creation of the build file, in the polymerisation process, in the imaging, in the three-dimensional reconstruction of the scanning data or in the method of assigning sizes to pores.

Figure 3.8 shows the pore size distribution of the built gyroid structure as determined by μCT according to the described algorithm. Pores ranging in size from 240 to 350 μm make up more than 80 % of the pore volume. The pore sizes smaller than 240 μm are an inevitable artefact of the employed assignment algorithm, which assumes a spherical pore geometry. As a result, pore voxels that do not lie in the largest sphere that fits in a non-spherical pore, are assigned a too small pore size.[21]

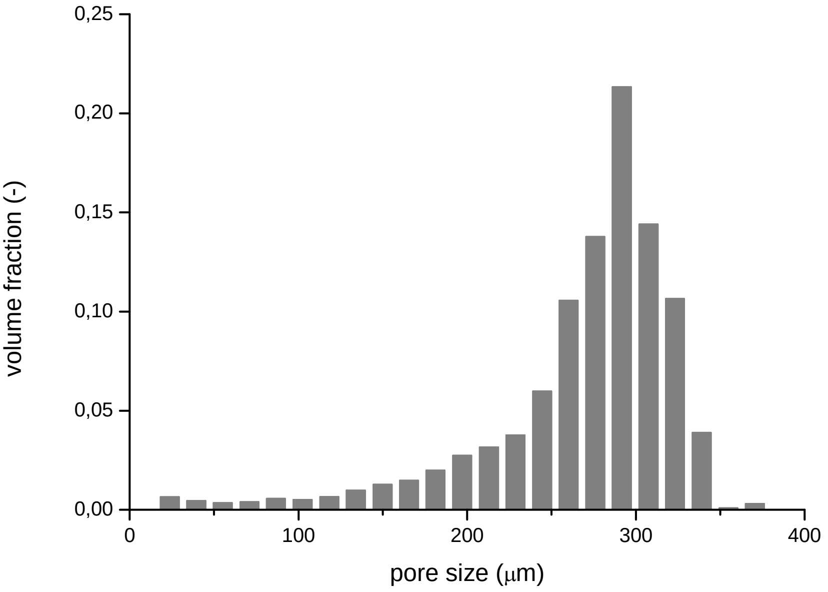

Figure 3.8: Pore size distribution of the porous gyroid structure shown in Figure 3.7 determined from μCT-data.

The interconnectivity of the pore structure of a scaffold can be quantified by assessment of its accessible pore volume, as is done in Figure 3.9. The accessible pore volume is the volume that can be reached from the outside of the imaged scaffold by simulating the permeation of a spherical particle. The figure shows that more than 90 % of the pore volume in this gyroid structure is connected to the outside by channels with diameters larger than 100 μm. This indicates high permeability of the scaffold for cells in a cell seeding procedure, and for nutrients and metabolites during cell culture or implantation.

From the μCT-data, a high specific surface area of 34 mm^2/mm^3 of scaffold could also be calculated. This large surface area and high porosity allows large numbers of cells to adhere, to proliferate and to deposit extra-cellular matrix.

Since these materials show good cell adhesion and the architecture of the prepared scaffolds is optimal for cell seeding and culturing, these structures are most suited as tissue engineering scaffolds. Currently the degradation behaviour, long-term cell culturing and in vivo application of these PDLLA 3-FAME/NVP materials and scaffolds prepared by stereolithography are being investigated.

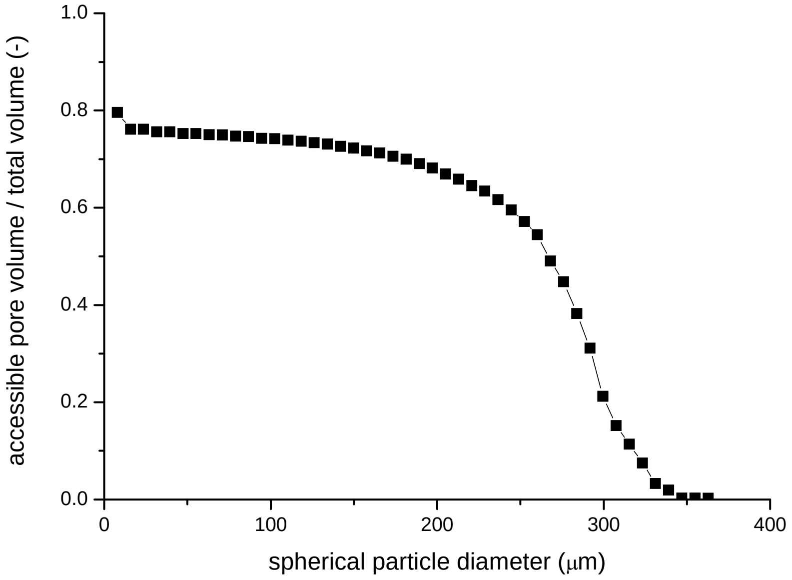

Figure 3.9: The accessible pore volume for simulated permeating spherical particles of different diameters.

Conclusions

Copolymerisation of FAME-functionalised PDLLA macromers with NVP as a reactive diluent resulted in the rapid formation of networks with high gel contents. By varying the amount of NVP, the material properties of the networks (such as water uptake and rigidity) can be tailored. Mouse pre-osteoblast cells adhered and spread well onto all materials, NVP content did not have a significant effect. Using stereolithography, a porous gyroid structure was prepared at high resolution from a PDLLA 3-FAME/NVP resin. This scaffold design was chosen for its favourable open and interconnected pore architecture. The obtained structure very closely resembled the computer-aided design. These resins may find wide application in stereolithography and tissue engineering.

Acknowledgements

We would like to acknowledge R. Gabbrielli and C.R. Bowen (University of Bath, UK) for providing the gyroid CAD-file and the EU for funding (STEPS project, FP6-500465).

References

[1] D. W. Hutmacher, *Biomaterials* **2000**, *21*, 2529.

[2] D. W. Hutmacher, M. Sittinger, M. V. Risbud, *Trends in Biotechnology* **2004**, *22*, 354.

[3] M. N. Cooke, J. P. Fisher, D. Dean, C. Rimnac, A. G. Mikos, *Journal of Biomedical Materials Research* **2003**, *64B*, 65.

[4] J. W. Lee, P. X. Lan, B. Kim, G. Lim, D.-W. Cho, *Microelectronic Engineering* **2007**, *84*, 1702.

[5] I. K. Kwon, T. Matsuda, *Biomaterials* **2005**, *26*, 1675.

[6] S.-J. Lee, H.-W. Kang, J. Park, J.-W. Rhie, S. Hahn, D.-W. Cho, *Biomedical Microdevices* **2008**, *10*, 233.

[7] T. Matsuda, M. Mizutani, *Journal of Biomedical Materials Research* **2002**, *62*, 395.

[8] M. Mizutani, S. C. Arnold, T. Matsuda, *Biomacromolecules* **2002**, *3*, 668.

[9] B. Dhariwala, E. Hunt, T. Boland, *Tissue Engineering* **2004**, *10*, 1316.

[10] G. Mapili, Y. Lu, S. Chen, K. Roy, *Journal of Biomedical Materials Research Part B: Applied Biomaterials* **2005**, *75B*, 414.

[11] K. A. Athanasiou, C. M. Agrawal, F. A. Barber, S. S. Burkhart, *Arthroscopy-the Journal of Arthroscopic and Related Surgery* **1998**, *14*, 726.

[12] S. Sharifi, H. Mirzadeh, M. Imani, M. Atai, F. Ziaee, *Journal of Biomedical Materials Research Part A* **2008**, *84A*, 545.

[13] M. J. Yaszemski, R. G. Payne, W. C. Hayes, R. Langer, A. G. Mikos, *Biomaterials* **1996**, *17*, 2127.

[14] J. H. Ko, in *Polymer Data Handbook*, Oxford University Press, **1999**, 962.

[15] J. Brandrup, E. H. Immergut, A. Abe, D. R. Bloch, *Polymer Handbook*, Wiley-Interscience, New York **1999**.

[16] G. Odian, *Principles of Polymerization*, Wiley-Interscience, New York **1991**.

[17] D. W. Grijpma, Q. Hou, J. Feijen, *Biomaterials* **2005**, *26*, 2795.

[18] A. Hassner, V. Alexanian, *Tetrahedron Letters* **1978**, *19*, 4475.

[19] A. H. Schoen, Nasa Technical Note, NASA-TN-D-5541 **1970**.

[20] T. Hildebrand, P. Ruegsegger, *Journal of Microscopy-Oxford* **1997**, *185*, 67.

[21] M. B. Claase, J. D. de Bruijn, D. W. Grijpma, J. Feijen, *Journal of Materials Science-Materials in Medicine* **2007**, *18*, 1299.

[22] S. J. Bryant, C. R. Nuttelman, K. S. Anseth, *Journal of Biomaterials Science, Polymer Edition* **2000**, *11*, 439.

[23] C. G. Williams, A. N. Malik, T. K. Kim, P. N. Manson, J. H. Elisseeff, *Biomaterials* **2005**, *26*, 1211.

[24] A. G. Mikos, M. D. Lyman, L. E. Freed, R. Langer, *Biomaterials* **1994**, *15*, 55.

[25] C. Hinczewski, S. Corbel, T. Chartier, *Journal of the European Ceramic Society* **1998**, *18*, 583.

Supporting Information

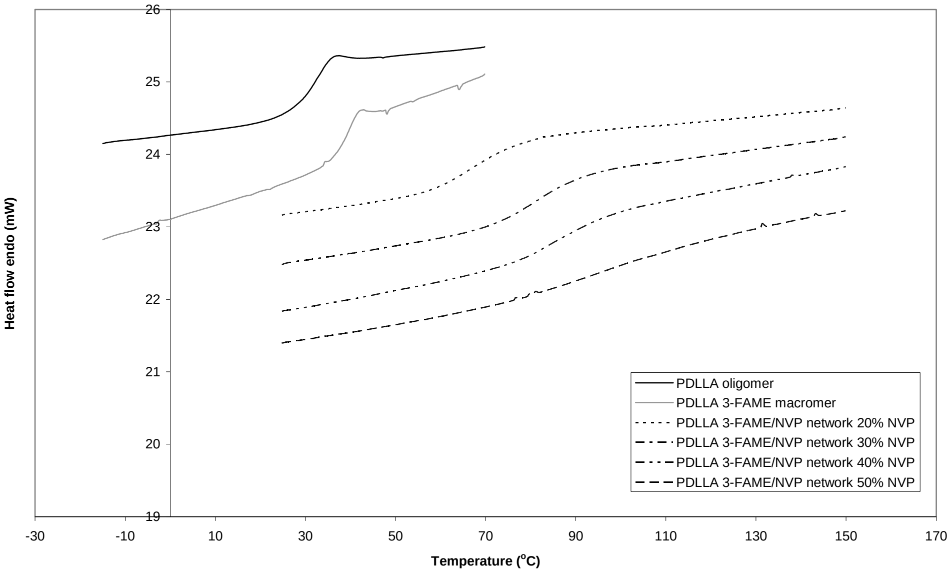

Figure 3.10: DSC traces of PDLLA oligomers, PDLLA 3-FAME macromers and PDLLA 3-FAME/NVP networks (second heating scan, sample size 5-10 mg).

Chapter 4 - A poly(D,L-lactide) resin for the preparation of tissue engineering scaffolds by stereolithography

Ferry Melchels[1], Jan Feijen[1] and Dirk Grijpma[1, 2]

Porous polylactide constructs were prepared by stereolithography, for the first time without the use of reactive diluents. Star-shaped poly(D,L-lactide) oligomers with 2, 3 and 6 arms were synthesised, end-functionalised with methacryloyl chloride and photo-crosslinked in the presence of ethyl lactate as a non-reactive diluent. The molecular weights of the arms of the macromers were 0.2, 0.6, 1.1 and 5 kg/mol, allowing variation of the crosslink density of the resulting networks. Networks prepared from macromers of which the molecular weight per arm was 0.6 kg/mol or higher had good mechanical properties, similar to linear high molecular weight poly(D,L-lactide). A resin based on a 2-armed poly(D,L-lactide) macromer with a molecular weight of 0.6 kg/mol per arm (75 wt%), ethyl lactate (19 wt%), photo-initiator (6 wt%), inhibitor and dye was prepared. Using this resin, films and computer-designed porous constructs were accurately fabricated by stereolithography. Pre-osteoblasts showed good adherence to these photo-crosslinked networks. The proliferation rate on these materials was comparable to that on high molecular weight poly(D,L-lactide) and tissue culture polystyrene.

---

[1] MIRA Institute for Biomedical Technology and Technical Medicine, and Department of Polymer Chemistry and Biomaterials, University of Twente, P.O. Box 217, 7500 AE, Enschede, The Netherlands

[2] Department of Biomedical Engineering, University Medical Centre Groningen and University of Groningen, P.O. Box 196, 9700 AD Groningen, The Netherlands

Introduction

Tissue engineering scaffolds prepared by rapid prototyping techniques have several advantages when compared to those fabricated by conventional techniques such as porogen leaching, phase-separation/freeze-drying and gas-foaming. These conventional techniques often result in inhomogeneous scaffolds with broad pore size distributions, poor pore interconnectivity and inferior mechanical properties. Rapid prototyping allows computer-designed architectures to be built in a reproducible manner. This enables the preparation of scaffolds with optimal properties regarding pore structure and connectivity, geometry, mechanical properties, cell-seeding efficiency, and transport of nutrients and metabolites.[1] Of the rapid prototyping techniques, stereolithography is the most versatile method with the highest accuracy and precision.[2] Its working principle is based on spatially controlled solidification of a liquid photo-polymerisable resin. Using a computer-controlled laser beam or a digital light projector with a computer-driven building stage, a solid, 3-dimensional object can be constructed in a layer-by-layer fashion.

The number of stereolithography resins available for use in biomedical applications is limited. Poly(ethylene glycol)dimethacrylate has been used to fabricate non-degradable cell-containing hydrogels in pre-designed shapes.[3-5] In tissue engineering however, resorbable constructs are desired. The only biodegradable macromers that have been applied are based on trimethylene carbonate and ε-caprolactone oligomers,[6, 7] or on poly(propylene fumarate). The latter requires a reactive diluent such as diethyl fumarate to obtain an appropriate reaction rate and viscosity of the resin.[8] Upon photo-polymerisation of these resins, networks are formed with low glass transition temperatures and low E-modulus values under physiological conditions. For tissue engineering of hard tissues such as bone, strong and rigid biodegradable materials are desired. Polylactide is such a material, and it has a long track record of successful application in the clinic and in the preparation of tissue engineering scaffolds. The amorphous form, poly(D,L-lactide) (PDLLA), has successfully been applied in resorbable bone fixation devices clinically[9, 10] and for scaffolds that proved well-suited for bone tissue engineering.[11-13] PDLLA has a glass transition temperature of approximately 55 °C, and an elasticity modulus close to 3 GPa; it is one of the few biodegradable polymers with mechanical properties that approach those of bone (the E-modulus of bone is 3 to 30 GPa).[14] The ability to process PDLLA-based materials by stereolithography would allow to significantly advance the field of bone tissue engineering as optimised structures with regard to mechanical properties, cell seeding and culturing can then be prepared.

PDLLA networks can be formed by (photo-initiated) radical polymerisation of poly(lactide) oligomers end-functionalised with an unsaturated moiety such as a methacrylate-,[15] acrylate-[16] or fumarate-[17] group. To be able to apply PDLLA macromers in stereolithography, the macromer must be in the liquid state. This can be achieved by heating or diluting. Reactive diluents such as methyl methacrylate, butane-dimethacrylate and N-vinyl-2-pyrrolidone have been used in regular photo-polymerisation reactions[15, 18] and in stereolithography.[19, 20] This, however, introduces significant amounts of a non-degradable component.

This work aims at developing a photo-curable PDLLA-based resin that is free of reactive diluents, and applying it in stereolithography. Ethyl lactate was employed as a non-reactive diluent. This poses a challenge to the optimisation of the resins, as shrinkage upon extraction of the photo-polymerised networks can be quite significant. Methacrylate end-functionalised poly(D,L-lactide) oligomers of varying molecular architectures were synthesised and photo-crosslinked in the presence of ethyl lactate. Suitable resin compositions were used in stereolithography to prepare porous structures with pre-designed architectures at high resolution. Cell attachment and proliferation on PDLLA networks prepared by stereolithography were assessed.

Experimental

Materials

D,L-lactide was obtained from Purac Biochem, The Netherlands. Hexanediol, glycerol, stannous octoate, methacryloyl chloride (MACl), hydroquinone, vitamin E, sodium pyruvate, N-methyl dibenzopyrazine methyl sulfate (PMS) and HistoChoice tissue fixative were purchased from Sigma-Aldrich, USA and used without further purification.

Sorbitol, triethyl amine (TEA), eosin-hematoxylin solution (Fluka, Switzerland), ethyl lactate (Merck, Germany), and technical grade isopropanol and acetone (Biosolve, The Netherlands) were used as received. Irgacure 2959 (2-hydroxy-1-[4-(hydroxyethoxy)phenyl]-2-methyl-1-propanone) and Orasol Orange G were gifts from Ciba Specialty Chemicals, Switzerland. Lucirin TPO-L (ethyl-2,4,6-trimethylbenzoylphenylphosphinate) was a gift from BASF, Germany. Analytical grade dichloromethane (Biosolve, The Netherlands) was distilled from calcium hydride (Acros Organics, Belgium).

Foetal bovine serum (FBS), L-glutamine, penicillin-streptomycin and trypsin were obtained from Lonza, Belgium. Alpha-Modified Eagle Medium (αMEM) and RPMI 1640 medium without phenol red were bought from Gibco, USA. Sodium 3'-[1-(phenylamino-carbonyl)-3,4-tetrazolium]-bis(4-methoxy-6-nitro)benzene sulfonic acid hydrate (XTT) was obtained from PolySciences, USA.

Polymer syntheses

Star-shaped oligomers were synthesised on a 30 g scale by ring opening polymerisation of D,L-lactide for 40 h at 130°C under an argon atmosphere, using stannous octoate as a catalyst. Hexanediol, glycerol and sorbitol were used as initiators, to prepare 2-armed, 3-armed and 6-armed oligomers, respectively. The molecular weights and arm lengths were varied by adjusting the monomer to initiator ratio. Proton-nuclear magnetic resonance spectroscopy (^{1}H-NMR, $CDCl_3$, Varian 300 MHz) was used to determine lactide conversion and oligomer molecular weights. Oligomers were functionalised by reacting the terminal hydroxyl groups with methacryloyl chloride (MACl) in dry dichloromethane under an argon atmosphere. The formed HCl was scavenged with triethyl amine (TEA). An excess of 20-50 mol% MACl and TEA per hydroxyl end group was used.

The macromer solutions were filtered and precipitated into cold isopropanol. The isolated macromers were then washed with water and freeze-dried. Macromers with molecular weights lower than 1 kg/mol are soluble in isopropanol. These macromers were purified by washing the dichloromethane solutions with a saturated aqueous sodium bicarbonate solution, drying with magnesium sulphate, filtrating and evaporating the solvent under reduced pressure. The yield was 70 to 90 %, depending on macromer molecular weight.

^{1}H-NMR was used to determine the degrees of functionalisation of the macromers. Throughout this chapter, all macromers are labelled as MAxB, in which A stands for the number of arms and B for the arm length. For example, M3x0.6k stands for a 3-armed methacrylated PDLLA macromer with each arm having a molecular weight of 0.6 kg/mol. The corresponding non-functionalised oligomer is designated as O3x0.6k, and the network obtained after photo-polymerisation of the macromer is designated as N3x0.6k.

As a reference material, high-molecular weight poly(D,L-lactide) (HMW PDLLA) was synthesised by ring opening polymerisation under similar conditions. The polymer was purified by precipitation from acetone into water, and vacuum dried. Molecular weights were determined using a Viscotek GPCmax gel permeation chromatography setup with Viscotek 302 Triple Detection Array and $CHCl_3$ as an eluent with a flow of 1 mL/min. The following values were obtained: $M_w = 4.3x10^5$ g/mol, $M_n = 3.6x10^5$ g/mol and $[\eta] = 5.5$ dL/g.

Resin formulation and network preparation

To formulate liquid polymerisable poly(D,L-lactide) resins, the different macromers were diluted with ethyl lactate. The resin viscosity was determined over a range of diluent concentrations at 25 °C using a Brookfield DV-E rotating spindle viscometer, equipped with a small sample adapter. The shear rate was varied between

0.56 and 56 s^{-1} (Brookfield s21 spindle, rotating at 0.6 to 60 rpm). To prevent premature crosslinking 0.2 wt% hydroquinone was added to the liquid.

To obtain networks, the resins containing 2.0 wt% Irgacure 2959 as a biocompatible UV photo-initiator,[21, 22] were irradiated with 365 nm UV-light for 15 min (Ultralum crosslinking cabinet, intensity 3-4 mW/cm^2). Silicone rubber moulds, covered with fluorinated ethylene-propylene (FEP) films to avoid oxygen inhibition, were employed to prepare specimens measuring 45x30x1.5 mm^3.

Network characterisation

The obtained PDLLA networks were extracted with 3:1 mixtures of isopropanol and acetone, and dried at 90°C under a nitrogen flow for 2 d. Gel contents were determined in duplicate from the mass of the dry network after extraction (m_{dry}) and the macromer mass initially present in the resin (m_0). The specimens were then swollen in ethyl lactate for 2 d. The volume degrees of swelling of the networks were calculated using the swollen mass (m_{wet}) and the densities of PDLLA (1.25 g/mL) and ethyl lactate (1.03 g/mL):

$$Q = 1 + \frac{m_{wet} - m_0}{m_0} \times \frac{\rho_{PDLLA}}{\rho_{EL}}$$

Mechanical properties were determined in 5-fold in 3-point bending tests and in tensile tests using a Zwick Z020 universal tensile tester. The dimensions of the extracted and dried PDLLA networks for the bending tests were approximately 30x20x1 mm^3. According to the ISO 178 norm used, the span-width and strain rate were adjusted to the specimen thickness. For the tensile tests, dumbbell-shaped samples were used according to the ISO 37-2 norm.

Water uptake of the different networks was assessed by conditioning extracted and dried samples in demineralised water at 37 °C for 15 hrs. Water uptake was defined as the relative increase in weight.

Stereolithography

To fabricate (porous) PDLLA structures by stereolithography, a resin comprising 75 wt% M2x0.6k PDLLA macromer, 19 wt% ethyl lactate, 6 wt% Lucirin TPO-L visible light photo-initiator, 0.025 wt% hydroquinone inhibitor and 0.2 wt% Orasol Orange G dye was formulated.

Tensile test specimens (ISO 37-2), films measuring 70x24x0.5 mm^3 and a scaffold with a gyroid architecture were designed using Rhinoceros 3D (McNeel Europe) and K3dSurf v0.6.2 (freeware obtainable from http://k3dsurf.sourceforge.net) computer software. The designs were built using an EnvisionTec Perfactory Mini Multilens stereolithography apparatus. This stereolithography apparatus (SLA) is equipped with a digital micro-mirror device[23] which enables projections of 1280 x 1024 pixels, each measuring 32x32 μm^2. Using a build platform step height of 25 μm, layers of resin were sequentially photo-crosslinked by exposure to a blue light pattern for 40 s. The intensity of the light was 20 mW/cm^2 and the wavelength ranged from 400 to 550 nm, with a peak at 440 nm.

After building, the scaffolds were extracted with 3:1 isopropanol and acetone mixtures and dried at 90 °C for 2 d. Imaging of gold-sputtered scaffolds was performed by scanning electron microscopy (SEM) employing a Philips XL30 FEG device with a 5.0 kV electron beam. Structural analysis was performed using micro-computed tomography (μCT) scanning on a GE eXplore Locus SP scanner at 6.7 μm resolution. The scan was carried out at a voltage of 80 kV, a current of 80 μA and an exposure time of 3000 ms. No filter was applied.

Cell culturing

Disk-shaped specimens (diameter 15 mm) of HMW PDLLA were punched out from compression moulded (140 °C, 250 kN) films. PDLLA network (N2x0.6k) disks were punched out from the films prepared by stereolithography. Prior to seeding, the samples were disinfected in 70 % isopropanol for 5 min, rinsed 3 times in phosphate-buffered saline (PBS) and incubated overnight in medium. Mouse pre-osteoblasts (MC3T3 cell line) were cultured in αMEM supplemented with 10 % FBS, 2 mM L-glutamine, 1 mM sodium pyruvate and 2 % PennStrep (penicillin-streptomycin). The cells were detached from the culture flask using 0.10 % (w/v) trypsin / 0.050 % (w/v) EDTA, after which 12×10^3 cells in 2 mL medium were pipetted onto each disk, in a 24-wells plate. For the TCPS controls, empty wells were used. The cells were cultured at 37 °C and 5 % CO_2 for 11 d, refreshing the medium at day 4 and day 8.

At each time point, specimens were fixed for 20 min in HistoChoice fixative solution and stained with eosin-hematoxylin. Light microscopy was used to visualise the adhered cells. Using NIH ImageJ software, the average area per cell on N2x0.6k PDLLA network films and TCPS was determined. Three images, each containing 25-80 cells, were evaluated. The HMW PDLLA films showed too many background irregularities to be analysed.

To quantify the number of live cells, other specimens were incubated for 60 min with colourless RPMI 1640 medium containing 1 mg/mL XTT and 7.66 μg/mL PMS. After incubation, the relative absorbance of the supernatant at 450 nm (with reference to the absorbance at 620 nm) was measured in triplicate. Aliquots of 150 μL were placed in a 96-well plate, and analysed using an SLT 340 ATTC plate-reader.

Mouse pre-osteoblasts were also seeded into the porous N2x0.6k PDLLA scaffolds (5x5x5 mm^3) with gyroid architecture prepared by stereolithography, by pipetting cell suspensions ($600x10^3$ cells in 200 μL medium) onto each scaffold. The seeded structures were observed microscopically after 1 d as described for the films.

Results and Discussion

Polymers and macromers

The monomer conversions and the arm lengths of the synthesised lactide oligomers could be derived from ^{1}H-NMR spectra. A typical spectrum is depicted in Figure 4.1. The lactide conversion was determined from the ratio of the peak areas corresponding to the monomer -C**H**COO- protons (5.05 ppm) and the oligomer -C**H**COO- protons (f, 5.15 ppm). In all cases, conversions reached were above 98 %. The degree of polymerisation *n* was determined from the ratio of the peak areas corresponding to the -C**H**COO- end group protons (f ', 4.35 ppm) and the -C**H**COO- protons in the repeat unit (f, 5.15 ppm). Using *n*, the arm length (expressed as the number-average molecular weight per arm) was calculated.

The degrees of functionalisation of the obtained macromers were also determined by ^{1}H-NMR analysis; an overview is presented in Table 4.1. The degree of functionalisation of the 2-armed macromers was determined from the peak areas corresponding to the methacrylate protons (h, 5.65 and 6.2 ppm) and the hexanediol -C$\mathbf{H}_2$O- protons (e, 4.1 ppm). The degrees of functionalisation of the 3-armed macromers were determined in a similar way, using the glycerol-residue peak (4.2 ppm). The peak corresponding to the sorbitol part of the 6-armed macromers is masked by the PDLLA -C**H**COO- (f) peak. Therefore, in case of these macromers, a degree of functionalisation of 100 % was inferred from the absence of -C**H**COO- end group peaks (f ', 4.35 ppm).

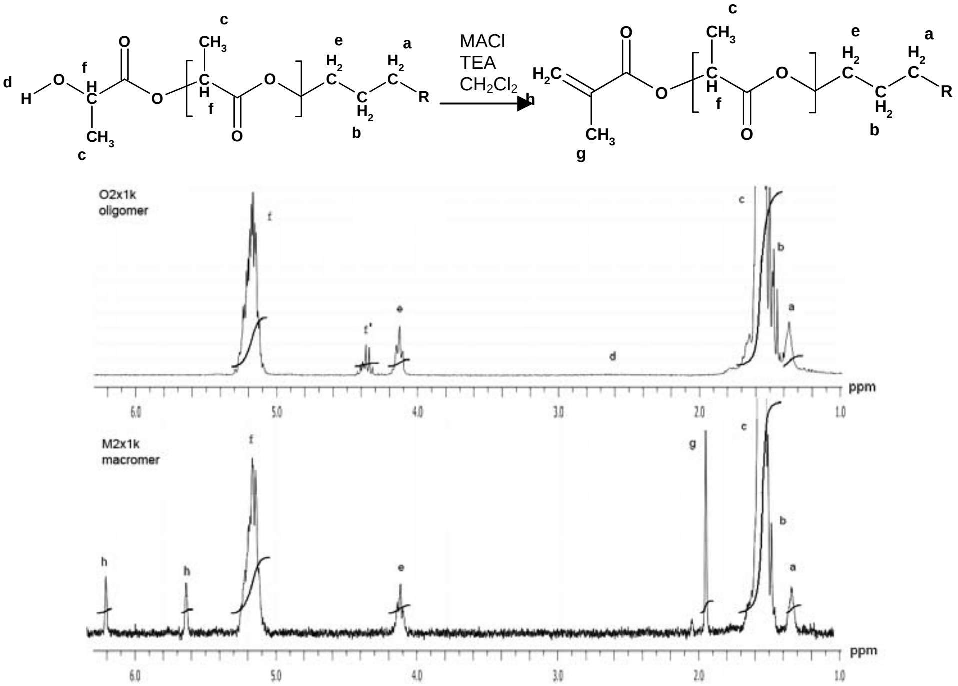

Figure 4.1: ^{1}H-NMR spectra of an O2x1k lactide oligomer (upper spectrum) and the corresponding M2x1k macromer (lower spectrum) after functionalisation with methacryloyl chloride. In the chemical structure, only one arm of the molecule is depicted.

Table 4.1: Average arm lengths and degrees of functionalisation (DF) of lactide macromers as determined by NMR analysis.

number of arms per macromer / designated arm length	2		3		6	
	$\overline{M}_n$ per arm (kg/mol)	DF (%)	$\overline{M}_n$ per arm (kg/mol)	DF (%)	$\overline{M}_n$ per arm (kg/mol)	DF (%)
0.2k	not prepared		0.22	100	not prepared	
0.6k	0.73	94	0.61	99	0.67	100
1k	1.1	100	1.1	97	1.0	100
5k	6.0	100	5.4	91	5.7	100

The synthesised macromers are termed MAxB, in which A stands for the number of arms per molecule and B for the designated arm length

The different macromers were diluted with varying amounts of EL, and their viscosities were determined at 25 °C. Over the measured range of shear rates, which was varied between 0.56 and 56 s^{-1}, the behaviour of the resins was essentially Newtonian. Figure 4.2 depicts the viscosities of different dilutions of the macromers at a shear rate of 9.3 s^{-1}. Clearly, the viscosities of all macromer formulations are strongly dependent on the amount of diluent.

The overall molecular weight of the macromers is determined by their arm lengths (the molecular weight per arm) and their molecular architecture (the number of arms per molecule). When comparing different macromers with a same number of arms, it can be seen that the overall molecular weight indeed has a significant effect on viscosity. Here, the length of the arms of the macromer primarily determines the amount of diluent that is needed to reach a suitable resin viscosity. Noticeably, for macromers of which the arm length is relatively high (5k), the number of arms has only a limited effect on the required amount of diluent. For macromers with relatively short arms (0.6k), the number of arms per molecule does have a considerable influence on viscosity. This implies that for these macromers, the overall molecular weight is the determining factor.

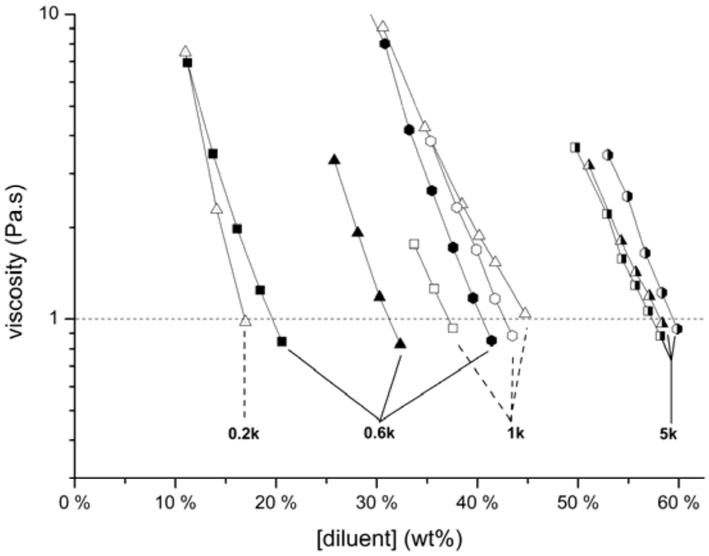

Figure 4.2: The resin viscosity of PDLLA macromers of different architectures and molecular weights as a function of the ethyl lactate diluent concentration. Macromers with 2, 3 and 6 arms are represented in the figure by squares, triangles and hexagons, respectively. A viscosity of 1 Pa·s is appropriate for application in stereolithography.

To obtain resins with a viscosity of 1 Pa·s, the different macromers were diluted with ethyl lactate. The required amounts, which will be referred to later, are given in Table 4.2. As a photo-initiator Irgacure 2959 was added, and the resins were cast and photo-crosslinked in a UV cabinet.

Table 4.2: The ethyl lactate diluent concentration (in wt% of the resin) required to formulate PDLLA macromer resins with a viscosity of 1 Pa·s. PDLLA macromers with different architectures (See Table 4.1 and Figure 4.2) are compared.

number of arms per macromer designated arm length	2	3	6
0.2k	not prepared	16.7	not prepared
0.6k	19.1	32.7	40.5
1k	37.1	44.5	42.2
5k	57.3	58.1	59.4

Network characterisation

Networks were formed by photo-crosslinking different ethyl lactate-containing PDLLA macromer resins with viscosities of 1 Pa·s. All PDLLA networks had very high gel contents of 96±3 %.

During the formation of a network, the glass transition temperature (T_g) increases as end groups react and macromers are incorporated into the network. This can lead to vitrification, especially for high-T_g polymers. As the T_g of the network approaches the prevailing temperature, the forming network becomes glassy and crosslinking reactions are quenched.[25] The high gel contents of our PDLLA networks are the result of the presence of the non-reactive diluent. It acts as a plasticizer that increases the mobility of macromers and non-reacted end groups. This enables the crosslinking reaction to proceed to high conversions and high gel contents.

As a consequence, networks with high T_g's that exceed the photo-polymerisation temperature, can be obtained after removal of the non-reactive diluent. Figure 4.3 shows the T_g values of the PDLLA macromers and of the corresponding photo-crosslinked networks. The T_g of the macromers with different molecular architectures increases with increasing arm length. After the photo-crosslinking reaction, however, the T_g of the extracted networks increases with decreasing arm length of the macromers used. This is the result of an increasing crosslink density.

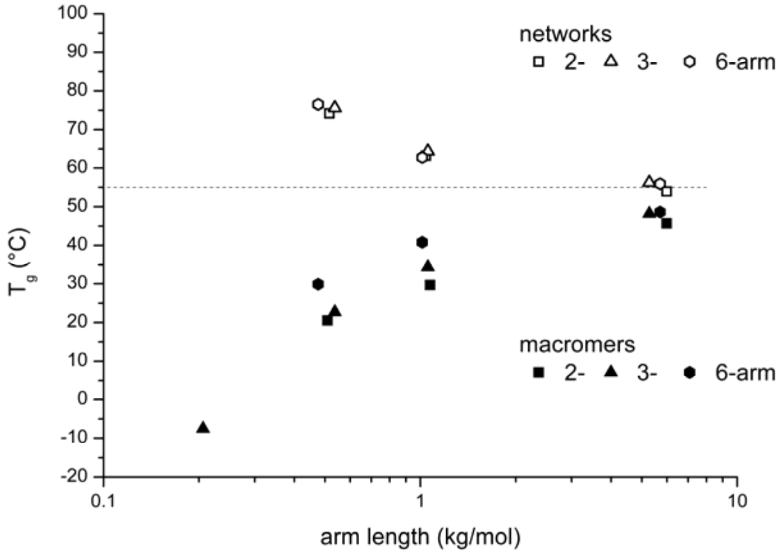

Figure 4.3: The glass transition temperatures (T_g) of PDLLA macromers of different architectures, and of the resultant extracted photo-crosslinked networks. The T_g of HMW PDLLA (55 °C) is indicated for comparison.

Compared to HMW PDLLA, with a T_g of approximately 55 °C, PDLLA networks with much higher glass transition temperatures can be obtained. For networks prepared from macromers with arm lengths of 0.6 kg/mol, T_g values close to 76 °C were determined. By DSC, a glass transition temperature could not be detected for the most densely crosslinked network (N3x0.2k). In contrast to the considerable effect of macromer chain length on the glass transition temperature of the networks formed, the effect of macromer architecture (the number of arms) is minimal.

The crosslink density of the PDLLA networks formed, will also have an effect on their swelling behaviour in solvents. Equilibrium swelling experiments were performed in ethyl lactate, which is the non-reactive diluent in our stereolithography resins. The degree of swelling of the different extracted (and dried) PDLLA networks is depicted in Figure 4.4. Networks formed from macromers with arm lengths less than 1 kg/mol take up small amounts of EL. Networks formed from macromers with arm lengths of approximately 1 kg/mol swell to up to 1.4 times their dry volume, while networks formed from macromers with arm lengths close to 5 kg/mol swell up to nearly 6 times their dry volume. This is not only caused by the difference in molecular weights of the macromers used in the preparation of the networks, but also by the different amounts of diluent in the resins that are required to reach suitable viscosities for processing by stereolithography. For example, the resins based on macromers with 5 kg/mol arm lengths contain 57 to 60 wt% diluent, while the resin based on a 2-armed macromer with arm length of 0.6k contains only 19 wt% of diluent, see Table 4.2. At high dilutions of the resin, the density of trapped entanglements in the corresponding network is decreased. And additionally, the number of intra-molecular reactions is relatively high, leading to elastically inactive chains in the network.[26] Consequently, the effective crosslink density is lower when the photo-polymerisations are carried out at high macromer dilutions. This results in higher degrees of swelling in ethyl lactate.

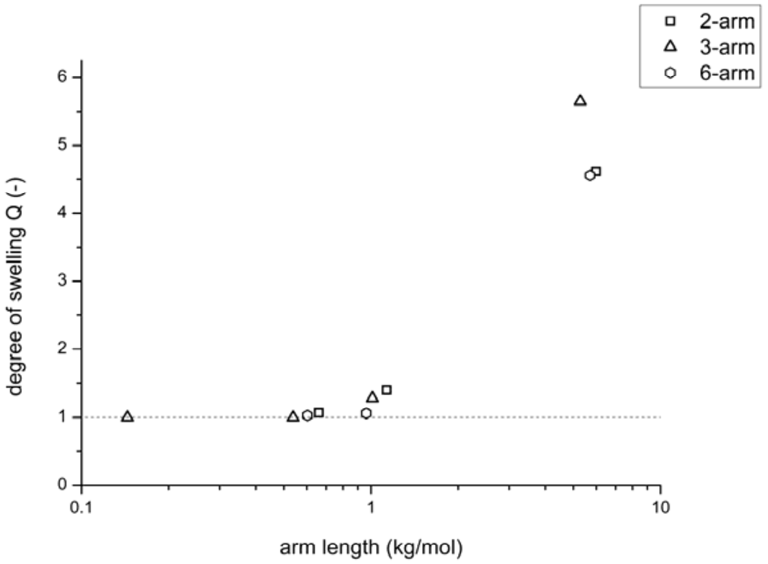

Figure 4.4: The degree of swelling in ethyl lactate of extracted PDLLA networks prepared from macromers with different architectures, as a function of the macromer arm length. The networks were prepared by photo-crosslinking PDLLA macromer resins diluted with ethyl lactate to a viscosity of 1 Pa·s, according to Table 4.2. The measurements were performed in duplicate with an error of less than 4 %.

Mechanical properties

High-molecular weight poly(D,L-lactide) is a rigid, amorphous and glassy polymer. Its mechanical properties are appropriate for bone fixation devices or application in bone tissue engineering. Photo-crosslinked materials are generally based on low-molecular weight macromers, resulting in densely crosslinked networks that are often brittle. It can be expected that the mechanical behaviour of photo-crosslinked PDLLA networks improves with increasing arm length of the precursors, approaching that of HMW PDLLA.

The mechanical properties of the extracted and dried networks were determined in 3-point bending tests; the results are listed in Table 4.3. An effect of the molecular architecture of the macromer on the properties of the networks cannot be observed. The mechanical properties of the networks are very similar to those of HMW PDLLA. Only the most densely crosslinked network, N3x0.2k, exhibits significantly lower strains at failure. These brittle materials may be less suited for application in load-bearing constructs. The data show that to obtain PDLLA networks with the most favourable mechanical properties, the arm length of the used macromer should not be lower than 0.6 kg/mol.

Table 4.3: The flexural properties of photo-crosslinked PDLLA networks and HMW PDLLA. Determinations of the flexural modulus (E_f), flexural strength (σ_f) and strain at failure (ε) were performed in 5-fold; the results are presented as average values±standard deviations.

number of arms per macromer designated arm length	2	3	6
0.2k	not prepared	E_f = 3.6±0.4 GPa σ_f = 79±19 MPa ε = 2.4±0.5 %	not prepared
0.6k	E_f = 2.9±0.1 GPa σ_f = 94±1 MPa ε = 5.0±0.1 %	E_f = 2.5±0.6 GPa σ_f = 83±22 MPa ε = 6.2±0.2 %	E_f = 2.5±0.5 GPa σ_f = 93±14 MPa ε = 6.1±0.2 %
1k	E_f = 2.5±0.5 GPa σ_f = 80±8 MPa ε = 5.3±0.5 %	E_f = 3.5±0.2 GPa σ_f = 118±16 MPa ε = 4.5±1.1 %	E_f = 2.7±0.3 GPa σ_f = 92±1 MPa ε = 5.6±1.0 %
5k	E_f = 3.4±0.1 GPa σ_f = 89±8 MPa ε = 4.2±0.8 %	E_f = 2.9±0.1 GPa σ_f = 87±2 MPa ε = 4.9±0.6 %	E_f = 3.4±0.4 GPa σ_f = 97±6 MPa ε = 4.1±0.3 %
HMW PDLLA	E_f = 2.9±0.6 GPa σ_f = 88±14 MPa ε = 4.9±1.1 %		

Stereolithography

While rapid prototyping methods such as fused deposition modelling and selective laser sintering are restricted to simple architectures, stereolithography allows the preparation of structures with more advanced designs. To prepare PDLLA structures by stereolithography, a resin based on the M2x0.6k macromer was formulated. This macromer requires only 19 wt% of non-reactive ethyl lactate diluent to reach the appropriate resin viscosity. This will result in minimal shrinkage upon extraction and drying of a built structure. Moreover, the resulting network has excellent mechanical properties.

Stereolithography is a layer-by-layer fabrication method.[27] Complex structures can be built by illuminating sequential layers of a polymerisable resin using digital pixel masks or arrays of mirrors. In stereolithography, the thickness of a solidified layer (cure depth, C_d in μm) is controlled by the light irradiation dose E (mJ/cm^2). A plot of the cure depth versus the irradiation dose is termed a working curve[27] and can be described by:

$$C_d = D_p \ln \frac{E}{E_c}$$

In a specific SLA setup, curing of the resin is characterised by a critical energy E_c (mJ/cm^2) and a penetration depth D_p (μm). E_c is the minimum energy required to reach the gel-point and start forming a solidified layer. The penetration of light into the resin is characterised by D_p.

To achieve good attachment between layers, the conversion of the macromer at the interface of the layers should be slightly higher than the gel point. In our experiments, a light irradiation dose that is 10 % higher than that required to obtain a cure depth that equals the step height of the build platform, was found to be well suited. This overexposure results in (further) curing into the preceding layer. Pixels or volume elements which according to the design were to remain uncured, will now have partially polymerised. This inevitable overcure will affect pore size and geometry when building porous structures. A high value of the extinction coefficient of the resin corresponds to a small D_p, and will allow minimal overcure and most accurate control of the building process. This is due to the fact that conversion of the photo-polymerisation reaction versus the distance from the resin surface is an exponentially decaying function (according to Beer-Lambert).

Figure 4.5 shows working curves for resins prepared from the M2x0.6k PDLLA macromer, which further contained 19 wt% ethyl lactate and 6 wt% photo-initiator. From the slopes of the working curves, it can be seen that the penetration depth of the resin decreased from 301 μm to 78 μm upon addition of 0.2 wt% Orasol Orange G dye. Under our experimental building conditions, this will reduce the overcure into a preceding layer from approximately 29 μm to only 7 μm.

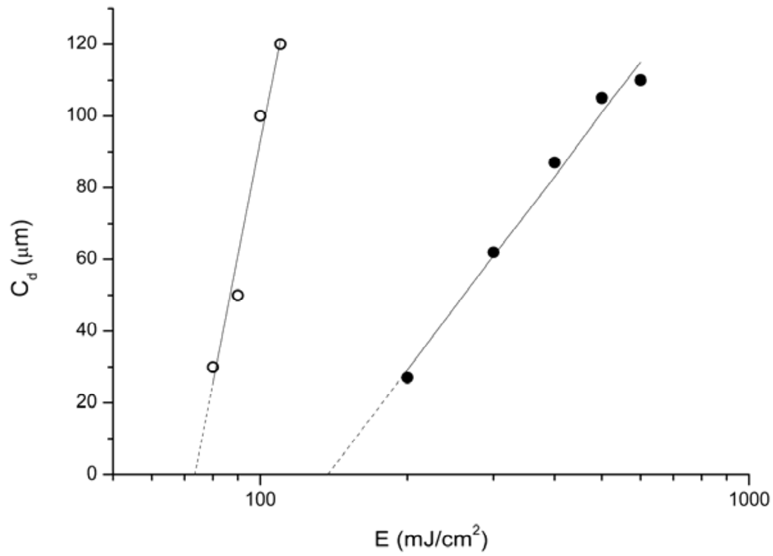

Figure 4.5: Stereolithography working curves of M2x0.6k PDLLA macromer-based resins containing 0.2 wt% Orasol Orange G dye (●) and containing no dye (○).

With this dye-containing resin, stereolithography was used to build ISO 37-2 non-porous, dumbbell-shaped specimens which were then subjected to tensile testing. The tensile strength, Young's modulus and elongation at break of the N2x0.6k PDLLA network photo-crosslinked in the SLA were 56±2 MPa, 3.3±0.2 GPa and 1.9±0.1 %, respectively. These values were very reproducible and compared favourably with those of compression moulded HMW PDLLA specimens. The latter values were respectively 44±5 MPa, 2.7±0.1 GPa and 2.0±0.5 %.

Cell culturing

To demonstrate the suitability of these materials for use in medical applications such as bone tissue engineering, mouse pre-osteoblasts (from the MC3T3 cell line) were seeded and cultured on photo-crosslinked PDLLA disks. These disks were punched out from a film that was also prepared from the M2x0.6k macromer-based resin by SLA. Compression-moulded HMW PDLLA was used as a reference material, and tissue culture polystyrene (TCPS) as a positive control. Figure 4.6 presents light microscopy images of the cells on the materials at 1 d, 4 d and 11 d after seeding. The images clearly show an increase in cell density in time. (The layering which is visible in the images of the N2x0.6k PDLLA networks results from the layer-by-layer nature of the stereolithography process.) Figure 4.7 shows high-magnification images of the pre-osteoblasts. The cells show similar spread morphologies on all materials. The cells had an average area of 3.9x10^2 μm^2/cell for the N2x0.6k PDLLA networks and 5.4x10^2 μm^2/cell for TCPS.

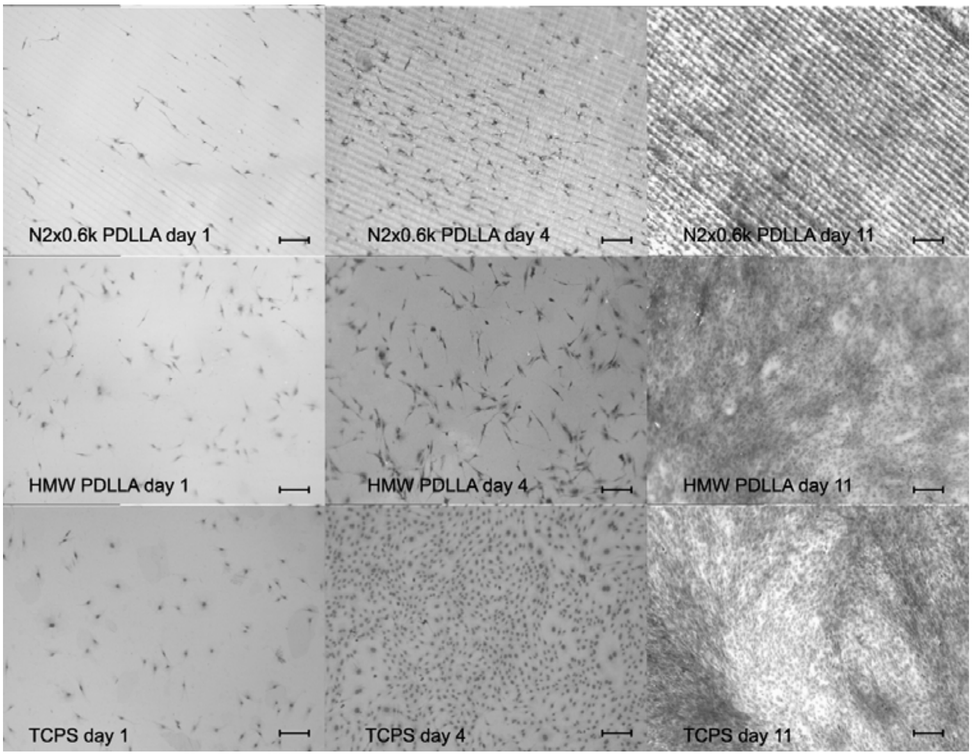

Figure 4.6: Light microscopy images of mouse pre-osteoblasts cultured on PDLLA network (N2x0.6k) films vertically prepared by stereolithography. HMW PDLLA and TCPS were used as controls. The scale bars represent 200 μm.

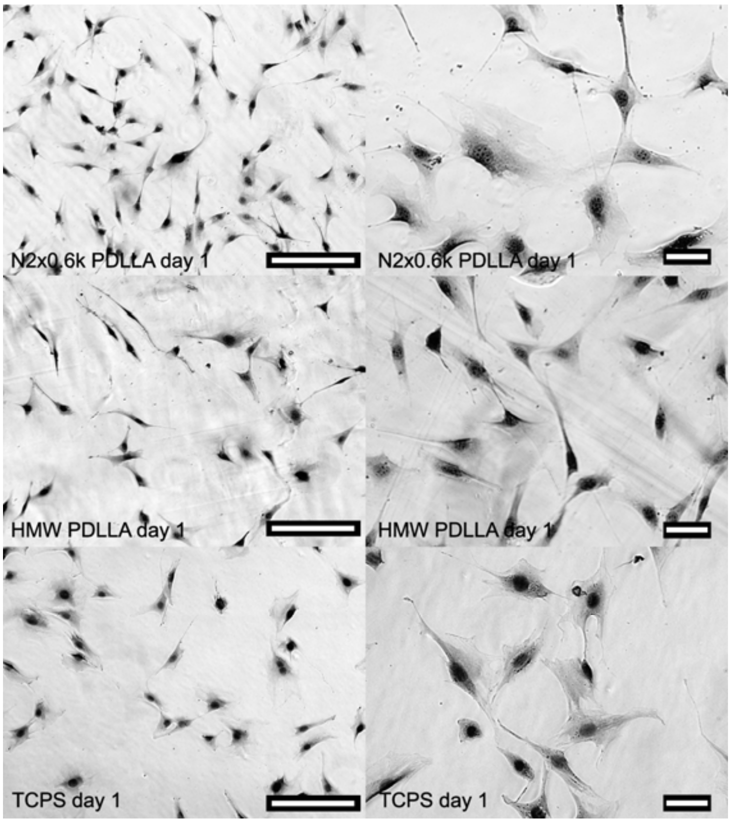

Figure 4.7: Light microscopy images showing the spreading of mouse pre-osteoblasts after 1 day of culturing on PDLLA network (N2x0.6k) films horizontally prepared by stereolithography. HMW PDLLA and TCPS were used as controls. The scale bars represent 100 μm.

In Figure 4.8, the cell numbers determined by the XTT assay are given as a function of time. For all materials, confluency (4.5×10^5 cells/cm^2) was reached within 11 d. Although initially the number of adhering cells on TCPS was higher than on HMW PDLLA and PDLLA network films prepared by stereolithography, the proliferation rates after day 1 are comparable. The doubling time is approximately 1 d. It can be stated that N2x0.6k PDLLA network films obtained by stereolithography are excellent substrates for the culturing of cells.

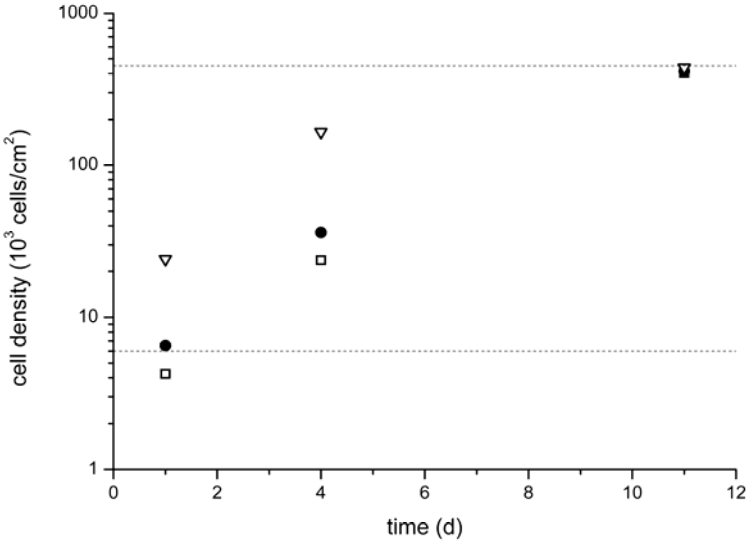

Figure 4.8: Proliferation of mouse pre-osteoblasts on PDLLA network films prepared from M2x0.6k macromers by stereolithography (●), on HMW PDLLA (□) and on TCPS (∇). The initial seeding density was 6x10^3 cells/cm^2, the cell density at confluency was 450x10^3 cells/cm^2.

Tissue engineering scaffolds

The ability to prepare PDLLA networks with excellent mechanical properties and cell culturing characteristics, now allows the preparation by stereolithography of porous scaffolds for tissue engineering. Under our experimental conditions, it is possible to build relatively large structures (up to 42x33x200 mm^3 in size) at high resolutions. The size of the smallest features that can be built are determined by the size of the light pixels (32x32 μm^2 in the x and y direction), the layer thickness (25 μm) and the overcure (only 7 μm for our M2x0.6k PDLLA macromer-based resin).

We prepared porous PDLLA network scaffolds with a gyroid architecture. This gyroid architecture is mathematically defined, allowing precise control of porosity and pore size of a fully interconnected pore network.[28] Such built structures are presented in Figure 4.9. Under the applied experimental conditions, building times were approximately 5 h. Our SLA setup allows the simultaneous building of up to 30 such structures.

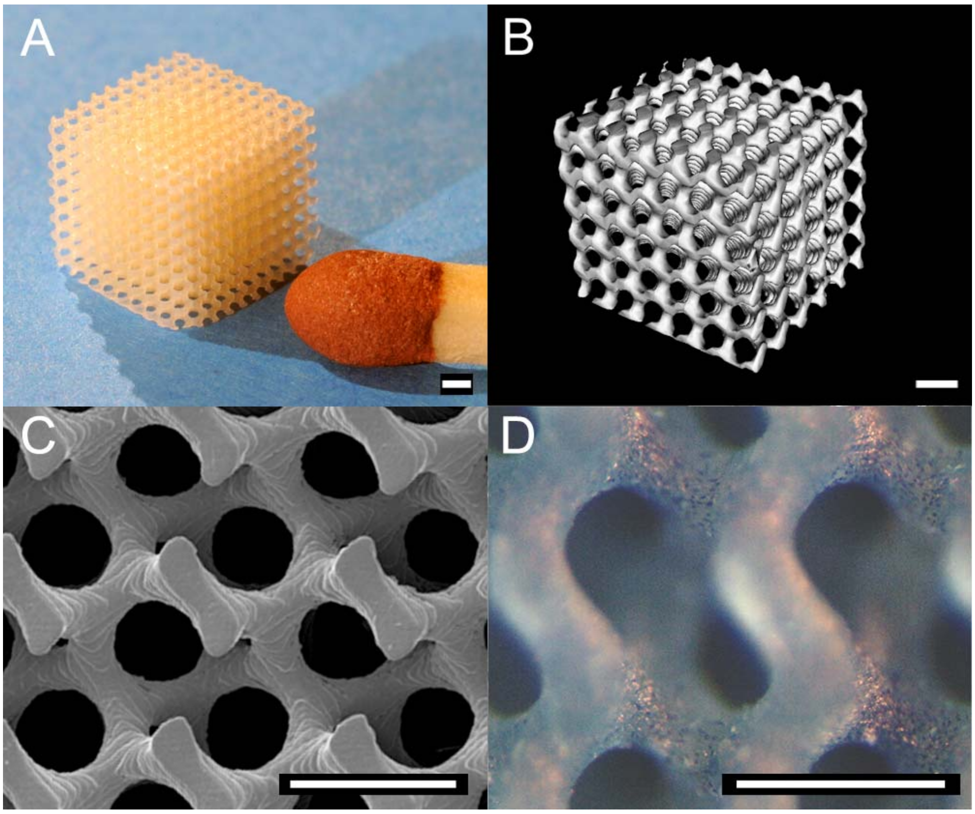

Figure 4.9: Images of PDLLA network scaffolds with a gyroid architecture, built by stereolithography. (A) photograph, (B) µCT visualisation and (C) SEM image. In (D) a light microscopy image is shown of a scaffold seeded with mouse pre-osteoblasts after 1 d of culturing. Scale bars represent 500 µm.

From the µCT data, the structural parameters of the built scaffolds after removal of the diluent were determined.[19, 29] It was found that in all directions the shrinkage was 10 %. As the shrinkage is isotropic, the designed architecture is preserved and porosity is almost unaffected; in the design the porosity was 75 %, while a porosity of 73 % was determined. This shrinkage occurs upon removal of the diluent, and can be accounted for in designing structures. µCT data also revealed a narrow pore size distribution; 83 % of the pore volume was occupied by pores ranging in size from 170 to 240 µm, with an average pore size of 200 µm. The specific surface area was 47 mm^2/mm^3.

Cell seeding of porous structures prepared from hydrophobic polymers, such as PDLLA is difficult.[30] All dry photo-crosslinked PDLLA networks absorbed only 0.6±0.2 wt% of water. For HMW PDLLA, a slightly higher water uptake of 0.9±0.1 wt% was determined. In scaffolds prepared by salt-leaching or freeze-drying methods, the penetration of a cell suspension is further hindered by the high tortuosity and poor interconnectivity of these pore networks.

The very open structure of the gyroid architecture facilitates the penetration of water into our PDLLA scaffolds prepared by stereolithography. The cell seeding could be performed effortlessly by simply pipetting the cell suspension onto the scaffold. Figure 4.9D shows a cross-section of such a scaffold 1 d after seeding with mouse pre-osteoblasts. It is clear that the cells are well attached and homogeneously distributed throughout the porous scaffold.

The excellent mechanical properties, the very good compatibility with cells, and the ability to build pre-designed (porous) architectures from a PDLLA macromer-based resin by stereolithography, makes these degradable materials very useful in medical applications. Currently, we are investigating the degradation behaviour of these photo-crosslinked PDLLA networks.

Conclusions

A resin based on poly(D,L-lactide) macromers and a non-reactive diluent was developed and applied in stereolithography. Designed solid structures and porous scaffolds were prepared and characterised. D,L-lactide oligomers with different molecular weights and molecular architectures were functionalised with methacrylate end groups, and photo-polymerised in the presence of ethyl lactate as a non-reactive diluent. Networks with high gel contents were obtained. After removal of the diluent, materials with excellent mechanical properties, similar to those of linear high molecular weight PDLLA, were obtained. Films and porous scaffolds with gyroid architecture were prepared by stereolithography, using a liquid resin based on a 2-armed PDLLA macromer and ethyl lactate. Mouse pre-osteoblasts readily adhered and proliferated well on these networks. As a result of the open pore architecture, these hydrophobic scaffolds could be seeded without difficulty. It is anticipated that degradable structures prepared by stereolithography from these resins will be very well suited for use as bone tissue engineering scaffolds.

Acknowledgements

We would like to acknowledge R. Gabbrielli and C.R. Bowen (University of Bath, UK) for providing the gyroid CAD-file and the EU for funding (STEPS project, FP6-500465).

References

[1] S. J. Hollister, *Nature Materials* **2005**, *4*, 518.

[2] M. M. Savalani, R. A. Harris, *Proceedings of the Institution of Mechanical Engineers Part H-Journal of Engineering in Medicine* **2006**, *220*, 505.

[3] B. Dhariwala, E. Hunt, T. Boland, *Tissue Engineering* **2004**, *10*, 1316.

[4] K. Arcaute, B. K. Mann, R. B. Wicker, *Annals of Biomedical Engineering* **2006**, *34*, 1429.

[5] G. Mapili, Y. Lu, S. Chen, K. Roy, *Journal of Biomedical Materials Research Part B: Applied Biomaterials* **2005**, *75B*, 414.

[6] S. J. Lee, H. W. Kang, J. K. Park, J. W. Rhie, S. K. Hahn, D. W. Cho, *Biomedical Microdevices* **2008**, *10*, 233.

[7] T. Matsuda, M. Mizutani, *Journal of Biomedical Materials Research* **2002**, *62*, 395.

[8] K. W. Lee, S. F. Wang, B. C. Fox, E. L. Ritman, M. J. Yaszemski, L. C. Lu, *Biomacromolecules* **2007**, *8*, 1077.

[9] G. M. Raghoebar, R. S. B. Liem, R. R. M. Bos, J. E. van der Wal, A. Vissink, *Clinical Oral Implants Research* **2006**, *17*, 288.

[10] H. L. Acosta, E. J. Stelnicki, L. Rodriguez, L. A. Slingbaum, *Cleft Palate-Craniofacial Journal* **2005**, *42*, 333.

[11] M. Silva, L. A. Cyster, J. J. A. Barry, X. B. Yang, R. O. C. Oreffo, D. M. Grant, C. A. Scotchford, S. M. Howdle, K. M. Shakesheff, F. Rose, *Biomaterials* **2006**, *27*, 5909.

[12] R. Tuli, S. Nandi, W. J. Li, S. Tuli, X. X. Huang, P. A. Manner, P. Laquerriere, U. Noth, D. J. Hall, R. S. Tuan, *Tissue Engineering* **2004**, *10*, 1169.

[13] M. B. Claase, M. B. de Riekerink, J. D. de Bruijn, D. W. Grijpma, G. H. M. Engbers, J. Feijen, *Biomacromolecules* **2003**, *4*, 57.

[14] S. F. Yang, K. F. Leong, Z. H. Du, C. K. Chua, *Tissue Engineering* **2001**, *7*, 679.

[15] R. F. Storey, S. C. Warren, C. J. Allison, J. S. Wiggins, A. D. Puckett, *Polymer* **1993**, *34*, 4365.

[16] A. S. Sawhney, C. P. Pathak, J. A. Hubbell, *Macromolecules* **1993**, *26*, 581.

[17] D. W. Grijpma, Q. P. Hou, J. Feijen, *Biomaterials* **2005**, *26*, 2795.

[18] A. O. Helminen, H. Korhonen, J. V. Seppala, *Journal of Applied Polymer Science* **2002**, *86*, 3616.

[19] J. Jansen, F. P. W. Melchels, D. W. Grijpma, J. Feijen, *Biomacromolecules* **2009**, *10*, 214; Chapter 3 of this thesis

[20] M. N. Cooke, J. P. Fisher, D. Dean, C. Rimnac, A. G. Mikos, *Journal of Biomedical Materials Research Part B-Applied Biomaterials* **2003**, *64B*, 65.

[21] S. J. Bryant, C. R. Nuttelman, K. S. Anseth, *Journal of Biomaterials Science-Polymer Edition* **2000**, *11*, 439.

[22] C. G. Williams, A. N. Malik, T. K. Kim, P. N. Manson, J. H. Elisseeff, *Biomaterials* **2005**, *26*, 1211.

[23] Y. Lu, G. Mapili, G. Suhali, S. C. Chen, K. Roy, *Journal of Biomedical Materials Research Part A* **2006**, *77A*, 396.

[24] C. Hinczewski, S. Corbel, T. Chartier, *Journal of the European Ceramic Society* **1998**, *18*, 583.

[25] J. J. Fitzgerald, C. J. T. Landry, *Journal of Applied Polymer Science* **1990**, *40*, 1727.

[26] K. Dusek, H. Galina, J. Mikes, *Polymer Bulletin* **1980**, *3*, 19.

[27] P. F. Jacobs, *Rapid Prototyping & Manufacturing: Fundamentals of Stereolithography*, Society of Manufacturing Engineers, Dearborn, MI **1992**.

[28] R. Gabbrielli, I. G. Turner, C. R. Bowen, *Key Engineering Materials* **2008**, *361-363 II*, 901.

[29] R. Müller, S. Matter, P. Neuenschwander, U. W. Suter, R. P, in *Morphological control in multiphase polymer mixtures*, Vol. 461 (Eds: R. M. Briber, P. D.G., C. C. Han), Materials Research Society, **1997**, 217.

[30] A. G. Mikos, M. D. Lyman, L. E. Freed, R. Langer, *Biomaterials* **1994**, *15*, 55.

Chapter 5 - Hydrolytically degradable poly(D,L-lactide) networks characterised by NMR

Ferry Melchels[1], Aldrik Velders[2], Jan Feijen[1] and Dirk Grijpma[1, 3]

To date, biodegradable networks -and particularly their kinetic chain lengths- have been characterised by analysis of their degradation products in solution. Here, we characterised the network itself, by NMR analysis in the solvent-swollen state under magic angle spinning conditions. The networks were prepared by photo-initiated crosslinking of poly(D,L-lactide)-dimethacrylate macromers (5 kg/mol) in the presence of a non-reactive diluent. Using diffusion filtering and 2D correlation spectroscopy techniques, all network components could be identified. By quantification of network-bound photo-initiator fragments, an average kinetic chain length of 9±2 methacrylate units could be determined. The PDLLA macromer solution was also used with a dye, to prepare computer-designed structures by stereolithography. For these network structures, the average kinetic chain length was 24±4. In all cases the calculated molecular weights of the polymethacrylate chains after degradation will be maximum 7.5 kg/mol, which is far below the threshold for renal clearance.

Upon incubation in phosphate buffered saline at 37 °C, the networks showed a similar mass loss profile in time as linear high-molecular weight PDLLA (HMW PDLLA). The mechanical properties were preserved longer for the PDLLA networks than for HMW PDLLA. The initial tensile strength of 47±2 MPa did not decrease significantly for the first 15 weeks, while HMW PDLLA lost 85 % of its strength within 5 weeks. The physical properties, kinetic chain lengths and degradation profile of these photo-crosslinked PDLLA networks make them most suited materials for orthopaedic applications and use in (bone) tissue engineering.

---

[1] MIRA Institute for Biomedical Technology and Technical Medicine, and Department of Polymer Chemistry and Biomaterials, University of Twente, P.O. Box 217, 7500 AE, Enschede, The Netherlands

[2] MESA+ Institute and Department of Supramolecular Chemistry and Technology, University of Twente, P.O. Box 217, 7500 AE, Enschede, The Netherlands

[3] Department of Biomedical Engineering, University Medical Centre Groningen and University of Groningen, P.O. Box 196, 9700 AD Groningen, The Netherlands

Introduction

Photo-initiated networks that degrade in the body are of great interest for biomedical applications. They can serve as surgical implants,[1] glues,[2] drug delivery devices[3] or as scaffolding materials for tissue engineering.[4, 5] Characteristic properties are ease of preparation and good mechanical performance. By altering the chemistry, material properties such as mechanical properties, hydrophobicity, cell-material interactions and degradation kinetics can be tailored.[6] Furthermore, photo-initiated networks exhibit good shape stability due to their crosslinked nature, even at temperatures higher than the polymer's glass transition temperature.[7, 8] Photo-initiation has several advantages over other methods of network formation: it is rapid, temporally and spatially controlled, and it can be performed under mild conditions. The latter is used for example in cell encapsulation[9] or in the preparation of injectable hydrogels that can be cured transdermally.[4, 10] Biodegradable networks have often been prepared from hydrolytically degradable oligomers composed of monomers such as lactide, caprolactone, and trimethylene carbonate, after end-functionalisation with methacrylate,[7] acrylate[11] or fumarate groups.[12] Upon light irradiation in the presence of a photo-initiator, the end groups polymerise via an addition-type reaction to form polyvalent crosslinks, and a network is formed.

In vivo, polymers and their networks usually degrade by a combination of hydrolytic and oxidative degradation, with or without mediation by enzymes. Hydrolysis reactions lead to scission of polymer (network) chains, and takes place either through a surface erosion[13] or bulk degradation mechanism[14]. The kinetics of hydrolytic degradation of such networks is governed mainly by the type of degradable bond and by the hydrophilicity of the network.[13] For example, anhydride bonds are hydrolysed much faster than ester bonds[15], and the carbonate bonds in poly(trimethylene carbonate) are hydrolysed particularly slow.[16] On the other hand, the amount of water that can be taken up by the network strongly influences the rate of chain scission. Degradation times can vary from several days for hydrogels consisting of poly(ethylene glycol) chains extended with lactide blocks and methacrylate groups,[11] to up to more than one year for hydrophobic ε-caprolactone[17] and networks thereof. Furthermore, components present in the network that can attract water, such as solvents or residual monomer, can significantly speed up the hydrolytic degradation;[8, 18] this is also the case for linear polymers.[19]

After complete hydrolysis, the degradation products of biodegradable networks are usually water-soluble compounds derived from the polymer network main chains, initiators used in the oligomer synthesis, and polyaddition chains formed in the photo-crosslinking process. The length and character of these chains determines if they can be removed from the body by renal clearance. Water-soluble polymers with molecular weights up to 50 kg/mol are cleared by the kidneys within a few days. Above 50 kg/mol, liver clearance via the uptake of Kupffer cells predominates.[20] A maximum accumulation in the circulatory system has been observed for polymers which have a molecular weight over 200 kg/mol, regardless of polymer type.[21] For this reason, the length of the kinetic chains in biodegradable networks has been the subject of a number of studies.[22-25] It can vary significantly depending on the photo-crosslinking conditions; however, exact chain lengths have been difficult to quantify. For example, kinetic chain lengths of poly(methacrylic acid) chains from sebacic acid-dimethacrylate based networks were studied using mass spectrometry[23] in one study and using gel permeation chromatography in another study.[22] The networks were prepared under similar conditions, but the outcomes were very different: average chain length values reported were 10-40 or 1000-2000 monomer units, respectively.

In this work we present the characterisation of photo-crosslinked poly(D,L-lactide) (PDLLA), and its hydrolytic degradation profile. Due to their good mechanical properties, these networks have great potential for orthopaedic and bone tissue engineering applications. Furthermore, they can be prepared in almost any desired shape using stereolithography.[26] In this technique, a computer-controlled laser beam or a digital light projector is used to locally solidify a liquid resin through photo-initiated polymerisation. In combination with a computer-driven building stage, a solid, three-dimensional computer-designed object can be constructed in a layer-by-layer fashion.

To date, biodegradable networks and particularly their kinetic chain lengths have been characterised by analysis of their degradation products in solution. Here, we characterise the molecular structure of networks photo-crosslinked from PDLLA-dimethacrylate precursors using sophisticated nuclear magnetic resonance spectroscopy techniques. This enables determination of the kinetic chain length without the need for degradation. Furthermore, we present the development of network properties, water uptake, mass loss and mechanical properties in time, during degradation at 37 °C in phosphate buffered saline.

Experimental

Hydroxyl-terminated oligomers were synthesised by ring-opening polymerisation (130 °C, 40 h under an argon atmosphere) of D,L-lactide (DLLA, Purac Biochem) using 1,6-hexanediol (Sigma-Aldrich) as initiator and stannous octoate (Sigma-Aldrich) as catalyst. The monomer-to-initiator ratio was adjusted to yield oligomers with a molecular weight of 5 kg/mol. The hydroxy-terminated oligomers were reacted with methacrylic anhydride (Sigma-Aldrich) in the presence of triethyl amine

(Sigma-Aldrich) (both in a 20 mol % excess) in dried dichloromethane (Biosolve) for 5 d to yield methacrylate end-functionalised lactide macromers. The macromers were purified by precipitation from isopropanol (Biosolve), followed by washing with water and freeze-drying.

With the macromers, a liquid photo-crosslinkable resin was prepared, consisting of 58 wt% PDLLA-dimethacrylate, 40 wt% dry N-methylpyrrolidone (NMP, Fluka) as a non-reactive diluent, 2 wt% ethyl-2,4,6-trimethylbenzoylphenylphosphinate (Lucirin TPO-L photo-initiator as a gift from BASF), 0.2 wt% α-tocopherol inhibitor (Fluka) to prevent preliminary crosslinking and 0.15 wt% Orasol Orange dye (gift from BASF). Using this resin and a commercial stereolithography apparatus (Envisiontec Perfactory Mini Multilens SLA), computer-designed porous structures a with a gyroid design were fabricated as described elsewhere.[26a] The stereolithography apparatus was also used to prepare films by projecting a 75x60 mm^2 rectangle of blue light (intensity 10 mW/cm^2) onto a 0.64 mm thick layer of resin for 5 min. In this case, a dye was not required in the resin. The solvent-swollen crosslinked films were washed in acetone (Biosolve) and postcured by irradiating with 365 nm UV-light for 15 min (Ultralum crosslinking cabinet, intensity 3–4 mW/cm^2) under a nitrogen atmosphere. The diluent and non-reacted photo-initiator were extracted from the films with acetone. The films were first dried at ambient conditions, after which the presence of a small acetone solvent residue allowed the effortless punching of disks (Ø 5 mm) and strips (4.8x60 mm) from the plasticised 0.5 mm thick films. The disks and strips were finally dried at 90 °C for 2 d under a nitrogen flow. Glass transition temperatures were determined using a Perkin-Elmer Pyris 1 differential scanning calorimeter (DSC) at a heating rate of 10 °C/min. The glass transition temperature was taken as the midpoint of the heat capacity change in the second heating run, after quenching (300 °C/min).

PDLLA-dimethacrylate macromer, photo-initiator Lucirin TPO-L and degradation product of the PDLLA network were analysed in solution (DMSO-d_6) by NMR spectroscopy, using a high-resolution solution probe (triple-nucleus TXI probe with z-gradient) interfaced with a Bruker Avance II 600 spectrometer operating at 600.34 MHz (^{1}H) or 150.2 MHz (^{13}C), and equipped with a Great 3/10 gradient amplifier.

Photo-crosslinked PDLLA was analysed in the solvent-swollen state using a high resolution magic angle spinning (HR-MAS) probe equipped with gradient coil along the rotor axis. The swollen networks were measured in 50 μL KelF rotors, spinning at 6 kHz. Regular 1D spectra were recorded, as well as 2D correlation spectra (COSY) and nuclear Overhauser effect spectra (NOESY) of the network material.

Pulsed-field gradient stimulated echo (PFGSE, or diffusion-filtered) 1D ^{1}H-NMR spectra were obtained using the bipolar stimulated echo sequence. Typically, field gradient strengths varying from 5 to 30 % of the maximum field strength, 128 averages per increment step, and 100 ms diffusion times were employed. Standard pulse sequences for homonuclear (HH-COSY and HH-NOESY), heteronuclear (HMQC and HMBC) and PFGSE experiments were taken from the Bruker library.

To investigate polymer (network) degradation behaviour, disk-shaped specimens (mass m_0) were placed in glass vials containing 5 mL phosphate buffered saline (PBS, supplemented with 0.02 wt% sodium azide (Sigma-Aldrich)) in a 37 °C water-bath under light agitation. The incubation medium PBS was refreshed every 2 weeks. At each time-point, 3 specimens were taken out, washed in demi-water, blotted and weighed (m_{wet}). Subsequently, the specimens were freeze-dried, weighed again (m_{dry}) and kept in dry NMP to reach equilibrium swelling (minimum 2 d). After blotting and weighing ($m_{swollen}$), the specimens were extracted with acetone, dried at 90 °C for 2 d under nitrogen flow and weighed again (m_{gel}). Gel contents were calculated as m_{gel}/m_0 and the volume degrees of swelling were calculated using the swollen mass $m_{swollen}$ and the densities of PDLLA (1.25 mg/mL) and NMP (1.03 mg/mL):

$$Q = 1 + \frac{m_{swollen} - m_0}{m_0} \times \frac{\rho_{PDLLA}}{\rho_{NMP}}$$

Tensile test strips were kept at 37 °C as well, in 15 mL centrifuge tubes filled with PBS. Also here, the incubation medium was supplemented with 0.02 wt% sodium azide and refreshed every second week. At each time-point, 4 strips were taken out and subjected to tensile testing in the wet state using a Zwick Z020 universal tensile tester at a rate of 10 mm/min. The grip-to-grip separation was 50 mm and mechanical extensometers were employed.

Of the photo-crosslinked PDLLA network film, 13.70 g was degraded in 0.2 L of 1.0 M NaOH (Merck) solution at 100 °C for 3 weeks, in a Teflon round-bottom flask equipped with a reflux condenser. After neutralising with 37 wt% HCl solution (Merck), the contents were dialysed to milliQ-water using a cellulose ester dialysis tubing (Spectra/Por, Spectrum Laboratories) with a molecular weight cut-off of 500 Da to remove lactic acid, hexane diol and salts. After dialysis and freeze-drying, the remaining degradation products were dissolved in DMSO-d_6 (Sigma-Aldrich) for NMR analysis as described above.

Linear, high-molecular weight PDLLA (HMW PDLLA) reference material was obtained from Purac Biochem. Granules were compression moulded (140 °C, 250 kN, 3 min) to 0.5 mm thick films. From these films, disks and strips of the same dimensions as mentioned before were punched out while plasticising the polymer at approximately 45 °C (10 °C below the glass transition temperature). Molecular weights were determined after compression moulding using a Viscotek GPCmax gel permeation chromatography setup with Viscotek 302 Triple Detection Array and

$CHCl_3$ as an eluent with a flow of 1 mL/min. Initial molecular weights of the polymer after compression moulding were M_n = 120 kg/mol and M_w = 289 kg/mol. NMR-analysis ($CDCl_3$, Varian 300 MHz) indicated the presence of 1.7 % residual lactide monomer in the polymer material.

Results and Discussion

Preparation of photo-initiated poly(D,L-lactide) networks

Figure 5.1 shows the ^{1}H-NMR spectrum of the synthesised poly(D,L-lactide)-dimethacrylate macromer that was used to prepare the PDLLA networks, and the assignment of all proton resonances. The number-average degree of polymerisation of lactide can be derived from the ratio of the integral values of the peaks corresponding to the lactide methine proton (c) and the protons of the hexane methylene that links to the lactide chain (e). This ratio is 35 lactic acid units per hexanediol-fragment terminus (a total of 70 lactic acids units in the oligomer), corresponding to a number-average molecular weight of the macromers of 5 kg/mol. By comparing the integral value of the hexane methylene peak (e) to those of the methacrylate =C**H**$_2$ proton peaks (k), quantitative functionalisation of the macromer termini can be concluded. Furthermore, a trace of isopropyl alcohol (IPA) is observed, resulting from the macromer purification.

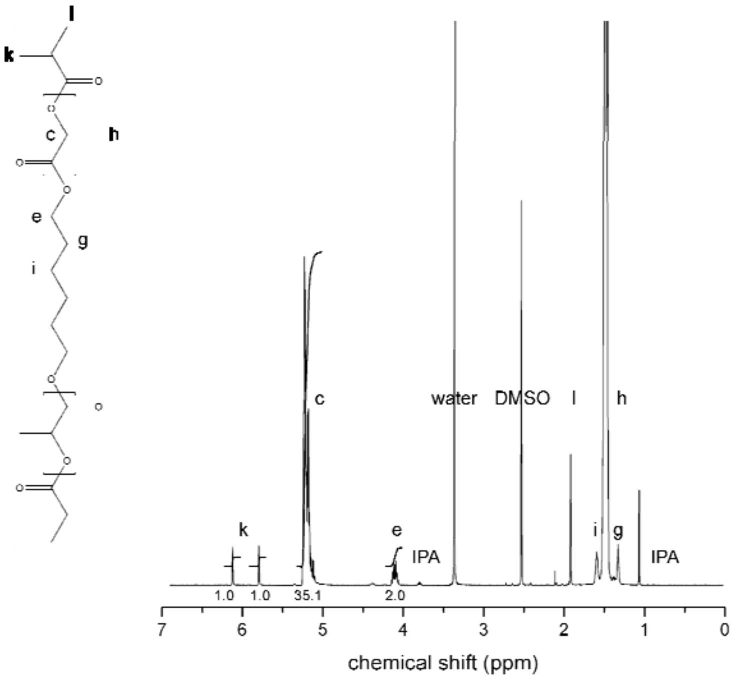

Figure 5.1: Chemical structure and ^{1}H-NMR spectrum of the PDLLA-dimethacrylate macromer in DMSO-d_6. The labels in the structure and spectrum correspond to those in the network structure depicted in Figure 5.2. The integrals are normalised to reflect half of the mactromer structure.

The PDLLA macromers were used with a non-reactive diluent and photo-initiator (PI) to prepare network films in a stereolithography apparatus. The chemical structure of the used photo-initiator Lucirin TPO-L, and its ^{1}H-NMR spectrum, can be found in the Supporting Info (Figure 5.10) Upon light irradiation, the photo-initiator produces two different radical species: a phosphine species (PI_p) and an alkanoate species (PI_a). Both can initiate polymerisation of the methacrylate end groups of the macromers, and a network is formed. Figure 5.2 shows the molecular structure of such a photo-crosslinked PDLLA network, in which characteristic protons are labelled for later reference. Note that from each methacrylate unit, a PDLLA chain links to another polymethacrylate chain. Each of the kinetic chains shown in the network structure was initiated by a different radical species, originating from the heterolytic scission of the photo-initiator.

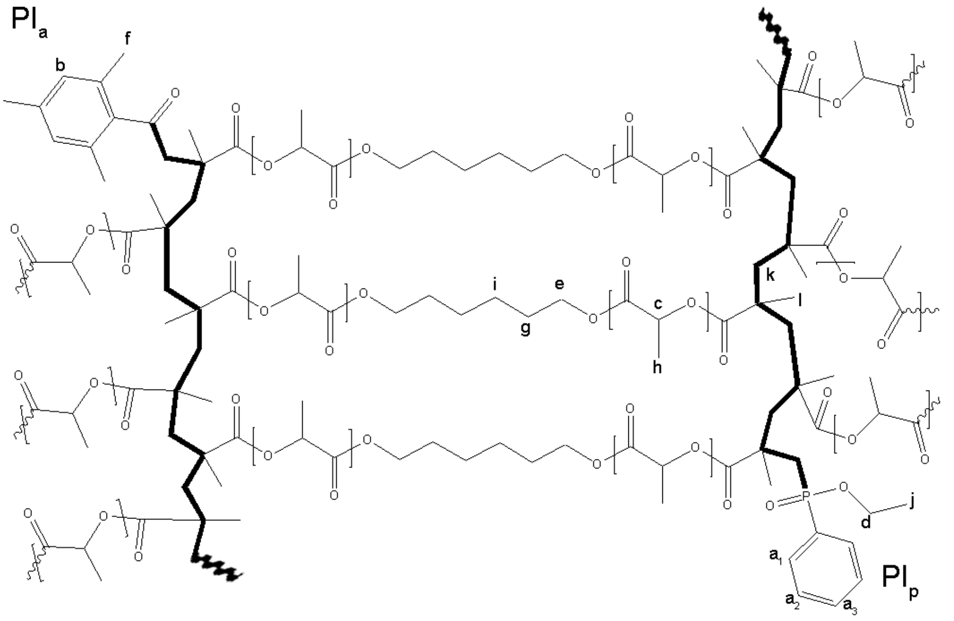

Figure 5.2: Chemical structure of a photo-crosslinked PDLLA network, in which characteristic protons are labelled for further reference. The polymethacrylate kinetic chains are drawn in bold.

The photo-initiated crosslinking of the PDLLA-dimethacrylate macromers in the liquid resin yields flexible solvent-swollen gels, which after extraction and drying become rigid, glassy networks. The physical properties of these networks are quite similar to those of linear high-molecular weight PDLLA: elastic modulus of 2.6±0.1 GPa, tensile strength of 47±2 MPa and elongation at break of 2.3±0.3 %. The networks show low water uptake of 0.7±0.1 wt% and a glass transition temperature of 58±1 °C. These properties make these biodegradable networks well suited for orthopaedic applications and as scaffold material for (bone) tissue engineering.

Network characterisation using NMR

To date, biodegradable networks and particularly their kinetic chain lengths have been characterised by analysis of their degradation products.[23, 25] However, mass spectrometry, gel permeation chromatography and NMR spectroscopy of dissolved degradation products have lead to very divergent results for kinetic chain lengths. We have embarked on a full characterisation study of the network itself, by NMR spectroscopy on solvent-swollen networks. High resolution ^{1}H-NMR data of the PDLLA network were obtained with an HR-MAS probe. Due to the spinning of the sample at the magic angle[27] the signals are sharp and remarkably high resolution spectra of the networks are obtained (Figure 5.3). The polymeric material yields broad peaks due its heterogeneous character; there is a distribution of chain lengths and many chiral centres are present. Interestingly, also isolated peaks with characteristic 3-bond spin-spin coupling patterns in the order of a few hertz are revealed. The 1D and 2D NMR data obtained are complementary and render very relevant information: the identification of the main components of the network, the conversion in the chain crosslinking reaction, the lactide to hexane ratio, the presence of solvents, and the relative amount of photo-initiator reaction products. Finally, it allows determination of the number-average kinetic chain length of the network.

First, the network spectra are dominated by the intense peaks around 1.4 and 5.2 ppm (Figure 5.3, insert) corresponding to the lactide methyl (h) and methine (c) protons, respectively. The dynamic range of the HR-MAS data is very large, and peaks with intensities in the range of a few % of the lactide peaks are still well resolved and can be observed. An important observation that follows from the NMR spectra is that in these post-cured networks no unreacted methacrylate double bonds are present, as confirmed by the absence of the vinyl peaks (k) at 5.6 and 6.2 ppm (that can be clearly seen in the macromer spectrum, Figure 5.1). With highly crosslinked glassy networks, a complete double bond conversion is rarely reached because of severe restrictions on the mobility of the reacting molecules. Attaining conversions approaching 100 % is important for the mechanics and biocompatibility of the resultant network, but has been difficult to achieve.[6] In our networks, full conversion is readily achieved as the relatively long PDLLA chains have high mobility in the presence of a non-reactive diluent.

Further, focussing in on the less intense peaks in the network spectrum, more than the proton signals of the lactide chains and hexane linkers are observed. To discriminate peaks belonging to the network from those of residual solvents or other impurities, diffusion-filtered pulsed field gradient stimulated echo (PFGSE) experiments were performed. Small, mobile molecules have relatively high diffusion constants and therefore the corresponding peaks decrease faster in intensity than the peaks corresponding to the network material. This becomes clear when comparing the spectra in Figure 5.3, where the insert shows an unfiltered spectrum, while the larger spectrum is obtained after diffusion-filtering. In the unfiltered spectrum, the water peak (3.4 ppm) is of comparable intensity as the lactide methine peak (c, 5.1 ppm), whereas in the larger, diffusion-filtered spectrum the peak has reduced in relative intensity with a factor of approximately 20. Also the residual solvent peak from partially protonated DMSO (i.e. DMSO-d_5, at 2.5 ppm) clearly looses intensity upon increase of the gradient strength. Interestingly, slightly upfield from this solvent peak another peak is observed that corresponds to DMSO-d_5 as well, and probably derives from the solvent molecules that are encapsulated within the network and therefore show slower diffusion than the free solvent itself. Also water shows as a second more slowly decreasing signal, corresponding to water molecules that are mixed with DMSO within the network structure (3.2 ppm).

Having identified the peaks of residual solvents and other impurities in the spectrum, assignment of all peaks belonging to the network was done recording homonuclear 2D HH correlation spectroscopy (COSY) experiments. The coupling of the lactic acid (CH_3-CH) peaks (h) and (c) is readily confirmed by the COSY spectrum (Figure 5.4). The COSY spectrum also identifies the proton signals of the hexane linker unit bridging the polylactide chains, connecting the 4.06 ppm peak (e) to the 1.55 ppm peak (g) just downfield from the lactide methyl peak, which consecutively shows a coupling to a peak (i) just upfield from the lactide peak. The length of the PDLLA chain that connects the polymethacrylate backbone and the hexane bridging unit can be calculated from the ratio between the smaller hexane methylene (e) and the lactic acid methine (c) peak in the HR-MAS spectrum of the gel (Figure 5.3), and is equal to the chain length obtained from the high-resolution NMR spectrum of the macromer in solution (Figure 5.1), about 35 lactic acid units.

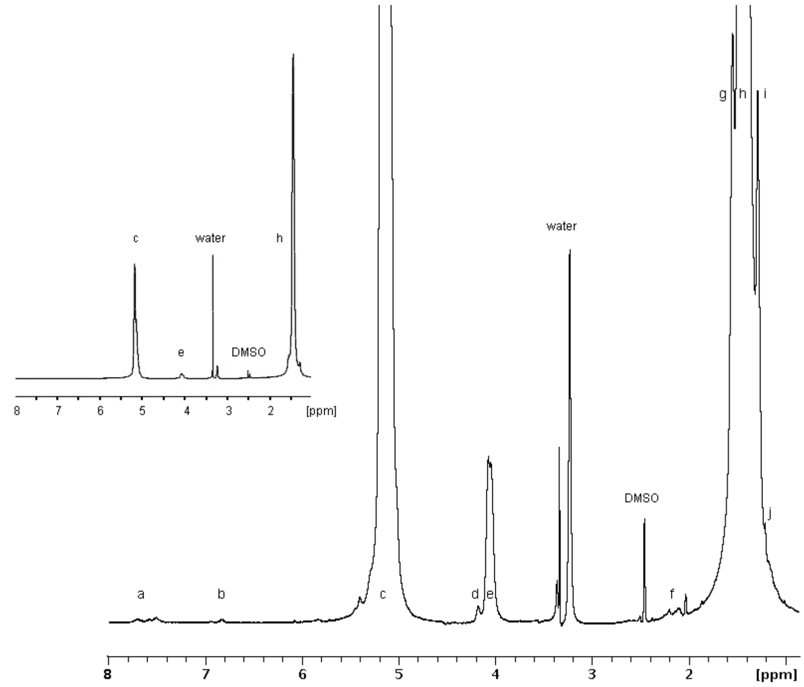

Figure 5.3: ^{1}H-NMR HR-MAS spectra of a photo-crosslinked PDLLA network swollen in DMSO-d_6. The insert shows the unfiltered spectrum, while the large spectrum was obtained after diffusion-filtering. The peak labels correspond to those in the network structure depicted in Figure 5.2.

In Figure 5.3, the diffusion-filtered spectrum shows small peaks in the aromatic region (6.8-7.8 ppm). These peaks belong to groups that are bound to the network, as can be concluded from the series of PFGSE experiments in which these peaks show the same signal attenuation as the other signals from the network. Comparison with the spectrum of the photo-initiator (Figure 5.10) indicates that these probably arise from PI-residues that initiated the chain crosslinking polymerisation. Also the small peaks at 1.3, 2.2 and 4.17 ppm can be attributed to the photo-initiator fragments that have initiated the polymerisation of the methacrylate end groups and therefore define the starting points of the polymethacrylate chains (Figure 5.2). The peaks at 6.8 (b, singlet) and 2.2 ppm (f, singlet) are from the initiating alkanoate species (PI_a), corresponding to the aromatic and methyl protons, respectively. Their assignment was further confirmed by a NOESY cross-peak (Figure 5.11 in the Supporting info). The other three broad signals more downfield in the aromatic region (a) correspond to the phenyl ring protons of the phosphinate species (PI_p). The ethoxy group of the PI_p unit shows peaks at 4.17 (d) and 1.3 ppm (j) (compare Figure 5.10). The coupling of these signals is also clearly shown by a (d,j) cross peak in the COSY spectrum (see enlarged area in Figure 5.4).

Comparison of the integrals of the aromatic peaks in the PDLLA network spectra reveals a ratio of 70 % PI_p-initiated polymethacrylate chains in the network to 30 % PIa-initiated chains. In the photo-polymerisation of styrene using a very similar photo-initiator (2,4,6-trimethylbenzoyl)diphenylphosphine oxide (TPO), the phosphinate radical exclusively initiates polymerisation.[28] In our system, however, also the PI_a species is found to initiate radical polymerisation of the methacrylate macromer end groups. This observation was confirmed by photo-polymerisation of methyl methacrylate initiated by Lucirin TPO-L. The resulting poly(methyl methacrylate) polymer could be characterised in solution by NMR, which clearly indicated the presence of both initiating species in the polymer (spectrum not shown).

Having assigned all proton signals in the network, the most informative region regarding determination of the kinetic chain length appears around 4 ppm. Here, the signal of the hexane methylene group next to a PDLLA-ester bond is present (e), just upfield by 0.1 ppm from the ethoxy-methylene of the photo-initiator unit PI_p (d). These peaks are partially overlapping but can be separated by deconvolution, enabling quantitative comparison (Figure 5.5). The two larger peaks are equally intense and correspond to the diastereotopic protons of the hexane methylene unit, neighbouring the two enantiomeric lactic acid groups that are statistically equally abundant in the sample. The downfield PI_p peak is a single broad peak, about 40 Hz wide at half height, due to spin-spin coupling to the methyl group as well as to the ^{31}P nucleus. As each hexane methylene that connects to a lactide ester corresponds to one methacrylate unit in the kinetic chain, the ratio of this hexane methylene peaks to the PI_p peak allows direct estimation of the average kinetic chain length.

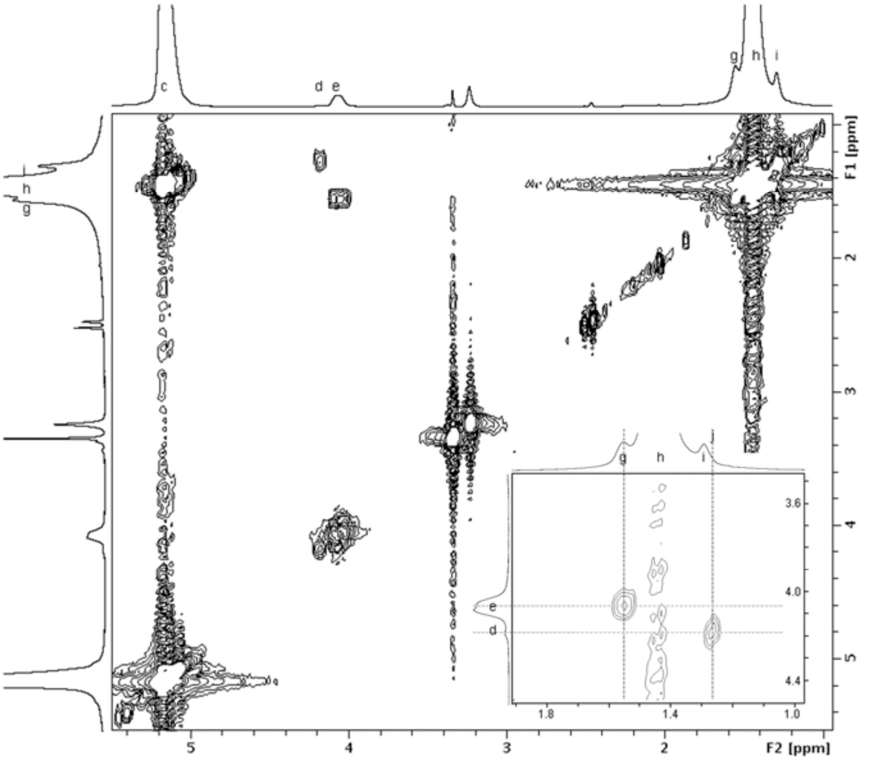

Figure 5.4: 2D HH-COSY NMR spectrum (HR-MAS) of the PDLLA network. The inserted magnification shows the coupling of the hexane peaks (e) and (g), and the coupling of the PI_p ethoxy methylene peak (d) to its neighbouring methyl peak (j). Note, the peaks e, g and i have the same intensity (all hexane peaks), whilst d and j are much less intense and the latter is barely visible in the 1D spectrum. However, the d-j cross peak is evident.

Taking into account the ratio of PI_p to PI_a chain ends, we can calculate an average ratio of 9±2 methacrylate units per PI initiator-residue. This value represents the average kinetic PMA chain length, assuming no chain transfer took place. The number-average degree of polymerisation X_n of the polymethacrylate chains depends on the mechanism of termination in the radical crosslinking reaction. Here, X_n is in the range of 9 to 18, in the extreme cases of termination by disproportionation only or by combination only, respectively.

In the resin the molar ratio of methacrylate groups to photo-initiator was 3.5, which implies a theoretical minimal average kinetic chain length of 1.75, assuming no chain transfer takes place. As we observe an average kinetic chain length of 9, this means approximately 27 % of the PI present in the resin is actually involved in the photo-initiated chain-crosslinking process. Nevertheless, relatively short kinetic chains are formed compared to other studies on methacrylate-crosslinked networks.[22, 23]

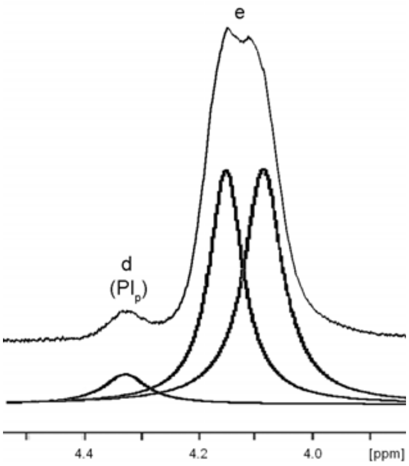

Figure 5.5: Example of peak deconvolution in ^{1}H-NMR HR-MAS spectrum. The measured (upper) spectrum is deconvoluted into the PI$_p$ ethoxy-peak, and the peaks that represent the hexane-methylene that is connected to a PDLLA chain.

The kinetic chain length strongly depends on photo-crosslinking conditions such as photo-initiator concentration and light intensity. In the layer-by-layer fabrication process that takes place in a stereolithography apparatus, a dye is often used to limit the penetration of light into the resin. Besides the network films of which the characterisation is described above, we also prepared porous structures by stereolithography.[29] For this we used the same resin as for the preparation of the network films, but also containing 0.15 wt% orange dye. The average kinetic chain length was found to be 24±4 for these network structures. The attenuation of light by the dye causes a lower average light intensity, hence lower initiation rates, lower concentrations of propagating chains and eventually, longer chains. Another interesting difference observed between bulk photo-crosslinked networks and stereolithography-fabricated structures is the presence of unreacted methacrylate groups in the latter (5 to 15 %). These unreacted groups could either be further polymerised by post-curing, or they remain available for subsequent covalent functionalisation. Possibilities are to adjust the hydrophilicity of the networks, or to immobilise cell-adhesive peptides at the surfaces of the porous structures.[30]

The PDLLA networks were degraded by refluxing in sodium hydroxide solution for 3 weeks, following removal of lactic acid, hexanediol and salts by dialysis. In the NMR spectrum of the degradation product depicted in Figure 5.6, the methacrylate protons are represented by the broad peaks around 1.8 (k') and 1.0 ppm (l'). The characteristic peaks of the PI-residues are not observed in the spectrum, so the average kinetic chain length could not be reproduced. Other small peaks are observed that were not present in the network spectrum, and could not be assigned by COSY, NOESY, HMBC or HMQC experiments. Strikingly, lactic acid peaks are still clearly present at 4.8 (c) and 1.4 ppm (h). The molar ratio of methacrylate to lactic acid is approximately one to one, indicating that the lactic acid unit connected to the polymethacrylate backbone remains unaffected under the degradation conditions used. This implies that the (PMA-LA) linking ester bond is much less prone to hydrolysis than the ester bonds within the polylactide chain. The insensitivity of methacrylate ester bonds to (alkaline) hydrolysis was observed earlier also for poly(ethylene glycol)dimethacrylate hydrogels and for poly(methyl methacrylate).[31] Taking into account the pendant lactic acid groups, and using the determined value of X_n of 9-18 units, we can calculate an average molecular weight of the poly(lactic acid methacrylate) chains after degradation of 1.4-2.8 kg/mol for the bulk photo-polymerised PDLLA networks. For the PDLLA network structures prepared by stereolithography the molecular weight of the degradation product will be 3.7-7.5 kg/mol assuming no chain transfer took place. In these ranges of molecular weights, renal clearance is still effective and fast, so no accumulation of degradation product is expected.

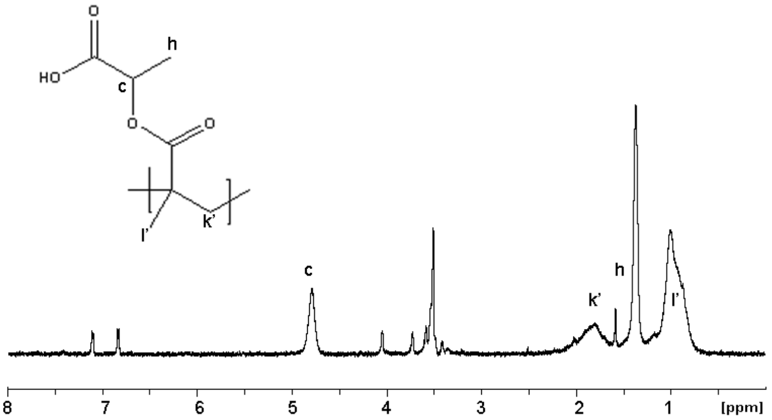

Figure 5.6: ^{1}H-NMR spectrum of the degradation product of photo-crosslinked PDLLA network in DMSO-d_6, after filtering out water and DMSO by a diffusion filter. The drawn structure represents the repeating unit of the poly(lactic acid methacrylate) chains. The labels correspond to those in the network structure (Figure 5.2).

Degradation kinetics of networks

These biodegradable PDLLA networks are suitable materials for biomedical applications such as orthopaedics and (bone) tissue engineering. They have favourable mechanical and physical properties, and can easily be prepared in any shape using stereolithography. Furthermore, we have seen that the kinetic chain lengths of the networks enable renal clearance of their degradation products. The time that it takes to degrade the networks is of utmost importance for their application. Photo-crosslinked PDLLA specimens were incubated at 37 °C in PBS to study the development of network properties in time. The degree of swelling in the solvent NMP was measured, as well as the gel content (Figure 5.7). These properties can give an indication of the extent of main chain scission before mass loss sets in. Both properties remained practically unchanged for the first 13 weeks of immersion in PBS. Due to PDLLA chain scission the degree of swelling starts to increase from around week 13, followed by a decrease in gel content starting from week 17. In this stage, dangling PDLLA chains that are cleaved at a second ester bond are removed from the network by solvent extraction. After 23 weeks, solvent-swollen networks were too fragile to be weighed so the degree of swelling could no longer be determined.

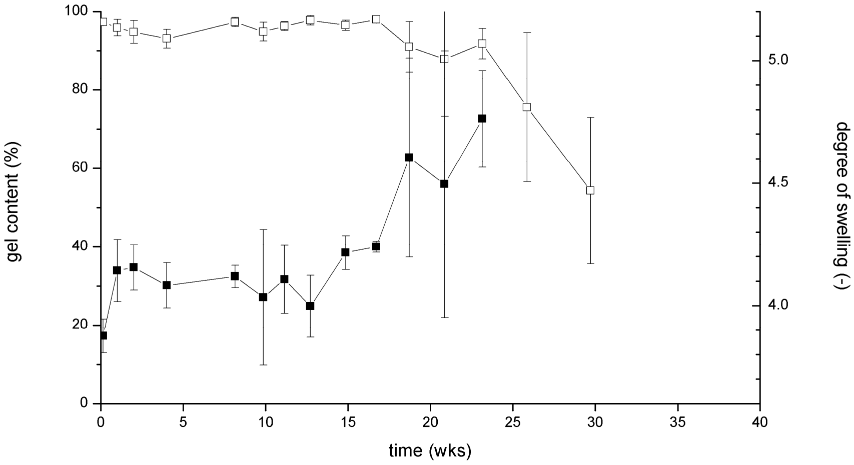

Figure 5.7: Network properties of photo-crosslinked PDLLA degraded in PBS at 37 °C: gel content (open squares) and degree of swelling in N-methyl-pyrrolidone (black squares). Each data-point represents average±standard deviation of 3 specimens.

Degradation of biodegradable implants such as tissue engineering scaffolds is often expressed in terms of decrease in molecular weight and mass loss. However, the period that a medical implant is functional depends more on the preservation of its mechanical stability, which is mostly much shorter. Figure 5.8 shows the development of the mechanical properties of photo-crosslinked PDLLA networks in time, together with the water uptake and mass loss. Here, the initial tensile strength was 47±2 MPa with an elongation at break of 2.3±0.3 %. Photo-crosslinked PDLLA retains its strength for a long time, compared to its mass loss profile. The strength remains practically unchanged up to 15 weeks (corresponding to the period that the network properties remain unchanged as well (Figure 5.7)) and it takes about 22 weeks -or 5 months- before half of its strength is lost. After loss of mechanical stability at week 24 (after which specimens become too fragile to be subjected to tensile testing), it takes only approximately 3 months before the network collapses and almost all mass is lost in a very short period. This degradation profile, in which the strength is retained for a long period compared to the mass loss, makes these networks very well suited for the intended application.

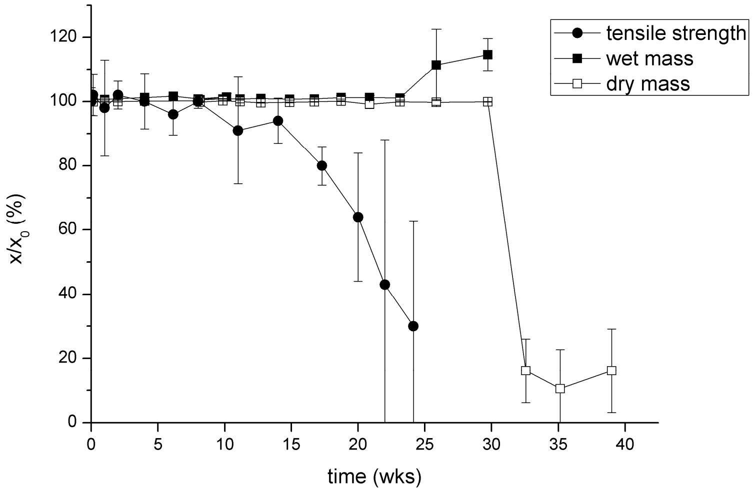

Figure 5.8: Properties of photo-crosslinked PDLLA networks degraded in PBS at 37 °C. Each data-point represents average±standard deviation of 3 specimens.

High molecular weight PDLLA (HMW PDLLA) was included in this degradation study as a reference material. As the presence of residual monomer strongly influences the degradation behaviour (decay in mechanical properties in particular),[19] it should be noted that this commercially available HMW PDLLA contained 1.7 % monomer (determined by ^{1}H-NMR). Although the mass loss profile is similar to the PDLLA networks, the decay in tensile strength differs greatly (Figure 5.9). HMW PDLLA loses its strength very rapidly, starting directly after immersing in PBS. After only 1 month it has lost most of its structural integrity and strength.

The intrinsic viscosity shows a similar decay in time as the tensile strength, indicating high chain scission rates in the polymer. Furthermore, HMW PDLLA shows an undesirably high water uptake of up to more than 100 % after 20 weeks, while the PDLLA networks increase in weight only with a few percent. In the networks, the crosslinks prevent extensive swelling and specimens retain their shape. The observations lead to the conclusion that the presence of crosslinks has little effect on the course of hydrolysis reactions, but strongly influences the geometrical and mechanical stability of the degrading specimens.

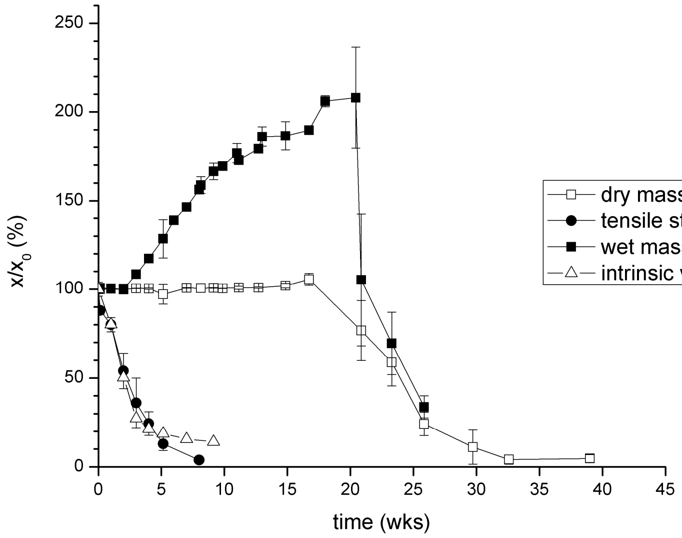

Figure 5.9: Properties of HMW PDLLA degraded in PBS at 37 °C. Each data-point represents average±standard deviation of 3 specimens, except for the intrinsic viscosity (n=1).

Often, semi-crystalline poly(L-lactide) (PLLA) is employed for medical applications rather than amorphous PDLLA. Although longer-term mechanical stability is achieved as the degradation is much slower in the crystalline phase, still the strength is lost long before mass loss sets in. Moreover, upon degradation of the amorphous phase PLLA releases crystallites, which can remain in the body for several years and induce foreign body reactions and swelling.[32] For these reasons, amorphous PDLLA networks form a good alternative to both amorphous PDLLA as well as crystalline PLLA. The chemical crosslinks preserve mechanical stability, while the degradation period after loss of strength is short and no potentially harmful crystalline regions are present.

Conclusions

The network structure and hydrolytic degradation of poly(D,L-lactide) (PDLLA) networks, photo-crosslinked from PDLLA-dimethacrylate oligomers, was studied. NMR analysis of the degradation products in solution revealed the presence of one lactic acid unit per methacrylate unit on the polyaddition chains, but could not be used to determine kinetic chain lengths. High-resolution NMR spectroscopy under magic angle spinning conditions (HR-MAS) proved a very useful and sensitive technique to characterise such polymer networks in the solvent-swollen state. Identification of all network components was achieved, and an average kinetic chain length of 9±2 could be determined. This implies an average molecular weight of the poly(lactide methacrylate) chains after degradation in the range of 1.4-2.8 kg/mol. For computer-designed PDLLA network structures prepared by stereolithography in the presence of a dye, the average molecular weights of these polyaddition chains are 3.7-7.5 kg/mol. These values are far below the threshold for renal clearance.

When incubated at 37 °C in PBS, the PDLLA networks were shape-stable and showed little mass change for approximately 6 months, shortly followed by complete collapse and near-complete mass loss. For the first 15 weeks, tensile strength, gel content and degree of swelling remained practically unchanged. After this time point, chain scission was evidenced by a reduction in strength and gel content, and by an increase in degree of swelling (implying a decrease in crosslink density).

The characterised PDLLA networks show excellent mechanical properties over a period of approximately 5 months in aqueous environments, and they degrade into water-soluble products with molecular weights far below the kidney cut-off. Therefore, these networks hold great promise for orthopaedic and (bone) tissue engineering applications.

Acknowledgements

We would like to acknowledge the European Union (STEPS project, FP6-500465) and Nanoned for their financial support.

References

[1] M. D. Timmer, C. G. Ambrose, A. G. Mikos, *Journal of Biomedical Materials Research Part A* **2003**, *66A*, 811.

[2] D. Miki, K. Dastgheib, T. Kim, A. Pfister-Serres, K. A. Smeds, M. Inoue, D. L. Hatchell, M. W. Grinstaff, *Cornea* **2002**, *21*, 393.

[3] B. Amsden, *Soft Matter* **2007**, *3*, 1335.

[4] X. Q. Jia, J. A. Burdick, J. Kobler, R. J. Clifton, J. J. Rosowski, S. M. Zeitels, R. Langer, *Macromolecules* **2004**, *37*, 3239.

[5] G. John, M. Morita, *Macromolecules* **1999**, *32*, 1853.

[6] J. L. Ifkovits, J. A. Burdick, *Tissue Engineering* **2007**, *13*, 2369.
[7] R. F. Storey, S. C. Warren, C. J. Allison, J. S. Wiggins, A. D. Puckett, *Polymer* **1993**, *34*, 4365.
[8] A. O. Helminen, H. Korhonen, J. V. Seppala, *Journal of Applied Polymer Science* **2002**, *86*, 3616.
[9] J. Elisseeff, W. McIntosh, K. Anseth, S. Riley, P. Ragan, R. Langer, *Journal of Biomedical Materials Research* **2000**, *51*, 164.
[10] J. Elisseeff, K. Anseth, D. Sims, W. McIntosh, M. Randolph, R. Langer, *Proceedings of the National Academy of Sciences of the United States of America* **1999**, *96*, 3104.
[11] A. S. Sawhney, C. P. Pathak, J. A. Hubbell, *Macromolecules* **1993**, *26*, 581.
[12] R. F. Storey, J. S. Wiggins, M. E. Tisack, K. A. Mauritz, A. D. Puckett, *Abstracts Of Papers Of The American Chemical Society* **1991**, *201*, 331.
[13] D. S. Muggli, A. K. Burkoth, K. S. Anseth, *Journal of Biomedical Materials Research* **1999**, *46*, 271.
[14] R. F. Storey, T. P. Hickey, *Polymer* **1994**, *35*, 830.
[15] A. C. Albertsson, M. Eklund, *Journal of Applied Polymer Science* **1995**, *57*, 87.
[16] K. J. Zhu, R. W. Hendren, K. Jensen, C. G. Pitt, *Macromolecules* **1991**, *24*, 1736.
[17] C. G. Pitt, M. M. Gratzl, G. L. Kimmel, J. Surles, A. Schindler, *Biomaterials* **1981**, *2*, 215.
[18] K. A. Davis, J. A. Burdick, K. S. Anseth, *Biomaterials* **2003**, *24*, 2485.
[19] S. H. Hyon, K. Jamshidi, Y. Ikada, *Polymer International* **1998**, *46*, 196.
[20] T. Yamaoka, Y. Tabata, Y. Ikada, *Journal of Pharmaceutical Sciences* **1994**, *83*, 601.
[21] Y. Murakami, Y. Tabata, Y. Ikada, *Drug Delivery: Journal of Delivery and Targeting of Therapeutic Agents* **1996**, *3*, 231.
[22] J. A. Burdick, T. M. Lovestead, K. S. Anseth, *Biomacromolecules* **2003**, *4*, 149.
[23] A. K. Burkoth, K. S. Anseth, *Macromolecules* **1999**, *32*, 1438.
[24] T. M. Lovestead, J. A. Burdick, K. S. Anseth, C. N. Bowman, *Polymer* **2005**, *46*, 6226.
[25] S. He, M. D. Timmer, M. J. Yaszemski, A. W. Yasko, P. S. Engel, A. G. Mikos, *Polymer* **2001**, *42*, 1251.
[26] F. P. W. Melchels, J. Feijen, D. W. Grijpma, *Biomaterials* **2009**, *30*, 3801; Chapter 4 of this thesis
[27] U. Haeberlen, J. S. Waugh, *Physical Review* **1968**, *175*, 453.
[28] H. H. Meng, T. Saito, P. L. Rinaldi, F. Wyzgoski, C. A. Helfer, W. L. Mattice, H. J. Harwood, *Macromolecules* **2001**, *34*, 801.
[29] F. P. W. Melchels, K. Bertoldi, R. Gabbrielli, A. H. Velders, J. Feijen, D. W. Grijpma; Chapter 6 of this thesis
[30] P. D. Drumheller, J. A. Hubbell, *Analytical Biochemistry* **1994**, *222*, 380.
[31] T. Shirahase, Y. Komatsu, Y. Tominaga, S. Asai, M. Sumita, *Polymer* **2006**, *47*, 4839.
[32] E. J. Bergsma, F. R. Rozema, R. R. M. Bos, W. C. Debruijn, *Journal of Oral and Maxillofacial Surgery* **1993**, *51*, 666.

Supporting Information

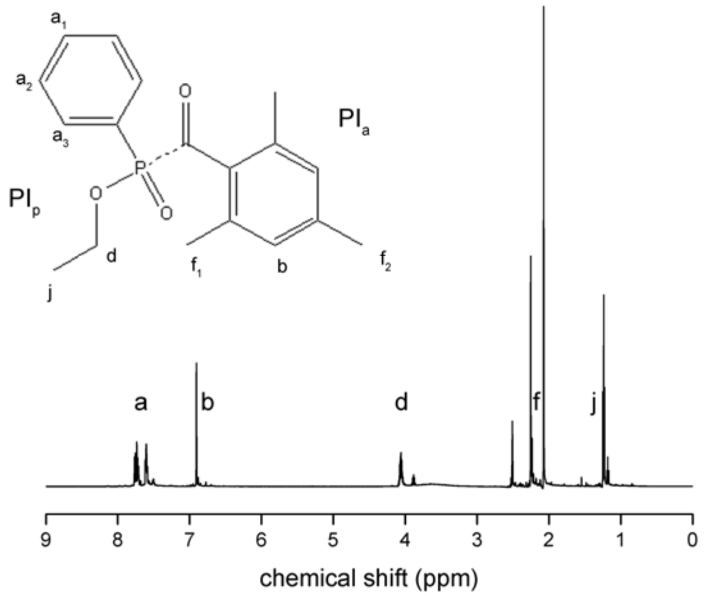

Figure 5.10: ^{1}H-NMR spectrum of the photo-initiator Lucrin TPO-L (ethyl (2,4,6-trimethylbenzoyl) phenylphosphinate) in DMSO. The peak assignments correspond to those in the network structure depicted in Figure 5.2. The photo-labile bond is drawn as a dashed line.

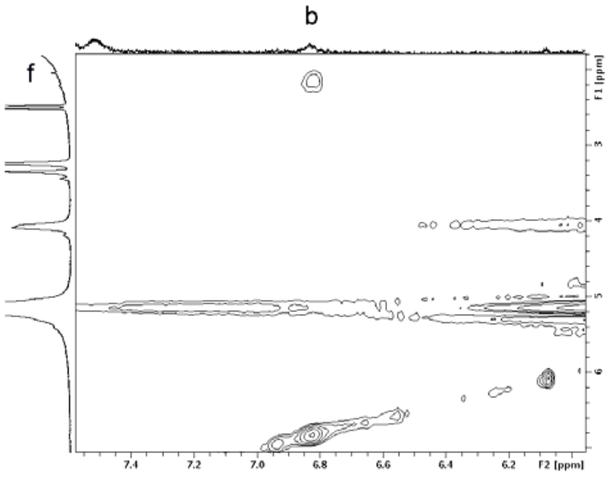

Figure 5.11: detail of a NOESY-spectrum of the PDLLA network obtained by HR-MAS spectroscopy, showing the coupling of the aromatic protons (b at 6.8 ppm) and methyl-protons (f at 2.2 ppm) originating from the PI$_a$ initiating species.

Chapter 6 – Advanced tissue engineering scaffolds with designed pore network architectures prepared by stereolithography

Ferry Melchels[1], Katia Bertoldi[2], Ruggero Gabbrielli[3], Aldrik Velders[4], Jan Feijen[1] and Dirk Grijpma[1,5]

The technology employed for the preparation of tissue engineering scaffolds restricts the choice of materials and the extent to which the architecture can be designed. In this chapter we show the versatility of stereolithography with respect to materials and freedom of design. Porous scaffolds are designed with computer software and built with either a poly(D,L-lactide)-based resin or a poly(D,L-lactide-*co*-ε-caprolactone)-based resin. Characterisation of the scaffolds by micro computed tomography shows excellent reproduction of the designs. The mechanical properties are evaluated in compression, and show good agreement with finite element predictions. The mechanical properties of scaffolds can be controlled by the combination of material and scaffold pore architecture. The presented technology and materials enable an accurate preparation of tissue engineering scaffolds with a large freedom of design, and properties ranging from rigid and strong to highly flexible and elastic.

---

[1] MIRA Institute for Biomedical Technology and Technical Medicine, and Department of Polymer Chemistry and Biomaterials, University of Twente, P.O. Box 217, 7500 AE, Enschede, The Netherlands

[2] Department of Multi Scale Mechanics, University of Twente, P.O. Box 217, 7500 AE, Enschede, The Netherlands

[3] School of Engineering, Swansea University, SA2 8PP, Swansea, United Kingdom

[4] MESA+ Institute and Department of Supramolecular Chemistry and Technology, University of Twente, P.O. Box 217, 7500 AE, Enschede, The Netherlands

[5] Department of Biomedical Engineering, University Medical Centre Groningen and University of Groningen, P.O. Box 196, 9700 AD Groningen, The Netherlands

Introduction

The preparation of porous structures on the micron-level with full freedom of design is still a challenge. One application is in tissue engineering, where porous biodegradable structures serve as temporary supports for the regeneration of tissue.[1] Such scaffolds should comply with the surrounding native tissue, which imposes requirements on properties such as stiffness, strength, biocompatibility and biodegradability.[2] Besides the properties of the material, also the pore architecture of a scaffold is of great influence on its functionality. The architecture influences mechanical properties, cell adhesion and proliferation, transport phenomena and degradation behaviour.

Conventional scaffold fabrication techniques such as salt-leaching, gas-foaming and phase-separation followed by freeze-drying, allow the tuning of only a few parameters like porosity and pore size.[3] Advances in rapid prototyping techniques have significantly improved the control over the whole design of three-dimensional (3D) solid and porous structures.[4, 5] Among these techniques are selective laser sintering,[5, 6] fused deposition modelling (or 3D fibre plotting),[7] 3D printing[8] and stereolithography.[9] The latter is particularly versatile with respect to the freedom of design and scale: sub-micron structures[10] to decimetre-sized objects[11] can be built. The working principle of stereolithography is based on spatially controlled solidification of a liquid photo-polymerisable resin. Using a computer-controlled laser beam or digital light projection, and a computer-driven support platform, a 3D object can be constructed in a layer-by-layer fashion. Structural parameters such as porosity and pore size, and even gradients thereof, can be freely varied. While by using fibre plotting methods little variation in patterning of structures is possible, and laser sintering is limited by the need to process small and monodisperse particles of semi-crystalline polymers, stereolithography requires a photo-sensitive polymer formulation. The availability of suitable resins is very limited, which in general leads to non-degradable addition-type polymer networks.

When fabricating medical implants such as tissue engineering scaffolds, biodegradability is essential. A degradable photo-polymerisable system can be obtained by chain-crosslinking hydrolysable oligomers with reactive end groups.[12, 13] For example, poly(D,L-lactide) (PDLLA) functionalised with methacrylate groups can be crosslinked to form rigid polymer networks.[14] With values of the elasticity modulus of approximately 3 GPa, poly(D,L-lactide) polymers are one of the few biodegradable polymers with mechanical properties that approach those of bone (the E-modulus of bone is 3 to 30 GPa[3]). They have been applied in resorbable bone fixation devices clinically and for use in bone tissue engineering. The ring opening polymerisation of cyclic esters (lactones) and cyclic carbonates is very versatile, and allows the preparation of oligomers and macromers of a wide variety of resorbable materials. Introducing ε-caprolactone (CL) by co-polymerisation reduces the glass transition temperature and flexible rubber-like networks are obtained.[15] Copolymers of lactide and caprolactone have successfully been applied in tissue engineering as well.[16] In this chapter we will show how to design biodegradable porous structures with refined architectures and prepare these by stereolithography at high resolution. Also, we will show in which ways the mechanical properties of these scaffolds can be tailored.

Experimental

Design of porous architectures

The cube architecture was designed using Rhinoceros 4.0 CAD software (McNeel). Starting from a solid cube measuring 830x830x830 μm^3, a porous construct was obtained by removal of rectangular beams with cross-sections of 530x530 μm^2 in the three directions. This results in a cubic unit cell with 150 μm thick struts and a porosity of 70%. K3DSurf v0.6.2 software (http://k3dsurf.sourceforge.net) was used to generate CAD-files that describe the surfaces of gyroid (G) and diamond (D) architectures. The following trigonometric functions with boundary conditions x,y=[-6π,6π] and z=[-12π,12π] were used:

$$G : \cos(x)\sin(y) + \cos(y)\sin(z) + \cos(z)\sin(x) = 0.60$$

$$D : \sin(x)\sin(y)\sin(z) + \sin(x)\cos(y)\cos(z) + \cos(x)\sin(y)\cos(z) + \cos(x)\cos(y)\sin(z) = 0.42$$

To obtain porous structures with porosities of approximately 70 %, offset values of -0.60 for the gyroid- and -0.42 for the diamond architecture are required. The gradient in pore size and porosity of the gyroid structure presented was introduced by adding the term $-0.032 \cdot z$ to the equation for z-values of [-12π,0]. With this linear term, the porosity is designed to gradually decrease from 70 % at thsine mid-section to 30 % at the bottom end of the structure. Rhinoceros software was used to scale the CAD-files of all three architectures to the desired dimensions. The 5x5x10 mm^3 designs were scaled-up by a factor 1.28, anticipating the shrinkage upon extraction of non-reactive diluent from the built structures. Envisiontec Perfactory RP2.0 software was used to slice the 3D CAD-files. The stack of bitmaps generated, is the input for the layer-by-layer building process.

Macromer synthesis

Hydroxyl-terminated oligomers were synthesised by ring-opening polymerisation (130 °C, 40 h) of D,L-lactide (DLLA, Purac Biochem) using 1,6-hexanediol (Sigma-Aldrich) as initiator and stannous octoate (Sigma-Aldrich) as catalyst. P(DLLA-*co*-CL) oligomers were synthesised in a similar way, using an equimolar mixture of D,L-lactide and ε-caprolactone (CL, Sigma-Aldrich). The monomer-to-initiator ratio was adjusted to yield oligomers with a molecular weight of 5 kg/mol (molecular weights were confirmed by ^{1}H-NMR analysis). The termini of the oligomers were reacted with methacrylic anhydride (Sigma-Aldrich) in the presence of triethyl amine (Sigma-Aldrich) (both in a 20 mol % excess) in dried dichloromethane for 5 d to yield methacrylate end-functionalised lactide macromers. After precipitation from isopropanol, washing with water and freeze-drying, pure macromers with a degree of functionalisation of 92-99 % (determined by ^{1}H-NMR analysis) were obtained.

Fabrication of porous structures

The resins used for stereolithography consisted of 58 wt% PDLLA macromer, 40 wt% dry N-methylpyrrolidone (NMP, Fluka) as a non-reactive diluent, 2 wt% ethyl-2,4,6-trimethylbenzoylphenylphosphinate (Lucirin TPO-L photo-initiator from BASF), 0.2 wt% Orasol Orange G dye (Ciba SC) and 0.1 wt% α-tocopherol inhibitor (Fluka). A commercial stereolithography apparatus (Envisiontec Perfactory Mini Multilens SLA) was employed to build designed structures. The building process involves subsequent projections of 1280x1024 pixels, each 32x32 μm^2 in size. Layers with a thickness of 25 μm were cured by irradiating for 30 s with blue light (intensity 16 mW/cm^2). Uncured excess resin was washed out and the diluent, non-reacted macromer and photo-initiator were extracted from the structures with acetone. The extracted structures were then dried at 90 °C for 2 d under a nitrogen flow.

A similar resin, containing camphorquinone instead of Lucirin TPO-L and chloroform instead of NMP, was used to prepare porous structures by a salt-leaching process. This resin did not contain a dye. The resin was mixed with NaCl particles sieved to sizes of 425-710 μm, brought into tubular polypropylene moulds (inner diameter 14 mm) and cured by irradiation through the tube wall with a Kerr dental light (mono-chromatic blue LED light, wavelength 470 nm, intensity 1000 mW/cm^2) for 40 s. The specimens were frozen in liquid nitrogen, cut to the desired dimensions, and post-cured by heating to 90 °C for 12 hrs. The salt-containing composites were extracted in acetone for 2 d, and the salt fraction was leached out with water during a period of 7 d. Then, the porous structures were dried at 90 °C for 2 d under a nitrogen flow.

Analyses of the porous structures

Structural analysis was performed by micro-computed tomography (μCT) using a GE eXplore Locus SP scanner (General Electric) at 14.3 μm resolution. Scanning was done at an X-ray tube voltage of 80 kV, a current of 80 μA and an exposure time of 3000 ms. No filter was applied. After reconstruction using the Feldkamp algorithm, thresholded isosurface images were obtained (GE MicroView software). The software was also used to generate pore size distribution maps of the structures. In these 3D matrices, size values are assigned to pore voxels. These sizes correspond to the diameter of the largest sphere that can be fitted in the pore space and contains that particular pore voxel. The maps were used to calculate porosities, pore size distributions, pore surface areas and pore accessibility curves (Mathworks Matlab 2008). In determining the porosity gradient curve (Fig. 4), the porosity at a particular scaffold height was determined by taking the pore volume fraction of every individual voxel plane. The accessibility of the pore networks was quantified by first thresholding the pore size distribution maps to exclude pores smaller than a certain diameter, then the remaining pore volume fraction connected to the exterior of the structure was determined. This was repeated for a range of diameters. To compare the built structures with the software designs, the latter were evaluated in the same manner as well. For this, the stacks of bitmaps used in the layer-by-layer fabrication of the structures by SLA, were also imported into the μCT analysis software.

To model and predict the mechanical behaviour of structures with different designed pore architectures, numerical simulations were conducted. First the compressive response of solid PDLLA and P(DLLA-*co*-CL) network specimens built by stereolithography was evaluated. Mechanical testing in compression was done using a Zwick Z020 universal tensile tester in a range of compression rates. The bulk properties of each material were described mathematically using a constitutive model. The model was implemented into finite element software code (ABAQUS), which then allowed simulating and predicting the deformation characteristics of the designed porous structures. See Supporting Information for details on the development of the constitutive models and the finite element analysis.

Nuclear magnetic resonance spectroscopy (^{1}H-NMR) was performed on networks swollen in deuterated acetone using a Varian 600 MHz apparatus equipped with a high-resolution probe operating under magic angle spinning (HR-MAS) conditions.

Results and Discussion

Design and fabrication of porous structures

PDLLA and P(DLLA-*co*-CL) dimethacrylate macromers with a molecular weight of 5 kg/mol were dissolved in a non-reactive diluent together with other resin components and used in the stereolithography rapid prototyping process. Figure 6.1 gives an overview of the designed and built architectures. Three sophisticated porous architectures were designed: a cube, a diamond, and a gyroid architecture. The cube architecture is an anisotropic lattice-like structure, similar to those that many rapid prototyping methods are restricted to. With the stereolithography technique used here, each layer is built using a distinct pattern of 1.3x106 light pixels that can be switched on or off independently. This allows for the fabrication of complex structures such as the diamond and gyroid architectures. Their surfaces are defined by trigonometric implicit functions, where the spatial variables are symmetrically ordered within the trigonometric terms. The functions are triply periodic and are uniquely defined by their unit cell.[17] They closely approximate the minimal surfaces of Schwarz and Schoen,[18, 19] of which the mean curvature is zero at every point. Addition of an offset value to these implicit functions allows designing porous structures with diamond or gyroid architectures and specific porosities. The functions employed are presented in the experimental section.

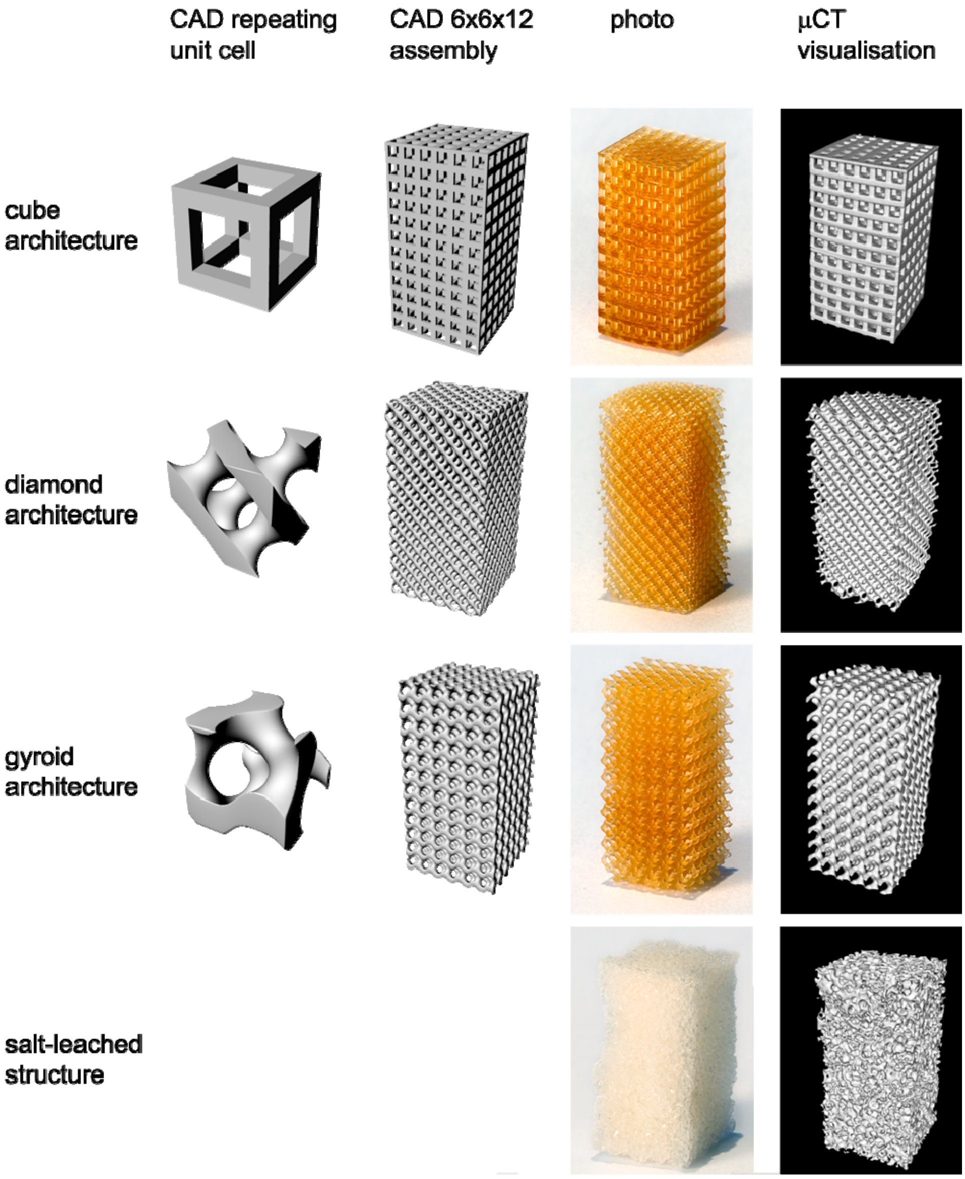

Figure 6.1: Visualisations of the different porous architectures. Columns: (1) CAD-designs of the repeating unit cells (2) CAD-designs of assemblies of 6x6x12 unit cells (3) photos of the built structures (4) visualisations obtained by µCT-scanning of the built structures. All structures measure approximately 5x5x10 mm.

For the different architectures, space-filling computer models can be generated from assemblies of the respective unit cells. Models consisting of 6x6x12 unit cells were then built by stereolithography using a resin based on PDLLA or P(DLLA-*co*-CL) macromers and a non-reactive diluent. Upon removal of the diluent by extraction and drying, the structures shrink by 22 %. This shrinkage is homogenous and reproducible, and could be compensated for by adjusting the dimensions of the design. Furthermore, to enable precise control over the depth of curing in the layer-by-layer stereolithography fabrication process, a dye is required to attenuate the light intensity. In our setup photo-polymerisation is induced by blue light, and in the resin an orange dye was used. This determines the colour of the structures built.

For comparison, porous structures with similar average pore sizes and porosities were prepared by a conventional porogen leaching method. Especially salt-leaching is a widely used method to prepare tissue engineering scaffolds. The PDLLA-based resin containing dispersed salt particles with sizes ranging from 425-710 μm was photo-polymerised, and porous structures were obtained upon leaching with water. In this case the presence of dye is not required.

The porous structures were analysed by micro computed tomography (μCT), of which visualisations are shown in the most right column of Figure 6.1. The μCT images precisely match the designed models of the different architectures. It is clear that the structure prepared by salt leaching is much less regular.

Analyses of built structures

To assess the accuracy of the stereolithography technique, a gyroid scaffold built from the PDLLA material was compared to its computer aided design. The graphical data obtained by μCT scanning was superimposed on the CAD data, enabling both visual and quantifiable comparisons. Figure 6.2 shows merged images of the gyroid design (in grey) and μCT data (in orange) both in three dimensions and in two dimensions. It can be seen that over the whole porous structure the designed and built architectures nearly coincide, indicating a very high accuracy of the technique. In the right of the figure, a cross-section of the μCT data of the built structure is depicted as a semi-transparent overlay over the CAD cross-section, showing exactly where the two match. Except for slight shearing of the built structure in the counter-clockwise direction and some overcure, the computer aided design is very well reproduced. When expressed in pixels, the agreement of the CAD and the μCT images of the built structures is 95 %.

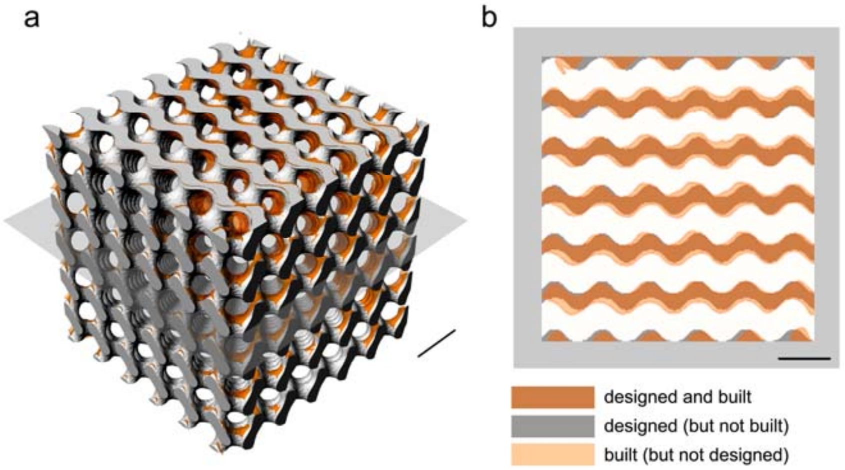

Figure 6.2: Superimposed 3D image of the gyroid computer aided design (in grey) and the μCT visualisation of the built structure (in orange). b: Semi-transparent overlay of a cross-section of the CAD (grey) and the μCT (orange) data. The overlapping area is shown in dark orange. Scale bars are 1 mm.

From μCT data of built scaffolds, structural parameters such as porosities, pore sizes and specific surface areas (surface area of pores per overall volume) can be assessed. For the different architectures, the determined values are compared to those of the corresponding designs in Table 6.1. The designs were evaluated in the same manner as the built structures. It can be seen that the results match those of the designs well.

Although scaffolds with relatively small pore sizes provide high surface areas for cells to adhere to and to proliferate on, larger pores that allow for vascularisation, tissue ingrowth and adequate nutrient transport are required as well. For *in vivo* bone tissue engineering for example, minimum pore sizes of 300 μm are needed for capillary formation to occur. For larger sizes, several studies revealed no statistical difference in bone ingrowth and bone formation in scaffolds with pores up to 800 μm in size.[20] The stereolithography technique presented here allows for the controlled preparation of scaffolds with pore sizes in the optimal range for (bone) tissue engineering.

Table 6.1: Comparison of structural parameters of the designed and built porous structures as determined by μCT.

		porosity (vol %)		pore size (μm)		specific surface area (mm^{-1})	
architecture		CAD	built[a]	CAD[b]	built[b]	CAD	built[a]
cubes	PDLLA	66	64±5	622±164	537±171	3.87	
diamond	PDLLA	68	68±2	398±57	378±74	6.56	7.10±0.44
	P(DLLA-*co*-CL)		67±3		352±94		7.32±0.55
gyroid	PDLLA	68	69±2	453±55	455±71	5.34	5.33±0.19
	P(DLLA-*co*-CL)		69±3		462±81		5.54±0.16
salt-leached	PDLLA	-	77±7	-	353±143	-	12.4±4.1

The pore size distributions of the built gyroid design and the prepared salt-leached structure, which is a typical scaffold used in tissue engineering, are compared and depicted in Figure 6.3. The data is visualised as an indexed colour-map and quantitatively presented as a histogram. The relatively narrow pore size distribution of the built gyroid structure results in a very even colouring in the indexed colour maps. These pore size distribution maps can also be used to assess the interconnectivity of the pores in a quantitative manner. Using an algorithm that mimics mercury porosimetry, the permeation of spheres of different diameters through the pore network is simulated. For a given sphere size, this simulation will allow to determine the volume of pores that is accessible for that sphere. This therefore represents the fraction of the pore volume that is connected to the exterior of the scaffold by channels with diameters larger than that sphere.

These resulting accessibility curves are also depicted in Figure 6.3. Here too, clear differences between the gyroid construct and the salt-leached structure can be observed. The built gyroid structure shows a very steep decrease in accessibility at pore sizes close to the average pore size value, whereas accessibility of pores in the salt-leached scaffold decreases gradually already from pore sizes much smaller than the average size. This implies that the interconnections between the pores are much smaller than the pores themselves. In contrast, the pore space throughout the gyroid

---

[a] average±standard deviation (n=3).

[b] volume average±standard deviation of the pore size distribution (n=3)

structure consists of channels with approximately equal diameters. This leads to the high accessibility observed for spheres with diameters up to the average pore size. The resulting high permeability ensures good transport properties, which is important in tissue engineering.

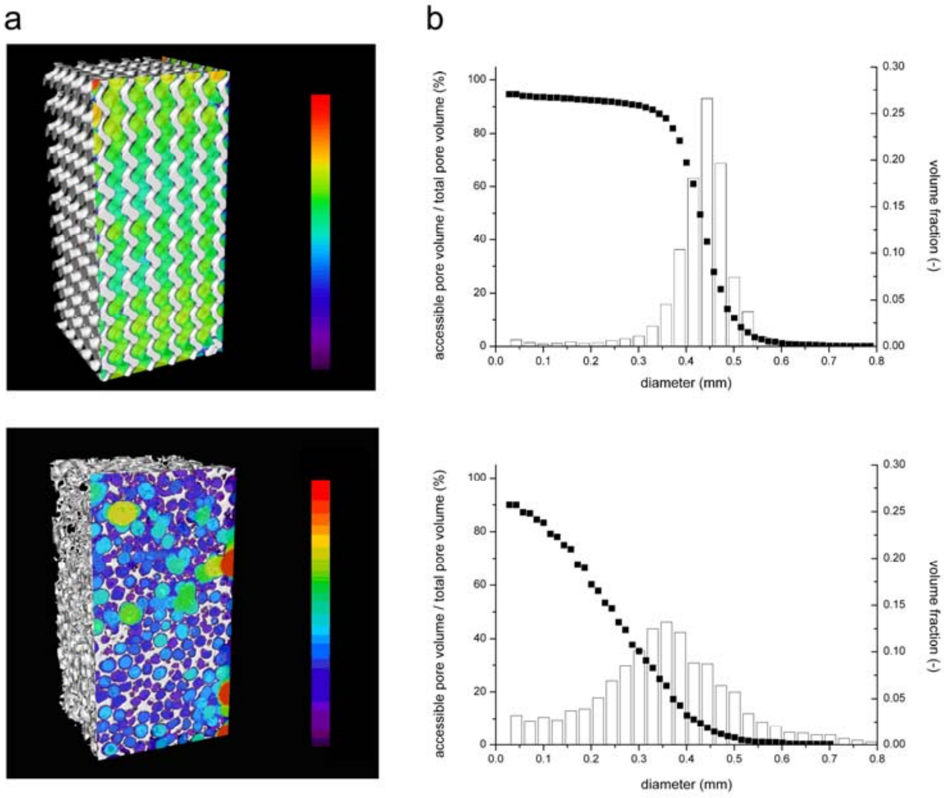

Figure 6.3: Pore size distributions and accessibility curves of built PDLLA gyroid structures and salt-leached scaffolds from μCT analyses. a: Pore size distribution maps with pore sizes indicated by a colour scale. b: The bars in the histogram correspond to volume fractions of pores with specific diameters. The curves represent the pore volume that is accessible for permeating spheres of different diameters in a simulation.

Mechanical properties of porous structures

The influence of the pore architecture on the mechanical properties of the structures was analysed as well. Figure 6.4a compares the compressive response of porous PDLLA structures with cubic and gyroid pore architectures at similar porosity (approximately 67 %). In the porous structures with cube architecture, a high stiffness is observed as result of the alignment of the vertical struts with the compressive force. The Young’s modulus is 324±39 MPa for structures with a porosity of 64±5 %. The gyroid architecture is characterised by curved surfaces; these porous structures exhibit less rigid behaviour (169±21 MPa at 69±2 % porosity).

Finite element simulations of the compression experiments were conducted using the different CAD unit cells. For this, the stress-strain responses of bulk PDLLA and P(DLLA-*co*-CL) were first determined using solid specimens that were also fabricated from the resins by stereolithography. Two different constitutive models were then used to capture the experimentally observed behaviour and were implemented into a finite element software code (see Supporting Information). Direct comparison shows excellent agreement between the model predictions and the experimental results. As numerical analyses allow us to predict the mechanical behaviour of porous structures *a priori*, it is now possible to optimise scaffold designs with respect to their mechanical properties.

The figure also shows that for gyroid architectures, stress and strain are much more homogeneously distributed throughout the structure than for cube architectures. A tissue engineering scaffold with gyroid architecture will expose adhering cells to more equal mechanical stimuli throughout the structure. As cells respond to deformation of the matrix to which they adhere,[21] this could be beneficial.

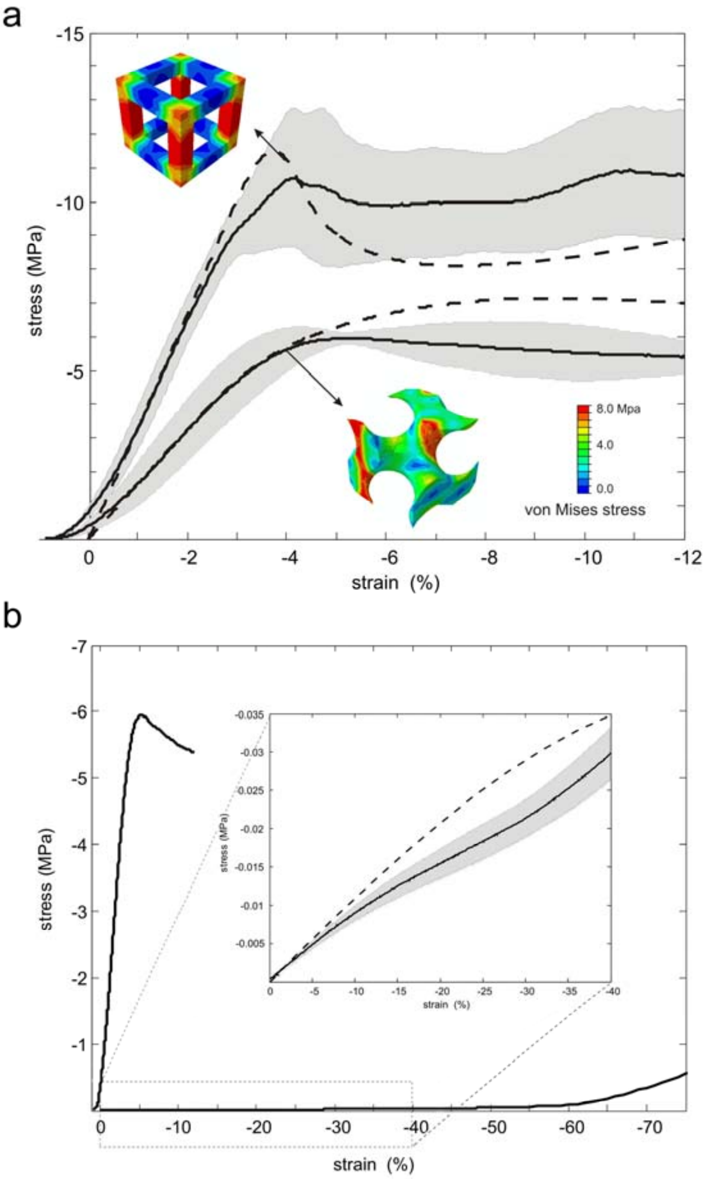

Figure 6.4: Compression stress-strain diagrams of built structures and simulations. a: Stress-strain diagrams of PDLLA structures with cube and gyroid architectures, at similar porosity. The experimental data are depicted as average (solid line) ± standard deviation (shaded area) of 5 samples and compared to the curve predicted by finite element analysis (dashed line). The inserted CAD unit cells show the von Mises stress distribution at a simulated 4% macroscopic strain. b: Compression stress-strain diagrams of gyroid structures built from rigid PDLLA and flexible P(DLLA-*co*-CL) at similar porosity. The insert presents the experimental data of the flexible gyroid structures as average (solid line) ± standard deviation (shaded area) of 5 samples and the curve predicted by finite element simulation (dashed line).

Compression data of gyroid structures of similar porosity built from rigid PDLLA and from flexible P(DLLA-*co*-CL) are shown in Figure 6.4b. The difference in the bulk elastic modulus of the different polymer networks (respectively 2.5x10^3 and 2 MPa) is reflected in the global stiffness of the approximately 70% porous structures (respectively 165 and 0.12 MPa). The structures show markedly distinct mechanical behaviour: while the PDLLA gyroid structures yield plastically at approximately 5 % strain and 6 MPa stress, a same structure built from the copolymer can be reversibly deformed up to 70 % strain and 0.43 MPa stress with little hysteresis. The mechanical behaviour of the latter structures was unaffected for at least 1000 cycles (Figure 6.5). Intermediate mechanical properties can be obtained by adjusting the copolymer composition, allowing for the preparation of designed structures that are suitable for the engineering of a wide range of tissues.

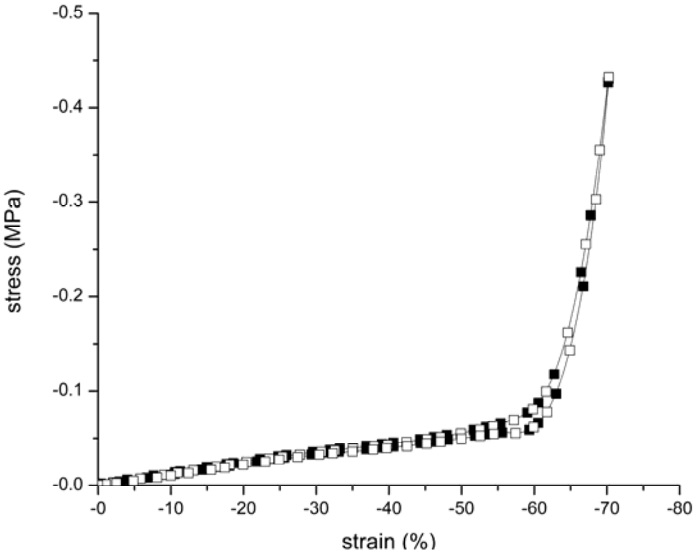

Figure 6.5: Overlay of stress-strain diagrams from cyclic compression (loading-unloading with a strain rate of 30 %/min) of a 69 % porous P(DLLA-*co*-CL) gyroid structure. Cycle 1 is depicted as a solid line, cycle 100 and 1000 are depicted as closed and open squares, respectively.

Advanced tissue engineering scaffolds

Ordered porous structures such as the built gyroid and diamond architectures, are envisaged to be very well suited for use as scaffolds in tissue engineering.[22] The good accessibility of pores and resulting high permeability of the scaffold will facilitate the seeding of cells[23] and the transport of nutrients and metabolites, either during in vitro culture or after implantation in the body. Furthermore, scaffold morphology is a key factor determining tissue formation, as the pore network initially provides the spatial template for cell adhesion and proliferation and the deposition of extra-cellular matrix.[24]

In specific cases, scaffolds with defined but non-uniform characteristics are desired. Bone tissue for example, varies spatially in structure and composition. In load-bearing bone, the properties of the tissue progressively vary from those of cortical bone to those of trabecular bone. In the engineering of other tissues, optimal conditions for cell culturing can differ from those of bone. To repair osteochondral defects, tissue constructs comprising both bone and cartilage are to be engineered.[25] For this, structures in which gradients of properties such as permeability and stiffness exist are desired.[26]

A gradient in size and volume fraction of the pores can be introduced by adding a linear term to the mathematical equation used to describe the pore architecture.[27] To part of the design of a scaffold with gyroid pore architecture, such a term was added. The scaffold was then built by stereolithography using the PDLLA-based resin. Figure 6.6a shows a μCT-visualisation of the resulting scaffold. It is clear that the top half of the structure is much more open than the bottom part, where a gradient in pore size and porosity can be seen. The right part of the figure is a quantification of the average porosity as a function of the height of the scaffold, as determined by μCT. These results are compared to the original design. The graph shows that the porosity gradually decreases from the middle of the structure downwards. This gradient in porosity and pore size will result in a stiffness and permeability gradient as well.

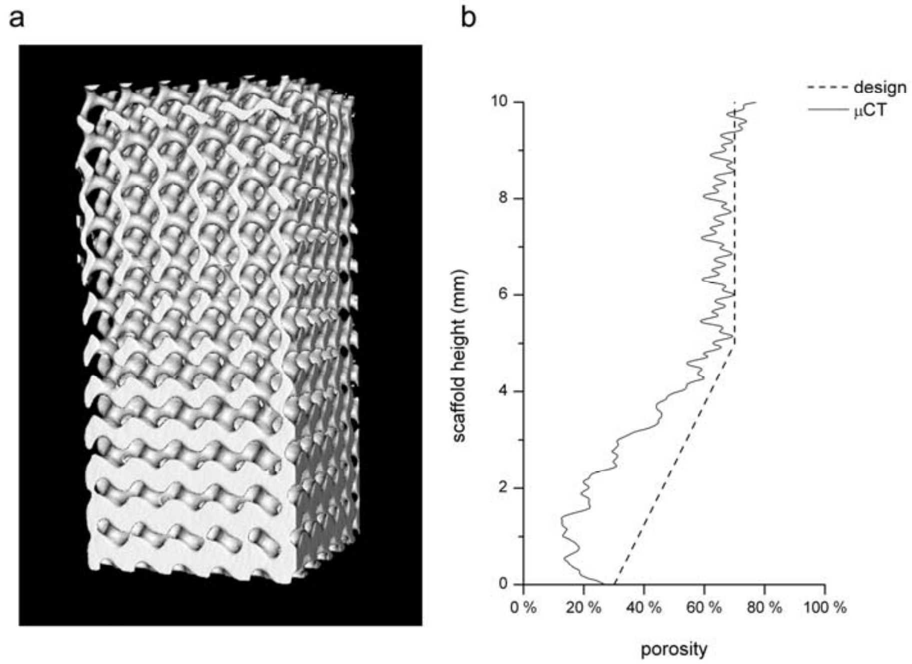

Figure 6.6: Built PDLLA scaffold with gyroid architecture showing a gradient in porosity and pore size. a: µCT visualisation. b: Change in the average porosity with scaffold height (solid line) in comparison with the designed porosity (dashed line).

The overall porosity of the built structure is somewhat lower than designed. This was also the case for the isotropic gyroid structures presented in Figure 6.2. It is likely that local warming up of the resin due to the intensity of the light and the exothermic polymerisation reaction has resulted in overcure. At lower porosities the absorbed energy per volume is relatively high, and deviation from the design is more pronounced. Figure 6.6 also shows that the effect of overcure is minimal at the boundaries of the structure, where heat can be exchanged with the surrounding non-illuminated resin.

In the photo-initiated polymerisation in stereolithography, the conversion of reactive end groups is incomplete. After swelling the polymer networks in deuterated acetone, conversions of 85 to 95 % could be determined by high-resolution NMR spectroscopy (see Figure 6.7 for an example spectrum). The unreacted double bonds remain available for subsequent covalent functionalisation. These can be used, for example, to adjust the hydrophilicity of the networks or to immobilise cell-adhesive peptides at the surfaces of the porous structures.[28]

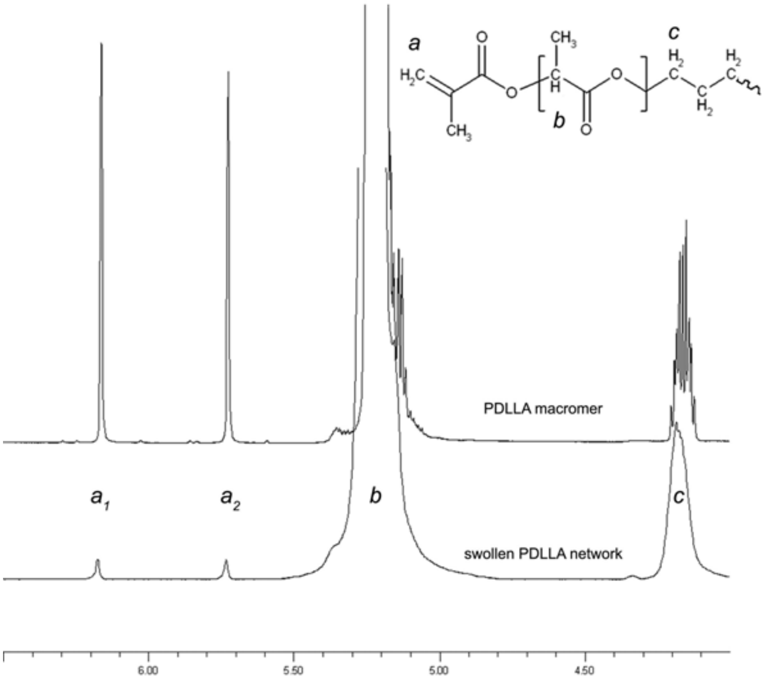

Figure 6.7: ^{1}H-NMR spectra (600 MHz) of a PDLLA macromer and network with acetone-d_6 as solvent or swelling agent. High-resolution spectra of networks were obtained under magic angle spinning conditions. Here, peaks a_1 and a_2 correspond to the vinyl protons of unreacted methacrylate groups in the network.

Conclusions

We have shown that stereolithography fabrication methods can be used to accurately prepare tissue engineering scaffolds with designs that can be modelled, allowing optimisation of the properties of the structures. By varying the composition of the macromers and the pore architecture, scaffolds with a large range of mechanical properties can be obtained. Furthermore, mathematically defined porous structures can be useful in many other applications as well. Tight control over the pore size distribution can lead to materials with photonic band gap properties,[29] thermal, acoustic or electrical insulating characteristics, or to mechanical materials that exhibit negative Poisson ratios.[30]

Acknowledgements

We would like to acknowledge the European Union (STEPS project, FP6-500465) and Nanoned for their financial support.

References

[1] L. E. Freed, G. Vunjak-Novakovic, R. J. Biron, D. B. Eagles, D. C. Lesnoy, S. K. Barlow, R. Langer, *Bio-Technology* **1994**, *12*, 689.

[2] D. W. Hutmacher, *Biomaterials* **2000**, *21*, 2529.

[3] S. F. Yang, K. F. Leong, Z. H. Du, C. K. Chua, *Tissue Engineering* **2001**, *7*, 679.

[4] S. J. Hollister, *Nature Materials* **2005**, *4*, 518.

[5] E. N. Antonov, V. N. Bagratashvili, M. J. Whitaker, J. J. A. Barry, K. M. Shakesheff, A. N. Konovalov, V. K. Popov, S. M. Howdle, *Advanced Materials* **2005**, *17*, 327.

[6] J. M. Williams, A. Adewunmi, R. M. Schek, C. L. Flanagan, P. H. Krebsbach, S. E. Feinberg, S. J. Hollister, S. Das, *Biomaterials* **2005**, *26*, 4817.

[7] D. W. Hutmacher, T. Schantz, I. Zein, K. W. Ng, S. H. Teoh, K. C. Tan, *Journal of Biomedical Materials Research* **2001**, *55*, 203.

[8] R. A. Giordano, B. M. Wu, S. W. Borland, L. G. Cima, E. M. Sachs, M. J. Cima, *Journal of Biomaterials Science-Polymer Edition* **1996**, *8*, 63.

[9] M. N. Cooke, J. P. Fisher, D. Dean, C. Rimnac, A. G. Mikos, *Journal of Biomedical Materials Research Part B-Applied Biomaterials* **2003**, *64B*, 65.

[10] S. Maruo, K. Ikuta, *Sensors and Actuators a-Physical* **2002**, *100*, 70.

[11] H. M. Klein, W. Schneider, J. Nawrath, T. Gernot, E. D. Voy, R. Krasny, *Fortschritte Auf Dem Gebiete Der Röntgenstrahlen Und Der Neuen Bildgebenden Verfahren* **1992**, *156*, 429.

[12] A. S. Sawhney, C. P. Pathak, J. A. Hubbell, *Macromolecules* **1993**, *26*, 581.

[13] J. Ericsson, A. Hult, *Makromolekulare Chemie-Macromolecular Chemistry and Physics* **1991**, *192*, 1609.

[14] R. F. Storey, S. C. Warren, C. J. Allison, J. S. Wiggins, A. D. Puckett, *Polymer* **1993**, *34*, 4365.

[15] A. O. Helminen, H. Korhonen, J. V. Seppala, *Macromolecular Chemistry and Physics* **2002**, *203*, 2630.

[16] K. Matsubayashi, P. W. M. Fedak, D. A. G. Mickle, R. D. Weisel, T. Ozawa, R. K. Li, *Circulation* **2003**, *108*, 219.

[17] H. G. Vonschnering, R. Nesper, *Zeitschrift Für Physik B-Condensed Matter* **1991**, *83*, 407.

[18] A. H. Schoen, Nasa Technical Note, NASA-TN-D-5541 **1970**.

[19] H. A. Schwarz, *Gesammelte Mathematische Abhandlungen*, Springer-Verlag, Berlin **1890**.

[20] V. Karageorgiou, D. Kaplan, *Biomaterials* **2005**, *26*, 5474.

[21] G. Bao, S. Suresh, *Nature Materials* **2003**, *2*, 715.

[22] S. Rajagopalan, R. A. Robb, *Medical Image Analysis* **2006**, *10*, 693.

[23] E. Figallo, M. Flaibani, B. Zavan, G. Abatangelo, N. Elvassore, *Biotechnology Progress* **2007**, *23*, 210.

[24] H. J. Wang, J. Pieper, F. Peters, C. A. van Blitterswijk, E. N. Lamme, *Journal of Biomedical Materials Research Part A* **2005**, *74A*, 523.

[25] I. Martin, S. Miot, A. Barbero, M. Jakob, D. Wendt, *J Biomechanics* **2007**, *40*, 750.

[26] D. J. Kelly, P. J. Prendergast, *Tissue Engineering* **2006**, *12*, 2509.

[27] R. Gabbrielli, I. G. Turner, C. R. Bowen, *Key Engineering Materials* **2008**, *361-363 II*, 901.

[28] P. D. Drumheller, J. A. Hubbell, *Analytical Biochemistry* **1994**, *222*, 380.

[29] W. N. Man, M. Megens, P. J. Steinhardt, P. M. Chaikin, *Nature* **2005**, *436*, 993.

[30] R. Lakes, *Science* **1987**, *235*, 1038.

Supporting Information: Constitutive models for polymer networks and numerical analysis

Constitutive model for crosslinked poly(D,L-lactide)

Experimental results

Uniaxial compression tests were conducted to characterise the material response of PDLLA. Cylindrical specimens were subjected to uniaxial compression at a constant nominal strain rate of 0.1, 0.01, 0.001 and 0.0001 s^{-1} using a Zwick Z020 screw-driven testing machine and the results are shown in Figure 6.8. The tests show that the material exhibits a rate-dependent behaviour, characterised by an initial elastic response, followed by yield, strain softening and strain hardening. The yield point is found to decrease with a decrease in strain rate.

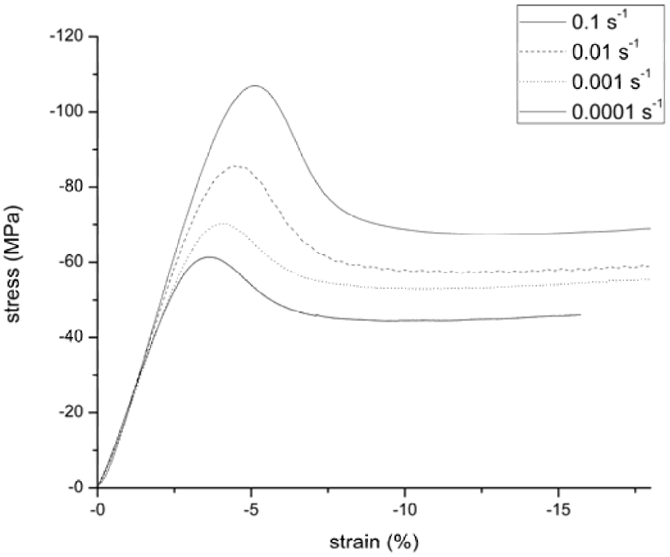

Figure 6.8: Experimental uniaxial compression stress-strain curves for PDLLA over four decades of strain rate from -0.1 to -0.001 s^{-1}.

Constitutive model

Following Boyce *et al.*[1] and using the finite strain kinematics framework of Bergstrom and Boyce[2] a two-mechanism thermo-mechanical constitutive model is used to capture the stress-strain behaviour of the material. Mechanism N represents the resistance due to stretching and orientation of the molecular network, and mechanism V represents the resistance to intermolecular interaction. Thus, the total stress acting on the material is given by the sum of the stress contributions from the two mechanisms:

$$\sigma = \sigma_N + \sigma_V .$$

Constitutive relations for Mechanism N

Mechanism N is modelled using an 8-chain network model as proposed by Arruda and Boyce[3], so that the Cauchy stress is given by:

$$\boldsymbol{\sigma}_\mathbf{N} = \frac{\mu}{J}\frac{\sqrt{N}}{\lambda_{chain}} L^{-1}\left(\frac{\lambda_{chain}}{\sqrt{N}}\right)\mathbf{B'},$$

where B' is the deviatory part of the left Cauchy-Green tensor $B=FF^T$ ($\mathbf{F} = \partial \mathbf{x} / \partial \mathbf{X}$ being the total deformation gradient that maps a material point from the reference position X to its current location x), J=det(F), $\lambda_{chain} = \sqrt{\frac{tr\mathbf{B}}{3}}$ maps the macroscopic deformation to an average chain stretch and L is the Langevin function defined as $L(\beta) = \coth\beta - \frac{1}{\beta}$. The shear modulus and the limiting chain extensibility are denoted by μ and $\sqrt{N}$, respectively.

Constitutive relations for Mechanism V

The deformation gradient F is then decomposed into elastic and plastic contributions $F = F^E F^P$ and the Cauchy stress σ_V is calculated using F_V^E as

$$\boldsymbol{\sigma}_V = \frac{1}{\det \mathbf{F}^E}\left(\underline{\mathbf{L}}^E\left(\ln \mathbf{V}^E\right) - \frac{p}{3}\mathbf{I}\right),$$

where $V^E = F^E R^E$ (R^E being a rotation tensor) and $\underline{\mathbf{L}}^E$ is the fourth order isotropic elasticity tensor

$$\underline{\mathbf{L}}^E = \frac{E}{1+\nu}\underline{\mathbf{I}}^4 + \frac{E\nu}{(1+\nu)(1-2\nu)}\mathbf{I}\otimes\mathbf{I}$$

G and λ being the Lame constants, $\underline{\mathbf{I}}^4$ the fourth order identity tensor and $\mathbf{I}$ the second order identity tensor.

The evolution of F^E is then determined considering the composition of the spatial velocity gradient

$$\mathbf{L} = \dot{\mathbf{F}}\ \mathbf{F}\ = \dot{\mathbf{F}}^{E}\mathbf{F}^{E\text{-}\mathbf{1}} + \mathbf{F}^{E}\mathbf{L}^{P}\mathbf{F}^{E\text{-}\mathbf{1}},$$

where L^P can be further decomposed into

$$\mathbf{L}^{P} = \dot{\mathbf{F}}^{P}\mathbf{F}^{P\text{-}\mathbf{1}} = \mathbf{D}^{P} + \mathbf{W}^{P}.$$

Without losing generality we can assume $W^P = 0$, whereas the viscoplastic stretch rate D^P is constitutively prescribed to be

$$\mathbf{D}^{P} = \frac{\dot{\gamma}_V^{P}}{\sqrt{2}\tau}\boldsymbol{\sigma}'_V,$$

where $\boldsymbol{\sigma}'_V$ denotes the deviatory part of $\boldsymbol{\sigma}_V$ and τ is the equivalent shear stress defined as

$$\tau = \sqrt{\frac{1}{2}\boldsymbol{\sigma}'_V \bullet \boldsymbol{\sigma}'_V}\ .$$

The viscoplastic shear strain rate $\dot{\gamma}_V$ is then constitutively prescribed as

$$\dot{\gamma}_V = \dot{\gamma}_0 \exp\left(\frac{-\Delta G}{k\theta}\left(1-\frac{\tau}{s-\alpha p}\right)\right) - \dot{\gamma}_0 \exp\left(\frac{-\Delta G}{k\theta}\left(1+\frac{\tau}{s-\alpha p}\right)\right),$$

where $\dot{\gamma}_0$ is the pre-exponential factor, ΔG is the activation energy, s is the athermal shear strength, θ is the absolute temperature, p is the pressure and α is the pressure coefficient. Further, the evolution rule for s is defined as

$$\dot{s} = h_0\left(1-\frac{s}{s_s}\right)\dot{\gamma}_V,$$

with the initial condition $s=s_0$ when $\dot{\gamma}_V = 0$.

Material parameters

The PDLLA model parameters determined by curve fitting are listed in Table 6.2.

Table 6.2: PDLLA model parameters.

Mechanism V								Mechanism N	
E (MPa)	ν	$\dot{\gamma}_0$ ($10^3 s^{-1}$)	ΔG ($10^{-19} J$)	s_0 (MPa)	s_s (MPa)	h_0 (MPa)	α	N	μ (MPa)
2100	0.33	1.58	1.05	90.73	30	350	0.075	2.4	22

Model predictions

Figure 6.9 reports the experimentally observed rate-dependent behaviour for PDLLA under uniaxial compression along with the model simulations of these test conditions. The constitutive model is found to accurately predict the strain rate dependence of the material behaviour during uniaxial compression at low strain rates. The values of the model parameters required used in the simulations are listed in Table 6.2

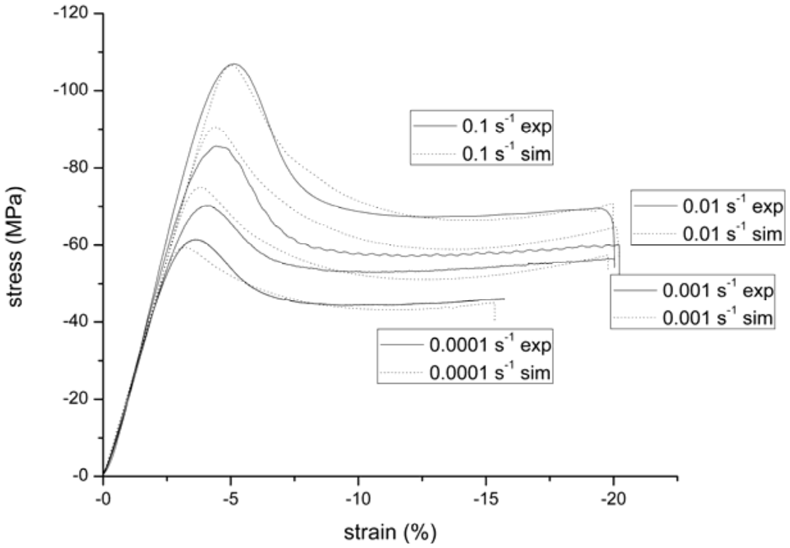

Figure 6.9: Nominal stress–nominal strain behaviour in uniaxial compression at low strain rates: experimental results (continuous lines) and model predictions (dashed lines).

Constitutive model for crosslinked poly(D,L-lactide-co-caprolactone)

Experimental Results

Uniaxial compression and tension tests were conducted to characterise the material response of P(DLLA-*co*-CL). Cylindrical specimens were subjected to uniaxial compression at a constant nominal strain rate of 0.1, 0.01, 0.001 and 0.0001 s^{-1} using Zwick Z020 screw-driven testing machine. The tests show that the material exhibits a behaviour typical for elastomers: large strain elastic behaviour with negligible rate dependence and negligible hysteresis during a loading–unloading cycle. The material behaviour at a strain rate of 0.01 s^{-1} is reported in Figure 6.10.

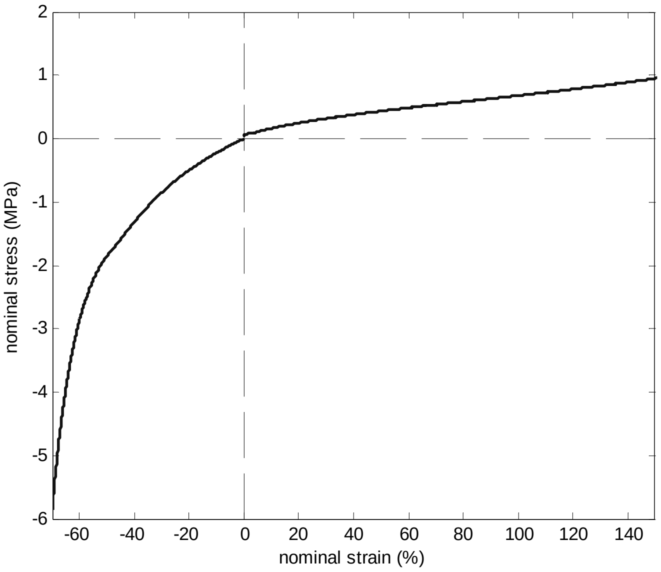

Figure 6.10: Experimental uniaxial stress-strain curves for P(DLLA-*co*-CL) at 0.01 s^{-1}.

Constitutive model

The observed constitutive behaviour is modelled as hyperelastic. Let $\mathbf{F} = \partial \mathbf{x} / \partial \mathbf{X}$ be the deformation gradient, mapping a material point from the reference position X to its current location x and J be its determinant, J=det(F). For an isotropic hyperelastic material the strain energy density W can be expressed as a function of the invariants of the right Cauchy-Green tensor $C = F^T F$ (or, alternatively, also the left Cauchy-Green tensor $B = F F^T$), $W = W(I_1, I_2, I_3)$, where

$$I_1 = \mathrm{tr}\,\mathbf{C},\quad I_2 = \frac{1}{2}\left[\left(\mathrm{tr}\,\mathbf{C}\right)^2 - \mathrm{tr}\,\mathbf{C}^2\right],\quad I_3 = \det\mathbf{C},$$

I_1 being essentially a scalar equivalent stretch measure and I_3 the square of the volume ratio. Here the P(DLLA-*co*-CL) stress–strain behaviour is modelled using a Neo-Hookean model modified to include compressibility (with a high bulk modulus):

$$W(I_1, I_3) = \frac{\mu}{2}(I_1 - 3) - \mu \log J + \frac{K}{2}(J-1)^2 \,,$$

where μ and K are the shear and bulk modulus, respectively. The nominal stress S is found as

$$\mathbf{S} = \frac{\partial W}{\partial \mathbf{F}} = \mu \mathbf{F} + J\left[K(J-1) - \frac{\mu}{J}\right]\mathbf{F}^{-T} \,.$$

The material was modelled as nearly incompressible, characterised by K/μ =1000. From the compression data shown in Figure 6.10 the initial Young's modulus was measured to be 1.35 MPa, so that μ =1.08 MPa.

Model predictions

Figure 6.11 reports the experimentally observed behaviour for P(DLLA-*co*-CL) under uniaxial tension and compression along with the model simulation of these test conditions. The constitutive model is found to accurately capture the material behaviour both under tension and compression.

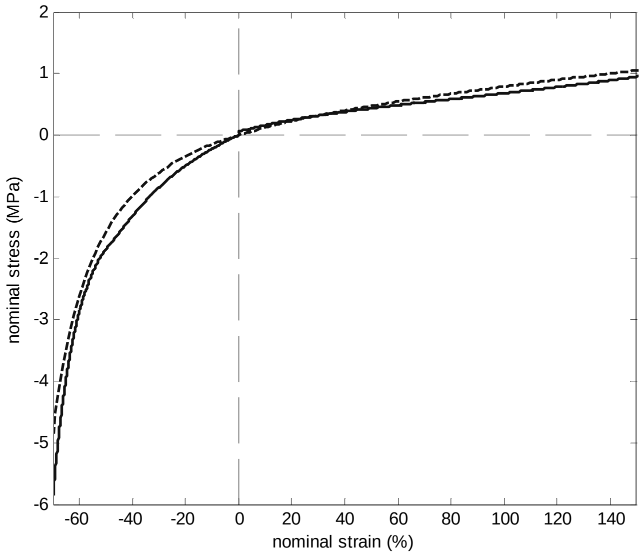

Figure 6.11: Nominal stress–nominal strain behaviour in uniaxial compression and tension: experimental results (continuous lines) and model prediction (dashed lines).

Numerical Simulations

Numerical simulations of the mechanical loading history of the structures were conducted utilising the nonlinear finite element code ABAQUS/Standard, version 6.6-1. Each mesh was constructed of 4-node, linear, 3-dimensional elements (ABAQUS element type C3D4). The constitutive models described above are implemented into two user material subroutine (UMAT) in the finite element software package ABAQUS and three-dimensional models of the periodic porous structures are constructed. Infinitely large structures are considered and the simulations are performed using the smallest repeating geometric unit, also referred to as representative volume element (RVE). In order to respect the periodicity of the microstructure, a series of constraint equations are applied to the boundaries of the RVE providing general periodic boundary conditions.

References

[1] M. C. Boyce, D. M. Parks, A. S. Argon, *Mechanics of Materials* **1988**, *7*, 15.
[2] J. S. Bergstrom, M. C. Boyce, *Journal of the Mechanics and Physics of Solids* **1998**, *46*, 931.
[3] E. M. Arruda, M. C. Boyce, *Journal of the Mechanics and Physics of Solids* **1993**, *41*, 389.

Chapter 7 - Effects of the architecture of tissue engineering scaffolds on cell seeding and culturing

Ferry Melchels[1], Ana Barradas[2], Clemens van Blitterswijk[2], Jan de Boer[2], Jan Feijen[1] and Dirk Grijpma[1,3]

The advance of rapid prototyping techniques has significantly improved the control over the design of the pore network in tissue engineering scaffolds. In this work we assessed the influence of scaffold pore architecture on cell seeding and static culturing, by comparing a computer-designed gyroid architecture to a random-pore architecture resulting from salt-leaching. Both scaffold types were prepared by photo-crosslinking of poly(D,L-lactide)-dimethacrylate macromers; the gyroid type in a stereolithography apparatus and the other type by bulk photo-polymerisation in the presence of salt particles. The scaffold types showed comparable porosity and pore size values, but the gyroid type showed a more than tenfold higher permeability, due to the absence of size-limiting pore interconnections. The higher permeability significantly improved the wettability of the hydrophobic scaffolds, and increased the settling speed of cells upon static seeding of immortalised mesenchymal stem cells. After dynamic seeding followed by 5 days of static culture, gyroid scaffolds showed large cell populations in the centre of the scaffold, while salt-leached scaffolds were covered with a cell-sheet on the outside and no cells were found in the scaffold centre. It was shown that scaffold interconnectivity and permeability prolongs the time of static culture before overgrowth of cells at the scaffold periphery occurs. Furthermore, novel scaffold designs are proposed to further improve the transport of oxygen and nutrients throughout the scaffolds, and to create tissue engineering grafts with designed, pre-fabricated vasculature.

---

[1] MIRA Institute for Biomedical Technology and Technical Medicine, and Department of Polymer Chemistry and Biomaterials, University of Twente, P.O. Box 217, 7500 AE, Enschede, The Netherlands

[2] MIRA Institute for Biomedical Technology and Technical Medicine, and Department of Tissue Regeneration, University of Twente, P.O. Box 217, 7500 AE, Enschede, The Netherlands

[3] Department of Biomedical Engineering, University Medical Centre Groningen and University of Groningen, P.O. Box 196, 9700 AD Groningen, The Netherlands

Introduction

In tissue engineering, two major challenges are the homogeneous seeding of cells throughout a porous scaffold, and to provide the seeded cells with sufficient oxygen and nutrients to sustain, proliferate and generate new tissue. Several methods have been proposed for the seeding of cells into microporous scaffolds. Static seeding – although still widely used- is characterised by low cell seeding efficiencies and inhomogeneous distributions.[1, 2] An improvement in both seeded cell density and uniformity of the distribution can be achieved by employing mild suction to inoculate cells into a porous scaffold.[3] A similar technique that showed good results but is only possible when using elastomeric scaffolds, is compression-induced suction.[4] Furthermore, several dynamic seeding methods have been developed using for example spinner flasks[2, 5] or perfusion bioreactors.[6] Besides the technique employed for cell seeding, the scaffold architecture and physical properties of the scaffolding material play an important role in the cell seeding procedure.[7] Most polymers used for tissue engineering scaffolds (such as poly(lactide), poly(ε-caprolactone) and poly(trimethylene carbonate)) are hydrophobic, which impedes the penetration of an aqueous cell suspension. These materials are often incubated in culture medium prior to cell seeding, in order to let proteins adsorb that make the scaffold surface less hydrophobic and improve cell attachment.[8] An open, permeable pore network architecture facilitates wetting by culture medium and aids in eventually achieving high densities of uniformly distributed cells upon seeding. Moreover, it can improve oxygen and nutrient transport in the culturing phase.[9] In static culture of cell-seeded porous scaffolds, cells that are too far from the periphery often go into necrosis because of hypoxia or lack of nutrients. Due to the diffusion constraints of foams fabricated using conventional techniques such as salt-leaching and phase-separation/freeze-drying, only the in vitro growth of tissues with cross-sections of less than 500 μm have proven successful in static culture.[10, 11] Cell colonisation at the scaffold periphery can consume, or act as an effective barrier for the diffusion of oxygen and nutrients into the interior of the scaffold.[12] Perfusion of medium through scaffolds in a bioreactor has been suggested to overcome cell death due to transport limitations.[13] It can increase the survival rate of cells in the centre of porous scaffolds, resulting in more homogeneous tissue engineered constructs.[14] However, perfusion alone is not always enough to ensure adequate oxygen supply inside porous scaffolds.[15] The use of solid freeform fabrication (SFF) or rapid prototyping (RP) techniques such as stereolithography may be an attractive approach to produce scaffolds with customised external shape and predefined and reproducible internal morphology. The pore networks of such scaffolds may be designed such to reduce resistance to mass transport by shortening diffusion paths (lower tortuosity) and increasing pore interconnectivity size.[16] In stereolithography, a computer-controlled laser beam or a digital light projector is used to locally solidify a liquid resin through photo-initiated polymerisation. In combination with a computer-driven building stage, a solid, three-dimensional object can be constructed in a layer-by-layer fashion.[17] Recently, we have reported the use of stereolithography and methacrylate end-functionalised poly(D,L-lactide) (PDLLA) oligomers to fabricate tissue engineering scaffolds by computer-aided designs (CAD).[18]

We aim to improve the scaffold architecture such that cell-seeded scaffolds can be cultured for prolonged time under static conditions, providing the proliferating cells with sufficient oxygen and nutrients. We use stereolithography to prepare highly accessible and permeable porous scaffolds of poly(D,L-lactide) and compare their cell seeding and cell culturing characteristics with more tortuous scaffolds prepared using the salt-leaching technique. The latter method is widely used to prepare porous tissue engineering scaffolds but has limited control of the pore network architecture.[19] Cell survival and proliferation are expected to improve for the more accessible architectures.

Experimental

Scaffolds

A liquid photo-polymerisable resin based on poly (D,L-lactide) (PDLLA) was synthesised in a similar way as previously described.[18] In short, 1,6-hexanediol (Sigma-Aldrich) and D,L-lactide (Purac) were reacted at 130 °C for 40 h under an argon atmosphere using stannous octoate (Sigma-Aldrich) as a catalyst. The hydroxyl termini of the oligomers were reacted with methacrylic anhydride (Sigma-Aldrich) in the presence of triethyl amine (Sigma-Aldrich) (both in a 20 mol % excess) in dried dichloromethane for 5 d at room temperature to yield methacrylate end-functionalised lactide macromers. These were purified by precipitation from isopropanol followed by washing with water and freeze-drying. ^{1}H-NMR ($CDCl_3$, Varian 300 MHz) indicated high purity, a molecular weight of 5 kg/mol and a degree of functionalisation of 92-99 %. The macromers were used to prepare a photo-polymerisable liquid resin with 40 wt% dry N-methylpyrrolidone (NMP, Fluka) as a non-reactive diluent, 2 wt% ethyl-2,4,6-trimethylbenzoylphenylphosphinate (Lucirin TPO-L photo-initiator as a gift from BASF), 0.15 wt% Orasol Orange G dye (gift from Ciba SC) to control the cure depth and 0.2 wt% tocopherol (Fluka) to prevent preliminary crosslinking reactions.

A scaffold design with an open and accessible gyroid architecture was generated using K3dSurf v0.6.2 software (http://k3dsurf.sourceforge.net). The surface of the gyroid pore architecture is described by a triply periodic function, closely approximating the minimal surfaces of Schwarz and Schoen.[20, 21] Addition of an offset value to the implicit function allows designing porous structures having specific porosities. A value of -0.60 was chosen for the offset, corresponding to 70 % porosity. The following equation was used to describe the scaffold design:

$$G : \cos(x)\sin(y) + \cos(y)\sin(z) + \cos(z)\sin(x) - 0.60 = 0$$

with boundary conditions $x^2 + y^2 < (14\pi)^2$ and $|z| < 10\pi$. A commercial stereolithography apparatus (Envisiontec Perfactory Mini Multilens SLA) was employed to build the designed gyroid scaffolds using the PDLLA-based resin. The building process involves subsequent projections of 1280x1024 pixels, each 32x32 μm^2 in size. Layers with a thickness of 25 μm were cured by irradiating for 30 s with blue light (intensity 16 mW/cm^2). Uncured excess resin was washed out and the diluent, non-reacted macromer and photo-initiator were extracted from the structures with acetone. The extracted structures with a height of 5 mm and a diameter of 8 mm were then dried at 90 °C for 2 d under a nitrogen flow. A similar resin, without dye and containing camphorquinone instead of Lucirin TPO-L, was used to prepare porous structures by a salt-leaching process. The resin was mixed with NaCl salt particles sieved to sizes of 425-710 μm, in a 1:3.5 weight ratio. The size range and weight ratio was chosen such that a porosity and average pore size similar to that of the stereolithography-built scaffolds was obtained. Then the mixture was brought into tubular polypropylene moulds (inner diameter 14 mm) and cured by irradiation through the tube wall with a Kerr dental light (mono-chromatic blue LED light, wavelength 470 nm, intensity 1000 mW/cm2) for 40 s. The specimens were frozen in liquid nitrogen, cut to the desired dimensions, and post-cured by heating to 90 °C for 12 h. The salt-containing composites were extracted in acetone for 2 d, and the salt fraction was leached out with water during a period of 7 d. Then, the porous structures with the same final approximate dimensions as the built gyroid scaffolds were dried at 90 °C for 2 d under a nitrogen flow.

Structural analyses were performed on the fabricated scaffolds by micro computed tomography (μCT) using a General Electric eXplore Locus SP scanner at 14.3 μm resolution. The scan was carried out at a voltage of 80 kV, a current of 80 μA and an exposure time of 3000 ms. No filter was applied. The scanned data was reconstructed with a Feldkamp-based algorithm to obtain three-dimensional images and for the calculation of porosities, pore size distributions and pore accessibility.

The resistance to water flow was determined for both scaffold types by measuring the time required for a fixed volume of water to flow through a fully pre-wetted scaffold inserted in a silicone rubber tube. Permeabilities were calculated using Darcy's law:

$$Q = -\kappa \frac{\Delta P}{\mu} \frac{A}{L}$$

where κ is the scaffold permeability (mm^2), Q is the flow rate (mm^3/s), μ the viscosity of water (0.001 Ns/mm^2 at room temperature), ΔP the pressure difference (N/mm^2), A the cross-section surface area (mm^2) and L the scaffold height (mm).

iMSC culturing

Telomerase immortalised bone marrow derived mesenchymal stromal cells (iMSC)[22] were kindly provided by Prof. Dr. Ola Myklebost (University of Oslo). Cells were expanded and cultured in proliferation medium consisting of α-MEM (Gibco), 10 % foetal bovine serum (FBS, Lonza), 2 mM L-glutamine (Gibco), 0.2 mM ascorbic acid (Sigma, A8960), 100 u/mL penicillin and 100 g/mL streptomycin (Gibco) and 1 ng/mL bFGF (Instruchemie). Medium was refreshed 3 times per week and cells were trypsinised whenever a confluency of 70-80% was reached. Standard culturing conditions were 37 °C and a 5 % CO_2, 100% humid atmosphere.

Scaffold cell seeding

Prior to seeding, the scaffolds were disinfected in 70% isopropanol for 15 min, washed twice in PBS and incubated in proliferation medium overnight to allow pre-wetting of the material and protein adsorption on its surface. A more extensive pre-wetting procedure for the salt-leached scaffolds and the consequences of this procedure on cell seeding is described in the Results and Discussion section.

For both seeding methods, iMSC were trypsinised and resuspended in proliferation medium at a concentration of 4×10^5 cells per scaffold seeding volume. Scaffolds were seeded both statically and dynamically (Figure 7.1). For static seeding, the seeding volume per scaffold was 60 μl, corresponding to 40 % of the pore volume of a scaffold (obtained from μCT data). The cell suspension was pipetted on top of the scaffolds that were placed each in a well of 4 cm^2 non cell-adherent polystyrene surface, and left to incubate for 4 h under standard culturing conditions. For the dynamic seeding, the seeding volume was 150 μl, corresponding to the full scaffold pore volume (obtained from μCT data). A scaffold was placed in a 2 mL syringe (Ø 8.7 mm) and one seeding volume of cell suspension was pipetted on top of the scaffold. Then a second scaffold was inserted on top of the first, followed again by one seeding volume of cell suspension. These steps were repeated up to 5 stacked scaffolds + 5 seeding volumes per syringe. After putting the scaffolds and cell suspension seeding volumes in the syringe tube, the plunger was pushed inside to expel the air bubbles trapped in the tube, and the tube tip was closed with a cap. The syringes were placed horizontally on a roller (0.5 Hz) under standard culturing conditions for 4 h to allow cell attachment onto the scaffolds.

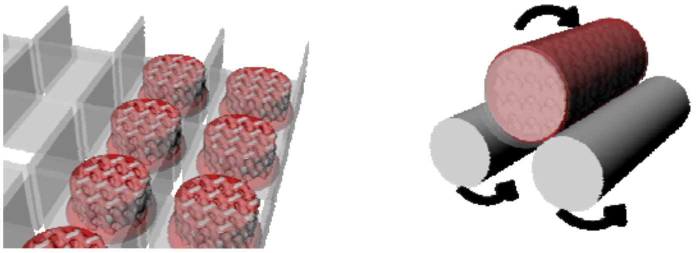

Figure 7.1: Schematic of static seeding (left) versus dynamic seeding (right). In the static seeding procedure, cell suspensions were pipetted on top of the scaffolds and left to stand for 4 h in an incubator. In the dynamic seeding procedure, the cell suspensions were pipetted on the scaffolds while sitting inside a syringe tube, followed by incubation on a roller (0.5Hz) for 4 h.

Static culturing

iMSC were seeded dynamically and after a 4 h incubation period, the scaffolds were taken out from the syringes and placed individually in empty wells of 4 cm^2 surface. Non-treated polystyrene well plates with ultra low cell adherence were employed to prevent growth of cells in the wells, competing for nutrients and oxygen. Two mL of proliferation medium was added per well to all scaffolds, followed by standard culturing conditions for 20 d. Medium was refreshed 3 times per week, and 5 scaffolds of each type were taken out after 5, 10 and 20 d.

DNA Assay

Medium was aspirated from the wells and the scaffolds were washed once in PBS from 3 samples per time point in the culturing experiment. After incubation at -80 ºC overnight to ensure cell lysis, 600 μL of 1× cell lysis buffer (CyQUANT®, Invitrogen) containing 1.35 Ribonuclease A Kunitz units/mL (Sigma Aldrich) was added to the scaffolds and incubated for 1 h on a shaking platform to assure that all cell content was released from the scaffold to the buffer solution. Next, 100 μL of 8×CyQUANT® dye was added to 100 μL of cell lysate and incubated for 15 min at room temperature in the dark. Fluorescence measurements were performed at 480/520 nm of excitation/emission peaks respectively.

Methylene blue staining, sectioning and imaging

Medium was aspirated from the wells and the scaffolds were washed once in PBS. Afterwards, scaffolds were incubated in HistoChoice fixative solution (Sigma Aldrich) for 20 min followed by washing in PBS. The scaffolds were immersed in a 1% methylene blue solution for 1 min after which they were washed several times in PBS until no blue staining was coming out of the scaffold. The stained scaffolds were visualised using a stereomicroscope (Nikon SMZ-10A with Sony 3CCD camera), both before and after sectioning through the middle using a diamond saw (Leica SP1600).

Hypoxia assay with A4-4 cells

A biological reporter system was used to compare hypoxic conditions in scaffolds with different architectures. The Hypoxia Responsive Element-Luciferase (HRE-Luc) transfected Chinese Hamster Ovary (CHO) A4-4 cell line[23] was kindly provided by Dr. Kiyoshi Nose (Showa University, Tokyo, Japan). The (HRE) promoter depends on hypoxia-inducible factor 1 (HIF1), of which the activity is regulated by the partial O_2 pressure in the cell. By adding luciferin to the cell lysate, light emission occurs as result of the luciferase-luciferin reaction. The intensity is a measure for the amount of luciferase expressed and for the lack of O_2 available for the cells.

A4-4 cells were cultured in α-minimum essential medium (Gibco) supplemented with 10% FBS (Lonza), 2 mM L-glutamine (Life Technologies), 100 U/mL penicillin (Life Technologies) and 10 µg/mL streptomycin (Life Technologies). The medium was refreshed 3 times per week, and the cells were grown under standard culturing conditions. For seeding of the scaffolds, the cells were trypsinised and $3.0 \cdot 10^5$ cells in 60 µL of medium were pipetted on top of each scaffold, which was placed in wells of non cell-adherent polystyrene plates and left to attach for 4 hours before adding additional culture medium. After 5 days, the cells were lysed and the luciferase activity was analysed according to the protocol of the luciferase assay kit (Promega). Luminescence was measured using a Bio-orbit 1253 Luminometer (ABOATOX). The luciferase activity was calculated in triplicate, normalising the luciferase activity to the DNA amounts from the same cell lysate, following the DNA assay procedure described above.

Results and Discussion

Scaffold architecture characterisation

The synthesised PDLLA-dimethacrylate macromer was used to prepare liquid resins for both stereolithography fabrication and for the preparation of porous scaffolds by photo-polymerisation and salt-leaching. After preparing both scaffold types, micro computed tomography (μCT) was used to obtain visualisations and quantitative data to characterise the scaffold pore networks (Figure 7.2).

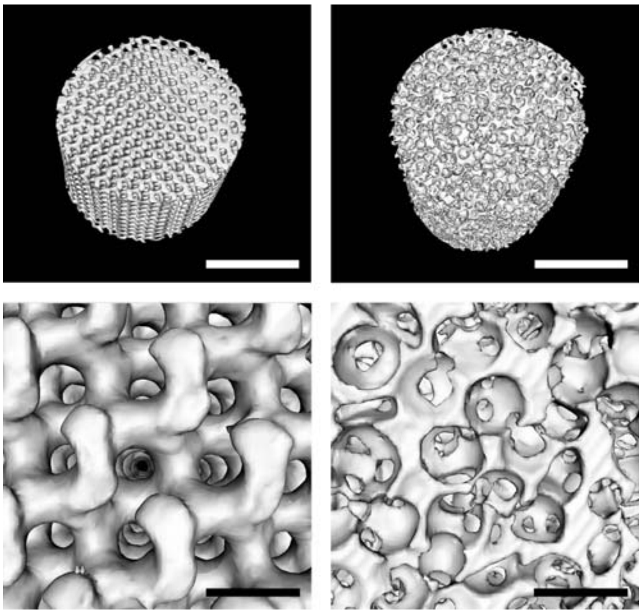

Figure 7.2: μCT-visualisations of gyroid scaffolds prepared by stereolithography (left) and salt-leached scaffolds (right), showing pores and pore interconnections. Scale bars are 4 mm (top) and 500 μm (bottom).

Table 7.1 shows parameters related to the pore network architecture of both scaffold types. The processing parameters for the preparation of both scaffold types were chosen such that a similar porosity and average pore size were obtained, in order to assess solely the effect of pore network architecture on cell seeding and culturing characteristics. Nevertheless, the salt-leached scaffolds have a higher specific surface area, as a result of the more random architecture of pores and pore walls as opposed to the designed gyroid architecture. A relative low surface area is one of the major restrictions of tissue engineering scaffolds prepared by rapid prototyping techniques. For example, some researchers have combined a fibre plotting technique with elecotrospun fibres to increase the surface area available for cell attachment.[24] The stereolithography technique used here has a higher resolution than most other rapid prototyping techniques, resulting in a specific surface area that is not more than 28 % lower than that of salt-leached structures at similar porosity and pore size. Furthermore, not al surface area in porous structures is available to cells, as cells usually do not enter pores with interconnections that are less than 5 to 10 times the diameter of a cell. After applying a threshold of 100 μm for pore interconnection size, the specific surface area remaining available to cells is even slightly higher for the gyroid type scaffold than for the salt-leached type scaffold.

Table 7.1: Structural parameters for both scaffold architectures, obtained from micro-computed tomography scanning data. Values are average ± standard deviation of 5 samples.

	porosity (vol%)	specific surface area (mm^{-1})		average pore size (μm)
		45 μm threshold	100 μm threshold	
gyroid	67.5±3.8	10.0±1.3	9.1±1.2	255±25
salt-leached	68.9±4.4	14.0±1.4	8.5±1.6	290±11

Figure 7.3 shows pore size distributions of the gyroid and salt-leached scaffolds as a histogram. The salt-leached scaffold shows a typical pore size distribution of scaffolds prepared by porogen leaching methods. Salt particles are sieved and one fraction (in this case 425-725 μm) is mixed with the polymer solution to make a composite. Leaching of the salt and extraction of the diluent then results in pores having a range of pore sizes. The gyroid architecture contains channels having approximately the same diameter throughout the structure, resulting in a smaller pore size distribution. This is also expressed by the standard deviation, that is 76±3 mm for the gyroid scaffold and 126±8 mm for the salt-leached scaffold (both n=5).

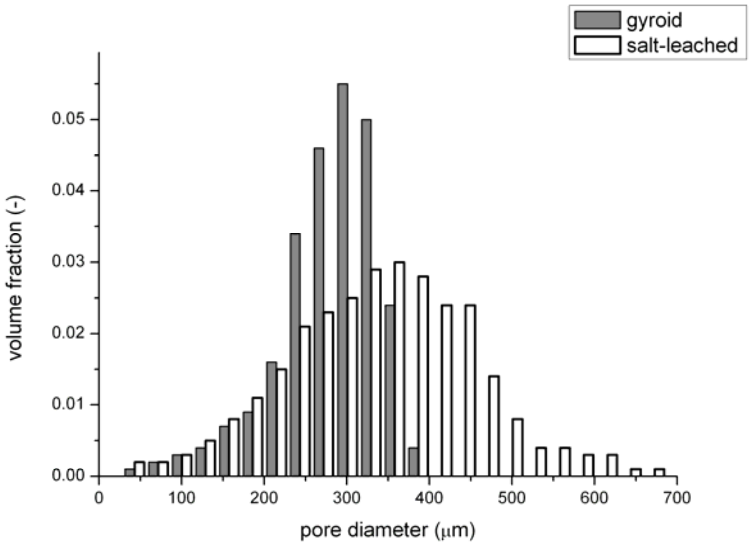

Figure 7.3: Pore size distributions for the gyroid and salt-leached scaffolds, obtained from μCT scanning data (average of 5 samples).

Despite the slightly smaller pore sizes in the prepared gyroid scaffolds, this scaffold architecture has a more open and accessible pore network. The number, size and location of the interconnections between pores play an important role in cell seeding, and in nutrient transport and cell migration during the cell culturing phase. While the gyroid pore network consists of channels with no clear boundaries between pores, the pore network of salt-leached scaffolds has interconnections smaller than the pores themselves, as can be clearly seen in Figure 7.2. These small pore interconnections impede flow; therefore the two scaffold architectures show a large difference in permeability, despite of the similar porosity and pore size. For both scaffold types, the resistance to water flow through the scaffold was measured. The resulting permeabilities are 0.519±0.045 mm^2 for the gyroid scaffold and 0.046±0.007 mm^2 for the salt-leached scaffold (both n=5). The large difference of more than 1 order of magnitude indicates the strong influence of scaffold architecture on transport phenomena.

Effect of wetting properties on cell seeding behaviour

iMSC were statically seeded by pipetting a cell suspension on top of both salt-leached scaffolds and gyroid scaffolds prepared by stereolithography. Prior to seeding, the scaffolds were disinfected in 70 % isopropanol, washed twice with PBS and incubated in culture medium overnight. The tortuous salt-leached scaffolds floated in all these liquids, indicating trapped air inside the scaffold as a result of poor wetting. As a consequence, the cell suspension did not penetrate deep into the scaffolds and cells were only found on the outside surface. The open gyroid scaffolds however were easily wetted by the isopropanol/water mixture, as well as by PBS and by culture medium, although PDLLA is a hydrophobic material. This allowed for intrusion of the cell suspension deep into the scaffolds, and cells were distributed all throughout. This is clearly seen in Figure 7.4, where blue stained areas indicate the presence of adhered cells.

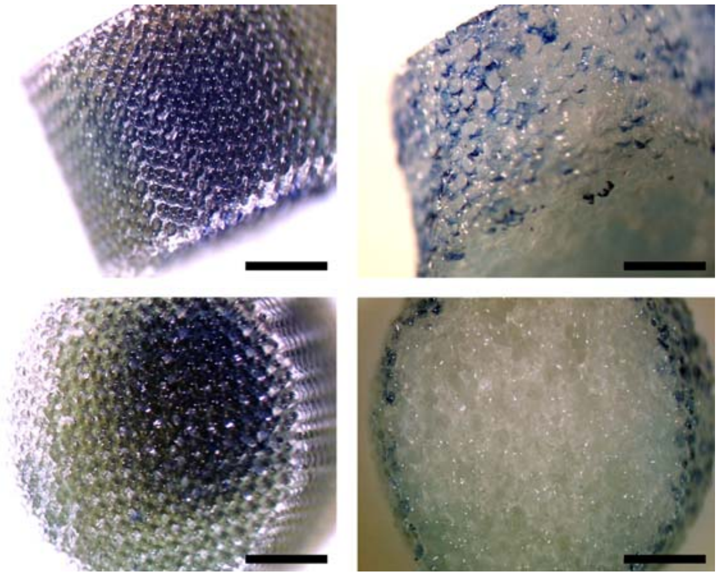

Figure 7.4: Stereomicroscope images of methylene blue-stained cells on gyroid (left) and salt-leached (right) scaffolds after static seeding. Top row: images were taken from the outside (side-views). Bottom row: images were taken from the middle cross-section of the scaffold. Scale bars are 2 mm.

The results demonstrate that the open architecture of the gyroid scaffold facilitates the infiltration of a cell suspension into the scaffold, despite its hydrophobic nature. Highly tortuous porous structures -such as salt-leached scaffolds- prepared from hydrophobic materials need extensive pre-treatment to ensure good wetting before cells can be seeded deeper into the scaffold.[25] All further seeding experiments on salt-leached scaffolds were performed after such pre-wetting treatment, as described below.

Static vs. dynamic seeding of iMSC on scaffolds

Cell seeding of both scaffold types was compared under static and dynamic conditions, after performing pre-wetting on the salt-leached scaffolds. Several evacuation-pressure release cycles were performed on the scaffolds in ethanol, to remove all air from the pores. Ethanol was then gradually replaced by PBS, leaving the scaffolds agitated for several hours to ensure adequate liquid exchange between the pores and the bulk liquid outside the scaffold. Finally, PBS was replaced by culture medium and incubated overnight, prior to cell-seeding. For the static seeding, a cell suspension was pipetted on top of the scaffold and left to attach for 4 h. For the dynamic seeding, cell suspensions were pipetted on top of scaffolds inserted in syringe tubes that were incubated on a roller (0.5 Hz) for 4 h. Images obtained by stereomicroscopy show methylene blue staining after both static (Figure 7.5) and dynamic (Figure 7.6) seeding.

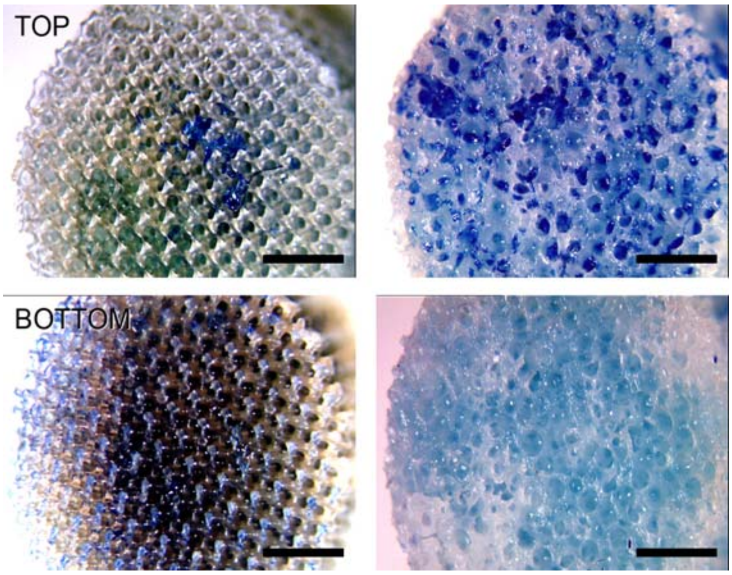

Figure 7.5: Stereomicroscope images of methylene blue-stained cells on gyroid (left) and salt-leached (right) scaffolds after static seeding. Images were taken from the top and bottom of the scaffold. Scale bars are 2 mm.

In the static seeding results, there is a clear effect of scaffold permeability on final cell distribution. For the very open gyroid scaffold, large cell clusters were found on the bottom of the scaffold, and below the scaffold in the well. The very open architecture does not allow sufficiently long entrapment of the cells, so many cells sink to the bottom before they are able to attach to the surface-adsorbed proteins. For the salt-leached scaffolds, the opposite is true. The cells sink into the scaffold, but due to the tortuous architecture they are retained in the upper part. Consequently, cell adhesion occurs here and confines the distribution of cells to this region. The permeability for which this static seeding procedure results in an optimal cell distribution lies in between those of the investigated scaffold types. However, the seeding kinetics cannot be altered without changing also the accessibility of the scaffold for nutrients etc., so other seeding methods are desired.

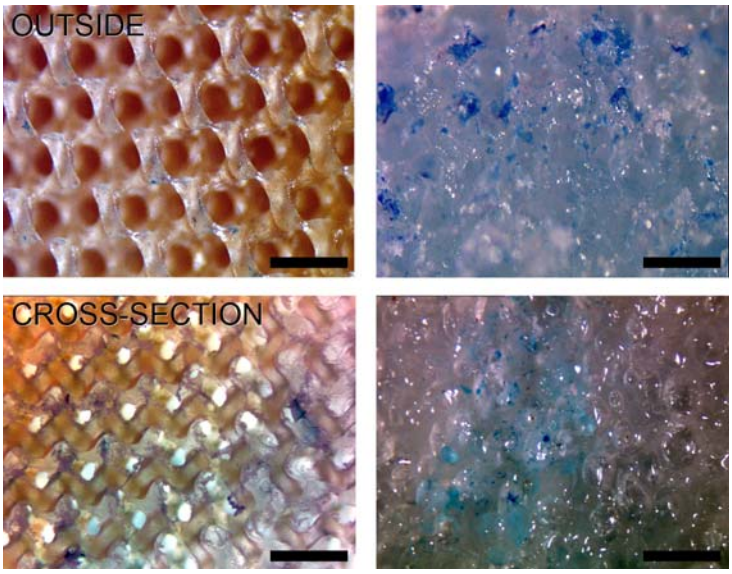

Figure 7.6: Stereomicroscope images of methylene blue-stained cells on gyroid (left) and salt-leached (right) scaffolds after dynamic seeding. Top row: images were taken from the outside of the scaffold. Bottom row: images were taken from the middle cross-section of the scaffold. Scale bars are 500 μm.

Using the dynamic method, the gyroid scaffold is seeded very homogeneously, much more than with the static method. The absence of intense blue coloured areas indicates the absence of clusters with high cell densities (Figure 7.6). In the salt-leached scaffold, cells are also distributed more homogeneously than by static seeding, although still cells are found in clusters. Overall, we observe that dynamic seeding increases the homogeneity of the seeding, and a regular open architecture adds to a homogeneous seeding of cells.

Static culturing of iMSC on scaffolds

Since transport limitations are mostly pronounced under static conditions and these are the prevailing method in the tissue engineering practice, we chose to assess the influence of scaffold architecture in static culturing. Gyroid scaffolds and salt-leached scaffolds were seeded dynamically for 4 h in syringes on a roller. Then the cells were cultured statically in non-adherent tissue culture plates and medium was refreshed 3 times per week. Samples were taken for methylene blue staining after seeding (4 h) and after 5, 10 and 20 d of culture. In Figure 7.7, microscopy images depict methylene blue-staining after 5 d of culture, both on the outside as well as on middle cross-sections of the scaffolds. After a 5 d culture period, a large increase in cell density can be seen on the outside for both scaffold types, as compared to the scaffolds just after seeding (Figure 7.6). However, the middle cross-sections show a clear difference between both scaffold architectures. In the gyroid scaffold, many cells can be seen distributed throughout the central part of the scaffold. In the middle section of the salt-leached scaffold however, hardly any cells can be observed. The outer pores of the salt-leached scaffolds are filled with cells and deposited matrix, thereby blocking the inside of the scaffold from inflow of oxygenated and nutrient-rich medium[12]. The small interconnections to deeper pores are completely obstructed. In the gyroid scaffold the pore channels are still open, allowing the supply of nutrients and oxygen to the cells inside the scaffold. The much higher cell number for the gyroid scaffolds was confirmed by a DNA assay, where an absorbance of 34±7 a.u. was measured for the gyroid scaffolds as opposed to 16±1 a.u. for the salt-leached scaffolds at day 5.

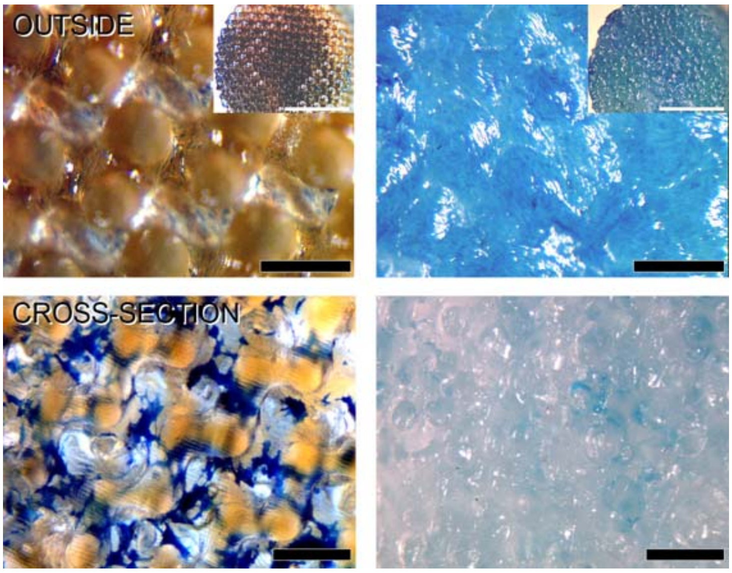

Figure 7.7: Stereomicroscope images of methylene blue-stained cells on gyroid (left) and salt-leached (right) scaffolds after 5 days of static culture. Top row: images were taken from the outside of the scaffold. Bottom row: images were taken from the middle cross-section of the scaffold. Scale bars are 500 μm or 4 mm in the inserts above.

Here, the benefit of open scaffold architectures on static cell culturing is clearly shown. Whereas the salt-leached scaffolds were totally blocked with cells and deposited matrix within 5 d, the channels in the gyroid scaffold were still accessible. This allowed for sufficient supply of oxygen and nutrients for cells in the centre of the scaffold to proliferate significantly (Figure 7.7).

Above, the benefit of well-defined, permeable scaffold pore architectures is shown, as it increases the period that cells inside a scaffold can access sufficient nutrients and oxygen, as compared to random-pore architectures with similar pore sizes. The possibility to culture cell-seeded scaffolds for at least 5 days provides an advantage for tissue engineering purposes. In bone tissue engineering, for instance, the *in vivo* bone forming potential of cells is often assessed by seeding them on scaffolds, followed by *in vitro* culturing for 7 days prior to implantation in an animal model.[26] Researchers frequently use scaffolds with poorly defined architectures, which compromises the quality of the tissue engineered grafts and the success of the *in vivo* bone formation. Here we present a designed gyroid scaffold that very well suits this application, as it guarantees good cell distribution and proliferation in a period of time that is common practice in tissue engineering applications.

After showing that the larger pore interconnections of the gyroid scaffolds as compared to those of the salt-leached scaffolds are advantageous regarding cell distribution and proliferation, we further assessed how larger pore interconnections and improved permeability of gyroid scaffolds could influence oxygen levels throughout the scaffold. For this, we used A4-4 cells that express luciferase on an O_2 concentration-dependent manner. The amount of expressed enzyme can be measured by quantifying the emitted light, resultant from the luciferase-luciferin reaction that depends on the availability of O_2 in the extracellular milieu. Gyroid scaffolds of two different average pore sizes were used to seed and culture A4-4 cells. After 5 days, the cells on the scaffolds with smaller pores (270 μm) expressed considerably more luciferase per cell than those with larger pores (350 μm), indicating different levels of available oxygen for the cells. This data clearly shows how a rational designed architecture can improve substantially the culturing conditions of cells.

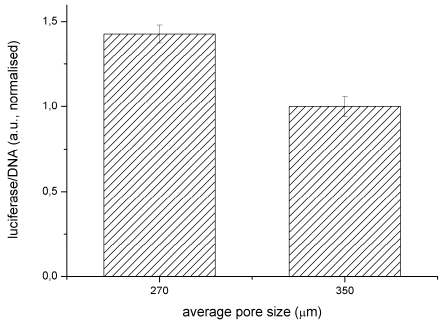

Figure 7.8: Luciferase activity of A4-4 cells cultured for 5 days on PDLLA gyroid scaffolds for two different average pore sizes. The data are based on 3 scaffolds each and normalised to amount of DNA.

Outlook

Although 5 days cultures showed encouraging results, after prolonged static culture of 20 days also gyroid scaffolds were found covered with a dense film of cells and matrix, with no surviving cells inside the scaffold (Figure 7.9). This suggests that for prolonged culturing periods, static culturing of any several mm sized scaffold will not lead to mature tissue with living cells throughout, regardless of pore architecture. However, the combination of a rationally designed scaffold architecture and active perfusion could improve cell viability throughout such constructs *in vitro* and, moreover, facilitate the graft invasion by the host´s vasculature. The penetration of natural capillary networks with oxygen and nutrients enriched blood connected to the main vasculature will ultimately ensure cell survival upon implantation.

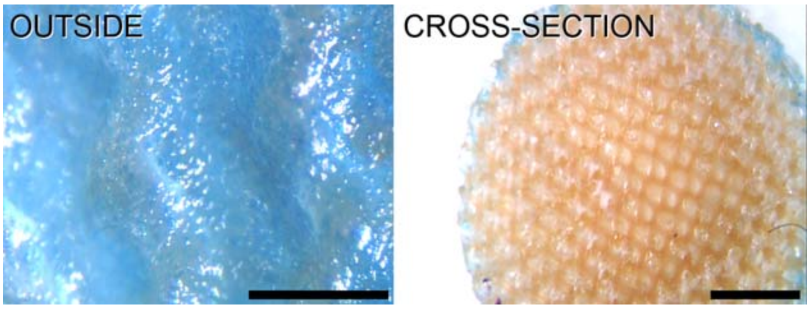

Figure 7.9: Stereomicroscope images of methylene blue-stained cells on gyroid scaffolds after 20 d of static culture. Scale bars are 500 μm (left) and 2 mm (right).

No cells, except for chondrocytes, exist further than 25-100 μm away from a blood supply[27] in order to access nutrients and oxygen. Therefore, we believe that tissue engineering scaffolds should embrace nature´s approach and mimic the vascular system present to increase the mass transport of oxygen and nutrients deep within and removal of waste products from the scaffold. To achieve such scaffold design, freeform fabrication can play a role.[16] In Figure 7.10 we present a novel scaffold design where we combine meso-scale pores (250 μm) in which cells can proliferate and deposit matrix, with macro-scale channels (600 μm).

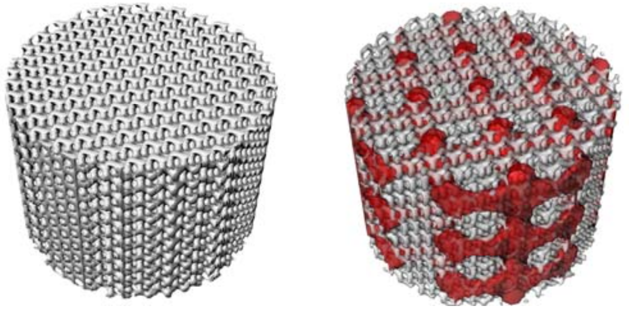

Figure 7.10: Original gyroid scaffold design (left) and novel gyroid scaffold design with integrated perfusion channels (right). The scaffold material and perfusion channels are co-visualised as semi-transparent layers.

The scaffold design is based on the same gyroid pore architecture that was built and used in the seeding and culturing experiments, but now channels are included to avoid parts of the scaffold from being blocked by cells and deposited matrix at an early stage of cell culturing. The deducted channels are described by another minimal surface architecture, the primitive surface. Here, the channels form a cubic lattice and are described by the following boundary condition:

$$\cos(u)+\cos(v)+\cos(w)-\frac{1}{2}\left\{\cos(u)\cos(v)-\cos(v)\cos(w)-\cos(w)\cos(u)\right\}<0.9$$
$$\text{where}\,\{u,v,w\}=\frac{1}{3}\cdot\{x,y,z\}$$

The scaffold architecture presented here is designed to improve the transport of nutrients and oxygen. Furthermore, the network of larger-sized channels could facilitate the invasion of the host vasculature after implantation, or be employed for pre-vascularisation *in vitro*. The co-culture of myoblasts, endothelial cells and embryonic fibroblasts has been found to stimulate blood vessel formation in biodegradable polymer scaffolds *in vitro*.[28] The stereolithography technique enables to prepare designed scaffolds that direct pre-vascularisation and angiogenesis. Here, we suggest to make use of the designed larger channels for engineering pre-fabricated vasculature. By first seeding and culturing iMSC in our designed scaffolds for several days, then followed by co-seeding of endothelial cells and embryonic fibroblasts in the still open meso-pore channels, endothelial vessel formation could be stimulated. Particularly for the engineering of tissues that require high levels of oxygen and nutrients, such as bone, the presented scaffold design and preparation technique are promising for future application.

Conclusions

Two scaffold architectures were compared with respect to cell seeding and cell culturing characteristics; a well-defined gyroid architecture prepared by stereolithography and a salt-leached scaffold with a more random pore network. Both had similar porosity, average pore sizes and specific surface area, but the permeability differed by more than an order of magnitude.

It was shown that the open, accessible architecture has improved cell seedability compared to the tortuous pore architecture. The scaffolds can be wetted and intruded by a cell suspension more easily, resulting in a more homogeneous cell distribution. In static seeding procedures, the high permeability of the open scaffolds caused many cells to sink through the pore network and leave the scaffold before adhering, while in the salt-leached scaffolds with low permeability, cells did not penetrate deep into the scaffold. Dynamic seeding in combination with high permeability results in the most homogeneous distribution of seeded cells.

In static culturing, where large gradients in oxygen and nutrient concentrations exist, a cell-sheet is formed around the scaffold that shields the inside from medium in- and outflow, eventually resulting in cell death inside the scaffold. The open pore architecture of the stereolithography-fabricated scaffold significantly delays the formation of this cell-sheet compared to that of the salt-leached architecture. As a result, scaffolds with high densities of relatively homogeneously distributed cells are obtained after dynamic seeding and 5 d of static culture.

Here we show that by tuning the architecture of a scaffold using rapid prototyping techniques such as stereolithography we can facilitate homogeneous cell distribution after seeding and prolong static culturing with sustained nutrient and oxygen accessibility. Novel scaffold designs with integrated perfusion channels are suggested to prevent large parts of the scaffolds from being blocked from medium in the generation of tissue grafts.

Acknowledgements

We would like to acknowledge the European Union (STEPS project, FP6-500465) and the TERM-Smart Mix program for funding.

References

[1] B. S. Kim, A. J. Putnam, T. J. Kulik, D. J. Mooney, *Biotechnology and Bioengineering* **1998**, *57*, 46.

[2] J. M. Unsworth, F. Rose, E. Wright, C. A. Scotchford, K. M. Shakesheff, *Journal of Biomedical Materials Research Part A* **2003**, *66A*, 425.

[3] Y. Li, T. Ma, D. A. Kniss, L. C. Lasky, S. T. Yang, *Biotechnology Progress* **2001**, *17*, 935.

[4] J. Xie, Y. Jung, S. H. Kim, Y. H. Kim, T. Matsuda, *Tissue Engineering* **2006**, *12*, 1811.

[5] G. VunjakNovakovic, L. E. Freed, R. J. Biron, R. Langer, *Aiche Journal* **1996**, *42*, 850.

[6] D. Wendt, A. Marsano, M. Jakob, M. Heberer, I. Martin, *Biotechnology and Bioengineering* **2003**, *84*, 205.

[7] J. M. Jukes, L. Moroni, C. A. Van Blitterswijk, J. De Boer, *Tissue Engineering Part A* **2008**, *14*, 135.

[8] J. L. Dewez, A. Doren, Y. J. Schneider, P. G. Rouxhet, *Biomaterials* **1999**, *20*, 547.

[9] J. Malda, T. B. F. Woodfield, F. van der Vloodt, F. K. Kooy, D. E. Martens, J. Tramper, C. A. van Blitterswijk, J. Riesle, *Biomaterials* **2004**, *25*, 5773.

[10] L. E. Freed, G. Vunjak-Novakovic, *Advanced Drug Delivery Reviews* **1998**, *33*, 15.

[11] S. L. IshaugRiley, G. M. Crane, A. Gurlek, M. J. Miller, A. W. Yasko, M. J. Yaszemski, A. G. Mikos, *Journal of Biomedical Materials Research* **1997**, *36*, 1.

[12] I. Martin, R. F. Padera, G. Vunjak-Novakovic, L. E. Freed, *Journal of Orthopaedic Research* **1998**, *16*, 181.

[13] J. Liu, A. Barradas, H. Fernandes, F. Janssen, B. Papenburg, D. Stamatialis, A. C. Martens, C. Van Blitterswijk, J. De Boer, *Tissue Engineering Part C-Methods* **2009**, *Epub ahead of print.*

[14] D. Wendt, S. Stroebel, M. Jakob, G. T. John, I. Martin, *Biorheology* **2006**, *43*, 481.

[15] E. Volkmer, I. Drosse, S. Otto, A. Stangelmayer, M. Stengele, B. C. Kallukalam, W. Mutschler, M. Schieker, *Tissue Engineering Part A* **2008**, *14*, 1331.

[16] E. Sachlos, J. T. Czernuszka, E*uropean Cells and Materials* **2003**, *5*, 29.

[17] J. J. Clair, *Journal of Materials Processing Technology* **1996**, *57*, 393.

[18] F. P. W. Melchels, J. Feijen, D. W. Grijpma, *Biomaterials* **2009**, *30*, 3801; Chapter 4 of this thesis.

[19] A. G. Mikos, A. J. Thorsen, L. A. Czerwonka, Y. Bao, R. Langer, D. N. Winslow, J. P. Vacanti, *Polymer* **1994**, *35*, 1068.

[20] A. H. Schoen, Nasa Technical Note, NASA-TN-D-5541 **1970**.

[21] H. A. Schwarz, *Gesammelte Mathematische Abhandlungen*, Springer-Verlag, Berlin **1890**.

[22] P. Noordhuis *et al.*, unpublished data.

[23] Y. Yamazaki, K. Egawa, K. Nose, S. Kunimoto, T. Takeuchi, *Biological & Pharmaceutical Bulletin* **2003**, *26*, 417.

[24] L. Moroni, R. Schotel, D. Hamann, J. R. de Wijn, C. A. van Blitterswijk, *Advanced Functional Materials* **2008**, *18*, 53.

[25] A. G. Mikos, M. D. Lyman, L. E. Freed, R. Langer, *Biomaterials* **1994**, *15*, 55.

[26] S. Teixeira, H. Fernandes, A. Leusink, C. van Blitterswijk, M. P. Ferraz, F. J. Monteiro, J. de Boer, in *Journal of Biomedical Materials Research Part A* **2009**, *93*, 567.

[27] A. J. Vander, J. H. Sherman, D. S. Luciano, *Human Physiology*, McGraw-Hill, New York **1985**.

[28] S. Levenberg, J. Rouwkema, M. Macdonald, E. S. Garfein, D. S. Kohane, D. C. Darland, R. Marini, C. A. van Blitterswijk, R. C. Mulligan, P. A. D'Amore, R. Langer, *Nature Biotechnology* **2005**, *23*, 879.

Chapter 8 - The influence of the scaffold design on the distribution of adhering cells after perfusion cell seeding

Ferry Melchels[1] and Beatrice Tonnarelli[2], Andy Olivares[3], Ivan Martin[2], David Wendt[2], Josep Planell[3], Damien Lacroix[3], Jan Feijen[1] and Dirk Grijpma[1,4]

In natural tissues, the extracellular matrix composition, cell density and physiological properties are often non-homogeneous. Here we describe a model system in which the distribution of cells throughout tissue engineering scaffolds after perfusion seeding can be influenced by the pore architecture of the scaffold. Two scaffold types, both with gyroid pore architectures, were designed and built by stereolithography: one with isotropic pore size (412±13 μm) and porosity (62±1 %), and another with a gradient in pore size (250-500 μm) and porosity (35 %-85 %). Computational fluid flow modelling showed a uniform distribution of flow velocities and wall shear rates (15-24 s^{-1}) for the isotropic architecture, and a gradient in the distribution of flow velocities and wall shear rates (12-38 s^{-1}) for the other architecture. The distribution of cells throughout perfusion-seeded scaffolds was visualised by confocal microscopy. The highest densities of cells correlated with regions of the scaffolds where the pores were larger, and the fluid velocities and wall shear rates were highest. Under the applied perfusion conditions, flow-induced cell detachment does not occur, and cell deposition rates are mainly determined by local wall shear rates. These, are strongly influenced by the architecture of the pore network of the scaffold.

---

[1] MIRA Institute for Biomedical Technology and Technical Medicine, and Department of Polymer Chemistry and Biomaterials, University of Twente, P.O. Box 217, 7500 AE, Enschede, The Netherlands

[2] Departments of Surgery and of Biomedicine, University Hospital Basel, Hebelstrasse 20, 4056, Basel, Switzerland

[3] Institute for Bioengineering of Catalonia (IBEC), Baldiri Reixac 4, 08028 Barcelona, Spain

[4] Department of Biomedical Engineering, University Medical Centre Groningen and University of Groningen, P.O. Box 196, 9700 AD Groningen, The Netherlands

Introduction

Zonal variations in extracellular matrix composition, as well as in cell distribution have been observed in native tissues like articular cartilage, meniscal- and osteochondral tissue. Engineered tissue grafts which mimic the various levels of organisation *in vivo* could lead to better tissue regeneration and integration than grafts with more isotropic composition and properties.[1]

Previously, the beneficial effect of perfusion on cell seeding and -culturing in a bioreactor was demonstrated using foam scaffolds with an isotropic random-pore architecture.[2] Compared to static seeding, cell seeding under perfusion conditions is highly efficient and uniform, and cell viability is high as well. During perfusion cell culturing deposition of extracellular matrix is homogenous. Anisotropic tissue grafts can be generated using designed porous structures. Using rapid prototyping techniques, stereolithography in particular, scaffolds with precise gradients in pore size, porosity or stiffness can be fabricated.[3] With such designed structures, gradients in cell distributions may be accomplished, and in perfusion seeding the scaffolds in a bioreactor the distribution of cells will depend on the flow profile of the cell-containing medium through the scaffold. As the adhesion process of cells to surfaces is strongly influenced by the hydrodynamic environment too,[4] computational fluid dynamics studies can play a key role in the rational design of pore network architectures of scaffolds and in optimising perfusion parameters.[5, 6]

Despite the beneficial role of perfusion demonstrated for 3D cell seeding and culture,[2, 7, 8] little is known regarding the optimal parameters of scaffold architecture[9, 10] and of flow conditions.[11, 12] Attempts have been made to study the effect of fluid-induced shear on cellular behaviour, but the irregularity of the porous structures made it difficult to model the flow and to find meaningful correlations between fluid flow and cell behaviour.[13] In this work we aim at developing a model system to influence the distribution of cells upon perfusion seeding. For this we make use of well-defined poly(D,L-lactide) scaffolds, with regular designed pore architectures prepared by stereolithography and applied controlled perfusion conditions for cell seeding. We hypothesise that gradients in fluid flow velocities, which are determined by the scaffold architecture, will correlate with gradients in the density of adhering cells upon perfusion seeding.

Experimental

Scaffolds

Photo-polymerisable poly(D,L-lactide) (PDLLA) macromers were synthesised in a similar way as previously described.[14] In short, 1,6-hexanediol (Sigma-Aldrich) and D,L-lactide (Purac) were reacted at 130 °C for 40 h under an argon atmosphere using stannous octoate (Sigma-Aldrich) as a catalyst. The linear hydroxy -terminated oligomers with a molecular weight of 1.2 kg/mol as determined by ^{1}H-NMR (Varian 300 MHz, $CDCl_3$) were reacted for 9 h with methacrylic anhydride (Sigma-Aldrich, 50 % molar excess) at 110 °C in the presence of 0.15 % α-tocopherol inhibitor (vitamin E, Fluka) to prevent preliminary crosslinking. The excess methacrylic anhydride and the formed methacrylic acid were removed by vacuum distillation (residues 0.7 and 0.4 wt%, respectively). The macromers were used to formulate a stereolithography resin further comprising 18 wt% dry N-methylpyrrolidone (NMP, Fluka) as a non-reactive diluent, 3.6 wt% ethyl-2,4,6-trimethylbenzoylphenyl-phosphinate (Lucirin TPO-L photo-initiator from BASF) and 0.15 wt% Orasol Orange G dye (Ciba SC).

Two scaffold designs were developed using K3DSurf v0.6.2 software. The first design is an isotropic design (type I) with constant porosity throughout the (cylindrical) scaffold. To induce different fluid flow profiles in the perfusion setup, another scaffold (type G) was designed to have a porosity gradient in the radial direction. In the type G scaffold, the porosity decreases from the central axis towards the periphery of the cylindrical scaffold. Both designs are based on a gyroid architecture, of which the surface is described by a triply periodic function, closely approximating the minimal surfaces of Schwarz and Schoen.[15, 16] Addition of an offset value to the implicit function (see below) allows designing porous structures with a specific porosity. For the type I gyroid scaffold, a value of -0.15 was chosen for the offset, corresponding to 55 % porosity. In the type G gyroid scaffold, the offset is 0.90 for $x,y=0$, corresponding to 80 % porosity in the centre of the scaffold. The offset increases with x^2+y^2, thus the porosity decreases quadratically with the scaffold radius to 30 % at the periphery of the scaffold. The following equations were used to describe the scaffold designs, both with boundary conditions $x^2 + y^2 < (10\pi)^2$ and $|z| < 5\pi$:

$$I : \cos(x)\sin(y) + \cos(y)\sin(z) + \cos(z)\sin(x) - 0.15 = 0$$

$$G : \cos(x)\sin(y) + \cos(y)\sin(z) + \cos(z)\sin(x) + 0.0015(x^2 + y^2) - 0.90 = 0$$

Scaffolds were fabricated from CAD designs using an EnvisionTec Perfactory Mini Multilens stereolithography apparatus.[14] After building, the structures were extracted in a mixture of isopropanol (75 wt%) and acetone (25 wt%), and subsequently dried at 90 °C for 2 d. The built scaffolds were cylindrical, with a diameter of 8 mm and a height of 5 mm. Structural analyses of the fabricated scaffolds were performed using micro computed tomography (μCT, GE eXplore Locus SP operated at 80 kV, 80 μA and 15 μm resolution without filter) to determine the accuracy of the building process, to quantify structural parameters such as pore size distribution and porosity distribution, and to obtain digital meshes as input for flow analyses (MicroView software).

Fluid flow modelling

The flow of fluid (medium) through the pore networks of both scaffold types was modelled using a finite element approach, and taking the geometry of the bioreactor chamber into account. With μCT iso-surface meshes as input, volumetric fluid meshes were made using Mimics software (Materialise) to obtain a total of 2,375,010 tetrahedral elements for the type I scaffold and 2,253,778 elements for the type G scaffold. The boundary conditions used in modelling the perfusion were in correspondence with the perfusion cell seeding experiment (see below). No-slip surface conditions and zero outlet pressures were assumed. In the model, the material from which the scaffolds were prepared was rigid and impermeable. Profiles of fluid flow velocity, fluid shear rates and fluid shear stresses were calculated using Fluent 6.3 (Ansys) software. The fluid was modelled using the viscosity ($\eta=1.45\cdot10^{-3}$ Pa·s) and density ($\varrho=1000$ kg·m^{-3}) of Dulbecco's modified eagle medium (DMEM, both at 37 °C).

Perfusion cell seeding

Expanded human articular chondrocytes (HAC, 5 million in 8 mL DMEM) were perfusion seeded throughout the scaffolds for 16 h in a bioreactor as previously described.[7] The used perfusion rate of 1.6 mL/min corresponds to an inlet fluid flow velocity of 1 mm/s (inlet diameter is 6 mm), and a fluid flow velocity of 0.5 mm/s inside an empty bioreactor chamber (diameter is 8 mm). Following seeding, the cells were stained with SYTO-13 to assess the distribution of live cells within the scaffolds. Confocal microscopy images were taken using a confocal laser scanning microscope (CLSM, 7500-Zeiss), with a 10x objective and the aperture set at 1 Airy unit (this corresponds to an image depth of 10 μm). Entire scaffold cross-sections were imaged in scanning mode on adjacent blocks of z-stacks, 500 μm in depth. The confocal microscopy images were thresholded to black-and-white and subsequently used to determine cell densities. Cell densities were expressed as the relative area of the image covered with cells (the fraction of black pixels). To obtain quantitative distributions as a function of the scaffold radius, the coordinates of each scaffold centre were first determined. The images were then partitioned in equidistant rings from the centre towards the periphery with radius increments of 100 μm. The cell density in each concentric ring was determined, again as the percentage of the area covered with cells.

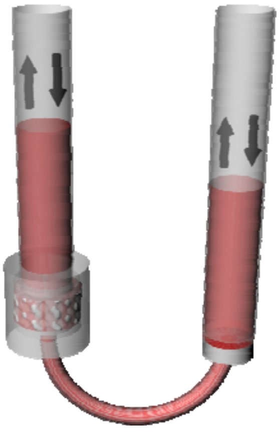

Figure 8.1: Schematic diagram of the perfusion cell seeding setup.

Results and Discussion

Scaffolds

Poly(D,L-lactide) (PDLLA) macromers were successfully synthesised, the degree of functionalisation of the end groups was more than 95 %. After mixing with diluent, photo-initiator and dye, the PDLLA resin was used to build the designed scaffolds by stereolithography. After extraction and drying, the built scaffolds were visualised by μCT imaging. Figure 2 shows that the scaffold designs were very accurately reproduced. The porosity gradients in the built type G scaffolds can be clearly seen.

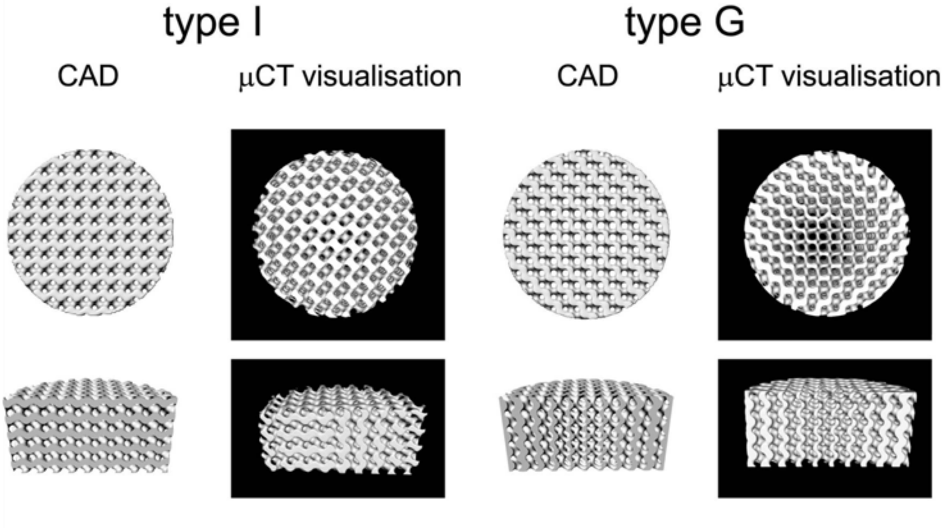

Figure 8.2: Top row: top-view images of type I (isotropic design) and type G (gradient design) gyroid scaffolds comparing the computer-aided designs (CAD) with μCT-visualisations of the built structures. Bottom row: cross-sections, clearly showing the gradient in porosity and pore size in the type G scaffold. The diameter of the scaffolds is 8 mm.

The μCT scan data was also used to calculate structural scaffold parameters (such as porosity and pore size) on different size scales: overall values (averaging the whole scaffold volume, corresponding to an 8 mm size scale) and local values (at a 100 μm size scale) were determined. For both scaffold types, Figure 8.3 shows the distribution of local porosity values as a function of distance from the scaffold central axis (calculated with increments of 100 μm). Data from the computer designs as well as from the μCT analyses are presented. The porosity gradient in the design of the type G scaffold as well as in the μCT scans of the built structures can clearly be seen. For both data sets, the local porosity shows a quadratic decrease (R^2>0.99) from porosity values of 85 % near the central axis of the scaffold to values of 35 % at the periphery. Accordingly, there is a gradient in pore size as well. Sizes range from approximately 500 μm in the centre of the scaffold to 250 μm at the periphery. It should be noted that in these gyroid scaffolds, the pore network is a channel-like architecture and pore interconnections of limited sizes are not present. Therefore, even the smallest determined pore size is very much larger than the size of a cell (10 μm in diameter) and blocking of the pore network channels by cells is unlikely to occur during perfusion seeding.

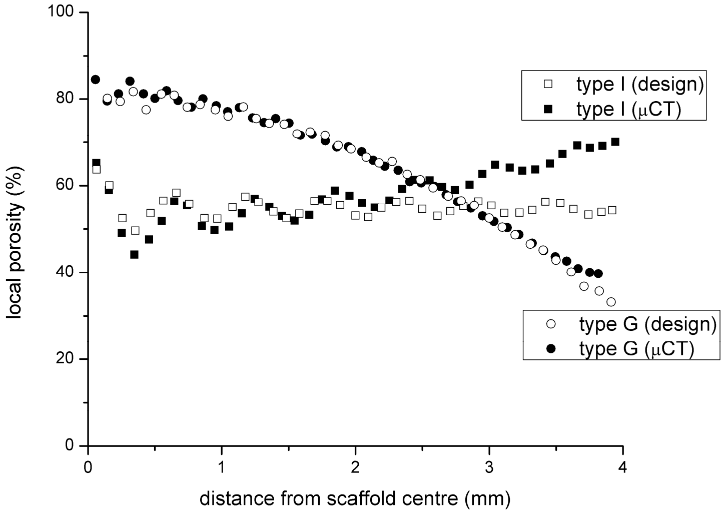

Figure 8.3: Local porosity as a function of the distance from the central axis of the scaffold, for cylindrical type I (isotropic) and type G (gradient) scaffolds. The data from the μCT analyses (average of 2 samples each) are compared to the computer-aided designs. Local porosity values are determined at 100 μm intervals.

The type I scaffold shows less variance in porosity and pore size. An overall porosity of 62±1 % was determined, with an average pore size of 412±13 μm. For the type I scaffold in particular, the periodicity of the trigonometric functions is reflected by the regular oscillations in the determined local porosity values from the centre of the scaffold outwards. Although in the case of this scaffold type an isotropic porosity of 55 % was designed, the μCT data show that the local porosity increases from the centre of the scaffold outwards towards its perimeter. This is the result of overcure, a phenomenon that can occur in the fabrication of porous structures by stereolithography.[14] As a result of the exothermic photo-polymerisation reactions and poor heat exchange, local warming up of the resin in regions with relatively low porosities within a structure are cured to a further extent than at its periphery. In the type G scaffold, the effect of overcure is minimal because of the high porosity values in the central region of the scaffold.

The overall specific surface area determined from the μCT data was 4.8 mm^{-1} for both scaffold types; a surface area of $1.2 \cdot 10^3$ mm^2 was determined for scaffolds with a volume of $2.5 \cdot 10^2$ mm^3. As a result of the well-defined and repetitive nature of the pore network architecture in an isotropic gyroid structure, the local value of the specific surface area remains constant throughout the scaffold. The specific surface area primarily depends on the size of a repeating unit cell in the design: the smaller the unit cell, the smaller the pores and the higher the specific surface area. The size of a unit cell is the same for both scaffold types: 800x800x800 μm^3. Also within the type G scaffold all unit cells are of equal size, despite the porosity and pore size gradient. In this case, however, the porosity gradient does lead to small variations in specific surface area, as the specific surface area to some extent also depends on porosity. In the type G scaffold, local values for the specific surface area can differ up to 10 % from the overall specific surface area of 4.8 mm^{-1}.

Fluid flow modelling

The flow of fluid through both scaffold architectures was modelled using a finite element approach. To represent the scaffold pore architectures, data from the μCT analyses of the built structures (and not that of the computer designs) were used. The modelling, in which the geometry of the perfusion bioreactor chamber was taken into account as well, resulted in the velocity profiles depicted in Figure 8.4. Here, the values of the local fluid velocities are shown as coloured vectors. The characteristic zero mean-curvature of the gyroid pore network architecture implies the absence of flow-disturbing elements. In the given perfusion regime, this results in laminar fluid flows (the maximum calculated Reynolds number is 0.12). Average fluid flow velocities are 0.86 mm/s for both scaffold types. Parabolic fluid velocity profiles develop in each of the channels that run through the scaffolds, the local velocity is highest in the centre of the channel. The modelling shows, that in the type I scaffold the flow profile is quite uniform with maximum velocities of approximately 2.8 mm/s. In the type G scaffold undisturbed laminar flows are also observed, but the radial gradient in porosity leads to a clear gradient in fluid flow velocities. For this scaffold architecture the maximum velocities in the central part of the scaffold are close to 4.0 mm/s, while they strongly decrease to near zero at the periphery.

At the scaffold wall the velocity of the fluid is zero, and wall shear rates are best used to describe the velocity with which suspended cells flow past the surface of the pores. Wall shear rate is defined as the slope of the velocity profile at the fluid-wall interface: $\dot{\gamma} = dv / dr$. The lower part in Figure 8.4 shows 3D views of the scaffolds, where part of the scaffolds is coloured to indicate the distribution of local wall shear rate values. Here, the uniformity of the fluid velocity profile in scaffold type I is also reflected in rather uniform wall shear rates throughout the structure. In contrast, scaffold type G shows considerably reduced wall shear rates towards the periphery of the scaffold when compared to wall shear rates in the centre.

The wall shear rate not only determines the velocity of the passing cell suspension, but it also determines the hydrodynamic force that adhering cells are exposed to. This force can be expressed per unit of area as the wall shear stress (in Pa), and is the product of the wall shear rate and the kinematic viscosity of the fluid medium. The wall shear stress is therefore an important parameter in cell adhesion processes.[17] The average wall shear stresses in scaffold types I and G are 31 and 27 mPa, respectively, and range from near-zero values to maximum local values of approximately 65 mPa. The effects of flow-induced shear stress on cell adhesion have been studied extensively.[18-20] The critical shear stress for cell detachment to occur depends on the material on which the cells are cultured, but has been found to range between 1 and 3 Pa.[21-23] For the range of wall shear stress values occurring in our perfusion setup, flow-induced cell detachment will not occur.

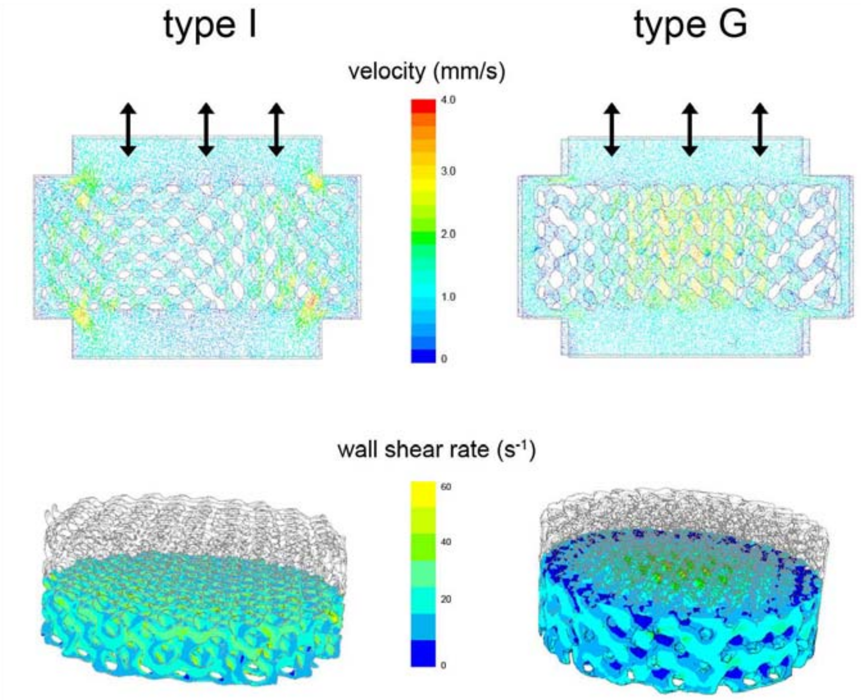

Figure 8.4: Fluid flow velocity- and wall shear rate profiles for scaffold types I (isotropic) and G (gradient). The velocity vectors between two parallel sections (at a distance of 0.5 mm) in the direction of the flow path are shown. The diameter of the scaffolds is 8 mm. The spots with high local velocities at the scaffold edges (inlet and outlet) are artefacts.

Assessment of cell distributions

To study the effect of pore network architecture of the scaffolds on cell distributions, the different scaffolds were seeded with cells in a bioreactor by back-and-forth perfusion of an 8 mL cell suspension (300-400 passages in 16 h). Considering the relative sizes of a cell (10 μm) and the determined sizes of a pore (250-500 μm), it can be assumed that the presence of adhered cells does not change the macroscopic flow profile. Also, the suspended non-adhered cells can be assumed to remain homogeneously distributed in the flowing medium as per passage depletion from the medium due to attachment of cells is minimal and the cell suspension is homogeneously mixed after each passage.

Live adherent cells were stained with Syto 13 and visualised using confocal microscopy. When used in scanning mode, this imaging technique allows imaging of the cross-section of the entire scaffold and to simultaneously investigate the structure in much more detail at smaller size scales. The example in Figure 8.5 shows a visualisation of seeded cells in a cross-section of a type I scaffold (10 μm confocal thickness). The image is obtained at a very high resolution of 26 megapixels, which makes it possible to distinguish individual cells (see insert). The right part of the figure shows the modelled wall shear rate profile in a cross-section. The insert shows that at a small size scale (within a pore), the shear rates range between 0 and 30 s^{-1}. The macroscopic distribution of shear rates, however, is homogeneous; only little differences in shear rate values are observed when comparing unit cells from the central part of the scaffold to those at the periphery. Imaging of the cell and the cell distribution by confocal microscopy and modelling the fluid flow during perfusion cell seeding, allows to compare the local density of adhering seeded cell with local fluid flow conditions.

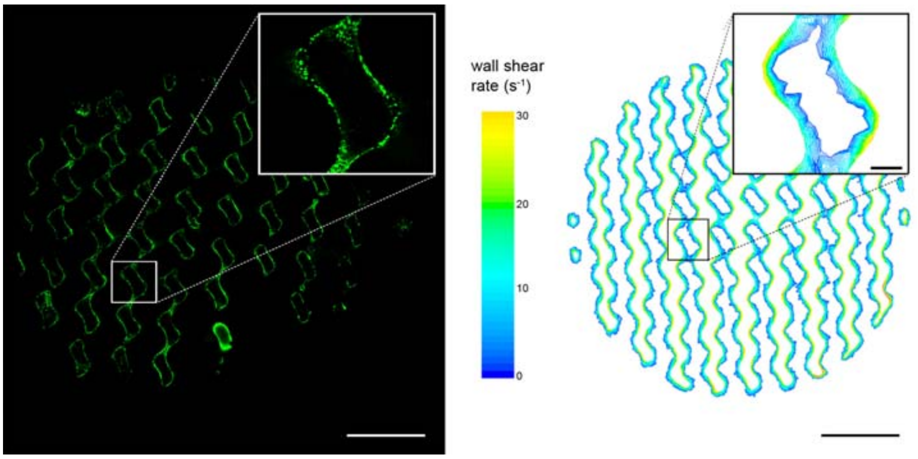

Figure 8.5: Left: confocal microscopy image of a type I gyroid scaffold seeded with cells, showing the distribution of live adhering cells throughout a cross-section of the scaffold. Right: image of a similar cross-section, showing the modelled distribution wall shear rates of the fluid during perfusion cell seeding. Scale bars are 2 mm for the larger images and 200 μm for the inserts.

To obtain three-dimensional images of adhering cell and their distributions, perfusion seeded scaffolds were scanned at different confocal depths. From these images, stacks in the z-direction were composed. The obtained z-stack images were subsequently thresholded to black-and-white, giving a quantitative impression of the distribution of the cells in the scaffolds. Figure 8.6 shows such thresholded confocal microscopy images after perfusion seeding both scaffold types. In the figure, 500 μm thick z-stacks composed of 50 layers are shown. The cell densities in confocal microscopy images will depend on the surface area available for cell adhesion. In irregular pore architectures the available surface area in a thin layer can vary greatly throughout the cross-section, making quantification of cell distributions nearly impossible. In contrast, the well-defined and repetitive nature of the gyroid architecture results in an isotropic surface area distribution for type I scaffolds, while variations in the available surface area in type G scaffolds are very small (see before). It is therefore possible to compare the observed cell densities in different regions of both scaffold types.

The top left image in Figure 8.6 shows a very homogeneous distribution of cells after seeding in the type I scaffold. A homogeneous cell distribution is often desired, and several methods of cell seeding have been developed throughout the past two decades. Perfusion seeding seems to result in the most homogeneous distribution of cells.[7, 24-26] In addition, the regularity of our isotropic designed scaffold architecture, leads to even more homogeneous seeding by inducing uniform velocity- and wall shear rate profiles of the flowing cell suspension. As mentioned before, anisotropic cell distributions can be desired as well, particularly when engineering zonal tissues. For the type G scaffold, with a radial gradient on pore size and porosity, an anisotropic distribution of cells is observed after perfusion cell seeding. The top right image in Figure 6 shows that cell density is markedly higher in the centre of the scaffold than at the periphery.

In our experiments, one time-point (the end-point) of the perfusion cell seeding process was evaluated. During seeding, adhering cells decrease the available pore surface area of the scaffold in time. This might affect the cell deposition rate and the final cell density. From the μCT data, the surface areas of the type I and the type G scaffold were both found to be $1.2 \cdot 10^3$ mm^2. From the thresholded confocal microscopy z-stack images depicted in Figure 8.6, similar overall cell densities of 7 % for the isotropic type I scaffold and 8 % for the gradient type G scaffold were determined. (Note that the cell densities are expressed as the relative area of the image covered with cells.) A spread chondrocyte occupies an area of approximately $1 \cdot 10^3$ μm^2, implying that the surface area of these scaffolds allows attachment of approximately 1.2 million spread cells in monolayer. DNA analyses showed that several millions of cells were seeded per scaffold. The initial seeding suspension contained 5 million cells, seeding efficiencies ranged from 40 to 60 %. From this, we can conclude that the cells were also seeded in multilayers. And indeed, confocal microscopy showed clustering of cells in the seeded scaffolds.

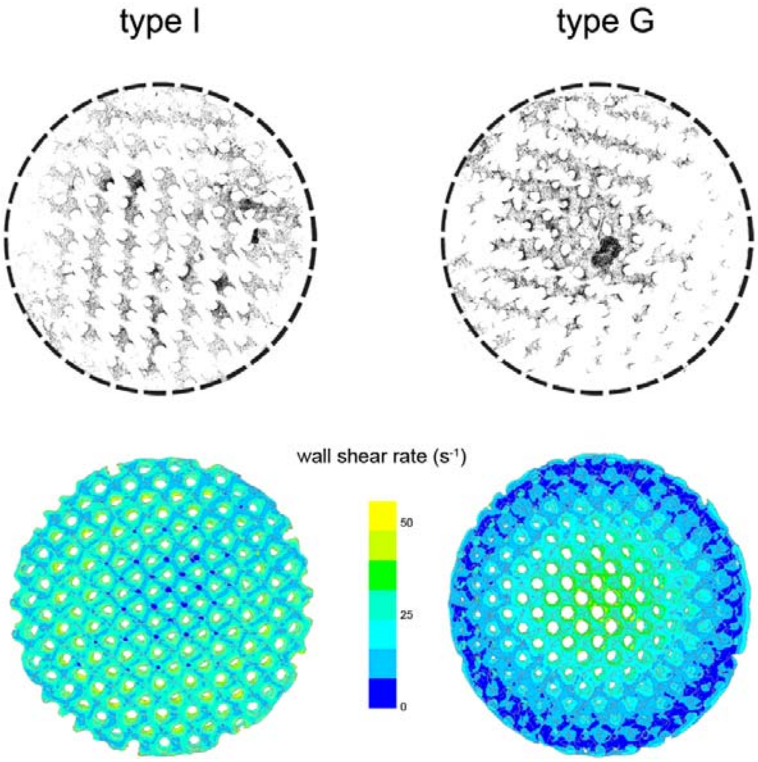

Figure 8.6: Comparison of the distribution of cell densities and wall shear rates in cross-sections of type I (isotropic) and type G (gradient) scaffolds. Top: thresholded z-stacks of confocal microscopy images (500 µm thickness) showing adhering cells after perfusion seeding. Bottom: middle cross-sections of scaffolds showing wall shear rate distributions of the fluid during perfusion cell seeding.

The distribution of adherent cells was quantified by determining the cell density as a function of the distance in radial direction from the scaffold centre. Figure 8.7 depicts the distribution of cell densities as histograms, determined from the thresholded images of the cell densities on the different scaffolds shown in Figure 8.6. Besides the cell distributions, the corresponding modelled local average wall shear rates are shown.

For the isotropic scaffold (type I), a uniform distribution in the cell density and in the modelled average wall shear rate can be observed. The average wall shear rate values are scattered over a relatively small range of 16-24 s^{-1}, the values show no relation with location in the scaffold or cell density. The regular isotropic architecture of the scaffold leads to a uniform distribution of flow and results in very homogeneously seeded scaffolds. The range of shear rates used in the experiments is well suited for perfusion cell seeding of these scaffolds with human articular chondrocytes.

In the gradient type G scaffold, we clearly see anisotropic distributions of seeded cell densities and wall shear rates. Both the cell density and the wall shear rate are high in the centre of the scaffold and much lower at the periphery. The correlation between the cell density and the modelled average wall shear rate is clearly visualised clearly in the bottom right image of Figure 7. It is apparent that the highest cell densities in the seeded scaffolds are observed in regions were the wall shear rate of the fluid flow was highest.

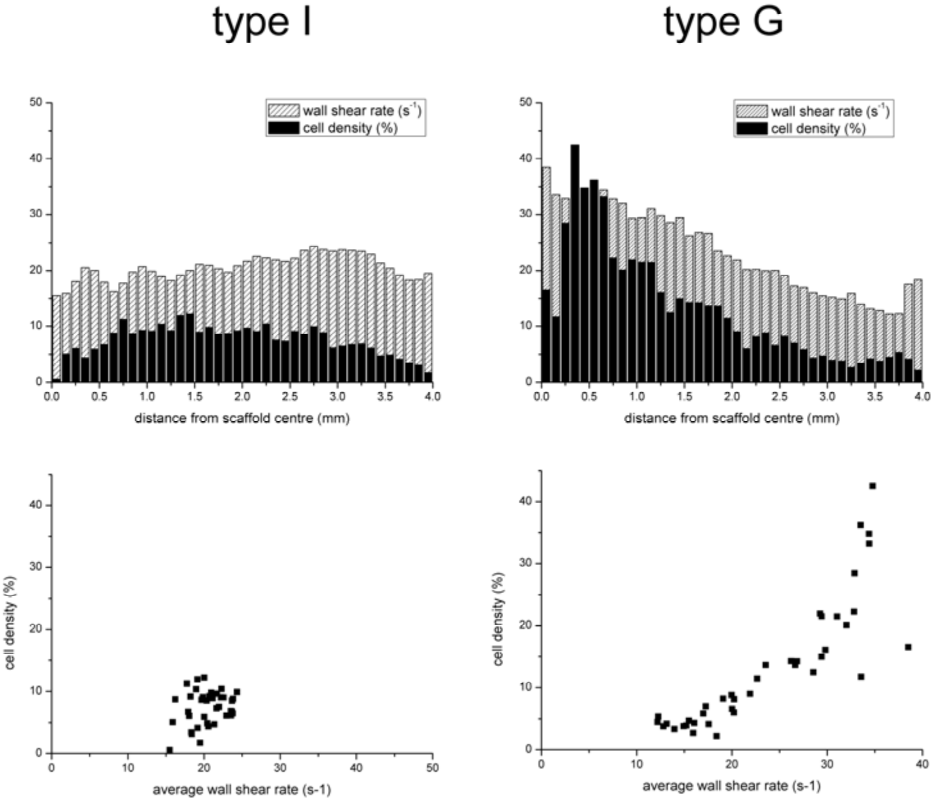

Figure 8.7: Quantitative comparison of the distributions in modelled wall shear rate and cell density in cross-sections of the isotropic type I (left) and gradient type G (right) scaffolds shown in Figure 8.6. Top: distributions of local average wall shear rates (s^{-1}) and of cell densities (expressed as the percentage of the area covered with cells in thresholded confocal microscopy images) as a function of the distance in the radial direction from the scaffold centre. Bottom: scatter plot of the cell density as a function of the modeled local average wall shear rate.

Description of the perfusion cell seeding process

Under flow conditions, the deposition rate of suspended particles on a surface depends on many parameters such as advective transport and diffusivity,[27] colloidal interactions,[28] concentrations of ligands and receptors,[29] binding strengths and bond-forming kinetics[30] and available surface area.[31] Because of the well-defined scaffold architectures and the constant perfusion conditions, many of these parameters do not vary throughout the scaffolds in our perfusion seeding experiments. We can therefore directly assess how flow parameters of the cells suspension affect the final distribution of seeded cells throughout the different scaffolds.

When a cell suspension flows along a ligand-covered surface, cell attachment proceeds as follows:[30] a cell that contacts the scaffold surface is deformed by the flow; thereby the contact area increases. An increased number of receptors on the cell surface are exposed to, and reversibly bind with, ligands on adsorbed proteins on the surface. A cell that has started binding to the surface slows down and starts rolling along the surface, bonds between cell receptors and surface-bound ligands are constantly broken and formed.[32] Finally, the cell is arrested on the surface and starts spreading. As an adhered cell spreads, more receptors face the ligand-covered surface and the number of bonds increases. Moreover, the hydrodynamic forces on the cell decrease as the cell adopts a spread morphology. As a result, in low-shear flow fields the cell will remain firmly adhered.

As in our experiments the flow is laminar, the suspended cells will follow the flow profile (like tracer particles), with minimal advective transport in directions perpendicular to the flow. Only cells close to the pore wall of the scaffold are likely to contact the surface. As the wall shear rate is a measure of the velocity of the cell suspension close to the scaffold pore wall, it determines the number of cells that flow past the surface per unit of time. This correlation is clearly shown in the right parts of Figure 8.7, where the highest cell numbers are close to the centre of the type G scaffold, where wall shear rates are highest.

From this, it follows that we can influence distributions of seeded cells in perfusion seeding by tailoring the architecture of the pore network of the scaffold. In well-defined isotropic gyroid architectures we can obtain very homogeneous distributions of adhering cells, while gradients in pore size and porosity lead to gradients in cell densities. The scaffold architecture affects the local fluid flow velocities of the cell suspension, the number of cell-scaffold contacts per time unit and, therefore, the local cell deposition rates. By preparing other scaffolds with designed architectures, other flow profiles and other cell distributions in the scaffolds may be obtained.

As we have studied only one time-point, the specific kinetics of the cell seeding process can not be derived from our data. For this, cell adhesion experiments using a flow displacement system should be performed as a function of time.[33] Shear rate-dependent adsorption rates can be determined in such experiments. The effect of the three-dimensional architecture of the porous structure could then be investigated separately, and better understanding and control of regional differences in cell deposition could be achieved. Furthermore, critical wall shear stress values could be determined at higher flow rates.

The developed model system enables to experimentally validate theories of mechano-regulation of cell behaviour. These theories are based on computational models, in which the probabilistic behaviour of cells resulting from mechanical stimuli acting at the cellular level is modelled. In this way, cell proliferation and differentiation and extracellular matrix formation could be predicted.[6, 34] Particularly the ability to visualise individual cells and compute their local hydrodynamic environment provides an experimental framework to test, adjust and support these theories.

Conclusions

We have developed a model system to assess the influence of local fluid flow characteristics in designed porous scaffolding structures on the distribution of cells upon perfusion seeding. Under the applied perfusion seeding conditions, maximum values of wall shear stress of 65 mPa are obtained; these very low values do not lead to cell detachment. The density of adhering cells was shown to be determined by the local wall shear rate at the surface of the pore walls of the scaffolds. While scaffolds with an isotropic gyroid pore network architecture show very homogeneous distributions of shear rates and cell seeding densities upon perfusion cell seeding, gyroid scaffolds prepared with gradients in pore size and porosity show anisotropic adherent cell densities. The highest cell densities in the scaffolds could be correlated to regions with larger pores, higher fluid flow velocities and higher wall shear rates. The ability to influence the distribution of seeded cells in a porous structure upon seeding, will be fundamental to control the engineering of complex three-dimensional tissue constructs with defined structural organisations.

Acknowledgements

This work was carried out within the Systems Approach to Tissue Engineering Processes and Products (STEPS) project. We would like to acknowledge the EU for funding.

References

[1] T. J. Klein, J. Malda, R. L. Sah, D. W. Hutmacher, *Tissue Engineering Part B-Reviews* **2009**, *15*, 143.

[2] D. Wendt, S. Stroebel, M. Jakob, G. T. John, I. Martin, *Biorheology* **2006**, *43*, 481.

[3] F. P. W. Melchels, K. Bertoldi, R. Gabbrielli, A. H. Velders, J. Feijen, D. W. Grijpma; Chapter 6 of this thesis.

[4] S. Jadhav, C. D. Eggleton, K. Konstantopoulos, *Current Pharmaceutical Design* **2007**, *13*, 1511.

[5] I. Martin, D. Wendt, M. Heberer, *Trends in Biotechnology* **2004**, *22*, 80.

[6] A. L. Olivares, E. Marshal, J. A. Planell, D. Lacroix, *Biomaterials* **2009**, *30*, 6142.

[7] D. Wendt, A. Marsano, M. Jakob, M. Heberer, I. Martin, *Biotechnology and Bioengineering* **2003**, *84*, 205.

[8] A. Braccini, D. Wendt, C. Jaquiery, M. Jakob, M. Heberer, L. Kenins, A. Wodnar-Filipowicz, R. Quarto, I. Martin, *Stem Cells* **2005**, *23*, 1066.

[9] M. Charles-Harris, M. A. Koch, M. Navarro, D. Lacroix, E. Engel, J. A. Planell, *Journal of Materials Science-Materials in Medicine* **2008**, *19*, 1503.

[10] J. D. Fromstein, P. W. Zandstra, C. Alperin, D. Rockwood, J. F. Rabolt, K. A. Woodhouse, *Tissue Engineering Part A* **2008**, *14*, 369.

[11] J. F. Alvarez-Barreto, S. M. Linehan, R. L. Shambaugh, V. I. Sikavitsas, *Annals of Biomedical Engineering* **2007**, *35*, 429.

[12] E. M. Bueno, G. Laevsky, G. A. Barabino, *Journal of Biotechnology* **2007**, *129*, 516.

[13] M. Cioffi, J. Kuffer, S. Strobel, G. Dubini, I. Martin, D. Wendt, *Journal of Biomechanics* **2008**, *41*, 2918.

[14] F. P. W. Melchels, J. Feijen, D. W. Grijpma, *Biomaterials* **2009**, *30*, 3801; Chapter 4 of this thesis.

[15] A. H. Schoen, Nasa Technical Note, NASA-TN-D-5541 **1970**.

[16] H. A. Schwarz, *Gesammelte Mathematische Abhandlungen*, Springer-Verlag, Berlin **1890**.

[17] M. Morigi, C. Zoja, M. Figliuzzi, M. Foppolo, G. Micheletti, M. Bontempelli, M. Saronni, G. Remuzzi, A. Remuzzi, *Blood* **1995**, *85*, 1696.

[18] J. Ando, K. Yamamoto, *Circulation Journal* **2009**, *73*, 1983.

[19] J. E. Rosenman, R. F. Kempczinski, W. H. Pearce, E. B. Silberstein, *Journal of Vascular Surgery* **1985**, *2*, 778.

[20] P. Feugier, R. A. Black, J. A. Hunt, T. V. How, *Biomaterials* **2005**, *26*, 1457.

[21] B. C. Isenberg, C. Williams, R. T. Tranquillo, *Annals of Biomedical Engineering* **2006**, *34*, 971.

[22] D. K. Macario, I. Entersz, J. P. Abboud, G. B. Nackman, *Journal of Surgical Research* **2008**, *147*, 282.

[23] R. L. Smith, B. S. Donlon, M. K. Gupta, M. Mohtai, P. Das, D. R. Carter, J. Cooke, G. Gibbons, N. Hutchinson, D. J. Schurman, *Journal of Orthopaedic Research* **1995**, *13*, 824.

[24] G. VunjakNovakovic, L. E. Freed, R. J. Biron, R. Langer, *Aiche Journal* **1996**, *42*, 850.

[25] B. S. Kim, A. J. Putnam, T. J. Kulik, D. J. Mooney, *Biotechnology and Bioengineering* **1998**, *57*, 46.

[26] J. Xie, Y. Jung, S. H. Kim, Y. H. Kim, T. Matsuda, *Tissue Engineering* **2006**, *12*, 1811.

[27] Z. Adamczyk, T. G. M. Vandeven, *Journal of Colloid and Interface Science* **1981**, *80*, 340.

[28] J. Sjollema, H. J. Busscher, *Journal of Colloid and Interface Science* **1989**, *132*, 382.

[29] C. Cozensroberts, J. A. Quinn, D. A. Lauffenburger, *Biophysical Journal* **1990**, *58*, 107.

[30] D. A. Hammer, D. A. Lauffenburger, *Biophysical Journal* **1987**, *52*, 475.

[31] J. M. Meinders, H. J. Busscher, *Colloid and Polymer Science* **1994**, *272*, 478.

[32] D. A. Hammer, S. M. Apte, *Biophysical Journal* **1992**, *63*, 35.
[33] H. J. Busscher, H. C. van der Mei, *Clinical Microbiology Reviews* **2006**, *19*, 127.
[34] C. Sandino, S. Checa, P. J. Prendergast, D. Lacroix, *Biomaterials* **2009**, *In Press*.

Chapter 9 - Designed biodegradable poly(ethylene glycol)/poly(D,L-lactide)-based hydrogel structures prepared by stereolithography

Tetsu Seck[1], Ferry Melchels[2], Jan Feijen[2] and Dirk Grijpma[2, 3]

Designed three-dimensional biodegradable poly(ethylene glycol)/poly(D,L-lactide) hydrogel structures were prepared for the first time by stereolithography at high resolutions. A photo-polymerisable aqueous resin comprising PDLLA-PEG-PDLLA-based macromer, visible light photo-initiator, dye and inhibitor in DMSO/water was used to build the structures. Porous and non-porous hydrogels with well-defined architectures and good mechanical properties were prepared. Porous hydrogel structures with a gyroid pore network architecture showed narrow pore size distributions, excellent pore interconnectivity and good mechanical properties. The structures showed good cell seeding characteristics, and human mesenchymal stem cells adhered and proliferated well on these materials.

---

[1] Institute of Organic Chemistry, Johannes Gutenberg Universität Mainz, Duesbergweg 10-14, D-55099 Mainz, Germany

[2] MIRA Institute for Biomedical Technology and Technical Medicine, and Department of Polymer Chemistry and Biomaterials, University of Twente, P.O. Box 217, 7500 AE, Enschede, The Netherlands

[3] Department of Biomedical Engineering, University Medical Centre Groningen and University of Groningen, P.O. Box 196, 9700 AD Groningen, The Netherlands

Introduction

The origins of stereolithography date back to the 1980s.[1] Of all rapid prototyping methods, stereolithography is the most developed technique with the highest accuracy. Three-dimensional designed constructs can be precisely fabricated in a layer-by-layer manner. Its working principle is based on the spatially controlled solidification of a liquid photo-polymerisable resin upon illumination with a computer-driven light source. Most commercially available resins for use in stereolithography are conventional epoxy- or acrylate-based resins. In preparing biomedical implants their use is limited, as these materials are usually not biocompatible or biodegradable. To prepare biocompatible and biodegradable network structures, macromers based on trimethylene carbonate (TMC) and ε-caprolactone,[2,3] on poly(propylene fumarate)[4,5] and on poly(D,L-lactide) (PDLLA)[6,7] have been developed.

Hydrogel structures prepared from polyethylene glycol (PEG)-based resins have also been fabricated using stereolithography.[8-10] The biocompatibility of these hydrogel structures was excellent, and allowed the encapsulation of living cells. However, the structures were not biodegradable. Polyethylene glycol itself is a stable hydrophilic polymer, but it can be excreted by the kidneys at molecular weights up to 30 kg/mol.[11] Poly(D,L-lactide) is a hydrophobic polyester with a glass transition temperature (T_g) of approximately 55 °C, and in contrast to PEG, can degrade by hydrolytic cleavage of the main chain ester bonds. Highly biocompatible hydrogels that degrade in the body can be prepared by crosslinking macromers based on block copolymers of PEG and PDLLA.[12]

In this chapter we describe the synthesis of PDLLA-PEG-PDLLA-based macromers, the resin formulation, and the photo-polymerisation process by stereolithography that allows the generation of designed three-dimensional crosslinked structures. The obtained hydrogel structures are characterised and seeded with mesenchymal stem cells, to evaluate cell adhesion and proliferation behaviour.

Experimental

Materials

D,L-Lactide was purchased from Purac Biochem (The Netherlands). Polyethylene glycol (PEG4k, with a molecular weight of 4 kg/mol) was supplied by Fluka. Stannous octoate (tin(II) bis(2-ethylhexanoate), $Sn(Oct)_2$ was obtained from Sigma Aldrich (USA). Methacrylic anhydride (MAAH) was purchased from Merck (Germany). Triethyl amine (TEA) was obtained from Fluka (Switzerland). Lucirin

TPO-L (ethyl-2,4,6-trimethylbenzoyl phenylphosphinate) was a gift from BASF (Germany). Phenol red was supplied by Riedel de Haën. Diethyl ether, dimethyl sulfoxide (DMSO), analytical grade isopropanol and dichloromethane (DCM) were supplied by Biosolve (The Netherlands). Dichloromethane was dried over calcium hydride (Acros Organics, Belgium) and filtered prior to use.

Alpha-Modified Eagle's Medium (α-MEM), foetal bovine serum (FBS), L-glutamine, penicillin-streptomycin and trypsin were obtained from Lonza (Belgium). Phosphate-buffered saline (PBS) was purchased from Invitrogen (USA). MTT (3-(4,5-dimethyl-2-thiazolyl)-2,5-diphenyl tetrazolium bromide) was obtained from Sigma Aldrich (USA).

Synthesis of PDLLA-PEG-PDLLA oligomers and macromers

PDLLA-PEG-PDLLA oligomers were prepared by ring opening polymerisation of D,L-lactide initiated from the terminal hydroxyl groups of PEG4k, in the presence of $Sn(Oct)_2$ as a catalyst (Figure 9.1A). The targeted molecular weights of the oligomers were between 4500 and 5000 g/mol. Using 600 W microwave irradiation, the PEG oligomer was first molten (3 min), the D,L-lactide monomer and the $Sn(Oct)_2$ catalyst were then mixed in and reacted for another minute at 600 W. The oligomers were precipitated in isopropanol and dried under reduced pressure for 3 days at room temperature. When monomer conversion of the oligomers was less than 95 %, the product was further purified by dissolution in chloroform and precipitation into diethyl ether. Otherwise, the oligomers were used without further purification in the subsequent functionalisation reactions.

Macromers were prepared by reacting the terminal hydroxyl groups of the PDLLA-PEG- PDLLA oligomers with methacrylic anhydride (Figure 9.1B). Under an argon atmosphere, the required amounts of oligomer were charged into a three-necked flask and methacrylic anhydride (100 % excess), dry DCM and TEA were added. The reaction was let to proceed at room temperature for 7 d, while continuously stirring the mixture. The formed MA-DLLA-PEG-DLLA-MA macromers were then precipitated into diethyl ether, and purified by dissolving in chloroform and precipitating once more into diethyl ether. In a similar manner, MA-PEG-MA macromers were prepared.

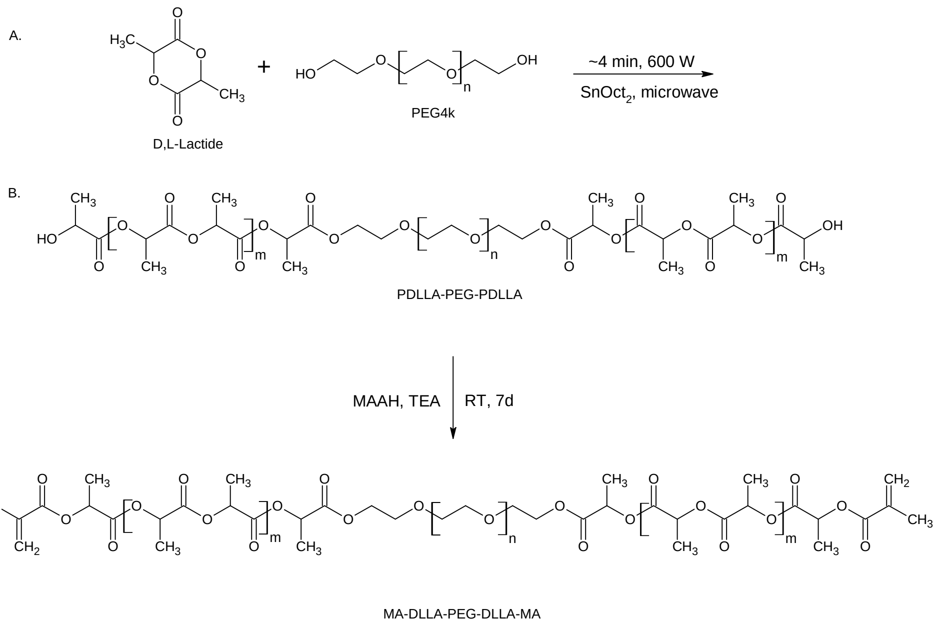

Figure 9.1: Synthesis of PDLLA-PEG-PDLLA oligomers (A) and subsequent functionalisation with methacrylic anhydride (MAAH) to give MA-DLLA-PEG-DLLA-MA macromers (B).

Formulation of a stereolithography resin and building of hydrogel structures

To formulate a liquid photo-polymerisable resin for use in stereolithography, the MA-DLLA-PEG-DLLA-MA macromer and the phenol red dye were first dissolved in water. Lucirin TPO-L (visible light photo-initiator) is water-insoluble, and was dissolved in DMSO. Then, the photo-initiator solution was mixed in with the macromer solution and stirred for 20 h at room temperature in order to obtain a clear liquid resin. The resin composition was: 54 wt% water, 33 wt% macromer, 11 wt% DMSO, 1.7 wt% photo-initiator and 0.19 wt% phenol red. To prevent premature crosslinking, 0.1 wt% hydroquinone was added.

The formulated PDLLA-PEG-PDLLA resin was used to prepare biodegradable hydrogel structures by stereolithography. Using a Perfactory Mini Multilens stereolithography apparatus (EnvisionTec, Germany), non-porous hydrogel structures in the shape of disks and films were prepared. Also porous hydrogel structures with a continuous gyroid pore network architecture were built. The structures were designed using Rhinoceros 3D (McNeel Europe) and K3DSurf computer software as described elsewhere.[7]

The stereolithography apparatus (SLA) is equipped with a digital micro-mirror device that enables projections of 1280 x 1024 pixels, each measuring 32 x 32 μm^2. Using a build platform step height of 15 μm, layers of resin were sequentially photo-crosslinked by exposure to a pixel pattern of blue light (wavelength 400 - 550 nm, peak intensity at 440 nm). The fabrication of the hydrogel structures was carried out by exposing the photo-polymerisable resin to light intensities of 20 mW/cm^2. The curing time per 15 μm thick layer was 32.5 s. After photo-polymerisation, the obtained structures were extracted with distilled water to remove soluble compounds and dried at ambient conditions for 3 d. Structures were also prepared by stereolithography using MA-PEG-MA materials.

Characterisation of oligomers, macromers and network structures

Proton nuclear magnetic resonance (^{1}H-NMR) spectra of the reaction products were recorded on a Varian Inova 300 MHz NMR spectrometer and used to determine monomer conversion, oligomer molecular weight and extent of functionalisation. $CDCl_3$ was used as the solvent. The thermal properties of oligomers, macromers and network structures prepared by stereolithography were evaluated using a Perkin Elmer Pyris 1 differential scanning calorimeter (DSC) connected to a liquid nitrogen cooling accessory. Oligomer, macromer and network specimens were heated from -100 °C to +100 °C at a heating rate of 10 °C/min and then quenched at a cooling rate of 100 °C/min, after which a second scan was run. The melting points and -enthalpies were determined in the first heating scan, while the glass transition temperatures were determined in the second scan.

To determine the degree of swelling of the photo-crosslinked networks, specimens of extracted fabricated structures were dried for 3 d at ambient conditions and weighed (w_0) before placing them in distilled water for 3 d. The specimens were blotted dry and weighed again (w_s). The degree of swelling is defined as:

$$Q = 1 + \frac{w_s - w_0}{w_0} \times \frac{\rho_p}{\rho_w}$$

where ρ_p is the density of the polymer (g/mL) and ρ_w the density of water (g/mL).

Porous and non-porous hydrogel structures measuring approximately 8 mm in diameter and 5 mm in height were prepared by stereolithography. Their mechanical properties were determined in compression using a Zwick Z020 mechanical tester after swelling in water, and after drying at room temperature for 3 d.

Structural analysis of porous structures built by stereolithography was performed using micro-computed tomography (μCT) on a GE eXplore Locus SP scanner at 14 μm resolution after conditioning the specimens in the ambient environment. GE Healthcare MicroView 2.2 software was used to assess porosities and pore size distributions.

To demonstrate the hydrolytic degradability of the PDLLA-PEG-PDLLA hydrogels, degradation experiments were conducted using 1 M NaOH solutions (pH 14) at room temperature. For comparison, photo-crosslinked PEG-dimethacrylate hydrogels, which do not contain a hydrolysable lactide linkage, were also incubated in the NaOH solutions.

Cell culturing experiments

Human mesenchymal stem cells (hMSC) were used in the experiments. The cells were cultured in 175 cm^2 cell culturing flasks that contained alpha-Modified Eagle's Medium (α-MEM) in a humidified 5 % CO_2 atmosphere at 37 °C. The medium was refreshed twice a week until the cells reached confluency, then they were trypsinised and counted.

Porous hydrogel scaffolds and non-porous hydrogel films were sterilised with 70 % ethanol for 3 h, washed 3 times with phosphate buffered saline (PBS) and left overnight in medium containing 10 % FBS. The hydrogel structures were then extensively washed with PBS, and placed in non-treated 24-well plates. The hMSC cells were seeded on the films, and on top of and inside the porous scaffolds (10^6 cells each). Fresh medium was added until the surfaces were fully covered. The cell-seeded films and scaffolds were kept at 37 °C for 1 d to allow cell attachment (porous scaffolds and films) and 5 d (films) to assess cell proliferation. As a control, the cells were also cultured on tissue culture polystyrene (TCPS) after seeding at the same cell density.

The morphology and distribution of hMSC cells in the attachment and proliferation experiments was assessed by light microscopy and scanning electron microscopy (SEM). The culture medium was removed, after which the samples were washed twice with PBS and fixed with 1.5 % glutaraldehyde in 0.14 M sodium cacodylic acid buffer pH 7.3 for 30 min at room temperature. Dehydration was performed with a series of ethanol solutions of increasing concentration beginning with 70 % and progressing through 80 %, 90 %, 96 % and 100 % ethanol. The samples were kept in absolute ethanol, transferred to the critical point dryer and dried using CO_2. Then, the samples were gold-sputtered and analysed using a Philips XL 30 ESEM- FEG.

Results and discussion

Synthesis of PDLLA-PEG-PDLLA oligomers and macromers

PDLLA-PEG-PDLLA oligomers could be conveniently prepared by conducting D,L-lactide ring opening polymerisation initiated by poly(ethylene glycol) using microwave irradiation. At an intensity of 600 W only 4 min reaction time was required. The chemical structure of the synthesised oligomers was confirmed by

NMR; a peak at δ 4.2-4.3, corresponding to methylene protons of the PEG connected to PDLLA could be discerned (Figure 9.2, upper spectrum). The average block length *n* of the PDLLA blocks was calculated by assigning the respective areas of the peaks corresponding to the methyl group of lactyl units (d in Figure 9.2, upper spectrum) and the methylene groups of PEG (a in Figure 9.2, upper spectrum). From the values of *n*, molecular weights (M_n) ranging from 4550 to 4620 g/mol were calculated. The conversion of the PEG hydroxyl groups was 88 to 100 %.

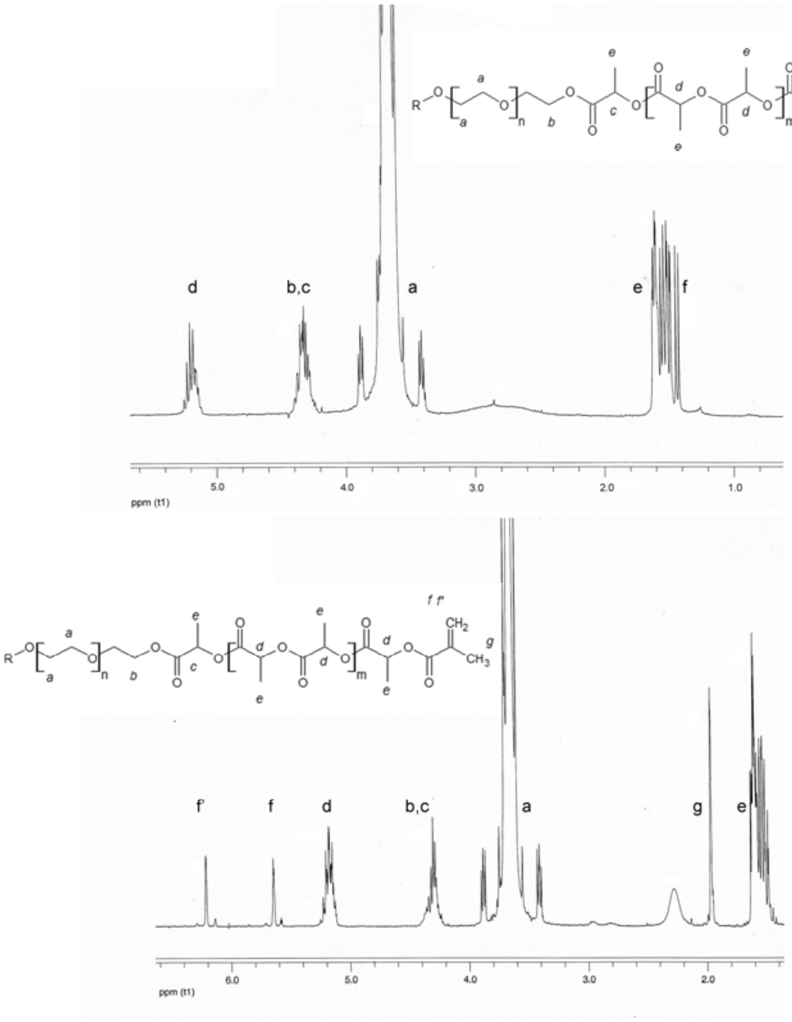

Figure 9.2: ^{1}H-NMR spectra of a PDLLA-PEG-PDLLA oligomer (upper) and the corresponding MA-DLLA-PEG-DLLA-MA macromer (lower) after functionalisation with methacrylic anhydride. In the chemical structures, only half of the molecule is depicted.

The hydroxyl end groups of the synthesised PDLLA-PEG-PDLLA oligomers were reacted with methacrylic anhydride to obtain MA-DLLA-PEG-DLLA-MA macromers. The coupling of MAAH to PDLLA-PEG-PDLLA was confirmed by the appearance of three peaks in the spectra of the macromers: at δ 6.21 (f'), δ 5.64 (f) and δ 1.97 (g) corresponding to the $=CH_2$ (f', f) and $–CH_3$ (g) of the methacrylate groups (Figure 9.2, lower spectrum). The degree of functionalisation was determined by comparing the integrals of the peaks corresponding to the methylene protons of the methacrylate group (δ 6.21 and 5.64) with those of the methylene protons of PEG (a at δ 3.65). A degree of functionalisation of 100 % was achieved. This implies that besides MA-PDLLA-PEG-PDLLA-MA triblock macromers, also small fractions of MA-DLLA-PEG-MA diblock copolymers and MA-PEG-MA macromers are formed.

The thermal properties of the oligomers and macromers were determined by DSC. Values of molecular weights (M_n, determined by NMR) and of melting points (T_m), melting enthalpies (ΔH_m) and glass transition temperatures (T_g) of the compounds are presented in Table 9.1. The block copolymerisation of PEG with short D,L-lactide blocks and the subsequent functionalisation with methacrylate groups leads to a small increase in molecular weight of the oligomers. The D,L-lactide block copolymerisation hinders crystallisation, which leads to lower melting temperatures and heats of fusion. As the T_g of PDLLA is approximately 55 °C, this value increases somewhat. Upon functionalisation using MAAH, the T_g of the macromer decreases only slightly.

Table 9.1: Molecular weights (M_n), melting points (T_m), melting enthalpies (ΔH_m) and glass transition temperatures (T_g) of synthesised PDLLA-PEG-PDLLA oligomers and macromers. The values of PEG4k are given as a reference.

	M_n (kg/mol)	T_m (°C)	ΔH_m (J/g)	T_g (°C)
PEG4k	4.1	63.0	190	-40
PDLLA-PEG-PDLLA oligomer	4.6	49.4	136	-30
MA-DLLA-PEG-DLLA-MA macromer	4.8	49.9	135	-32

Biodegradable hydrogel structures prepared by stereolithography

In order to build designed biodegradable hydrogel structures, a PDLLA-PEG-PDLLA based photo-polymerisable resin was formulated. The mixture contained 33 wt% MA-DLLA-PEG-DLLA-MA macromer, 1.7 wt% Lucirin TPO-L (photo-initiator), 0.19 wt% phenol red (colorant), 0.1 wt% hydroquinone (to prevent premature crosslinking), 54 wt% water and 11 wt% DMSO.

In stereolithography, the liquid photo-polymerisable resin is exposed to a light source in order to be cured in a layer-by–layer manner. The thickness of a solidified layer (cure depth C_d in μm) is controlled by the light irradiation dose E (mJ/cm^2). A plot of the cure depth versus the natural logarithm of the energy ln(E) yields a straight line, with slope D_P and intercept E_C. This curve is known as a working curve and is represented by the following equation:[13]

$$C_d = D_p \ln \frac{E}{E_c}$$

The critical exposure or critical energy (E_C in mJ/cm^2) and penetration depth (D_P in μm) are considered fundamental properties of each photo-polymerisable resin formulation. E_C represents the minimum energy level required to transform the resin from liquid to solid. D_P describes the penetration depth of light into the photo-polymer resin, and therefore the increase of cured layer thickness with exposed energy.[14] If a layer is not cured deep enough, the interlayer bonding fails and delamination occurs. On the other hand, if the exposure is too much, inaccuracies and deviations from the designed architecture occur. To determine the most suitable parameters for the building process, E_C and D_P need to be evaluated. This can be done experimentally by measuring the depth of the solidified photo-polymer at different exposure values.

Working curves for different resin compositions were determined by varying the light exposure at the resin surface (E) and measuring the resulting cure depths (C_d) of the resins. We observed that the penetration depth (D_P) of the resin decreased from 58 μm to 15 μm upon addition of 0.19 wt% phenol red (Figure 9. 3). The addition of the dye to the resin is very important; as the penetration depth decreases, control over the layer thickness becomes better and more precise. The required curing time per 15 μm thick layer was 32.5 seconds at a light intensity of 20 mW/cm^2.

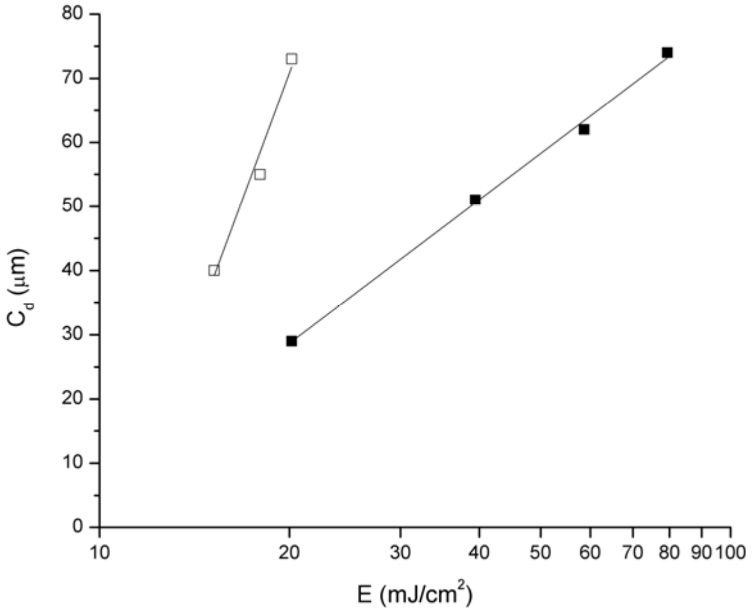

Figure 9.3: Stereolithography working curves of PDLLA-PEG-PDLLA macromer-based resins containing 0.19 wt% dye (phenol red ■) and not containing dye (□). Note the logarithmic scale of the x-axis.

Designed hydrogel structures were prepared in the stereolithography apparatus using the MA-PDLLA-PEG-PDLLA-MA resin containing 0.19 wt% phenol red dye. Solid structures as well as porous scaffolds were built (Figure 9.4). Due to the phenol red, the colour of the hydrogels scaffolds varies between orange and yellow. The intensity of the colour depends on the time of extraction. The built hydrogel structures were soft and highly flexible, their shape and structure precisely matched their design.

In the photographs, the porosity and the regularity of the gyroid pore network structure of the porous hydrogel scaffolds can be readily recognised. The gyroid architecture is mathematically defined, allowing precise control of porosity and pore size of a fully interconnected pore network.[15] Gyroid structures have a large specific surface area and high pore interconnectivity. These characteristics are quite important for cell seeding and proliferation at high cell densities, ensuring homogeneous distributions of cells and unhindered transport of nutrients throughout the scaffolds.

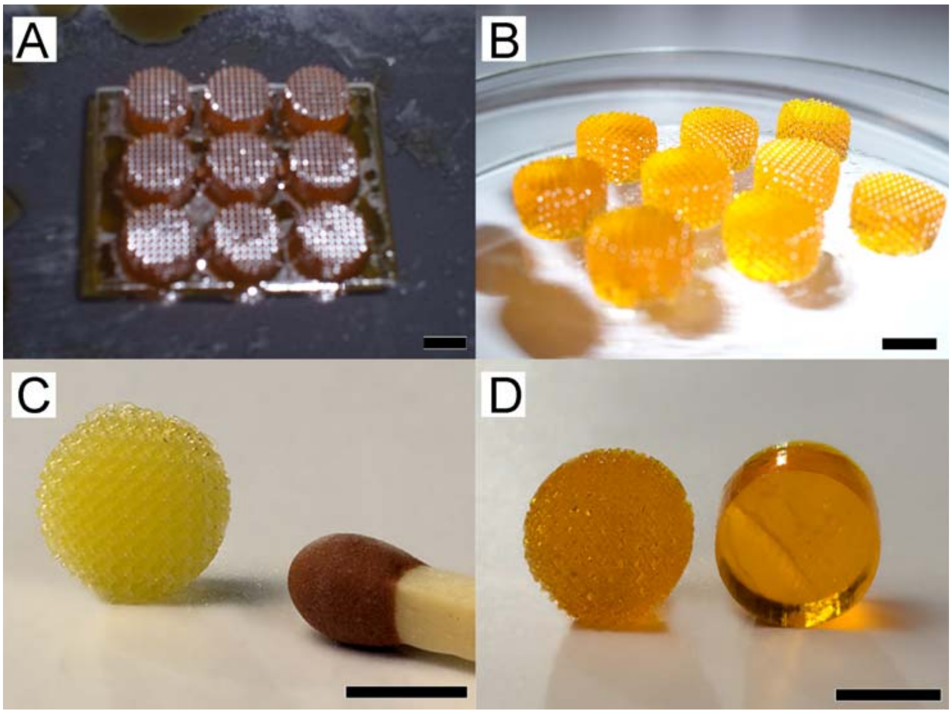

Figure 9.4: Hydrogel scaffolds built by stereolithography using a MA-PDLLA-PEG-PDLLA-MA based resin. (A) Porous gyroid hydrogel scaffolds on a build platform immediately after the photo-polymerisation process. (B) Hydrogel scaffolds after washing with water to remove uncured resin from the pore network. (C) Hydrogel scaffold with gyroid pore network design after several days of extraction. (D) Cylinder-shaped porous (left) and solid (right) hydrogel scaffolds after extraction for several hours. Scale bars are 5 mm.

Micro-computed tomography (μCT) was used to assess structural parameters of the pore network architecture of the built scaffolds. Figure 9.5 depicts μCT images of two built porous structures with gyroid pore network architectures after drying at ambient conditions. As can be clearly seen in the images, this architectural design and the fidelity of the stereolithography technique in building the designed structures has allowed precise control of porosity and pore size of the fully interconnected pore network of the porous hydrogel structure. From the μCT data a porosity of 52 % was determined, while the porosity of the designed architecture was 55 %.

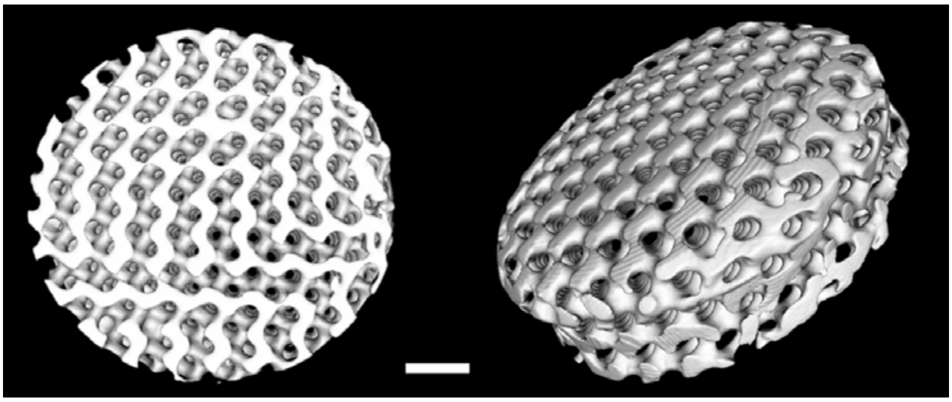

Figure 9.5: Three-dimensional images reconstructed from μCT analyses of designed hydrogel structures prepared from PDLLA-PEG-PDLLA based macromers by stereolithography. Scalebar is 1 mm.

The pore size distribution of the gyroid pore network architecture in the built hydrogel structures is visualised in Figure 9.6. As a result of the regularity of the design and the precision of the building technique employed, the histogram shows a narrow pore size distribution. The average pore size was 423 μm, and pore sizes ranging from 387 to 558 μm account for more than 76 % of the pore volume.

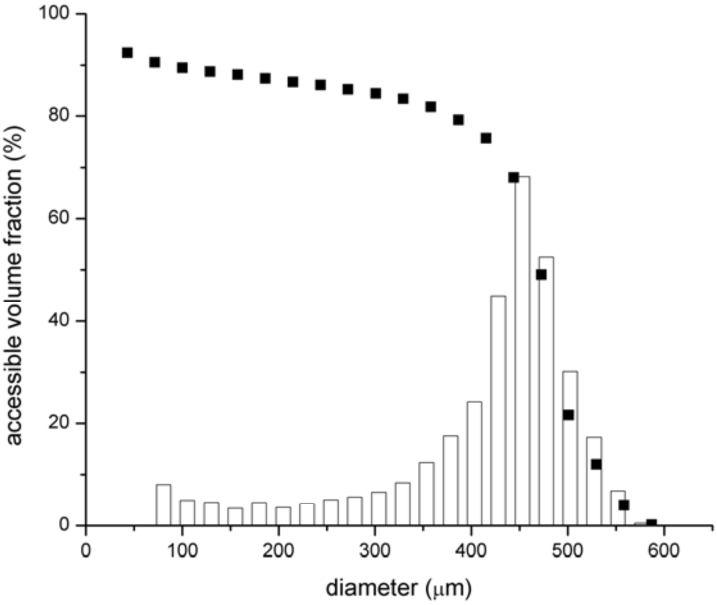

Figure 9.6: Pore size distribution (histogram) and accessible pore volume (black squares) of porous hydrogel structures with a gyroid pore network architecture prepared by stereolithography.

To quantify the interconnectivity of the pore network, the accessible pore volume was determined. This was done by simulating the permeation of a spherical particle.[6] The figure shows the accessible pore volume (as a fraction of the total pore volume) versus the diameter of the permeating particle. More than 90 % of the pore volume in the built structures is connected to the outsides of the scaffolds with pores and channels of sizes of the order of magnitude of cells. The specific surface area of the porous structures, to which cells can attach upon cell seeding in tissue engineering applications, could also be obtained from the μCT-data: a high value of 6.23 mm^2/mm^3 was determined for these scaffolds.

With these results we have demonstrated that using a MA-PDLLA-PEG-PDLLA-MA macromer based resin, designed hydrogel structures with narrow pore size distributions and high pore interconnectivities can be prepared by stereolithography.

Properties of biodegradable PDLLA-PEG-PDLLA hydrogel structures built by stereolithography

The thermal properties of the prepared network structures were measured in the dry and in the wet state. By DSC, the melting temperature of the dry network was 45 °C and the heat of fusion 68 J/g; a glass transition temperature could not be detected. No crystallinity could be detected in the wet state, but a glass transition temperature of -67 °C could be determined. Upon equilibration in water, large amounts of water are taken up by the built hydrogel structures. The degree of swelling of non-porous PDLLA-PEG-PDLLA hydrogel structures was 7.39 ± 0.1, while that of the porous gyroid structures was 11.5 ± 0.3. Note that in the later determinations water may still have been present within the pore network of the porous gyroid structures. In any case, it is clear that the presence of the short hydrophobic PDLLA segments in the networks does not severely hinder the uptake of water.

When the hydrogel structures prepared from the PDLLA-PEG-PDLLA based macromers were immersed in a 1 M NaOH solution (pH 14), the networks very rapidly degraded and clear solutions were obtained in approximately 5 s. This implies that the ester bonds in the short PDLLA blocks are available to water and can be readily hydrolysed. In demineralised water, hydrolysis is much slower and the hydrogels remained unchanged for several weeks. Hydrogel structures prepared from MA-PEG-MA macromers that do not contain degradable PDLLA ester bonds were very stable, and did not degrade at pH 14 in the course of several days.

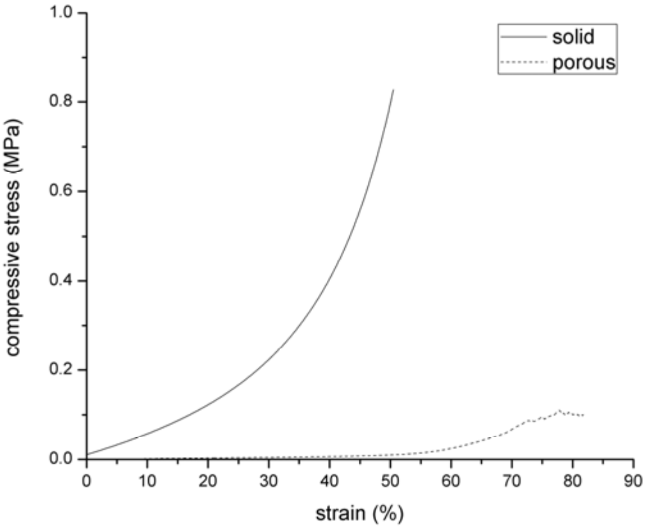

Figure 9.7: Mechanical properties in the wet state of non-porous and porous hydrogel structures fabricated by stereolithography using PDLLA-PEG-PDLLA based macromers. E-modulus values: non-porous structures 420 kPa, porous structures with gyroid pore network architecture 14 kPa.

The mechanical properties of the porous and non-porous hydrogel structures fabricated by stereolithography were evaluated in the wet and in the dry state in compression tests. The compressive stress-strain curves in the wet state are presented in Figure 9.7. The porosity of a structure has a large influence on its mechanical properties; it can be observed that the E-modulus and compressive strength of a non-porous water-swollen hydrogel is very much higher than that of the hydrated porous hydrogels with gyroid pore network architecture. (The compression modulus values for the non-porous and the porous water swollen hydrogels are respectively 420 kPa and 14.0 kPa.) However, the porous structures show higher maximal deformations than the solid structures; the solid scaffolds fragmented into small pieces at 50 % strain, while the porous scaffolds could be compressed to more than 80 % (first damage occurring after 70 %, the structures behave elastically before reaching this value).

In the dry state (after drying at 90 °C for 2 d) the mechanical properties of the built PDLLA-PEG-PDLLA structures are very different than those in the wet state, although here too porosity has a large effect on the mechanical properties. The E-modulus values for the dry non-porous and porous structures are respectively 154 MPa and 7.35 MPa. It is evident that regarding their use as implants, the properties of the network structures in their wet state are most relevant.

Cell adhesion and proliferation on PDLLA-PEG-PDLLA-based structures built by stereolithography

To evaluate their compatibility with cells, human mesenchymal stem cells were cultured on non-porous hydrogel films and on porous hydrogel structures prepared from PDLLA-PEG-PDLLA based macromer resins by stereolithography. Cell morphology was assessed by scanning electron microscopy SEM. Although PEG is a polymer that is known to minimise the adhesion of cells to surfaces, we observed that hMSCs were able to attach to the surfaces of MA-PDLLA-PEG-PDLLA-MA based structures prepared by stereolithography. Before cell-seeding, the hydrogel structures were incubated in culture medium that contained 10 % FBS overnight. This could have lead to adsorption of proteins in the medium that might provide attachment sites for the cells. Nevertheless, the presence of hydrophobic PDLLA segments in the network structure might also have diminished the suppressive effect of the hydrophilic PEG on the adhesion and proliferation of cells on the network surfaces. Figures 9.8A and 9.8B show light microscopy images of hMSCs attaching to the surface of the porous hydrogel scaffolds after 24 h. The pores are black, while the bright areas show light coming through the walls of the scaffold. The attaching cells are better recognised in the right picture (Figure 9.8B).

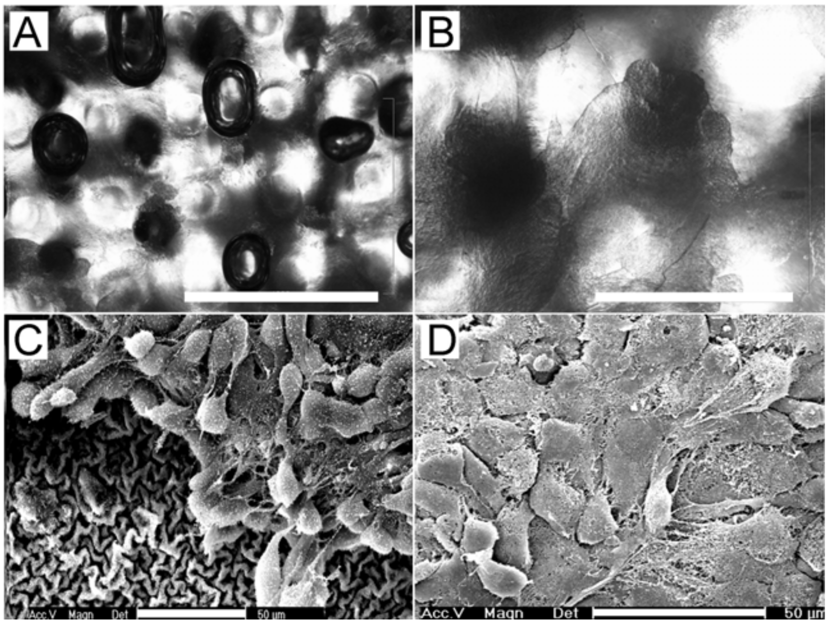

Figure 9.8: (A, B) Light microscopy images of the attachment of hMSCs after 24 hrs on porous PDLLA-PEG-PDLLA-based hydrogel scaffolds prepared by stereolithography. (C) Cell attachment after 24 hrs of hMSCs on PDLLA-PEG-PDLLA-based hydrogel films prepared by stereolithography. (D) Cell proliferation of hMSC (after 5 days) on PDLLA-PEG-PDLLA-based hydrogel films prepared by stereolithography. Scale bars are 1 mm (A, B) and 50 μm (C, D).

To distinguish their morphology in more detail, SEM pictures were made of hMSCs seeded on hydrogel films that were also prepared by stereolithography. In these experiments with PDLLA-PEG-PDLLA hydrogel films, the attachment of hMSCs and proliferation was evaluated. Figure 9.8C illustrates the attachment of cells on hydrogel films at day 1, while Figure 9.8D shows their proliferation after five days. The adhering hMSCs cells showed a spread morphology, although it seems that the cells have a tendency to aggregate. This might be due to the lack of proteins that support cell attachment; Stupack *et al.* have shown that in the absence of interaction with the matrix, cells undergo apoptotic progression.[16]

We have demonstrated the suitability of these PDLLA-PEG-PDLLA-based hydrogel structures prepared by stereolithography in cell culturing. To ensure even better cell attachment and cell proliferation within the pore network of the hydrogel structures, cell-binding ligands such as RGD-containing peptide sequences could be incorporated. This can be done for example by Michael addition reactions of cystein thiol groups with unreacted methacrylate groups present in the network.

Future work will address the encapsulation of living cells within the matrix of the designed hydrogel networks. This seems quite feasible, as preliminary experiments showed that the viability of hMSC cells that were exposed to the non-crosslinked resin for 24 h was approximately 70%.

Conclusions

We have successfully used stereolithography to fabricate designed three-dimensional porous and non-porous biodegradable hydrogel structures at high resolutions. For this an aqueous photo-curable resin based on methacrylate-functionalised poly(ethylene glycol)/poly(D,L-lactide) macromers and Lucirin TPO-L as a visible light photo-initiator was developed. After the building process and extracting with water to remove unreacted components, the crosslinked network structures closely matched their design. In compression experiments, the specimens showed very good mechanical properties similar to those of soft tissues. The porous hydrogel structures had a well-defined pore network architecture, with narrow pore size distribution and high interconnectivity of the pores. Good pore interconnectivity is a prerequisite for efficient cell-seeding and -proliferation, and transport of nutrients and metabolites during cell culturing in three-dimensional structures.

The resin and the built structures were compatible with cells. Upon seeding, human mesenchymal stem cells attached to the surfaces of the hydrogel structures and showed a spread morphology. After five days in culture, proliferation of the cells was observed. Suitable applications of these hydrogel structures could therefore be in tissue engineering, drug delivery, cell-transplantation and other biomedical applications.

Acknowledgements

We would like to acknowledge Sandra Teixeira for her help in the cell work, prof. dr. Holger Frey for supporting the Erasmus exchange project of the first author, and the EU for funding (STEPS project, FP6-500465).

References

[1] S. Upcraft, R. Fletcher, *Assembly Automation* **2003**, *23*, 318.
[2] I. K. Kwon, T. Matsuda, *Biomaterials* **2005**, *26*, 1675.
[3] T. Matsuda, M. Mizutani, *Journal of Biomedical Materials Research* **2002**, *62*, 395.
[4] M. N. Cooke, J. P. Fisher, D. Dean, C. Rimnac, A. G. Mikos, *Journal of Biomedical Materials Research Part B-Applied Biomaterials* **2003**, *64B*, 65.
[5] K. W. Lee, S. F. Wang, B. C. Fox, E. L. Ritman, M. J. Yaszemski, L. C. Lu, *Biomacromolecules* **2007**, *8*, 1077.
[6] J. Jansen, F. P. W. Melchels, D. W. Grijpma, J. Feijen, *Biomacromolecules* **2009**, *10*, 214; Chapter 3 of this thesis.
[7] F. P. W. Melchels, J. Feijen, D. W. Grijpma, *Biomaterials* **2009**, *30*, 3801; Chapter 4 of this thesis.
[8] G. Mapili, Y. Lu, S. C. Chen, K. Roy, *Journal of Biomedical Materials Research Part B-Applied Biomaterials* **2005**, *75B*, 414.
[9] B. Dhariwala, E. Hunt, T. Boland, *Tissue Engineering* **2004**, *10*, 1316.
[10] K. Arcaute, B. K. Mann, R. B. Wicker, *Annals of Biomedical Engineering* **2006**, *34*, 1429.
[11] T. Yamaoka, Y. Tabata, Y. Ikada, *Journal of Pharmaceutical Sciences* **1994**, *83*, 601.
[12] A. S. Sawhney, C. P. Pathak, J. A. Hubbell, *Macromolecules* **1993**, *26*, 581.
[13] P. F. Jacobs, *Rapid Prototyping & Manufacturing: Fundamentals of Stereolithography*, Society of Manufacturing Engineers, Dearborn, MI **1992**.
[14] I. H. Lee, D. W. Cho, *International Journal of Advanced Manufacturing Technology* **2003**, *22*, 410.
[15] R. Gabbrielli, I. G. Turner, C. R. Bowen, *Key Engineering Materials* **2008**, *361-363 II*, 901.
[16] D. G. Stupack, X. S. Puente, S. Boutsaboualoy, C. M. Storgard, D. A. Cheresh, *Journal of Cell Biology* **2001**, *155*, 459.

Appendix A - Poly(D,L-lactide)/hydroxyapatite composite tissue engineering scaffolds prepared by stereolithography

Ferry Melchels[1], Jan Feijen[1] and Dirk Grijpma[1, 2]

Introduction

Hydroxyapatite (HAP) is a major component of bone and has osteoconductive and -inductive properties. It has been successfully applied as a substrate in bone tissue engineering, either with or without a biodegradable polymer such as polycaprolactone or polylactide.

Recently, we have developed a stereolithography resin based on poly(D,L-lactide) (PDLLA) and a non-reactive diluent, that allows for the preparation of tissue engineering scaffolds with designed architectures. In this work, designed porous composite structures of PDLLA and HAP are prepared by stereolithography.

Experimental

HAP powder (particle size <15 μm) was dispersed at 60 °C in poly(D,L-lactide) dimethacrylate macromer (molecular weight 1.2 kg/mol, end group conversion 96%). Then, a solution of Lucirin TPO-L photo-initiator (ethyl-2,4,6-trimethylbenzoylphenylphosphinate) and Orasol Orange G dye in N-methyl-2-pyrrolidone (NMP) was mixed in. The final resin composition was 63 wt% macromer, 19 wt% HAP, 15 wt% NMP, 3.1 wt% Lucirin photo-initiator, 0.06 wt% dye and 0.2 wt% inhibitor. This resin was used to prepare designed porous structures with a commercial stereolithography setup (Envisiontec Perfactory). The exposure time was 3.5 s per 25 μm thick layer, at a blue light intensity of 20 mW/cm². After extraction of diluent, dye and unreacted photo-initiator, the resulting PDLLA/HAP

---

[1] MIRA Institute for Biomedical Technology and Technical Medicine, and Department of Polymer Chemistry and Biomaterials, University of Twente, P.O. Box 217, 7500 AE, Enschede, The Netherlands

[2] Department of Biomedical Engineering, University Medical Centre Groningen and University of Groningen, P.O. Box 196, 9700 AD Groningen, The Netherlands

structures were analysed by micro computed tomography (μCT), X-ray photo-electron spectroscopy (XPS) and scanning electron microscopy (SEM).

Results and Discussion

The stereolithography resin was a homogeneous dispersion that showed no settling of HAP particles on the timescale of days.

Different composite porous structures were prepared from this resin by stereolithography, as shown in Figure A.1. The left cubic scaffold has a diamond architecture with a porosity of 74% and an average pore size of 707 μm (determined by μCT). The right disk-shaped scaffold has a gyroid architecture and is 53% porous with an average pore size of 310 μm.

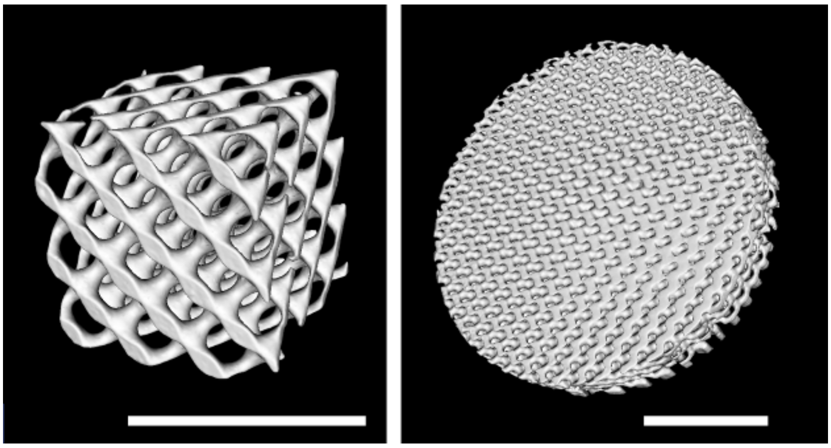

Figure A.1: μCT visualisations of two different PDLLA/HAP scaffolds built by stereolithography. Scalebar is 5 mm.

The XPS-results shown in Figure A.2 reveal the presence of Ca and P at the surface of the photo-crosslinked composite structures. The Ca:C molar ratio at the surface was 1:8.8, compared to 1:17.6 for the resin components. The SEM-images confirm the higher HAP concentration at the surface, as they show HAP particles sticking out of the network surface.

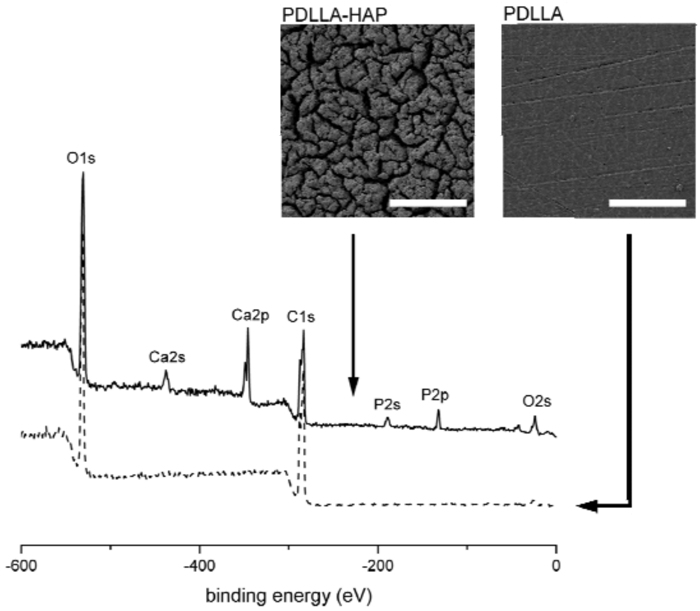

Figure A.2: XPS-analysis of photo-crosslinked PDLLA networks, with and without HAP. The scalebars in the SEM insets represent 200 μm.

The combination of an open porous architecture and the availability of HAP at the surface will make these structures most suited for bone tissue engineering.

Conclusions

Designed porous PDLLA/HAP composite structures were prepared by stereolithography. The ceramic particles are exposed to the surface, allowing the interaction of cells with HAP.

Acknowledgements

We would like to acknowledge the European Union for funding (STEPS project, FP6-500465).

Appendix B - Autoclave sterilisation of photo-crosslinked PDLLA networks

Ferry Melchels[1], Jan Feijen[1] and Dirk Grijpma[1, 2]

Introduction

Autoclaving is the golden standard of sterilising surgical tools and biomedical materials in the clinic. As hydrolytically degradable polymers are sensitive to moisture and high temperatures they can usually not be sterilised in this way, which impedes large-scale clinical application. However, crosslinking can greatly improve the thermal stability of a polymer, possibly enabling autoclave sterilisation. Here we show the effects of autoclave treatment on photo-crosslinked poly(D,L-lactide) (PDLLA) networks.

Experimental

Strips, disks and designed porous structures of photo-crosslinked PDLLA were prepared as described in Chapter 5, and subjected to autoclave treatment (121 °C for 27 min) using an autoclave setup (Astell scientific). Both treated and non-treated networks were characterised with regard to their mass, gel properties (gel content and degree of swelling) and tensile properties. The results were compared to those of linear high-molecular weight poly(D,L-lactide) (HMW PDLLA), obtained from Purac Biochem. Granules of the polymer were compression moulded into disks and strips. Molecular weights after compression moulding were M_n = 120 kg/mol and M_w = 289 kg/mol (determined by gel permeation chromatography).

Before and directly after autoclave treatment, structural analysis was performed on the stereolithography-built porous structures by micro-computed tomography (μCT) using a GE eXplore Locus SP scanner (General Electric) at 14.3 μm resolution. Scanning was done at an X-ray tube voltage of 80 kV, a current of 80 μA and an exposure time of 3000 ms (no filter). After reconstruction using the Feldkamp

---

[1] MIRA Institute for Biomedical Technology and Technical Medicine, and Department of Polymer Chemistry and Biomaterials, University of Twente, P.O. Box 217, 7500 AE, Enschede, The Netherlands

[2] Department of Biomedical Engineering, University Medical Centre Groningen and University of Groningen, P.O. Box 196, 9700 AD Groningen, The Netherlands

algorithm, GE MicroView software was used to obtain thresholded isosurface images and values for porosity and average pore size.

Results and Discussion

Table B.1 shows the mechanical and physical properties of photo-crosslinked PDLLA networks and high-molecular weight (HMW) PDLLA reference material in the dry state before autoclave sterilisation, and after the treatment. Both PDLLA materials take up only small amounts of water, but the influence of the treatment on the properties differs very much. HMW PDLLA lost more than half of its tensile strength on average, ranging from 20-90 % decrease in strength for 4 samples. The decrease for the PDLLA network was only 13 %, and similar for all of the measured samples. When comparing the gel properties and strength of the autoclaved networks to the results of the long-term degradation experiment at 37 °C (Chapter 5), it can be concluded that autoclave sterilisation corresponds to a period of between 1 and 8 weeks of immersing in PBS at body temperature.

Table B.1: Mechanical and physical properties of PDLLA networks and HMW PDLLA, before and after autoclave sterilisation.

		E (GPa)	σ (MPa)	ε (%)	water uptake (%)	gel content (%)	degree of swelling (-)
SLA	before	3.32±0.09	56.5±4.0	2.2±0.3		99.0±0.6	3.78±0.02
	after	3.41±0.08	49.4±2.5	2.1±0.1	0.43±0.02	96.7±0.5	4.09±0.08
HMW	before	2.86±0.06	41.7±0.6	1.8±0.1			
	after	1.98±0.35	15.5±12.2	0.9±0.7	1.37±0.43		

To demonstrate the shape-stability of PDLLA networks under the conditions of autoclave sterilisation, porous structures having well-defined architectures were fabricated by stereolithography using a PDLLA-based resin and autoclaved. The structures were scanned using micro computed tomography (μCT) before and directly after the autoclave treatment, in the hydrated state. Figure B.1 shows visualisations of the porous structures. It can be seen that the regular nature of the pore architecture is retained upon autoclave sterilisation. This is supported quantitatively by determining the porosity, the average pore size and the specific surface from the μCT-data (Table B.2).

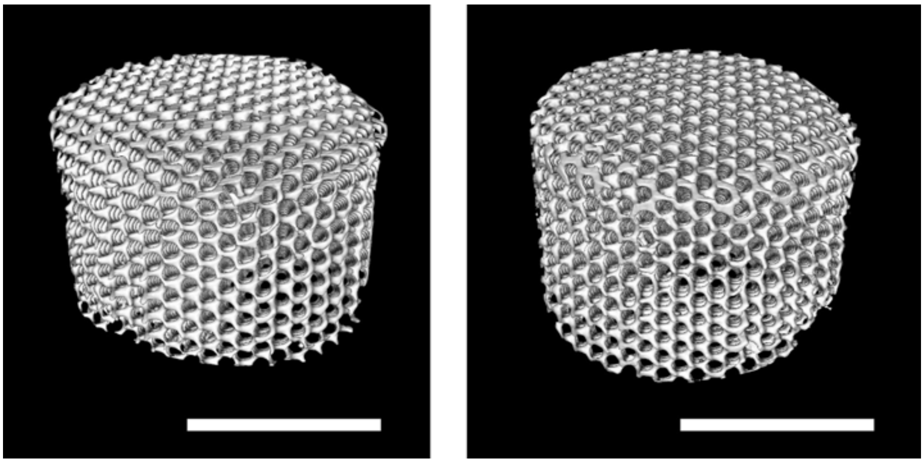

Figure B.1: Visualisations obtained from µCT scan data of stereolithography-built PDLLA scaffolds before (left) and after (right) autoclave treatment. Scale bars are 5 mm.

Table B.2: Comparison of structural parameters of porous structures before and after autoclave treatment, as determined by µCT. The values are average±standard deviation of 4 samples.

	porosity (vol %)	average pore size (µm)	specific surface area (mm^{-1})
before autoclave treatment	67.1±1.7	247±12	9.6±0.4
after autoclave treatment	67.5±1.6	230±21	9.5±0.6

Conclusions

Photo-crosslinked PDLLA networks are very well suited for autoclave treatment. The presence of crosslinks prevents deformation upon heating above the glass transition temperature. The minimal extent of hydrolytic degradation during the treatment ensures preservation of the network's strength. The ability to autoclave this degradable biomaterial makes it very well suited for clinical applications.

Acknowledgements

We would like to acknowledge the European Union for funding (STEPS project, FP6-500465).

Summary

Here the results of this thesis are summarised, referring to the aims as stated in **Chapter 1**. A review of the application of stereolithography in biomedical engineering is given in **Chapter 2**.

New stereolithography resins and their photo-crosslinked networks

Throughout this thesis, the syntheses of several new resins for stereolithography were described. All resins consisted of (in order of decreasing relative content): end-functionalised macromer, diluent, photo-initiator, dye and inhibitor.

As the main component, the macromer is also the main determinant for the physical properties of the final networks. Polylactide has a high glass transition temperature of 55 °C, and the use of polylactide oligomers leads to rigid, high-T_g networks (**Chapter 4**). On the other hand, the use of poly(D,L-lactide-*co*-ε-caprolactone) macromers leads to rubbery networks with a T_g below room temperature (**Chapter 6**). Also the mechanical properties and hydrophobicity (water uptake) of the networks are similar to those of their non-crosslinked, high molecular weight counterparts. Only when very low molecular weight macromers are used (<0.6 kg/mol), the resulting densely crosslinked networks show strongly deviating properties; an increased T_g and elastic modulus in particular. Macromers of molecular weights between 0.6 and 5 kg/mol have shown to be processable by stereolithography. Lower molecular weights lead to inferior (mechanical) properties. Higher molecular weights lead to too high viscosities, although this limit may be pushed higher when using lower T_g macromers, more diluent, or when fabrication at elevated temperatures.

The diluent used in the photo-crosslinking process can be either reactive or non-reactive. A *reactive* diluent becomes part of the network and therefore strongly influences its properties. The relative amount of NVP in polylactide-fumarate networks was shown to influence particularly the water uptake and the mechanical properties of the wet networks (**Chapter 3**). In order to obtain networks with low NVP contents, one could use a combination of NVP and a non-reactive diluent to obtain resins with appropriate viscosities. A *non-reactive* diluent is used to decrease resin viscosity during the fabrication process, and is extracted from the network afterwards. This results in shrinking of the built parts, but this shrinking is isotropic and can be accounted for in the design (**Chapter 6**). The amount of diluent that is required to obtain a suitable viscosity, depends on the molecular weight and molecular architecture of the macromer (**Chapter 4**). Higher molecular weight macromers require more diluent, and result in more flexible but also more fragile solvent-swollen networks structures during the building process. However, these networks also have a lower crosslink density and can swell and shrink more without building up too much stress in the network. Here, we used dimethacrylated PDLLA oligomers of two different molecular weights for stereolithography fabrication: 0.6 kg/mol with 19 wt% diluent (**Chapters 4 and 8**) and 5.0 kg/mol (**Chapters 5, 6 and 7**) with 40 wt% diluent. It is expected that the optimum for ease of fabrication with minimal stresses in the network lies in-between these values, although this will depend on the application.

The choice of photo-initiator depends primarily on the used light source and solubility in the resin. A concentration of photo-initiator as used here (2-6 wt%) ensures high reactivities in the fabrication process and networks with low kinetic chain lengths (**Chapter 5**).

A dye was shown to be essential for accurate fabrication by stereolithography. At the wavelength of the used light source, the used photo-initiator alone does not result in an adequate decay in light intensity with distance from the illuminated surface. Addition of 0.15 wt% orange dye limits the penetration depth of the light, so thin layers with a controlled thickness could be cured in the layer-by-layer fabrication process (**Chapter 4**).

Finally, a small amount of inhibitor proved a valuable addition for any stereolithography resin as it improves the shelf-life by preventing preliminary crosslinking reactions.

Besides the aforementioned resins, also a PDLLA-hydroxyapatite composite resin (**Appendix A**) and a poly(ethyleneglycol-*co*-lactide)-based resin for the fabrication of structured hydrogels (**Chapter 9**) were synthesised and used in stereolithography fabrication. The fabricated composite structures were shown to have a high hydroxyapatite content at the surface and are promising for bone tissue engineering applications. The hydrogel structures are the first reported biodegradable hydrogels prepared by stereolithography. The designed pore network was very well reproduced, resulting in structured gels with high pore interconnectivity that were highly deformable (up to 70 % strain) without damage. The prepared hydrogel scaffolds supported attachment and proliferation of human mesenchymal stem cells. With some adjustments (particularly type and concentration of initiator), the encapsulation of living cells in biodegradable hydrogels with well-defined architectures might become possible. With the new resins for stereolithography described in this thesis, the number of available resins and range of properties of biodegradable stereolithography-built parts has been extended significantly.

The resin based on 5 kg/mol PDLLA-dimethacrylate macromers and 40 wt% NMP non-reactive diluent was used most, and the corresponding network material of particularly this resin was characterised thoroughly (**Chapter 5**). The physical properties of these networks are quite similar to those of linear high-molecular weight PDLLA: elastic modulus of 2.6±0.1 GPa, tensile strength of 47±2 MPa and elongation at break of 2.3±0.3 %. The networks show low water uptake of 0.7±0.1 wt% and a glass transition temperature of 58±1 °C. However, the degradation behaviour is quite different. Whereas linear high-molecular weight PDLLA looses its strength upon immersion in phosphate buffered saline at 37 °C already within one month, the network material retains its shape and mechanical stability for up to 4 months. Then, it takes only a short time for the material to collapse and loose most of its mass. Sophisticated nuclear magnetic resonance spectroscopy of the networks in the solvent-swollen state revealed the number-average molecular weight of the polymethacrylate chains that will be formed upon degradation of the networks. These are in the range of 1.4-2.8 kg/mol for bulk photo-initiated networks, and 3.7-7.5 kg/mol for computer-designed network structures prepared by stereolithography in the presence of a dye. These values are far below the threshold for renal clearance. Their chemical and physical properties and their degradation behaviour make these biodegradable networks well suited for orthopaedic applications and as scaffold material for (bone) tissue engineering.

All the described photo-crosslinked materials were shown to support cell seeding and culturing, mediated by adsorbed proteins from the culture medium. The proliferation rate on PDLLA-dimethacrylate networks was shown to be comparable to that on high molecular weight poly(D,L-lactide) and on tissue culture polystyrene (**Chapter 4**). For the hydrogel structures, cell adhesion would be facilitated by the incorporation of cell adhesive peptides such as the RGD-sequence.

Novel tissue engineering scaffolds prepared by stereolithography

In **Chapter 6** we showed the versatility of stereolithography with respect to materials and freedom of design. Porous scaffolds were designed with computer software and built with either a poly(D,L-lactide)-based resin or a poly(D,L-lactide-*co*-ε-caprolactone)-based resin. The designs were either composed using 3D design software (the cubes architecture) or described by mathematical equations (the gyroid and diamond architectures). Characterisation of the scaffolds by micro computed tomography shows excellent reproduction of the designs, with pore sizes and porosities suitable for (bone) tissue engineering. The mechanical properties were evaluated in compression, and show good agreement with finite element predictions. The mechanical properties of scaffolds can be controlled by the combination of material and scaffold pore architecture; which are the optimal properties will depend on the application.

In **Chapter 7**, we demonstrated the consequences for tissue engineering application when employing well-defined, open pore network architectures such as the gyroid, compared to random-pore architectures such as those obtained by salt-leaching. Scaffolds of these types were prepared and showed comparable porosity and pore size values, but the gyroid type showed a more than tenfold higher permeability, due to the absence of size-limiting pore interconnections. The higher permeability significantly improved the wettability of the hydrophobic scaffolds, facilitating the inoculation of cells. After dynamic seeding followed by 5 days of static culture, gyroid scaffolds showed large cell populations in the centre of the scaffold, while salt-leached scaffolds were covered with a cell-sheet on the outside and no cells were found in the scaffold centre. It was shown that scaffold interconnectivity and permeability prolongs the time of static culture before overgrowth of cells at the scaffold periphery occurs. Furthermore, the freedom of design enables to further improve the transport of oxygen and nutrients throughout the scaffolds in the future.

This freedom of design also makes it possible to prepare scaffolds with gradients in pore size and porosity. The ability to prepare such scaffolds was first demonstrated in **Chapter 6**, and applied in a tissue engineering environment in **Chapter 8**. A model system was developed in which the distribution of cells throughout tissue engineering scaffolds can be influenced by means of scaffold pore architecture, using perfusion seeding. Two scaffold types with gyroid pore architectures were designed and prepared by stereolithography: one with an isotropic pore size (412±13 μm) and porosity (62±1 %), and another with a gradient in pore size (250-500 μm) and porosity (35 %-85 %). In the isotropic scaffolds, homogeneous distributions of cells were found after seeding, whereas in the gradient type scaffolds, higher densities of seeded cells were found in the scaffold centre, where the pores are largest. These results were compared to local flow parameters, wall shear rate in particular, using computational fluid flow modelling. The highest densities of seeded cells correlated to scaffold regions with larger pores, where the fluid velocities and wall shear rates were highest. Under the applied perfusion conditions, flow-induced cell detachment does not occur, and the cell deposition rate is mainly determined by local wall shear rates. These, in turn, are influenced strongly influenced by the architecture of the scaffold's pore network. The demonstrated ability to influence the distribution of seeded cells will be fundamental to control the engineering of complex 3D constructs with defined structural organisation, including zonal grafts.

Overall, we can conclude that a number of useful resins for stereolithography fabrication of biomedical devices have been developed. The possibility to sterilise these devices by autoclave treatment with preservation of shape and strength, is of particular interest for clinical application (**Appendix C**). The newly developed resins allowed the fabrication of tissue engineering scaffolds with well-defined pore network architectures. These architectures resulted in good and predictable mechanical properties, prolonged times of static culture with high cell densities throughout the scaffolds, and the ability to influence the distribution of seeded cells upon perfusion seeding. In the future, further tests both *in vitro* and *in vivo,* will allow optimisation of scaffold architectures and materials for the engineering of a wide range of tissues.

Samenvatting

Hier volgt een samenvatting van de resultaten van dit proefschrift, aan de hand van de doelstellingen zoals opgesomd in **Hoofdstuk 1**. Een overzicht van toepassing van stereolithografie in de biomedische technologie is gegeven in **Hoofdstuk 2**

Nieuwe harsen voor stereolithografie en hun gefotopolymeriseerde netwerken

In dit proefschrift is de synthese van diverse nieuwe harsen voor stereolithografie beschreven. Alle harsen bestaan (op volgorde van afnemende relatieve hoeveelheid) uit: eind-gefunctionaliseerd oligomeer (macro-monomeer of macromeer genoemd), verdunner, foto-initiator, kleurstof en polymerisatieremmer.

Het macromeer is als hoofdbestanddeel bepalend voor de fysische eigenschappen van de uiteindelijke netwerken. Poly(D,L-lactide) heeft een hoge glasovergangstemperatuur (T_g) van 55 °C, en het gebruik van poly(D,L-lactide) macromeren resulteert in stijve, glasachtige netwerken (**Hoofdstuk 4**). Het gebruik van poly(D,L-lactide-*co*-ε-caprolacton) macromeren daarentegen leidt tot rubberachtige netwerken met een T_g beneden kamertemperatuur (**Hoofdstuk 6**). Ook de mechanische eigenschappen en hydrofiliciteit (wateropname) van de netwerken zijn vergelijkbaar met die van hun niet verknoopte, hoog-molecuulgewicht tegenhangers. Een uitzondering geldt wanneer macromeren met een zeer laag molecuulgewicht worden gebruikt (<0.6 kg/mol). In dat geval vertonen de netwerken sterk afwijkende eigenschappen, met name een toename in de T_g en in de elasticiteitsmodulus. Van macromeren met een molecuulgewicht tussen 0.6 en 5 kg/mol is gebleken dat ze geschikt zijn voor gebruik in stereolithografie. Lagere molecuulgewichten leiden tot inferieure (mechanische) eigenschappen. Hogere molecuulgewichten leiden tot te hoge viscositeiten, hoewel deze limiet verder opgeschoven zou kunnen worden door macromeren met een lagere T_g te gebruiken, of te werken bij hogere temperaturen.

De verdunner die gebruikt wordt in het foto-polymerisatieproces kan reactief, danwel niet-reactief zijn. Een *reactieve* verdunner (zoals n-vinyl pyrrolidon, NVP) wordt onderdeel van het netwerk, en beïnvloedt daarom sterk de netwerkeigenschappen. Het gehalte NVP in poly(D,L-lactide)-fumaraatnetwerken beïnvloedt met name wateropname en de mechanische eigenschappen van natte netwerken (**Hoofdstuk 3**). Om een stereolithografiehars met een geschikte viscositeit te verkrijgen, en toch netwerken met een laag NVP-gehalte, zou een combinatie van NVP en een niet-reactieve verdunner gebruikt kunnen worden. Een *niet-reactieve* verdunner wordt gebruikt om de viscositeit van de hars te verlagen voor het fabricatieproces, en wordt nadien uit het netwerk geëxtraheerd. Dit resulteert in krimp van de gebouwde onderdelen, deze krimp is echter isotroop en er kan voor gecorrigeerd worden in het ontwerp (**Hoofdstuk 6**). De hoeveelheid verdunner die nodig is voor een geschikte viscositeit hangt af van het molecuulgewicht en de moleculaire architectuur van het macromeer (**Hoofdstuk 4**). Hogere molecuulgewichten vereisen meer verdunner, en resulteren in flexibelere, maar ook fragielere gezwollen netwerkstructuren tijdens het bouwproces. Deze netwerken hebben echter ook een lagere verknopingsdichtheid en kunnen meer zwellen en krimpen zonder dat er teveel spanning in het netwerk opgebouwd wordt. In dit proefschrift hebben we poly(D,L-lactide)-dimethacrylaat macromeren van twee verschillende molecuulgewichten gebruikt: 0.6 kg/mol met 19 gewichtsprocent verdunner (**Hoofdstukken 4 en 8**) en 5.0 kg/mol met 40 gewichtsprocent verdunner (**Hoofdstukken 5, 6 en 7**). Het is te verwachten dat het optimum voor probleemloze fabricatie en minimale spanningen in het netwerk tussen deze twee waarden in ligt. Dit zal echter van het ontwerp van de te bouwen structuur afhangen, alswel van de toepassing.

De keuze van foto-initiator hangt voornamelijk af van de golflengte van de gebruikte lichtbron, en van de oplosbaarheid in de hars. Een foto-intiatorconcentratie zoals hier gebruikt (2 tot 6 gewichtsprocent) verzekert hoge reactiviteiten in het bouwproces en netwerken met lage kinetische ketenlengtes (**Hoofstuk 5**).

Voor nauwkeurige fabricatie door middel van stereolithografie bleek toevoeging van een kleurstof aan de hars essentieel. De lichtabsorptie van de foto-initiator leidt niet tot voldoende afname van de lichtsterkte bij de golflengte van de gebruikte lichtbron. Toevoeging van 0.15 gewichtsprocent oranje kleurstof beperkt de indringdiepte van het licht, zodat dunne laagjes met een gecontroleerde dikte uitgehard kunnen worden in het laag-voor-laag bouwproces (**Hoofdstuk 4**).

Als laatste bleek een kleine hoeveelheid polymerisatieremmer een waardevolle toevoeging aan de harsen, omdat het de houdbaarheid verbetert door ongewenste vroegtijdige uithardingsreacties te voorkomen.

Behalve de voorgenoemde harsen, zijn ook een poly(D,L-lactide)/hydroxyapatiet hars voor composieten (**Bijlage A**) en een poly(ethyleenglycol-*co*-lactide) hars voor hydrogelen (**Hoofdstuk 9**) ontwikkeld en gebruikt in stereolithografie. De gebouwde composietstructuren hadden een hoog hydroxyapatietgehalte aan het oppervlak en zijn veelbelovend voor toepassing in botweefselregeneratietechnologie. De vervaardiging van bioafbreekbare hydrogelstructuren met behulp van stereolithografie werd nog niet eerder gerapporteerd. Het porienetwerk van de structuren kwam zeer goed overeen met het ontwerp, wat resulteerde in poreuze gelen met een hoge porie-doorverbondheid. De gelstructuren waren zeer vervormbaar (tot 70 % vervorming) zonder blijvende schade. De vervaardigde hydrogelen ondersteunden hechting en vermenigvuldiging van humane mesenchemale stamcellen. Met enkele aanpassingen (met name het type en de concentratie foto-initiator) zou het inkapselen van levende cellen in bioafbreekbare hydrogelen met goed gedefinieerde architecturen mogelijk gemaakt kunnen worden. Met de nieuwe harsen voor stereolithografie die in dit proefschrift beschreven zijn, is het aantal beschikbare harsen en het bereik aan eigenschappen van bioafbreekbare structuren gebouwd met stereolithografie, aanzienlijk uitgebreid.

De hars gebaseerd op 5 kg/mol poly(D,L-lactide)-dimethacrylaat macromeren en 40 gewichtsprocent NMP niet-reactieve verdunner werd het meest gebruikt, en het corresponderende netwerkmateriaal werd grondig gekarakteriseerd (**Hoofdstuk 5**). De fysische eigenschappen van deze netwerken zijn vergelijkbaar met die van lineair poly(D,L-lactide) van een hoog molecuulgewicht: een elasticiteitsmodulus van 2.6±0.1 GPa, een treksterkte van 47±2 MPa en een rek bij breuk van 2.3±0.3 %. De netwerken vertonen een lage wateropname van 0.7±0.1 gewichtsprocent en een glasovergangstemperatuur van 58±1 °C. Het degradatiegedrag is echter behoorlijk afwijkend. Terwijl lineair hoog-molgewicht poly(D,L-lactide) in een fosfaatgebufferde zoutoplossing bij 37 °C zijn sterkte al binnen een maand verliest, behoudt het netwerkmateriaal zijn vorm en mechanische stabiliteit tot 4 maanden. Vanaf dat moment duurt het slechts een korte tijd voor het materiaal uiteenvalt en het grootste deel van zijn massa verliest. Na degradatie blijven er polymethacrylaatketens over, waarvan het molecuulgewicht bepaalt of ze via de nieren uitgescheiden kunnen worden. Met behulp van nucleair-magnetische resonantie spectroscopie van de netwerken gezwollen in oplosmiddel, werd het het aantalgemiddelde molecuulgewicht van deze ketens vastgesteld. Voor in bulk licht-uitgeharde netwerken ligt deze waarde tussen 1.4 en 2.8 kg/mol, en voor netwerkstructuren vervaardigd met stereolithografie (in de aanwezigheid van een kleurstof) is de waarde 3.7 tot 7.5 kg/mol. Deze waarden liggen alle ver onder de drempelwaarde voor uitscheiding door de nieren. De chemische en fysische eigenschappen van deze netwerken, evenals het degradatieprofiel, maken deze bioafbreekbare materialen zeer geschikt voor zowel orthopedische toepassingen als (bot)weefselregeneratietechnologie.

Alle beschreven netwerkmaterialen ondersteunen het zaaien en kweken van cellen, na adsorptie van eiwitten uit kweekmedium. De vermenigvuldigingssnelheid van cellen op poly(D,L-lactide)-dimethacrylaat netwerken was vergelijkbaar met die op hoog-molecuulgewicht poly(D,L-lactide) en die op polystyreen voor weefselkweek (**Hoofdstuk 4**). Voor de hydrogel-structuren zou celhechting vergemakkelijkt kunnen worden door bijvoorbeeld het inbouwen van peptiden die RGD-sequenties bevatten.

Nieuwe dragerstructuren voor weefselregeneratietechnologie vervaardigd met behulp van stereolithografie

In **Hoofdstuk 6** hebben we de veelzijdigheid van stereolithografie met betrekking tot materiaalkeuze en ontwerpvrijheid gedemonstreerd. Poreuze dragermaterialen werden ontworpen met computersoftware en gebouwd met zowel een op poly(D,L-lactide) gebaseerde hars als een op poly(D,L-lactide-*co*-ε-caprolacton) gebaseerde hars. De ontwerpen werden samengesteld met 3D ontwerpsoftware (de kubussen-architectuur) of beschreven met wiskundige vergelijkingen (de gyroid- en diamant-architectuur). Karakterisatie van de gebouwde structuren met behulp van micro-CT scans onthulde een uitzonderlijk goede overeenkomst met de ontwerpen, met poriegrootten en porositeiten die geschikt zijn voor (bot)weefseltechnologie. De mechanische eigenschappen werden bepaald door middel van mechanische drukproeven, en kwamen goed overeen met voorspellingen gebaseerd op eindige-elementenanalyse. De mechanische eigenschappen van poreuze structuren kunnen gestuurd worden door de combinatie van materiaal en porie-architectuur; de optimale eigenschappen hangen af van de toepassing.

In **Hoofdstuk 7** hebben we het gebruik van goed gedefinieerde, open netwerkstructuren als dragermaterialen voor weefseltechnologie onderzocht. De regelmatige gyroid-architectuur werd vergeleken met de willekeurige porie-architectuur die verkregen wordt met zout-uitwassing. Beide poreuze structuren vertoonden vergelijkbare porositeit en poriegrootte, maar het gyroid-type had een meer dan tienvoudige permeabiliteit als gevolg van grotere porieverbindingen. De hogere permeabiliteit verbeterde de bevochtigbaarheid van de hydrofobe structuren aanzienlijk, wat het zaaien van cellen vergemakkelijkte. Na dynamisch zaaien gevolgd door 5 dagen statisch kweken, vertoonden de gyroid dragers grote celpopulaties in het midden van de structuren. De zout-uitgewassen dragerstructuren waren daarentegen bedekt door een cellaag aan de buitenkant en er werden geen cellen gevonden in het midden van de structuren. Er werd aangetoond dat een hoge interconnectiviteit en permeabiliteit het moment van dichtgroeien van de periferie uitstellen. Bovendien geeft de ontwerpvrijheid mogelijkheden om het transport van zuurstof en voedingsstoffen door de dragerstructuur te verbeteren.

De genoemde ontwerpvrijheid maakt het ook mogelijk om dragerstructuren te maken met een gradiënt in poriegrootte en porositeit. De mogelijkheid om zulke structuren te vervaardigen werd eerst gedemonstreerd in **Hoofdstuk 6**, en toegepast voor weefseltechnologie in **Hoofdstuk 8**. Er werd een modelsysteem op basis van een perfusiebioreactor ontwikkeld, waarmee de verdeling van cellen door dragerstructuren beïnvloed kan worden middels de porie-architectuur. Twee typen dragerstructuren met een gyroid-architectuur werden ontworpen, en vervaardigd met stereolithografie: één met een isotrope poriegrootte (412±13 μm) en porositeit

(62±1 %), en één met een gradiënt in poriegrootte (250-500 μm) en porositeit (35 %-85 %). In de isotrope structuren waren de cellen na het zaaien homogeen verdeeld, terwijl in de structuren van het gradiënt-type hogere celdichtheden werden gevonden in het midden. De resultaten werden vergeleken met lokale stromingsparameters, verkregen door computersimulaties van vloeistofstroming. De hoogste celdichtheden kwamen voor in de grootste poriën, waar tevens de hoogste waarden voor stroomsnelheid en afschuifsnelheid gevonden werden. Onder de toegepaste stromingscondities vindt er geen celonthechting veroorzaakt door stroming plaats, en wordt de depositiesnelheid van cellen voornamelijk bepaald door lokale afschuifsnelheden aan de wand. Deze worden op hun beurt sterk beïnvloed door de porie-architectuur van de drager. De getoonde mogelijkheid om de verdeling van gezaaide cellen te beïnvloeden is belangrijk voor het kweken van complexe weefsels met gedefinieerde zones.

Over het geheel kunnen we concluderen dat een aantal nuttige stereolithografieharsen voor biomedische toepassingen zijn ontwikkeld. De mogelijkheid om gebouwde structuren in een autoclaaf te steriliseren met behoud van vorm en sterkte, opent de weg naar klinische toepassing (**Bijlage B**). De nieuw ontwikkelde harsen maken de vervaardiging van dragerstructuren met goed gedefinieerde porienetwerk-architecturen mogelijk. De vervaardigde structuren hebben goede en voorspelbare mechanische eigenschappen, staan langere kweektijden toe met hogere celdichtheden door het porienetwerk heen, en geven de mogelijkheid om de verdeling van gezaaide cellen te beïnvloeden. Verdere optimalisatie van de architectuur van dragermaterialen zal naar aanleiding van *in vitro* en *in vivo* experimenten mogelijk worden, evenals de vervaardiging van een variatie aan weefsels.

Epilogue

This thesis not only forms the embodiment of nearly five years of work, it also marks the end of an era. In August 1998, I left the house where I was born to settle in Enschede, where I would spend the next 11½ years of my life. I met many friends and enjoyed the student life on the campus; the sports, the music, the Grolsch. I also liked the subject of my studies and masters project, so it didn't take much thinking when my supervisor Dirk Grijpma offered me a chance to continue my exploratory work on stereolithography as a PhD student in the Polymer Chemistry and Biomaterials group.

I first learned the skills of polymer synthesis, chemical modification and photo-polymerisation in the old Langezijds-labs, according to the Dutch saying 'op een oude fiets moet je het leren'. It had the advantage that you didn't need to work all that clean and tidy, and the smelliness and the rainwater-collecting buckets in the corridors created a certain atmosphere as well. We also had our MTP- and RBT-colleagues there, insuring lots of birthday cakes at the coffee breaks, as well as many borrels and crazy parties. In November 2006 we moved to the brand new facilities in the Zuidhorst. A new environment also meant a different atmosphere and new friends. With all these health-freaks, there suddenly was severe competition at the yearly triathlon. And of course, in the Zuidhorst, I got my 'toy' from Bilthoven, so the real work could start.

My work was part of a project financially supported by the European Union, with many partners all throughout Europe. This meant travelling around for meetings, which was absolutely great. I saw lots of Italy and went to Barcelona, Warsaw, Ulm and Paris. I also went to Liverpool, but got there one week too early so I missed the meeting and just did the holiday part. Being in this consortium also meant possibilities for collaborations, which resulted in Chapter 8. Ivan, David and Bea, grazie mille for the great time I've spent with you in Basel and all the things I learnt. Damien and Andy, muchas gracias for our collaboration as well.

Within the University of Twente there were also several collaborations. I thank Ana, Katia and Aldrik for the nice times we had, the work we did together and the value you've added to my thesis. Through the years, I've also supervised several students for their bachelors, masters or Erasmus projects. Joram, Janine, Richelle and Tetsu Melissa, thanks for the work and the good times we had. Another person I'd like to thank but who doesn't fall into any category in many aspects, is Ruggero. To me you've been at least as inspiring as you've been confusing, and my thesis wouldn't have looked as good as it does if we hadn't met back in Brighton. Grazie.

And then there is the PBM-crowd that I've spent many good years with. I will remember by promoter professor Jan Feijen as a hard-working man with a good sense of humour. A few keywords: het peerd van ome Loek, champagne, a dozen of blue-and-red ties. Dirk, you've put a lot of work in converting me from a 'prutser' to a PhD. I really enjoyed learning an awful lot from you, and for me you will remain a kind of Grote Smurf. Of the other staff, I would like to mention Karin and Zlata in particular, who have always been of great support.

I will not try to mention all AIO's, students, post-docs and staff members I've shared good times with by name, as I'm sure I will forget some. I thank you all!! I would just like to mention some colleagues whose friendship I value in particular. Erhan, you showed me that not everyone can so easily get a position like ours, and that made me appreciate it more. Although it sometimes made me feel a bit guilty to see you work so hard, you have been a great example. For that and our friendship: teşekkürler! Siggi, I feel we have looked well after each other through the years; there's not much we didn't share. Vielen Dank dafür. Sameer, I've always appreciated your good moods, singing and dancing in the lab. Also thanks for the life lessons you taught me (or tried at least). Jet, I'm really happy we stayed friends after you left the group, let's keep it up!

To be able to work hard, I was happy to have some hobbies and people to distract me from it every now and then. The runs in the forest over lunch breaks were really good for this, so I thank Jetse, Wico and Hugo for 'taking me out'. Possibly the best distraction was the band, CupSizeD. I cherish our years of rehearsals, jams, WAP-sessions and -of course- the gigs. Many thanks for that to Ric, Ruben, Thomas, Thijs, Wico, Anita and Bart.

To save the best for last: I owe an inexpressible load of thanks to Willeke. You enabled me to do things that I often thought I would never accomplish. When I was giving up on running because of my knee injury, you made me see several doctors. Finally, I ran a marathon. With this PhD and the thesis it was often the same. You were not only there to help me with things I couldn't find time for, but you've helped me with the work itself as well: reviewing texts and presentations, coming up with ideas, and showing me the big picture when I was lost in details. You have always been there for me, while often I was not there for you. You deserve to be a co-author of this thesis, I'm sorry that you'll have to do with just this paragraph… I love you!

Ferry
April 2010